Optically-Active Nanomaterials for Diagnostic and Therapeutic Applications in Ovarian Cancer

Optically-Active Nanomaterials for Diagnostic and Therapeutic Applications in Ovarian Cancer

A dissertation presented

by

Alexander Bagley

to

The Committee on Higher Degrees in Biophysics

in partial fulfillment of the requirements

for the degree of

Doctor of Philosophy

in the subject of

Biophysics

Harvard University

Cambridge, Massachusetts

May 2014

Dissertation Advisor: Professor Sangeeta Bhatia, M.D., Ph.D. Alexander Bagley

Optically-Active Nanomaterials for Diagnostic and Therapeutic Applications in Ovarian Cancer

ABSTRACT

The clinical management of cancer has principally relied upon surgery, radiation therapy, and chemotherapy for many decades. Despite recent advances in molecularly-targeted diagnostic and therapeutic agents, the long-term survival rates in patients with solid malignancies including ovarian cancer have improved only incrementally. Nanotechnologies designed to locally interrogate and modulate the tumor microenvironment offer a promising opportunity to enhance existing treatment modalities and establish new therapeutic paradigms. By virtue of their elemental composition, geometry, and surface chemistry, nanomaterials can be engineered with optical and pharmacokinetic properties which permit these agents to localize, fluoresce, and deposit energy within tumors. Nanomaterials therefore provide a clear route towards future approaches for sensitive diagnosis and imaging of tumors and targeted therapeutic delivery.

This thesis describes the development and application of optically-active nanomaterials for non-invasive imaging, localized heating of deep tumors, and enhanced therapeutic delivery, each explored in the context of ovarian cancer. Because effective cytoreduction of ovarian tumors remains one of the most significant prognostic factors for long-term survival, the first part of this thesis explores a nanomaterial-inspired imaging approach for guiding cytoreductive surgery. Single-walled carbon nanotubes are shown to selectively target deep ovarian tumors and through their fluorescence in the second near-infrared window, guide cytoreduction of sub-millimeter tumors. The second component of the thesis focuses on the application of plasmonic gold nanorods for locally heating tumors in clinically-relevant anatomical contexts, including photothermal ablation of a genetically-engineered sarcoma model and milder heating of orthotopic ovarian xenografts using an implanted near-infrared source. Lastly, because therapeutic delivery to solid tumors can be enhanced by heating, the final section of the thesis explores the effects of gold nanorod-mediated heating on therapeutic delivery in ovarian tumor models. In the clinic, chemotherapy is administered in multiple cycles spanning weeks to months, so we investigated multiple exposures to gold nanorod heating; a transient period of thermotolerance was observed and a role for the endothelial heat shock response identified. Collectively, this work demonstrates how next-generation nanomaterials may prove useful in the clinic for diverse applications in cancer management ranging from imaging to drug delivery.

TABLE OF CONTENTS

LIST OF FIGURES

ACKNOWLEDGEMENTS

Completing a thesis is far from a solitary pursuit. Many individuals have contributed directly to the work described here and more broadly, to my development as a physician-scientist and person. To each person who has played a role – big or small – I am deeply appreciative and thankful. Here, I would like to acknowledge those individuals who have been particularly important towards the completion of this thesis.

First and foremost, Professor Sangeeta Bhatia has consistently been an exceptional mentor and role model. Her encouragement, optimism, and guidance were essential to the design and completion of this work. As a professional role model, Sangeeta has taught me many things through her example: the ability to keep one's eye focused on the big questions in the field, the confidence to pursue those questions with ambitious, creative, outside-the-box approaches, and the importance to find balance between one's work and family life. It has been an honor to learn from Sangeeta, and I am most thankful for her unwavering support during my time in her laboratory.

I am grateful to each member of my thesis committee for collectively providing their insights and direction, as well as these additional reasons: Professor Robert Langer, for inspiring me as a high school student to pursue biomedical research and attend MIT to study engineering; Professor Angela Belcher, for setting an example for bold, creative thinking in science; Professor Elazer Edelman, for being a wonderful role model to aspiring physician-scientists; and Professor Dan Kohane, as my premedical advisor at MIT, for helping me clarify and articulate my desire to become a physician-scientist in the first place.

Navigating not one, but two large institutions over the course of completing this thesis has been made immeasurably easier because of the Harvard Biophysics Program and MD-PhD program. Professor Jim Hogle and Michele Jakoulov provided a friendly, welcoming, stress-free, and supportive home department, and by doing so, managed to make the entire process – from the qualifying exam to DAC meetings to preparing the thesis – run very smoothly. Thank you Michele and Jim for your support from beginning to end! From the MD-PhD program, many thanks to Steve Blacklow, Loren Walensky, Linda Burnley, Yi Shen, Robin Lichtenstein, and Amy Cohen.

I have been very fortunate to work alongside such an intelligent, passionate, and fun group of scientists and staff in the Laboratory for Multiscale Regenerative Technologies (LMRT). In particular, Gabe Kwong has not only been a terrific research mentor and baymate, but has also been a great workout partner and friend. To Angela Zhang, my talented and dedicated UROP student, I appreciate all of your efforts in the lab, your focus, attention to detail, and your friendly personality – you're well on your way to becoming a talented physician-scientist. To Heather Fleming, Sue Kangiser, and Lia Ingaharro, I appreciate your efforts to make the lab run so smoothly, helping every lab member focus on their science. To postdocs Kathleen Christine, Rob Schwartz, Kelly Stevens, Ester Kwon, Tal Danino, Sabine Hauert, Arnout Schepers, Piyush Jain, and Salil Desai: thank you for your willingness to help me with questions ranging from the technical to experimental design and for being the thought leaders in the lab with a wealth of knowledge, experiences, and perspectives to share. Among the graduate students, I am particularly grateful to Shengyong Ng, for being a friendly, supportive, and knowledgeable labmate; Kevin Lin, for teaching me a number of methods and for being a great collaborator early on in my thesis; and Justin Lo, a fellow MD/PhD candidate and MIT graduate, for his friendship, enthusiasm, and incredible generosity of time and effort towards helping others in the lab. I am part of a continuum of LMRT students, some who have come before (Nate Reticker-Flynn, Cheri Li, Kartik Trehan, Yin Ren, David Braga Malta, Geoffrey von Maltzahn, Alice Chen, Todd Harris) and others who represent the next generation (Andrew Warren, Vyas Ramanan, Jaideep Dudani, Arnav Chhabra, Nil Gural) – simply put, I am proud to be among such a group of talented, hard-working, and creative scientists.

It was a privilege to collaborate with scientists from MIT, the Boston area, and beyond during this thesis. In particular, Debadyuti (Rana) Ghosh was fantastic to work beside, learn from, talk sports and music with, and always keep it fun in the lab. Dr. Young Jeong Na graciously offered his time and surgical expertise on numerous occasions. Ruthie Scherz-Shouval and Pete Galie were wonderful to work with on various aspects of the endothelial heat shock response project. Sam Hill, Gary Rogers, Daniel Karl, and Alexia Zhang were enthusiastic, reliable, and hard-working collaborators. The Koch Institute Core Facilities and staff were indispensable to this work. Jeff Wyckoff is a master of intravital microscopy and the intravital data would not have been possible without his help. I am also thankful for the help of Scott Malstrom (ATWAI), Glenn Paradis (Flow), Mike Brown (Histology), Denise Crowley (Histology), Kathy Cormier (Histology), and Dr. Rod Bronson (Pathology). I am also deeply appreciative of all the animals involved in this research.

Having spent the past decade at MIT, I have been fortunate to have a number of dedicated and inspirational mentors from the MIT community. Professor David M. Sabatini was very gracious to invite me to spend a summer in his laboratory during high school and throughout college; it was an ideal place to begin my research career – working beside such smart and friendly people (Siraj Ali, Dave Guertin, Yasemin Sancak, Andrew Markhard, Shomit Sengupta, Rob Lindquist, Doug Wheeler, Steve Bailey, Caitlin Higgins, and more). As a scientist, David continues to inspire me for his abundance of creative insights and I am thankful for his support over the years. My undergraduate advisor, Institute Professor Daniel I.C. Wang, was a very generous and committed mentor and helped guide me during my undergraduate years. My basketball coaches, Larry Anderson, Dr. Oli Eslinger, and Paul Grant, demanded excellence and our fullest effort for the team; the lessons learned on the court have translated to other aspects of my life (including this thesis), and for helping instill that internal intensity and drive to succeed, I am thankful to each of my coaches.

To my MD-PhD colleagues, I feel privileged to share this lengthy training journey with you. To Rishi Puram, the journey goes back further still, to our freshman year at MIT. Rishi has been a great friend, a brother, through all the years, and I am so thankful for his friendship. To my Anatomy partners and good friends, Jon Herman and Billy Hwang, thank you for being so passionate and talented about your work; it's an honor to call you both friends. To Vineeta Agarwala, Jeff Ishizuka, Katie Lee Hwang, Laura Jacox, Eric Bent, HST friends (Albert Chiou, Khang Nguyen, Mike Coulter, Albert Kwon, Nina Mann, Gaurav Gulati, et al.), and friends from outside medical school (Jon Reisman, Albert Chi, Sravanti Kusuma, David Lin, and Dan Hart) we have shared many great memories together and I will always carry those with me and cherish them.

Throughout this thesis, I have been lucky to call Winthrop House my home. To House Masters Ron Sullivan and Stephanie Robinson, Resident Dean Gregg Peeples, fellow Tutors (Gaurav Upadyhay and Smita Singh, Laura Ralston, Josh and Judy Rosenbloom, Brian and Laura McCammack, Luke Leafgren and Lindsay Noll, Joel Yao, and the rest of Team Awesome), the wonderful staff (Joanna Miller, Dennis Mallinson, Heather Grant, David Simms, Enoch and Joe), and the many undergraduates I have had the pleasure to advise and see go off to medical schools across the country, thank you for creating such a wonderful, inclusive, diverse, and enjoyable community to call home.

To my sister and brother, Sarah and Ben, I am so proud to be your big brother. I have watched both of you blossom into the smart, kind, and honest young adults who you are today. I hope that you always remember that within each of you is the capacity to do great things, and trust that your talents, work ethic, and kind hearts will lead you to a fulfilling life. Thank you for being the best siblings that I could ever ask for. I love you guys!

To my Nana, Myrna Bagley, and late grandfather William Bagley, Christine, all of my aunts, uncles, and cousins, and my future family members from the Mombell and Maribona families, thank you for showing your support and interest towards my work over the years. I am greatly appreciative to have all of you in my life and I look forward to many more happy memories together.

To my father, Norman Bagley, since those long ago days of solving math word problems together at Cravings ice cream store – thank you for helping cultivate my interest in science from an early age. Your skill as an engineer, in frequently thinking up inventions or proposing new ideas, in creating and maintaining a business – all of these elements are qualities I have tried or will try to incorporate in my own career. Above all, thank you for encouraging me to ask bold, big picture questions and instilling the belief that I can contribute to their solutions.

To my mother, Norine Glick: Words cannot do justice to my thankfulness and gratitude to you. Throughout my entire life, you have always been there as my #1 supporter, guiding me towards my true interests, helping me through tougher times, and encouraging me to pursue my dreams. The person who I am today, what I value most in this life, and what I aspire for later on – a loving family, a career blending compassion and discovery, and a humorous, good-natured outlook on life – are all due to you. Growing up, I always felt supported and free to explore my interests. You are truly an amazing parent and person, full of compassion, humor, and intelligence, and I am blessed to have you as my mother.

To Laura, my best friend and the love of my life, thank you for making the 3,000+ mile trek to Boston so that we could finally meet each other. On that note, thank you for your genuine interest in science – and for actually enjoying it when our first conversation ever was about gold nanoparticles. Your support and constant encouragement during this thesis meant so much. I am excited to continue building our life together, as the proud dog parents of Reggie among other highlights, and have many more adventures together.

Lastly, this thesis is dedicated to my grandparents, Sidney and Shirley Glick, two of the strongest and wisest human beings I have ever known, who showed me what true love is, and who often reminded me of the importance of finding pure and simple enjoyment in one's endeavors.

EPIGRAPH

"What would the properties of materials be if we could really arrange the atoms the way we want them? […] I can hardly doubt that when we have some control of the arrangement of things on a small scale we will get an enormously greater range of possible properties that substances can have, and of different things that we can do."

– Richard Feynman, "Plenty of Room at the Bottom" (1959)

"Much has been written about the nature of scientific discovery. […] Originality and simplicity are certainly crucial elements. Even more important are the intellectual fearlessness and emotional drive to put it all together, step forward, do the right experiment, promulgate it to the world, defend the new insights, and go forward to further innovation."

– Solomon Snyder, "The Audacity Principle in Science" (2005)

"To see the world in a grain of sand,
And a heaven in a wild flower,
Hold infinity in the palm of your hand,
And eternity in an hour."

– William Blake (1863)

CURRICULUM VITAE

Alexander F. Bagley
550 Winthrop Mail Center
Cambridge, MA 02138

EDUCATION:

2008 – Present	Harvard Medical School, Boston, MA M.D./Ph.D. Candidate
2004 – 08	Massachusetts Institute of Technology, Cambridge, MA B.S., Chemical-Biological Engineering; B.S., Biology; Phi Beta Kappa
2000 – 04	St. John's Preparatory School, Danvers, MA Valedictorian Medal

PROFESSIONAL HONORS AND AWARDS:

2014	Koch Institute Public Galleries Image Award
2013	Koch Institute Stanley (1958) and Bonnie Klein Research Travel Fellowship
2011	American Medical Association (AMA) Foundation Leadership Award
2008	Medical Scientist Training Program (MSTP) Fellowship
2008	Phi Beta Kappa, MIT Chapter
2008	Jack Barry Award, MIT Basketball
2008	ESPN the Magazine Academic All-District Team
2007	Sigma Xi, MIT Chapter
2007	Merck Engineering and Technology Fellowship
2006	Barry M. Goldwater Congressional Scholarship
2005	Tau Beta Pi, MIT Chapter
2004	Stephen Phillips Memorial Scholarship
2004	Jewish War Veterans National Scholarship

PUBLICATIONS:

1. **Bagley, A.F.**, *et al*. "Endothelial Heat Shock Response Modulates Nanoparticle Accumulation in Tumors." (2014) *In Preparation*.
2. Ghosh, D.*, **Bagley, A.F.***, Na, Y., Birrer, M., Bhatia, S.N., Belcher, A.M. "Deep, non-invasive imaging for surgical guidance of sub-millimeter ovarian tumors using targeted single-walled carbon nanotubes." (2014) *In Revision*.
3. Hauert, S., Rubenstein, M., Berman, S., **Bagley, A.F.**, Nagpal, R., Bhatia, S.N. "Swarm-robotic experiments to validate and improve the penetration of targeted nanoparticles into tumors." (2014) *In Review*.
4. **Bagley, A.F.**, Hill, S., Rogers, G.R., Bhatia, S.N. "Plasmonic Photothermal Heating of Intraperitoneal Tumors through the Use of an Implanted Near-Infrared Source." ACS Nano. (2013)
   Featured in Science Translational Medicine Editor's Choice "Implantable Lanterns for Cancer Therapy" (2013)
5. **Bagley, A.F.**, Daneshvar, D.H., Schanker, B.D., Zurakowski, D., D'Hemecourt, C.A., Nowinski, C.J., Cantu, R.C., Goulet, K. "Effectiveness of the SLICE Program for Youth Concussion Education." (2012) Clin J of Sport Med. 22(5): 385-389.
6. Lin, K.Y.*, **Bagley, A.F.***, Zhang, A.Y., Karl, D.L., Yoon, S.S., Bhatia, S.N. "Gold Nanorod Photothermal Therapy in a Genetically Engineered Mouse Model of Soft Tissue Sarcoma." (2011) Nano LIFE. 1(3-4): 277-87.

7. Sarbassov, D., Ali, S.M., Sengupta, S., Sheen, J.H., Hsu, P.P., **Bagley, A.F.**, Markhard, A.L., Sabatini, D.M. "Prolonged Rapamycin Treatment Inhibits mTORC2 Assembly and Akt/PKB." (2006) Molecular Cell 22(2), 159-68.

PATENTS:

1. **Bagley, A.F.**, Bhatia, S.N. "Gold Nanoparticles for Enhanced Accumulation of Therapeutic and Diagnostic Cargoes." Filing Date: 08/20/2013. *Pending*.
2. Belcher, A.M., Bhatia, S.N., Bhardan, N.M., **Bagley, A.F.**, *et al*. "Enhancing video-rate fluorescence imagery collected in the second near-infrared optical window for diagnostic, real-time surgical and post-surgical monitoring applications." *In Preparation*.

PRESENTATIONS:

1. **Bagley, A.F.** "Blood, Heat, and Tumors: Improving Drug Delivery with Gold Nanorods." Oral Presentation. SCIENCE with/in/sight: 2014 Koch Institute Image Awards. Cambridge, MA (2014).
2. **Bagley, A.F.** "Optically Active Nanomaterials for Ovarian Cancer Imaging and Therapy." Oral Presentation. Harvard Medical School MD-PhD Program Annual Retreat. Hyannis, MA (2013).
3. **Bagley, A.F.** "Plasmonic Heating of Deep Tumors Using Implanted NIR Sources." Oral Presentation. Koch Institute Annual Retreat. Falmouth, MA (2013)
4. **Bagley, A.F**., Ghosh, D., Na, Y., Birrer, M., Belcher, A.M., Bhatia, S.N. "Deep, non-invasive imaging for surgical guidance of sub-millimeter ovarian tumor resection using targeted single-walled carbon nanotubes." Oral Presentation. BMES Annual Meeting. Seattle, WA (2013).
5. Ghosh, D., **Bagley, A.F.**, Belcher, A.M. "Deep, non-invasive imaging for surgical guidance of sub-millimeter ovarian tumors using targeted single-walled carbon nanotubes." Abstract. World Molecular Imaging Congress. Savannah, Georgia (2013).
6. **Bagley, A.F.** "Optically Active Nanomaterials for Ovarian Cancer Imaging and Therapy." Oral Presentation. HST Biomedical Engineering Seminar Series (Course HST.590). Cambridge, MA (2013).
7. **Bagley, A.F.** "Optically Active Nanomaterials for Ovarian Cancer Imaging and Therapy." Oral Presentation. BRP Amplify Meeting. Buellton, CA. (2012).
8. **Bagley, A.F.** "Enhancing Therapeutic Delivery with Gold Nanorods." Oral Presentation. Center for Cancer Nanotechnology Excellence – MIT. Cambridge, MA. (2012)
9. **Bagley, A.F.** "Targeted NIR2 Imaging Probe Sensitively Detects Peritoneal Implants and Assists Cytoreductive Surgery for Ovarian Carcinoma." Oral Presentation. National MD/PhD Student Conference. Keystone, CO. (2012)
10. **Bagley, A.F.**, Daneshvar, D.H., Nowinski, C.J. "Effective Concussion Education for Young Athletes: Strategy and Messaging Lessons from the SLICE Program." Brain Trauma and the Athlete Conference. Framingham, MA. (2011)
11. **Bagley, A.F.*,** Lin, K.Y.*, Zhang, A.Y., Karl, D.L., Yoon, S.S., Bhatia, S.N. "Gold Nanorod Photothermal Therapy in a Genetically Engineered Mouse Model of Soft Tissue Sarcoma." Poster presentation. National MD/PhD Student Conference. Keystone, CO. (2011)
12. **Bagley, A.F.**, Shaham, O., Kelleher, J.K., Mootha, V.K. "Mitochondrial Regulation of Phospholipid Synthesis." Poster presentation. Harvard MD-PhD / Joslin Diabetes Center Symposium. (2008)

TEACHING AND SERVICE:

2009 – Present	Resident Tutor, John Winthrop House, Harvard College
2012 – Present	Chair, Winthrop Premedical Committee
2009 – 13	Creator & Co-Founder, Sports Legacy Institute Community Educators (SLICE)
2013	Volunteer, Keys to Empowering Youth (KEYS) Program
2012	Panelist, Bridges to Bioengineering, Whitehead Institute
2007 – 08	Volunteer, Massachusetts General Hospital
2005 – 08	Founder, MIT Elderly Assistance Program
2005 – 08	Partner, Whitehead Institute Science Education Program
2006	Teaching Assistant, MIT Biology Department, Genetics (7.03)

2006	Teacher, MIT High School Studies Program
2006	Orientation Leader, MIT Biology Department, ‘Discover Biology’ Program

CHAPTER 1. BACKGROUND AND SIGNIFICANCE

1.0 Ovarian Cancer

1.0.1 Epidemiology

Ovarian cancer is one of the most lethal malignancies for women in the United States and worldwide. In 2014, approximately 22,000 new cases will be diagnosed and more than 14,000 deaths will result from this disease.[1] The majority of women present with ovarian cancer in the fifth and sixth decades of life, with an overall lifetime risk of developing ovarian cancer of 1 in 70.[2] While screening for ovarian cancer in the general population is not currently recommended, women who have a family history of breast or ovarian cancer, infertility, endometriosis, or are at an otherwise increased risk may benefit from disease screening in certain cases. Epidemiological studies suggest that women who have been pregnant, breastfeed, or use oral contraception are at a reduced risk of developing ovarian cancer.

For patients deemed to be at high risk for developing ovarian cancer, several screening methods have been proposed. Genetic mutations in the DNA repair genes BRCA1 and BRCA2 confer significantly increased risk; women with mutant alleles in these genes have a 15 to 40 percent chance of being diagnosed with ovarian cancer during their lifetime, which is substantially higher than the rate in the general population. The prevalence of certain mutant BRCA alleles in Ashkenazi Jewish populations is 2.5 percent compared with a population prevalence of 0.2 percent.[3] Other genetic mutations and syndromes that may predispose patients to ovarian cancer include the DNA mismatch repair genes MSH2 and MLH1 associated with Lynch syndrome or HNPCC. Blood biomarkers, most notably CA-125 which is elevated in half of women with early stage ovarian cancer, have been investigated but have low specificity for disease detection.[4] While CA-125 is useful for diagnosing recurrent disease in patients who

have undergone treatment, it is not useful for general population screening.[2] Non-invasive imaging methods including transvaginal and abdominal ultrasound can be useful for differentiating between simple and complex cysts, and this can guide the decision to pursue the diagnosis further or monitor in an outpatient setting.

Despite gradual advances in the diagnosis and clinical management of ovarian cancer, long-term survival rates of 20-40% have remained static for several decades (**Fig. 1.1**).[5, 6] The majority of women present with advanced stage disease (Stage III/IV) in which tumors are disseminated throughout the peritoneal cavity.[2, 7, 8] These patients typically undergo a rigorous treatment regimen consisting of surgical resection (cytoreduction) and chemotherapy, but eventual relapse of drug-resistant disease is common, leading to an average overall survival of approximately one year. Clinical evidence has established that two important criteria for extending overall survival are the effectiveness of cytoreduction (i.e., how much tumor is resected during surgery) and intraperitoneal (versus intravenous) administration of chemotherapy. [2, 5, 8-17] These clinical findings point to specific areas in which technological innovations could yield benefits to ovarian cancer patients.

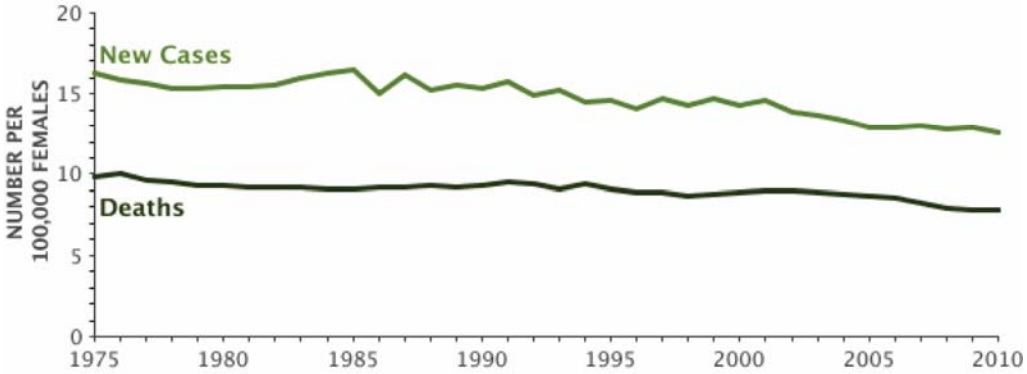

Figure 1.1. Rates of new diagnosed cases and deaths from ovarian cancer. (From SEER 9 Incidence & U.S. Mortality 1975-2010)

1.0.2 Clinical Management

1.0.2.1 Diagnostic Imaging

Several imaging modalities are currently used for diagnosis and management of ovarian cancer. Broadly, these imaging studies are used to distinguish between cancerous lesions and benign cysts, determine the extent of disease and necessity of cytoreduction, and monitor response to chemotherapy and disease progression. The primary imaging modalities include ultrasound, computed tomography (CT), positron emission tomography (PET), and magnetic resonance imaging (MRI). More recently, optical imaging probes in the visible and near- infrared (NIR) spectral regimes have been investigated for intraoperative utility.

Pelvic and abdominal ultrasound is commonly used for screening procedures to distinguish benign cystic lesions from tumors. Ultrasound transmits acoustic waves with frequencies on the order of 1 MHz into the body where they interact with and reveal structural and pathologic features of soft tissues. Ultrasound offers a fast, inexpensive, safe, and non-invasive method for obtaining structural information in the pelvis. The technique is limited by comparatively lower spatial resolution, and while it is effective at distinguishing liquid from solid structures, it is less capable of distinguishing between solid tumors and soft tissues in the peritoneum. Nevertheless, because ultrasound offers roughly equivalent predictive qualities for less cost, it is the recommended method for an initial diagnostic evaluation. For monitoring disease recurrence, transvaginal ultrasound may have utility in combination with CA-125 and physical examination as well.[18]

Computed tomography (CT) offers another method for obtaining structural information in the peritoneum. CT imaging involves a series of x-ray images that are reconstructed into a three-dimensional representation of the region of interest. CT offers excellent spatial resolution, and

when used with vascular contrast agents, can be helpful in delineating tumor from normal tissue in the peritoneum. CT imaging is widely used for cancer diagnosis in diverse tissue sites. One anatomic region where CT has proven particularly useful is the lung because the air-tissue interface provides a direct way to distinguish solid tumor from background with high contrast. CT subjects patients to a significant amount of ionizing radiation so it is undesirable for patients to undergo CT scanning unless there is a strong clinical rationale for doing so. Additionally, allergic reactions and nephropathy induced by vascular contrast agents represents a finite risk to patients. Finally, the lengthy period of image processing required to generate a three-dimensional representations is not particularly well-suited for intraoperative procedures where rapid feedback is more desirable. For ovarian cancer, the sensitivity of CT imaging for monitoring disease recurrence varies widely (32-84%) based on the anatomic location and size of the tumors and is therefore not ideally suited for diagnostic applications in this disease.[19, 20]

More recently, CT imaging has been combined with positron emission tomography (PET). PET imaging relies of the use of functional imaging probes containing radioactive isotopes. Many PET tracers have been developed to probe various biological and pathological processes, with fluorodeoxyglucose (^{18}F-FDG) as the prototypical agent to visualize glucose metabolism in metabolically active tissues including tumors and the brain. PET offers excellent sensitivity for larger tumors, but sensitivity decreases significantly for smaller tumor nodules less than 1 centimeter.[18, 21-23] Because many of these radioactive probes have half-lives on the order of minutes to hours, PET-CT facilities typically require a cyclotron on site to synthesize the imaging probes immediately prior to use. This creates a logistical barrier for PET and PET-CT imaging that limits its widespread adoption and particularly its use in operating room settings. However, in the past decade, PET-CT has proven very useful for the field of oncology

where it has helped to guide surgery and radiation, as well as monitor disease progression during and after chemotherapy.

Magnetic resonance imaging (MRI) offers yet another approach to non-invasively visualize soft tissues with excellent spatial resolution and without exposing patients to ionizing radiation. During MRI procedures, a large, uniform magnetic field is generated around the patient, leading to dipole alignment in the hydrogen atoms present in water molecules. By varying the magnetic field gradients and positions with time, structural information may be deduced by the differences in the frequency and relaxation times of the water molecules, as tissues contain varying water content and therefore will respond differently to the applied magnetic fields. MRI requires significant instrumentation including a magnet with a field strength on the order of 1 Tesla, uses vascular contrast agents like CT, and is not ideally suited for the operating room. Furthermore, MRI, while superior to CT or ultrasound at resolving soft tissue structure, can still be inefficient and not sensitive at distinguishing ovarian tumor nodules from healthy tissues in the peritoneum. For ovarian cancer recurrence, as with CT imaging, the reported sensitivities for detecting tumors by MRI vary widely based on tumor size (35% for < 2 cm; 82% for larger tumors) and anatomic location (83% for abdominal wall tumors; 67% for upper abdominal disease and lymph nodes).[24, 25]

Optical imaging approaches have gained increasing attention for applications in medicine due to the development of optically-active probes with molecular specificity for ligands present in healthy and diseased tissues. NIR light at wavelengths of 700-950 nm is relatively transparent to tissues in the body. The major sources of light absorption and scattering *in vivo* include hemoglobin in erythrocytes, lipids, and water. Between these spectral regions, however, there

exist optical ‘windows’ where light can pass through tissue relatively unimpeded.[26] Many reagents which emit light in these regions are being explored for a variety of imaging applications. These reagents often have low toxicity, provide real-time imaging capabilities, and the instrumentation including light sources and photodetectors is generally safe and does not expose patients to ionizing radiation. Probes that emit light in the visible spectrum (400-700nm) such as fluorescein are already in clinical use and being explored for real-time intraoperative imaging.[27] However, visible dyes have comparatively low tissue transmittance, making them less useful for non-invasive imaging applications such as monitoring tumor progression during chemotherapy. Visible dyes are also susceptible to photobleaching, rendering them less useful for scenarios required extending periods of excitation such as cytoreductive surgery, which could last for several hours or longer. Intrinsic tissue autofluorescence creates additional difficulty for dyes in the visible regime by reducing signal-to-noise ratios *in vivo*. NIR imaging agents such as indocyanine green (ICG) have been used in the clinic for ophthalmic, cardiovascular, and hepatic applications for decades.[26, 28, 29] These NIR agents offer superior tissue penetration and sensitivity to visible dyes, but are still limited to a centimeter or less for tissue penetrance.

At wavelengths beyond the first near-infrared window between wavelengths of 950-1400 nm, the second near-infrared window (NIR2) offers great promise for non-invasive optical imaging (**Fig. 1.2**). Theoretical simulations predict that fluorescent agents emitting light in the second near-infrared window can have up to 10 cm tissue penetration depth, which would be sufficient for many procedures in human patients.[30] Furthermore, the signal-to-noise ratio in the second near-infrared window would be considerably higher than in the ‘first window’ regime. One challenge for imaging in the second near-infrared window has been the availability of imaging probes that retain their fluorescence *in vivo*.

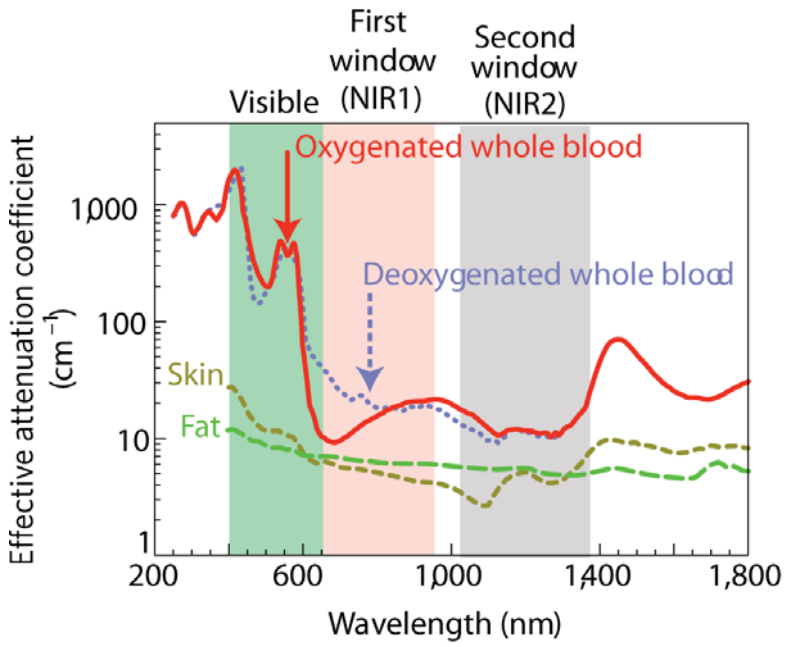

Figure 1.2. Optical attenuation in tissues due to absorption and scattering of light with primarily blood, skin, and fat tissue. Two optical windows (NIR1 and NIR2) exist at wavelengths of 650nm-950nm for NIR1 and 950nm-1,400nm for NIR2. Adapted with permission from [26].

One material with emission in the second near-infrared window is the single-walled carbon nanotube (SWNT), a rolled-up sheet of graphene, whose fluorescent properties are dictated by the chirality and layers of bundling in the structure. Based on the chirality, SWNTs can be either metallic or semiconducting, and only semiconducting carbon nanotubes fluoresce in the second near-infrared window. SWNTs have been explored in a number of pre-clinical imaging studies, although there has been reported concern about the clearance and toxicity of this material particularly involving entrapment and irritation in the lungs.[31-33] Clinical trials are currently underway to assess the safety of these materials in humans, but their potential as imaging probes has been well-established in pre-clinical models.

One translational challenge for the development of carbon nanotubes as a new class of imaging agents has been the ability to target carbon nanotubes to tissues of interest in a manner

that preserves their fluorescence. Stabilizing carbon nanotubes with biocompatible lipids such as sodium cholate or proteins such as the p8 coat protein of the M13 bacteriophage virus have been two methods that have been adopted to successfully prevent aggregation and loss of fluorescence of carbon nanotubes in living systems.[33-36] Additionally, bacteriophage have been engineered to express peptides from the p3 protein at the proximal tip of the bacteriophage. Libraries of distinct bacteriophage expressing unique targeting peptides have been used for *in vivo* phage display to identify peptides that target specific biological structures such as tumor extracellular matrix proteins.[37-40] Bacteriophage therefore represent suitable carriers for carbon nanotubes because of their ability to stabilize carbon nanotubes along their coat protein surface to preserve fluorescence and provide molecular targeting to deliver carbon nanotubes to the tumor site and reveal the tumor's location.

1.0.2.2 Cytoreduction

When complex ovarian cysts are identified by diagnostic imaging and the patient is deemed to be a good surgical candidate, cytoreductive surgery (cytoreduction) is performed as the initial step of therapy. Cytoreduction, or tumor debulking, serves at least two important roles. First, cytoreduction allows for precise staging of disease and this can in turn guide subsequent therapeutic decisions involving chemotherapy. Second, cytoreduction allows for the debulking of tumors disseminated throughout the peritoneal cavity. The process of tumor spread in this setting, known as peritoneal carcinomatosis, is distinct from traditional metastasis because the route of spread is not initially hematogenous, but rather via shedding of the primary ovarian tumor and implantation on organ and tissue surfaces throughout the peritoneum. In advanced stage disease, the number of tumor nodules can number in the hundreds, and these nodules may

not be easily palpable or visible to surgeons exploring the complex and crowded anatomical space of the peritoneum.

The maximal removal of tumors in advanced ovarian cancer has been shown to have a significant survival benefit for patients.[41] Over three decades of clinical evidence have revealed that patients who receive 'optimal' cytoreduction experience a 20 month improvement in median overall survival.[9, 11-13, 16, 17, 42, 43] In a meta-analysis of outcomes following optimal versus sub-optimal cytoreduction, it was observed that every 10% increase in maximal cytoreduction was associated with a 5.5% improvement in overall survival, making "maximal cytoreduction [one of the] most powerful determinants of cohort survival among patients with Stage III or IV ovarian carcinoma."[8]

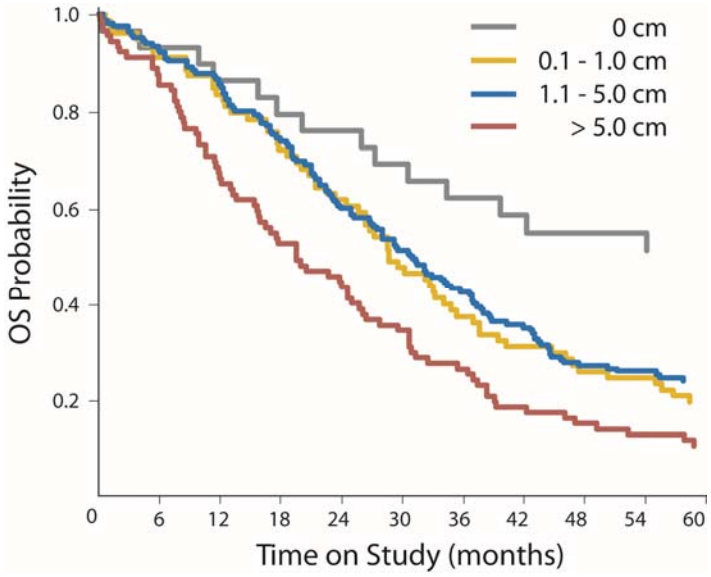

Figure 1.3. Kaplan-Meier overall survival curves for ovarian cancer patients based on amount of residual disease present after surgical cytoreduction. Adapted with permission from [41].

By the current guidelines of the Gynecologic Oncology Group, 'optimal' cytoreduction is defined as the removal of all tumors with a maximum diameter of 1 centimeter or larger.[44]

However, there is emerging evidence that more aggressive surgical interventions seeking to remove all visible tumor burden and leave no apparent residual disease may lead to improved patient outcomes.[45] The reasons behind this clinical observation are still being understood, but there are several leading explanations. First, a smaller residual tumor burden may be more effectively eradicated by adjuvant chemotherapies leading to increased cure rates and limited recurrence of disease. Second, by removing more tumor burden while it is still confined to the peritoneum, this reduces the likelihood of residual tumor from metastasizing to distant organs and increase mortality. Third, removing more tumor burden can decrease the incidence of secondary effects such as intestinal blockage, ascites formation, and hemorrhage which can directly increase morbidity and mortality in patients. Finally, patients who are able to undergo optimal cytoreduction may represent a unique patient population that responds more effectively to chemotherapy and has increased survival independent of the surgical procedure itself.[44, 45]

The high rate of disease recurrence following therapy (95% within 5 years) suggests that although surgeons may identify the majority of tumors by traditional approaches, a population of tumor implants remains in the peritoneum that is left unidentified, either because they are too small to be detected by eye, indistinguishable from normal tissues, or are located in anatomically privileged sites. Given the significant survival benefit of effective surgery and the high rates of disease recurrence following surgery, it is clear that improved methods of detecting disease burden in the peritoneum could be advantageous for achieving optimal cytoreduction and thereby improve patient survival (**Fig. 1.3**).

1.0.2.3 Chemotherapy

Following cytoreduction, patients receive adjuvant chemotherapy to treat residual disease burden. Patients initially receive platinum-based chemotherapeutics such as cisplatin or

carboplatin either alone or in combination with taxanes, including paclitaxel and docetaxel. While most patients receive multiple cycles of chemotherapy often lasting months, the optimal dosing regimens are dependent on the drug combination, disease stage, and the patient's overall health. The mechanisms of action of platinum-based chemotherapies and taxanes are non-overlapping and therefore exert complementary effects. Platinum-based chemotherapy leads to intrastrand DNA cross-linking, whereas taxanes stabilize tubulin and inhibit mitosis in cancer cells. In one trial, when taxanes were included alongside platinum-based chemotherapy, survival was increased significantly by 25 to 37 months.[46] For patients treated by cytoreduction and chemotherapy when diagnosed an advanced stage of disease, the median survival is 5 years and about half of patients achieve complete remission as determined by examination, imaging studies, and clinical biomarkers such as CA-125.[2] However, these patients ultimately have a 70-90% rate of recurrence. When disease is recurrent, first-line chemotherapy agents are often no longer effective because the tumors develop drug resistance. The high rate of recurrence underscores the need for effective initial treatment of residual disease to minimize the development of drug resistance and disease relapse.

Interestingly, for ovarian cancer there is clinical evidence that intraperitoneal administration of chemotherapies is more effective at eradicating residual disease than intravenous administration (**Fig. 1.4**).[5] This suggests that vascular transport limitations in ovarian tumors may be limiting the efficacy of intravenously administered chemotherapeutics. Intravenous administration requires higher dosages that can lead to hematologic, gastrointestinal, and neurologic toxicities. By circumventing these barriers through intraperitoneal delivery, a significantly higher concentration of drug becomes accessible to residual tumors. Furthermore, small tumor nodules may be hypovascularized and unable to receive intravenously administered

chemotherapeutics at concentrations sufficient to be cytotoxic. Although survival was improved with intraperitoneal administration, however, patients reported lower qualities of life and higher toxicities during treatment. These findings were attributed to factors including the catheter used to deliver chemotherapy and the higher dosages of chemotherapy administered.[5] More efficient approaches to deliver chemotherapies to ovarian tumors would be expected to provide similar therapeutic benefits with reductions in systemic toxicities.

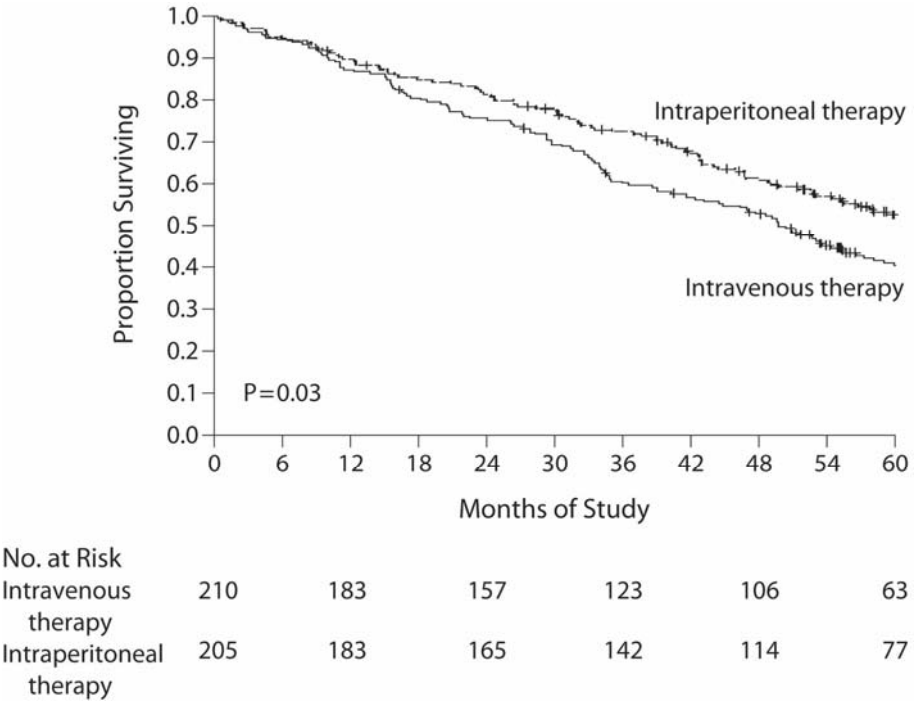

Figure 1.4. Kaplan-Meier overall survival curves for stage III ovarian cancer patients randomly assigned to receive intravenous chemotherapy or intraperitoneal chemotherapy (with intravenous paclitaxel). Adapted from [5]. Reproduced with permission from New England Journal of Medicine, Copyright Massachusetts Medical Society.

An experimental delivery method known as hyperthermic intraperitoneal chemotherapy (HIPEC) or intraperitoneal hyperthermic chemoperfusion (IPHC) has been used in patients, often immediately following cytoreduction.[47, 48] During HIPEC procedures, a heated solution containing chemotherapy is infused directly into the peritoneal cavity and spread throughout the

cavity by physical manipulation techniques. Because the mode of delivery is confined to the peritoneal cavity, a substantially higher concentration of chemotherapy can be tolerated in comparison to intravenous administration. However, the penetration depth of chemotherapy into tumors has been estimated to be less than 5 mm from the tumor surface.[49] In addition, the sensitivity of intraperitoneal organs such as the small intestine to diffusely elevated temperatures increases the risk of complications during HIPEC procedures and has led to debates of the relative merits of the approach.[50]

1.1 Drug Transport in Solid Tumors

Over the past decade, our understanding of the genomic complexity of ovarian and other cancers has greatly expanded. Tumors previously identified by their tissue of origin or pathologic appearance are increasingly being classified based on their underlying genetic mutational patterns. This molecular classification of cancer has been brought about largely by the ability to rapidly sequence cancer genomes in a more cost-efficient manner than was possible a decade ago. The hope of such efforts is that by capturing the full compendium of mutations that contribute to cancer, we will be better able to diagnose patients, provide more personalized therapeutic options, design smarter clinical trials, and understand the key molecular drivers for this disease. The success of molecularly-targeted cancer therapeutics such as vemurafenib for BRAF-mutant melanoma and imatinib for BCR-ABL-mutant chronic myelogenous leukemia (CML) at temporarily slowing the growth or completely curing these cancers has provided hope to patients and the biomedical community that similar approaches will be discovered for many other types of cancer.[51-54]

The success of imatinib, or Gleevec, at transforming CML from a fatal to a chronic or cured disease is often cited as a harbinger of future successes of molecular therapeutics. However, at least part of its success may be attributed to the high bioavailability of the drug to the leukemia cells, as both are present in the circulating blood and bone marrow, increasing the likelihood that this small molecule therapy will reach its intended target. For many solid tumors, however, the accessibility of systemically administered chemotherapeutics to tumor cells is limiting (**Fig. 1.5**). This low accessibility can be attributed to several transport bottlenecks or barriers that impede the delivery of therapeutics to tumors: (1) blood flow, (2) transvascular transport, (3) interstitial diffusion, and (4) cellular uptake.[55-59]

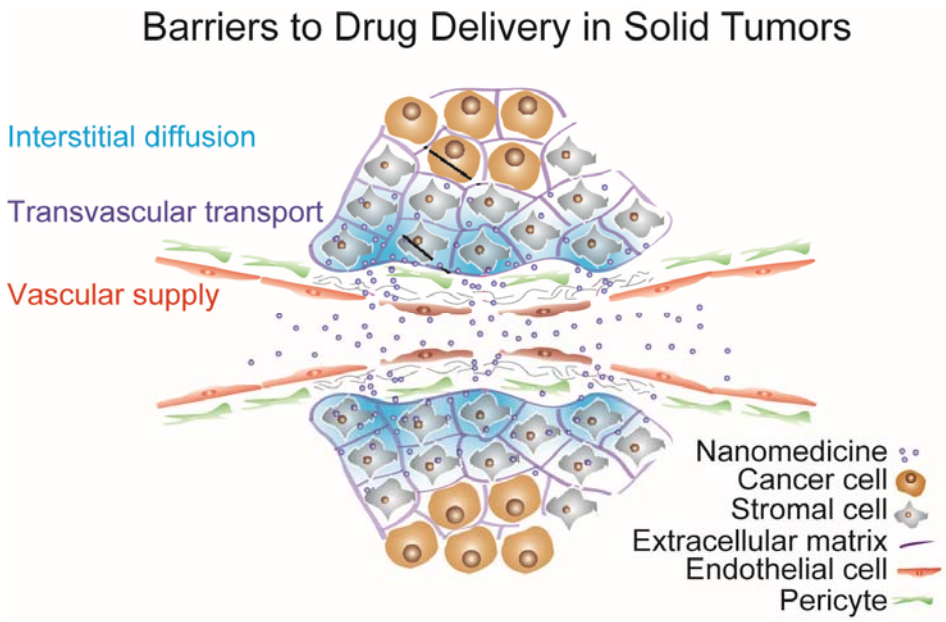

Figure 1.5. Barriers to drug delivery in solid tumors for nanomedicines and conventional diagnostic or therapeutic agents include vascular supply, transvascular transport, and interstitial diffusion. Strategies to actively modulate these delivery barriers are being explored to improve the delivery of nanotherapeutic agents into tumors with greater sensitivity and potency. Adapted with permission from [55].

1.1.1 Blood Flow

Adequate blood flow in the tumor is a prerequisite for systemically delivered therapeutics to reach tumor cells. In tumors, blood flow is impaired by irregular vascular structure, variable flow rates, and impaired lymphatic drainage. The process of angiogenesis creates a tortuous network of microvessels in the tumor with variable lengths and diameters. This disorganized, heterogeneous arrangement leads some regions of tumors to receive adequate blood flow, whereas other regions may experience poor or absent blood flow.[56] In addition to limiting drug transport, poor blood flow creates hypoxic, acidic conditions within tumors that facilitate drug resistance, cellular transformation to malignancy, and metastatic progression.[56] The irregular architecture contributes to one form of resistance that impedes blood flow. In addition, blood flow rates in tumors are reduced by increased blood viscosity. The leakage of plasma and proteins across permeable tumor vessels results in an increased hematocrit and apparent viscosity, thereby decreasing tumor blood flow.[60] Finally, impaired lymphatic drainage in solid tumors caused by compression of lymphatic vessels by proliferating tumor cells creates an increased interstitial pressure which can directly compromise blood flow.[61]

The concept of vascular 'normalization' was conceived as a strategy to improve the overall blood flow in tumors.[57, 62-70] To normalize the tumor vasculature, anti-angiogenic antibodies such as bevacizumab, traztuzumab, and cediranib have been used to prune angiogenic neovasculature and decrease vascular permeability, thereby decreasing the structural and viscous resistance and increasing overall blood flow to tumors.[62, 66, 71] Small molecule and endogenous angiogenesis inhibitors such as endostatin and the VEGFR inhibitor AZD2171 have demonstrated similar behavior in pre-clinical and clinical studies.[63, 72] This approach has been shown to improve delivery of multiple therapeutic agents to solid tumors and correlates with

improved survival in pre-clinical tumor models. Emerging evidence in small-scale clinical trials indicates that this approach may have both diagnostic and therapeutic utility in humans as well.[62] The corresponding reduction in vascular permeability by this method, however, suggests that it may be most useful for small molecule chemotherapeutics that are not as limited by movement across the vessel wall or diffusion through the interstitium.[59]

Physical stimuli including heat have also been explored as methods to modulate blood flow in tumors. Normal tissues respond to heat with increased blood flow when the temperature does not exceed 45°C, and blood flow returns to baseline levels within hours.[73] Previous studies have reported that from basal flow rates of 3-5 mL/min per 100 grams of tissue, heating induced 15-fold and 10-fold increases in blood flow in the skin and muscle, respectively.[73] The reported effects of heating on tumor blood flow are more variable, however, with studies reporting both positive and negative effects based on the tumor model, heating regimen, and heating method employed. For instance, localized heating induced by high-intensity focused ultrasound (HIFU) generates a smaller increase in tumor blood flow versus heated water bath methods because of differing boundary conditions and thermal gradients generated at air-skin and water-skin interfaces, respectively.[73] One group examined the effects of multiple rounds of heating on tumor blood flow by exposing tumors to five cycles of heating with intervals between heating of 1-3 days.[74] They observed a roughly 2-fold increase in blood flow with the initial heating cycle at 43.5°C, but no subsequent changes to blood flow with further heating cycles applied in one day intervals.[74] This finding is suggestive of a vascular adaptation to heating referred to as vascular thermotolerance.

1.1.2 Transvascular Transport

The second primary barrier to therapeutic delivery in tumors is transvascular transport. Although tumor blood vessels are typically more permeable than normal vessels, transport across the endothelium is often rate-limiting for larger therapeutics such as antibodies and nanoparticle formulations.[59, 75] Transvascular transport is governed by a combination of convection and diffusion reactions that depend on the vessel structure, microenvironmental variables, and properties of the therapeutic itself. Several of the key relevant parameters include intravascular and interstitial concentrations of the drug, hydrostatic and osmotic pressure gradients, effective endothelial pore size, and the molecular properties of the therapeutic including charge, size, and geometry. A consequence of both the increased vessel permeability in tumors and diminished lymphatic drainage, elevated interstitial fluid pressure (IFP) poses a significant challenge for transvascular transport.[56] Additionally, just as the blood flow in tumors is heterogeneous, the effective vascular pore sizes in vessels and permeability varies significantly throughout the tumor from several nanometers to one micrometer or larger. Therefore, while certain regions of the tumor including the periphery may have highly permeable vasculature, other regions in the same tumor such as the core regions may be significantly less permeable, leading to spatially different patterns of accumulation of therapeutics within individual tumors.

To understand the mechanisms for transvascular transport in tumors, it is helpful to first consider the cellular structure and composition of blood vessels. A normal blood vessel is composed of endothelial cells, smooth muscle cells, and extracellular matrix proteins arranged in three concentric layers called the intima, media, and adventitia.[76] The intima is the innermost layer in contact with the circulating blood and is composed of an endothelial cells. The internal elastic lamina separates the intima from the media, and the media is composed of smooth muscle cells, which provide vessel stability and contract or dilate in response to chemical stimuli or

input from the nervous system. The outermost layer of a blood vessel, the adventitia, consists of connective tissue, nerves, and the *vasa vasorum*, a network of vessels that provides oxygen and nutrients to the outermost layers of the vessels themselves. Vessels span a wide range in diameters, and the structure is dictated largely by the physiological demands of the particular vessel. Large arteries like the aorta have high elasticity, and give rise to smaller, more muscular arteries. These arteries in turn branch into smaller arteries, arterioles, and capillaries. Capillaries, which exhibit slow blood flow and are the site of oxygen transfer into tissues, consist of an endothelial monolayer on a basement membrane. Endothelial cells are not simply passive barriers to nutrient, oxygen, and macromolecular diffusion, but instead play an important physiological role in regulating processes such as coagulation and leukocyte trafficking.[76]

Transvascular transport in tumors occurs most prominently in capillary and post-capillary venule networks. Several classes of tumor capillaries have been identified in tumors and include continuous, fenestrated, and discontinuous capillaries.[75] The distinction between these structures is largely based on extent of coverage of their endothelial linings. Continuous capillaries are characterized by a functionally intact endothelial barrier and have been previously identified in pre-clinical tumor models.[75, 77] Fenestrated capillaries such as those found in renal glomeruli have also been observed in tumor models; these capillaries contain interendothelial fenestrations, or openings, that contribute to vascular permeability. Discontinuous, or sinusoidal, capillaries represent a more extreme variation of fenestrated capillaries and are found not only in tumors, but also in the liver and spleen. With larger pore sizes between adjacent endothelial cells and diminished basement membrane accumulation, discontinuous capillaries also contribute to the enhanced vascular permeability observed in tumors. These capillary networks ultimately converge into post-capillary venules, which are

typically between 20-60 μm in diameter, possess weak interendothelial cell junctions, and are therefore the principal site of exudation of fluids and leukocytes in tumors.[75, 76]

While transvascular transport occurs across each type of capillary and post-capillary venule network, the relevant transport pathways vary for each type of vascular structure and molecule being transported. In general, the mechanisms for transvascular transport can be categorized as endothelial cell diffusion, lateral membrane diffusion, interendothelial junctions, fenestrations, and vesicle transport.[75] Small molecules, water, and lipophilic solutes diffuse through endothelial cells or via lateral membrane diffusion, whereas transport through interendothelial junctions or fenestrations occurs for larger macromolecules including many nanoparticle therapeutics. Transport across continuous capillaries occurs primarily through endothelial cell diffusion, lateral membrane diffusion, narrow interendothelial junctions, and vesicular transport. Fenestrated capillary transport shares these mechanisms, but additionally involves transport through closed and open fenestrations across the endothelium. Discontinuous capillary transport involves the mechanisms of continuous capillaries as well as large interendothelial cell junctions.[75]

The mechanisms of vascular permeability, in particular during inflammatory responses to a variety of chemical, physical, and microbial insults, have been well documented and have served as a framework for strategies to overcome transvascular transport limitations in tumors. The primary consequence during an acute inflammatory response is the extravasation of fluid, proteins, and cells from the vessel lumen into the injured tissue.[76] The mechanisms responsible for these effects have provided specific areas to mimic as therapeutic strategies. In the immediate aftermath of a tissue injury, degranulation of mast cells releases the vasoactive agents such as

histamine, which within minutes induce endothelial cell contraction and increased vascular permeability primarily in post-capillary venules.[78-80] Additionally, inflammatory cytokines such as tumor necrosis factor (TNF) and interleukin-1 (IL-1) can induce endothelial cell contraction, although the effects of these cytokines may occur after several hours in contrast to the rapid action of vasoactive compounds. Hours after injury to a tissue, leukocytes recruited to sites of inflammation can also act upon the endothelium to increase the effective vascular permeability. In the context of tumor vasculature, permeability is governed by mediators such as vascular endothelial growth factor (VEGF) that promote the formation of angiogenic vessels with increased permeability relative to normal vasculature. Importantly, the lack of significant pericyte coverage in angiogenic vessels plays an important role in the permeability of macromolecules across the endothelium.

1.1.3 Diffusion

Upon extravasation from the blood vessels, macromolecular compounds must diffuse through the interstitial space of the tumor. The tumor interstitium is composed of a dense extracellular matrix of collagen fibers and charged glycosaminoglycans (GAGs), along with non-malignant cells recruited to the tumor site such as macrophages, leukocytes, and fibroblasts. While the prevalence of specific matrix proteins or cell populations varies significantly based on the tumor type, site of disease, and tumor stage, these factors collectively pose a large hurdle for diagnostic or therapeutic nanoparticle formulations of large hydrodynamic radius or surface charge. Particles may become sequestered within dense regions of extracellular matrix or engulfed by macrophages through processes such as phagocytosis or macropinocytosis. These factors effectively reduce the concentration of free therapeutic compound that is available to target tumor cells directly.

Several proof-of-concept studies in pre-clinical models have demonstrated that reductions in ECM density or macrophage populations can enhance therapeutic diffusion in solid tumors. Groups have used matrix-degrading enzymes and hormones such as collagenase, matrix metalloproteinases (MMPs), and relaxin to decrease the collagen concentration in tumors and demonstrated superior distribution of therapeutic particles in regions with reduced collagen concentration.[81-85] However, given the abundance of collagen in the body, the inability to target this matrix-degrading enzymatic activity specifically to tumors creates a narrow therapeutic window for approaches involving collagenase. Pharmacologic strategies using the FDA-approved angiotensin receptor blocker losartan have also demonstrated that antagonism of transforming growth factor beta 1 (TGFβ1) activity in cancer-associated fibroblasts reduces the collagen density in tumors and improves diffusion of both oxygen and therapeutic molecules.[86, 87] To deplete phagocyte cell populations that may sequester diffusing therapeutics, studies have examined the effect of co-administration of therapeutic compounds with clodronate liposomes, which deplete peripheral phagocytic CD68+ and CD163+ cells. In one study, this strategy led to five- to ten-fold improvements in intratumoral therapeutic concentrations of oncolytic viruses.[88] Finally, more recent reports have described tumor-penetrating peptides such as iRGD that when co-administered with a variety of therapeutics can significantly increase the penetration of compounds into solid tumors.[89]

1.1.4 Cellular Uptake

A final barrier for diagnostic and therapeutic agents with intracellular mechanisms of action is the transport across cellular membranes and release from endocytic vesicles. Certain molecules such as the PET imaging probe fluorodeoxyglucose (FDG) are not limited by blood flow, transvascular transport, or diffusion, but rather by cellular binding and intracellular

reactions.[59] In addition, emerging classes of therapeutics such as siRNAs must act in the cytoplasm and therefore escape from endocytic vesicles in order to demonstrate therapeutic utility. Pathogens that must co-opt eukaryotic cellular machinery to proliferate have evolved mechanisms to penetrate cell membranes and escape from acidified endocytic vesicles. Typically cationically charged, cell-penetrating peptides isolated from these pathogens such as transportan have been incorporated into nanotherapeutic carrier complexes as a strategy for penetrating cellular and vesicular membranes with higher efficiency.[90]

While there is reason for considerable hope and excitement with the identification of highly specific and potent molecular therapeutics for cancer, it is important to consider the physical transport barriers, which greatly diminish the therapeutic efficacy of these compounds in solid tumors and fuel the development of drug resistance. Advances in overcoming these barriers will need to occur in parallel to drug development in order for the potential for these compounds to be fully realized in the clinic.

1.2 Heating and Therapeutic Transport

1.2.1 History

The use of heating in cancer therapy dates back to ancient times when it was described in Egyptian, Indian, and Greek civilizations as a method for treating ailments such as breast cancer. In the nineteenth century, fever therapy gained in prominence after Dr. William Coley and others administered bacterial toxins from *Streptococcus pyogenes* and *Serratia marcescens* to induce fever and observed tumor regression in their patients. It was not until the 1970s, however, that formal clinical trials and pre-clinical studies began to address the utility and molecular mechanisms of heating in cancer therapy. Trials thus far have investigated heating in the context of ovarian cancer, head and neck cancer, breast cancer, melanoma, esophageal cancer, gastric

cancer, cervical cancer, colorectal cancer, and soft tissue sarcoma.[91-108] Collectively, the randomized clinical trials to date have shown mixed results, with some trials demonstrating improved tumor responses and survival benefit while others not showing a significant difference from control groups.

While heat itself exerts direct cytotoxic effects on tumor cells, most trials have examined the combined effects of heating with existing therapeutic modalities including radiation therapy and chemotherapy. Because mild heating in the range of 40-43°C enhances blood flow and oxygenation in tumors, it has been shown to radiosensitize tumors to radiation therapy, which relies on the generation of oxygen free radicals for its antitumor effects. The clinical effectiveness of radiosensitization by localized heating has been examined for superficial tumors including head and neck, melanoma, sarcoma, and breast tumors in trials comparing radiotherapy and local heating to radiotherapy alone. While the patient cohorts and clinical endpoints varied between these trials, about half of the trials demonstrated an improved response with combined radiotherapy and heating, but the majority did not demonstrate a survival benefit. [95, 97, 99, 102-106]

Non-specific, whole-body heating approaches have been shown to alter the systemic pharmacokinetics and metabolism of chemotherapeutics due to altered metabolism and filtration in the liver and kidney, respectively. The effect of systemic heating on the functioning of healthy organs has made these approaches less predictable in terms of their therapeutic benefit to patients. Because heating in the liver may delay drug metabolism by several hours, considerations of the relative timing between drug administration and induction of heating may be important for developing an optimized protocol, although most current studies support

synchronous administration of chemotherapy and heating. The biological basis for heat-based chemosensitization has been described primarily as an effect of pharmacodynamic enhancement. Many studies have reported that tumor cells from multiple lineages and tissues are more sensitive to elevated temperatures relative to normal, non-tumorigenic cells owing to genetic aberrations present within the cells that render them more vulnerable to undergoing apoptotic or necrotic cell death. At higher temperatures in excess of 50°C, heat has been used as a single modality approach for direct ablation of tumor tissue. Acting in combination with cytotoxic or cytostatic chemotherapies, mild heating can promote greater frequency of cell death. As a result, studies have looked at mild heating in the range of 40-43°C as a mechanism for chemosensitization. However, in addition to its pharmacodynamic effects directly on tumor cells, heating also exerts pharmacokinetic effects through modulation of the tumor microenvironment.

1.2.2 Role in Transport

There has been significant previous work on understanding the role of mild heating, or hyperthermia, in helping chemotherapeutics overcome the major transport barriers present in solid tumors. These studies have focused on the impact of mild heating on the endothelium in particular, as this tissue serves as the interface between the systemic circulation and the tumor cells. Systemically administered therapeutics of diverse sizes, electrostatic charge, hydrophobicity, and molecular composition must traverse the endothelium in order to reach their target cells within the tumor, and for many of these therapeutics, transport across this endothelial layer is the rate limiting step of the entire process. Using pre-clinical glioma tumor models, investigators demonstrated that heating using a water bath led to a four-fold enhancement in the delivery of therapeutic monoclonal antibodies into tumors. [109]Similar results have been demonstrated for liposomes, large molecular weight dextrans, and iron oxide ‘nanoworm’

formulations, suggesting a generalized approach for enhancing therapeutic delivery.[110-112] Various mechanisms have been proposed to account for the enhancement in delivery induced by heating, including thermally-induced endothelial cell contraction, release of vasoactive mediators and inflammatory cytokines, direct injury to the endothelium, increased rates of transcytosis across the endothelium, and enhanced blood flow and interstitial diffusivity.[111]

Studies investigating the role of heating in therapeutic transport have focused almost exclusively on the effects of single heat exposures on the tumor vasculature. In clinical settings, however, chemotherapy regimens typically include multiple rounds of administration spanning periods of days to months. As heating methods are considered as adjuncts to chemotherapy regimens, there is surprisingly little known about the efficacy of multiple heat exposures on the tumor vasculature in the context of therapeutic delivery. Much more has been studied about the effects of repeated thermal stress on cells grown in culture. In particular, an effect known as thermotolerance has been described that effectively renders cells more resilient to thermal stress if the cells were previously exposed to a sub-lethal thermal stress.

1.2.3 Heat Shock Response and Thermotolerance

The mechanistic details of thermotolerance have focused on the involvement of the heat shock response. An evolutionarily conserved pathway shared by yeast, plants, and mammals, the heat shock response consists of a coordinated cellular response that enables cells to survive a variety of physical and chemical stresses including elevated temperature, toxins, heavy metals, and oxidative stress.[113] In vertebrates, the master regulator of the heat shock response is the transcription factor Heat Shock Factor 1 (HSF1). In the unstressed state, HSF1 exists in the cytoplasm in an inactive monomeric form; upon cellular stress, HSF1 proteins form homotrimers, translocate to the nucleus, and initiate transcription of target genes involved in a

variety of cellular processes that collectively help the cell survive during periods of stress.[113] HSF1 is recruited to target genes by DNA sequences called heat-shock elements (HSEs).[114-116] The classical genes induced by HSF1 include the family of heat shock proteins (HSPs), which act as chaperones to help stabilize and refold denatured proteins during thermal or other stresses. Certain heat shock proteins including HSP27 have been implicated in increasing the stability of actin filaments during heating.[117-119] However, while some studies have observed vascular thermotolerance develop within tumors, this phenomenon has not been extensively investigated in the setting of drug delivery across the tumor endothelium.[110]

From a therapeutic standpoint, because many tumors rely on HSF1 activity during periods of rapid growth and protein synthesis, inhibitors of HSF1 may have utility in the clinic in combination with chemotherapy or other existing therapeutic strategies. Studies have demonstrated that deletion of HSF1 in cells and animal models is tolerated, suggesting that selective HSF1 inhibitors, if identified, could have a moderate therapeutic index.[120] Recently, a compound called rocaglamide A was identified in a high-throughput small molecule screen as a potent inhibitor of translation and HSF1 activation.[121] In cell lines highly dependent on HSF1 activation, rocaglamide A and its structural analog with enhanced potency RHT significantly decreased the levels of mRNA transcripts associated with the heat shock response including HSP70 and HSP40 and exhibited a pronounced effect on cell viability.[121] While there is enthusiasm for HSF1 inhibition as a tumor-specific therapeutic strategy, its inhibition in the tumor microenvironment to diminish vascular thermotolerance may have complementary effects in the context of drug delivery to solid tumors.

1.2.4 Technologies in the Clinic

Technologies to induce elevated temperatures can be divided into whole body, regional, and local approaches. Whole body hyperthermia (WBH) systems have been utilized for patients with metastatic disease and can safely elevate the body temperature to approximately 42°C without significant systemic side effects. WBH systems consist of moisture-controlled chambers that emit NIR radiation, which is absorbed in the patient's skin to depths of several millimeters.[122] This heat is transferred into the systemic circulation and within a period of 1-2 hours the body temperature can reach 42°C. Clinical challenges of WBH approaches include the need for deep sedation or anesthesia, continuous skin temperature monitoring, frequent fluid replacement, and the possibility of hematological and cardiovascular side effects including cardiac arrhythmias and disseminated coagulation.[123, 124] The most positive outcomes for WBH trials have combined WBH with systemic chemotherapy in patients with sarcoma and ovarian cancer, but the complex implementation and systemic toxicities of WBH in comparison to local or regional methods has slowed the further development of these approaches.

Regional approaches utilize antenna arrays to generate electromagnetic energy over a defined anatomic region. These systems may be particularly useful for simultaneously treating multiple tumors confined to a specific anatomic compartment such as the peritoneum. Using antenna arrays has allowed clinicians to develop more precise patterns of energy deposition because the spatial location, emitted frequency, and number of the antennas can be modulated to deposit energy more specifically at sites of disease. One group has combined a regional heating system with real-time thermometry by magnetic resonance-based imaging techniques, which provides a way to monitor temperature both in tumors and in adjacent healthy tissue.[125] Regional perfusion of limbs has a longer history of clinical use. In regional perfusion approaches, blood from a major artery is removed from the body, heated outside of the body, and

returned through a large vein in the same limb. Regional perfusion is considerably safer than WBH approaches and allows for greater concentrations of chemotherapy to be administered compared with systemic administration.[126-128]

Several approaches to locally increase the temperature in a tumor include radiowaves and microwaves, high intensity focused ultrasound (HIFU), and laser-induced interstitial therapy.[128, 129] These approaches have found the greatest utility for superficial tumors and tumors present in the liver due to metastatic spread that are not surgically resectable. For tumors located close to the skin surface, applicators emitting microwaves and radiowaves can be placed on the skin and linked to a thermal monitoring device placed within the target tumor tissue for continuous monitoring and feedback control.[130] While these devices may cover relatively large areas up to 15 cm in diameter, the energy penetration depth is limited to only 3 cm, which diminishes their utility for deeper tumors.[128] A variety of implanted applicators have been developed to be placed directly within isolated tumors or hollow organ structures such as the esophagus, rectum, and urethra. These devices can emit radiowaves, microwaves, ultrasound, or laser-generated energy to directly heat tumor tissue less than 5 cm in diameter.[128, 129] While these locally applied ablative procedures are typically not curative, they can nevertheless reduce disease morbidity significantly and allow patients to experience an improved quality of life.

One challenge has been developing methods to locally heat tumor tissue disseminated over a wide region without damaging adjacent healthy tissue. This is particularly true for advanced ovarian cancer because tumors disseminated in the peritoneum are situated amongst temperature-sensitive tissues such as the intestine. Methods to locally and specifically heat ovarian tumors in this setting may have therapeutic advantages compared with non-specific

heating methods such as HIPEC. Furthermore, with radiofrequency, microwave, or HIFU approaches, the heating localization is dependent on the location and placement of the transducer, which requires knowledge of the location of tumors prior to the intervention.

1.3 Optically Active Nanomaterials

Over the past two decades, a wide array of nanoparticles and nanomaterials have been engineered for applications ranging from electronics to energy storage to medicine. These particles and materials vary widely in terms of their chemical compositions, geometries, surface modifications, and electrostatic charges, but share the common feature of having at least two dimensions measuring between 1 and 1,000 nanometers.[131] The impact of nanomaterials on the field of medicine is already being realized with at least forty distinct nanomaterial formulations having received FDA approval or currently being assessed in clinical trials.[132] Many more nanomaterials are under development and being evaluated in pre-clinical studies. Nanomaterials for medical applications are typically composed of lipids (Doxil liposomes, micelles), proteins (Abraxane), polymers (dendrimers, block copolymer micelles), and inorganic materials such as metals (gold and silver nanoparticles, iron oxide).[131] Carbon-based nanomaterials including carbon nanotubes have also garnered increasing interest particularly for their non-invasive imaging capabilities.[33] In the setting of cancer, nanomaterials are being investigated as new classes of imaging agents to help detect disease at an earlier stage, detect biomarkers at greater sensitivity than with traditional assays, deliver chemotherapeutics more

efficiently and selectively to tumors, and physically modify tumors for therapeutic benefit.

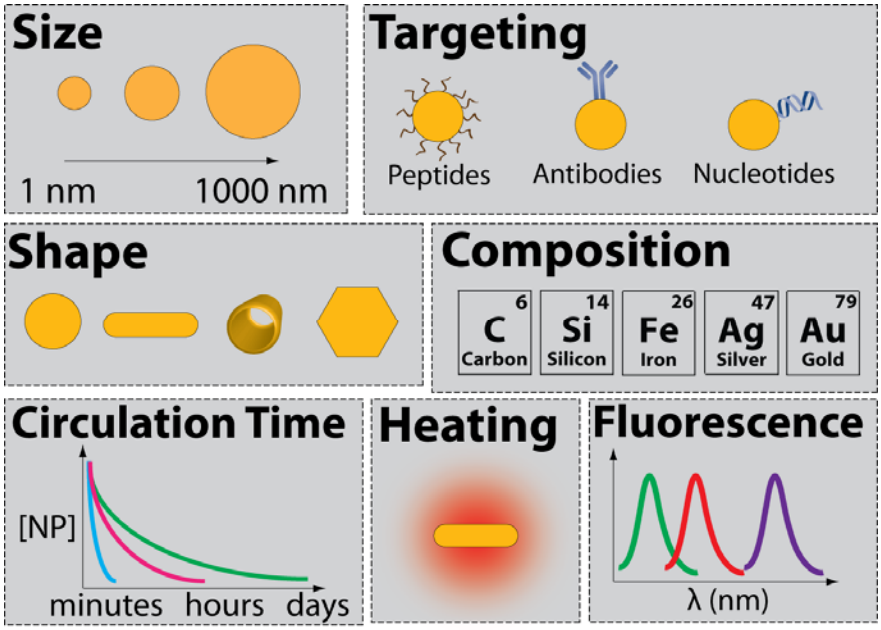

Figure 1.6. Design parameters of nanomaterials for medical applications. Controlling geometric parameters including particle size and shape, as well as incorporating targeting ligands, influences pharmacokinetics and pharmacodynamics. Elemental composition of nanomaterials embeds certain functions into material, including the ability to generate heat or emit fluorescence.

1.3.1 Plasmonic Nanomaterials

One class of materials that has shown great utility for biomedical applications are plasmonic nanomaterials. Plasmonic materials are composed of noble metals such as gold and silver that have unique optical properties including strong scattering and absorption due to their electronic structure.[133-138] When these particles are exposed to electromagnetic fields, free electrons on the surfaces of these particles undergo collective oscillations along the axis of the particles.[134] This effect is known as surface plasmon resonance (SPR) and has been utilized for a diverse array of applications including diagnostic biosensing, imaging, and therapy. The energy of the electronic oscillations can either dissipate into the environment as scattered light or be absorbed by the metallic lattice to generate localized heating. Of particular relevance to *in*

vivo applications, the resonant frequency of plasmonic nanomaterials is inversely proportional to the geometric aspect ratio of the particle. This property has allowed for the design of plasmonic nanostructures that exhibit localized SPR in the NIR regime at wavelengths with improved tissue penetrance relative to visible light.[112, 139-141] Biocompatible formulations of gold nanorods (PEG-NRs) coated in polyethylene glycol (PEG) polymers have been developed to increase circulation half-life, diminish systemic clearance by the reticuloendothelial system, and enhance intratumoral accumulation.

1.3.2 Single-walled Carbon Nanotubes

The carbon nanotube is a second type of optically active nanomaterial that has generated considerable interest for its potential biomedical applications including optical imaging. Carbon nanotubes consist of graphene sheets that are rolled into hollow cylinders. The chirality of these materials dictates whether they have metallic or semiconducting electronic properties, as well as the excitation and emission spectral characteristics. Semiconducting carbon nanotubes emit light in the second near-infrared window between wavelengths of 950-1400 nanometers.[26, 33, 36] Because these long wavelengths are significantly more transparent to tissue than the NIR or visible regimes, there is hope that novel imaging probes containing carbon nanotubes can be developed for non-invasive imaging applications.

1.3.3 Enhanced Permeability and Retention (EPR) Effect

The ability of systemically administered nanomaterials to reach their intended disease sites is essential for their function and clinical utility. Delivery of nanomaterials into tumors is governed in part by a phenomenon known as the enhanced permeability and retention (EPR) effect.[131, 142-146] Studies have demonstrated that permeable angiogenic tumor vasculature coupled with defective clearance by tumor lymphatic vessels facilitates the accumulation and

retention of nanomaterials in certain tumor microenvironments. EPR-mediated passive targeting of nanomaterials requires plasma half-lives on the order of hours to avoid rapid clearance by renal filtration and the reticuloendothelial (RES) system in the liver and spleen. To prolong the plasma half-life of nanomaterials, 'stealth' approaches involving the addition of biocompatible PEG polymers to particle surfaces have been developed successfully.[132, 147] PEG-coated nanomaterials with longer plasma half-lives can accumulate in tumors at higher concentrations. However, the addition of PEG polymers on nanomaterials can increase the particle diameter and diminish transvascular transport within tumors.[132]

While many studies describing the EPR effect have relied on subcutaneous xenograft models, it is becoming increasingly clear that the relative contribution of the EPR effect on nanomaterial accumulation is dependent on cell-autonomous and non-autonomous factors including the tumor model, site of implantation, growth kinetics, and stromal characteristics such as interstitial fluid pressure, vascular and lymphatic density, and infiltrating immune cell populations. For example, the presence of adjacent healthy tissue, vascular architecture, and other stromal elements in genetically engineered mouse models (GEMMs) can be very different from subcutaneous models and therefore the significance of the EPR effect in GEMMs does not immediately follow from similar studies in xenografts.[148-150] These stromal variations, which can lead to tumor-dependent differences in nanotherapeutic transport, may explain in part why some promising nanoparticle therapeutics to emerge from pre-clinical studies have failed to show therapeutic utility in human patient populations. In one study of 17 patients with locally advanced cancer, the pharmacokinetics of radiolabeled pegylated liposomes was measured by scintigraphy on a gamma camera.[151] Liposome accumulation varied based on the site and size of the tumors; head and neck tumors displayed the highest accumulation (33% ID/kg), lung

tumors showed intermediate accumulation (18.3% ID/kg), and breast tumors displayed the lowest accumulation (5.3% ID/kg). Accumulation varied inversely with tumor size, as smaller tumors in the head and neck displayed greater accumulation than larger tumors in the breast and lung. While the EPR effect is a widely acknowledged mechanism of nanomaterial accumulation in solid tumors, the magnitude of its effect in different tumor models remains an important consideration for effective clinical translation.

1.3.4 Diagnostic Applications – Biosensing and Imaging

Plasmonic nanomaterials are strongly scattering at their SPR wavelength, and this property has been developed for an array of solution-based biosensing applications.[135, 138, 152-171] The majority of these methods take advantage of small local surface plasmon resonance (LSPR) spectral shifts that occur upon binding of an analyte from a biofluid such as blood or cerebrospinal fluid to a capture probe in the vicinity of the plasmonic material. The degree of spectral shift in the plasmon resonance frequency is proportional to the concentration of analyte present in the local environment, and the sensitivity of plasmonic biosensors can be modulated by varying the particle geometry. Surface-enhanced Raman spectroscopy (SERS) has been applied to detect single molecules, as well as many biological analytes from clinical specimens. Plasmonic nanoparticles have been functionalized to facilitate antibody-antigen, lectin-saccharide, and biotin-streptavidin interactions for analyte detection. Plasmonic scattering-based biosensors have been shown to detect glucose concentration from biofluids, amyloid beta from blood and cerebrospinal fluids for Alzheimer's disease, and human papilloma virus DNA detection.[155, 159] These applications are highly sensitive, do not require prohibitively costly equipment, and have wide applicability in diverse fields of clinical medicine. Other studies have

used cancer-targeted plasmonic materials to perform imaging and have observed spectral shifts corresponding to cellular binding and particle uptake.

1.3.5 Therapeutic Applications – Heating and Drug Delivery

Plasmonic nanomaterials can also absorb the energy of the surface electron oscillations into the metallic lattice during the process of photothermal heating. The localized heat generated in these materials can be efficiently transmitted to the surrounding environment. This effect has been harnessed to create localized heating within specific tissues such as solid tumors.[141, 172-179] In these approaches, plasmonic nanomaterials accumulate passively in tumors by the EPR effect or by active targeting with antibodies, peptides, or other targeting ligands. Exposure of tissues to laser irradiation at the particle's SPR wavelength causes the particles to convert benign NIR light into heat locally within the tumor environment.

Applications involving photothermal ablation have relied on gold nanoparticles of varying geometries, principally gold-coated silica nanoshells and gold nanorods. Surface plasmon absorption peaks in the NIR regime have made these particles attractive for biomedical applications requiring heat delivery to deeper tissue structures. Preclinical studies have focused on subcutaneous or genetically engineered tumors just beneath the skin. This approach has been used to selectively ablate tumors by heating to 50°C or higher.[141, 179] Most studies utilize passive targeting to deliver gold nanoparticles into tumor environments via the EPR effect. Additionally, there has been effort to incorporate targeting ligands to selectively deliver gold nanoparticles to lymphocytes and atherosclerotic plaques for photothermal ablation and imaging in non-tumor settings.[180, 181] However, NIR penetration depth remains a limiting factor for disease processes not occurring near the skin surface and strategies to deliver NIR light more

efficiently could create new applications for plasmonic nanomaterials involving photothermal ablation.

Therapeutic applications of mild photothermal therapy in the range of 40-43°C have focused on utilizing plasmonically-active gold and silver nanoparticles to modulate a variety of temperature-sensitive polymers and hydrogels containing therapeutic cargoes.[141, 178, 182-191] Nanomaterials are either embedded within or co-administered with heat-sensitive carriers to induce local burst-release of therapies in a spatially-controlled manner. Other studies have shown that localized heating in the tumor microenvironment can create novel binding targets for subsequent delivery of therapeutic payloads. In addition, a limited group of studies have investigated antimicrobial applications of sub-ablative photothermal therapy. As with photothermal ablation, NIR light delivery remains an important barrier for many clinical applications of sub-ablative photothermal therapy.

1.4 Thesis Aims

The clinical challenges related to disease detection and monitoring, surgical resection, and delivery of therapeutics are well-suited to be addressed by novel nanomaterials and related technologies that can be engineered to target tumors, fluoresce, and locally deposit energy.[3, 6, 15-18] For ovarian cancer management, limitations related to diagnostic imaging, local heating, and therapeutic delivery represent significant barriers and therefore promising areas to address with nanotechnologies (**Fig. 1.7**). Towards this end, **the overall goal of this thesis is to harness optically-active nanomaterials to (1) non-invasively image, (2) locally heat, and (3) enhance therapeutic delivery to ovarian tumors**.

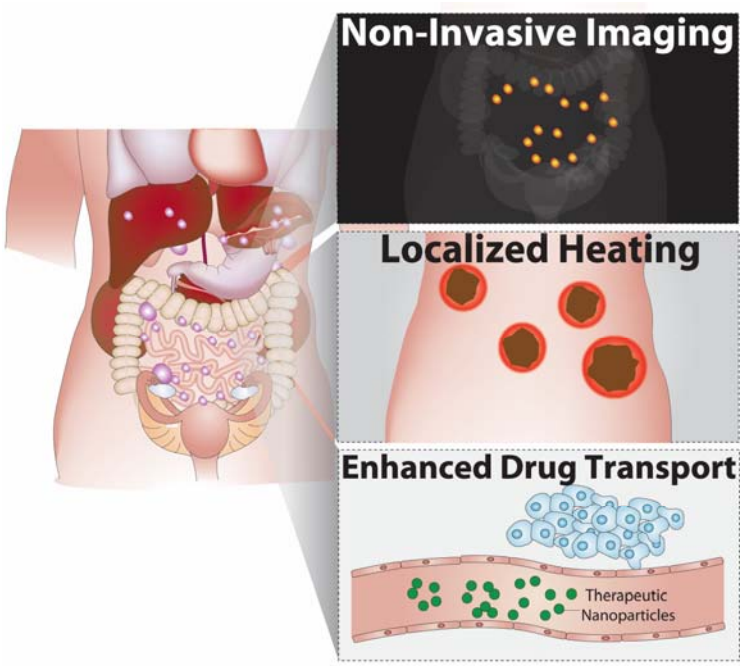

Figure 1.7. Overall summary of Aims. This thesis describes the development and application of optically-active nanomaterials for advancing three aspects of ovarian cancer management. Specifically, technologies for non-invasive tumor imaging, localized heating, and enhanced drug transport are addressed.

1.4.1 Non-invasive Imaging

In Chapter 2, a novel nanomaterial-based method for non-invasive imaging of disseminated ovarian tumor nodules is described (**Fig. 1.8**). We characterize an ovarian tumor-targeted imaging probe consisting of M13 virus-stabilized single-walled carbon nanotubes (SWNTs). The fluorescence emission spectra of SWNTs resides in the second near-infrared window (950-1400 nm), permitting deep-tissue imaging and superior signal-to-noise ratios compared to comparable probes in the NIR and visible regimes. We assess the probe's stability, fluorescence, and pharmacokinetics in physiological environments both *in vitro* and *in vivo*. We demonstrate that the SWNT probe binds to ovarian tumors embedded on the intestine, liver, and spleen with high tumor-to-background ratios and use histopathological analysis to confirm the probe's tumor sensitivity. To illustrate the utility of this approach for clinical applications, we

demonstrate that SWNT image guidance led to improved detection and excision of ovarian tumors during cytoreductive surgery performed by a gynecological surgeon.

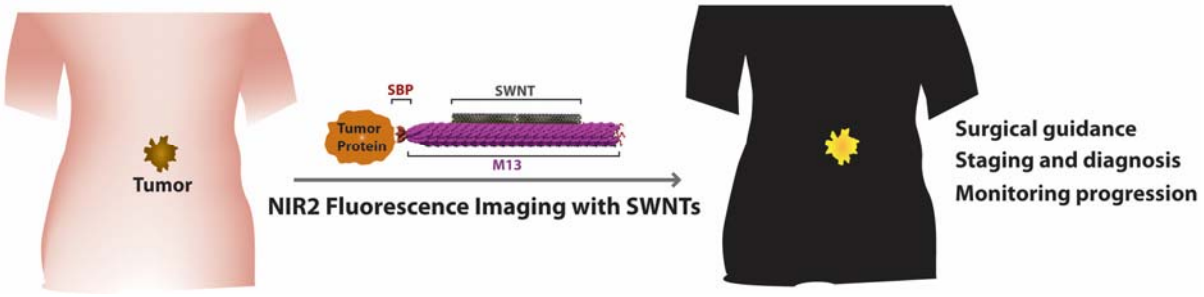

Figure 1.8. Schematic for Chapter 2. Tumor-targeted single-walled carbon nanotubes (SWNTs) are developed to selectively bind to deep ovarian tumors. Imaging in the second near-infrared window permits highly sensitive, non-invasive imaging of tumor nodules for surgical guidance and may assist diagnostic tumor staging and monitoring progression after therapy.

1.4.2 Localized Heating

1.4.2.1 Photothermal ablation in GEMM

Chapter 3 describes the development of a therapeutic protocol for PEG-NR-mediated photothermal ablation in a genetically engineered mouse model (GEMM) of soft tissue sarcoma. While plasmonic nanomaterials are being evaluated for the clinical management of diverse cancer types, pre-clinical studies have utilized tumor xenograft models that fail to recapitulate important stromal and parenchymal features of human tumors such as vascularity, blood flow, and mutational landscape. We investigate the EPR-mediated passive accumulation of PEG-NRs within GEMM tumors and develop a therapeutic photothermal ablation protocol that demonstrates significant antitumor effect and enhanced survival. We also describe non-specific heating effects of photothermal ablation that are not observed in tumor xenograft models, illustrating an added advantage of the GEMM model. Collectively, this Chapter validates the effectiveness of PEG-NR-mediated photothermal ablation in a more representative model of

human cancer, providing further rationale for studying the utility of plasmonic nanomaterials in clinical settings.

1.4.2.2 Implanted NIR Source

In Chapter 4, we explore a nanomaterial-based strategy for the localized heating of deeply-seated and disseminated ovarian tumors (**Fig. 1.9**). Because biological tissues such as skin, blood, and fat attenuate NIR light and limit its penetration depth, studies utilizing plasmonic nanomaterials have traditionally focused on extracorporeal energy sources directed upon isolated subcutaneous tumors. By combining systemically-delivered PEG-NRs with an implanted NIR source, we describe a novel approach for achieving localized heating for deeper tumors. In this Chapter, we characterize a series of implanted NIR light sources by computational modeling, fluence and thermographic measurements, and *in vivo* functionality. In orthotopic ovarian tumor xenograft models, we observe selective, localized heating of ovarian tumors and correlate this with enhanced accumulation of diagnostic and therapeutic cargoes. This work highlights how the combination of optically-active nanomaterials and implanted NIR sources can lead to effective photothermal therapy in complex anatomic environments.

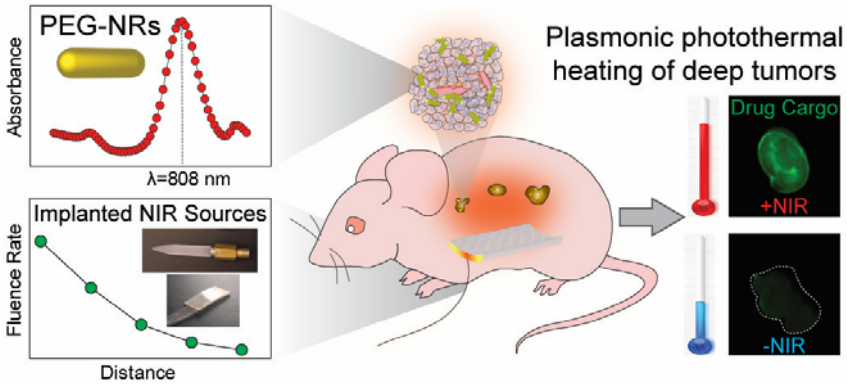

Figure 1.9. Schematic for Chapter 4. Localized heating of deep ovarian tumors is described using a combination of systemically-administered PEG-NRs and implanted NIR sources.

1.4.3 Enhanced Therapeutic Delivery

Chapter 5 addresses a role for PEG-NR heating to enhance the delivery of diagnostic and therapeutic cargoes to ovarian tumors (**Fig. 1.10**). Because chemotherapeutic regimens in the clinic are often administered as multiple cycles spanning weeks to months, we specifically focused on the effects of single exposures versus re-exposure to PEG-NR heating on tumor transport. We observed a transient resistance to therapeutic cargo accumulation termed 'thermotolerance' after an initial PEG-NR heat exposure and implicated the endothelial heat shock response as a contributor to this phenomenon. This work reveals an endothelial adaptation to nanomaterial-mediated heat exposure known as vascular thermotolerance and highlights a functional consequence on the delivery of diagnostic and therapeutic cargoes in tumors.

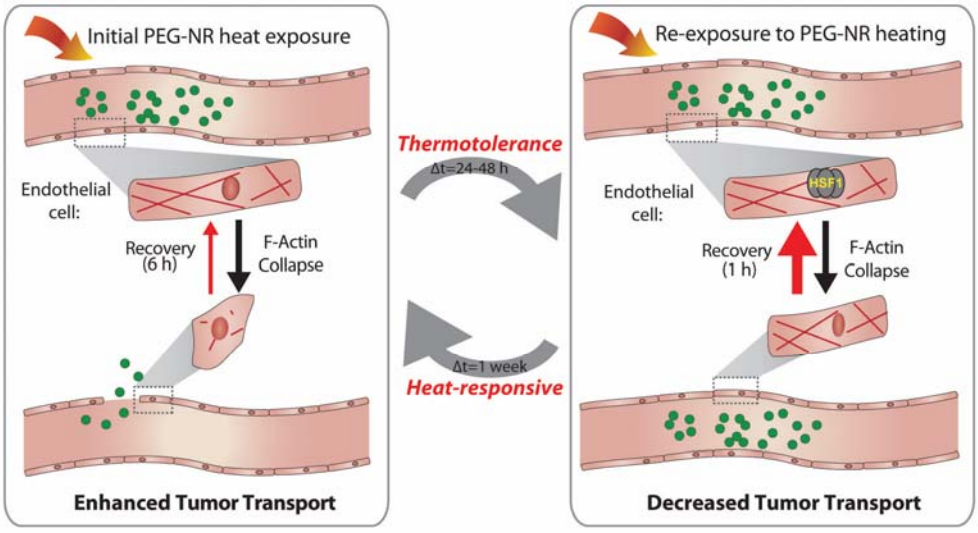

Figure 1.10. Schematic for Chapter 5. The effects of PEG-NR heating on tumor transport are explored. Following an enhancement in tumor transport after an initial PEG-NR heat exposure, the tumor endothelium, mediated by the heat shock response and *Hsf1*, develops thermotolerance, leading to decreased tumor transport upon re-exposure to heating. We explore this effect using a combination of *in vivo* accumulation studies, *in vitro* microfluidic vessel models, cytoskeletal dynamics, intravital microscopy of the tumor environment, and genetic models to elucidate the role of the heat shock response. We apply the kinetic and mechanistic details to evaluate therapeutic protocols involving diffusion-limited chemotherapeutic compounds.

CHAPTER 2. NANOMATERIALS FOR NON-INVASIVE TUMOR IMAGING

2.0 Abstract:

Highly sensitive, non-invasive detection of small, deep tumors for early diagnosis and surgical interventions remains a challenge for conventional imaging modalities. Second window near-infrared light (NIR2: 950-1400 nm) is promising for *in vivo* fluorescence imaging due to deep tissue penetration and low tissue autofluorescence. With their intrinsic fluorescence in the NIR2 regime and lack of photobleaching, single-walled carbon nanotubes (SWNTs) are highly attractive contrast agents to detect tumors. Here, targeted M13 virus-stabilized SWNTs are used to non-invasively visualize deep, disseminated tumors *in vivo*. This nanoprobe demonstrates excellent tumor-to-background uptake and exhibits higher signal-to-noise performance compared to visible and near-infrared (NIR1) dyes for delineating tumor nodules. Detection and excision of tumors by a gynecological surgeon improved with SWNT image guidance and led to the identification of sub-millimeter tumors. Collectively, these findings demonstrate the promise of targeted SWNT nanoprobes for non-invasive disease monitoring and guided surgery.

2.1 Introduction:

In clinical oncology, *in vivo* fluorescence imaging has emerged as a valuable tool for improving diagnosis, staging tumors, monitoring response to therapy, and detecting recurrent or residual disease. Compared to existing imaging modalities, fluorescence imaging offers a low cost, portable and safe alternative (i.e. non-ionizing radiation), with key advantages including real-time imaging, superior resolution, and high specificity for small tumor nodules during diagnostic and intraoperative surgical procedures.[192, 193] While efforts have focused on using visible and short near-infrared (NIR1: 650 nm – 900 nm) wavelength fluorescent dyes as contrast

agents for delineating tumor margins in both pre-clinical cancer models [193, 194] and human patients[27], these agents are suboptimal for non-invasive, reflectance-based imaging due to limited penetration depth (3-5 mm) and high tissue autofluorescence. During intraoperative surgery, these dyes may additionally undergo photobleaching, thereby reducing the ability of the surgeon to readily locate and resect tumors. Alternative approaches to specifically permit non-invasive imaging and limited photobleaching would be highly desirable for diagnostic and surgical applications.

Single-walled carbon nanotubes (SWNTs) hold great promise as fluorescence imaging agents due to the large interband difference between their excitation and emission wavelengths, resulting in minimal spectral overlap and tissue autofluorescence. In particular, the low tissue autofluorescence observed with SWNTs greatly enhances target-to-background ratios necessary for improved detection of small tumor nodules in confined anatomic regions. SWNT emission at longer wavelengths in the near-infrared second window (NIR2: 950-1400 nm) results in less optical scattering and deeper tissue penetration compared to shorter wavelength visible and NIR1 imaging agents. Simulations and experimental results suggest greatest tissue penetration depth is achieved in the NIR2 regime, which further highlights using SWNTs for biological imaging applications.[30, 195] Additionally, unlike visible and near-infrared dyes, well-functionalized SWNTs are less susceptible to photobleaching or quenching effects, which make them attractive for continuous, long-term imaging required during many surgical procedures.[196] Previously, we have demonstrated that M13 bacteriophage-stabilized SWNTs can target subcutaneous prostate tumors in pre-clinical models for fluorescence imaging in the second near-infrared window.[36] SWNTs have also been utilized for vascular and deep tissue fluorescence imaging.[33, 197] To date, however, there has been no report of a molecularly-targeted,

fluorescence imaging agent capable of non-invasive imaging and guiding diagnosis for surgical resection.

Here we report an M13-stabilized SWNT probe that selectively targets SPARC (Secreted Protein, Acidic and Rich in Cysteines)-expressing tumor nodules in an orthotopic mouse model of human ovarian cancer. Ovarian cancer remains a major health care problem for women. Annually, 225,000 women worldwide are diagnosed with epithelial ovarian cancer (EOC) and approximately 140,000 women die from it.[198] While women with early stage ovarian cancer (FIGO stage I/II) can be cured, advanced stage ovarian cancer (FIGO III/IV) remains considerably more difficult to treat. Unfortunately, eighty percent of women with EOC have metastatic disease at the time of diagnosis, and many undergo a treatment regimen of surgery and chemotherapy. Our study focused on ovarian cancer because clinical evidence indicates that optimal surgery can significantly prolong the median overall survival of patients as well as reduce disease morbidity.[45] Using the NIR2 emission of these fluorescence probes, we determine the detection limit of labeled tumors and their target-to-background ratios. We demonstrate that this SWNT-based probe detects tumors not observed with visible and NIR1 dyes, thereby aiding the discovery of smaller tumors during surgery. Collectively, our results highlight the potential for molecularly-targeted NIR2 fluorescence probes to non-invasively monitor disease processes such as cancer with enhanced sensitivity compared to current state-of-the-art optical probes.

2.2 Materials and Methods:

SBP-M13-SWNT Complexation

To prepare the starting SWNTs, non-acid treated HiPCO SWNTs (Unidym) were diluted in aqueous 2 wt% sodium cholate (SC). The solution was then homogenized for 1 hour, cup-horn sonicated for 10 minutes at 90% amplitude and then centrifuged at 30,000 rpm for 4 hours to disperse individual SWNTs. SWNT concentration was determined by measuring absorbance at 632 nm and calculated using the extinction coefficient of HiPCO SWNT at 632 nm, □632 nm=0.036 L/mg•cm. Complexation of M13 to SWNT was performed as previously described.[36] Briefly, the calculated amount of SWNT-binding phage solution was mixed with the calculated volume of SWNTs dispersed by 2 wt% SC in water to achieve a 1:1 stoichiometric ratio of phage-to-SWNT. The solution was placed in a dialysis membrane with MWCO 12,000-14,000 and dialyzed against water (10 mM NaCl, pH =5.3) for 48 hours with frequent buffer exchange. pH of the dialyzing solution was increased to 10 after 48 hours of dialysis. After dialysis, the phage-SWNT complex was removed and placed in a conical tube. Prior to experiments, samples were resuspended in 1X PBS, vortexed and centrifuged at 6000 rpm for 5 minutes.

Cell Culture and Establishment of an Orthotopic Ovarian Cancer Model

All animal studies and procedures were approved by the MIT Institutional Animal Care and Use Committee. This study used the established human ovarian epithelial carcinoma cell line OVCAR8, engineered to constitutively express firefly luciferase. OVCAR8 cells were grown in RPMI 1640 medium containing 10% fetal bovine serum, penicillin, and streptomycin. Approximately 2 x 10^6 OVCAR8 cells suspended in 200 μL DMEM (high glucose, phenol-red free) (Invitrogen) were implanted into the peritoneal cavity of athymic (nu/nu) mice to establish orthotopic ovarian tumor models. Mice were monitored by whole-animal bioluminescence

imaging to assess tumor burden. Imaging experiments were performed approximately 7-14 days following tumor cell injection based on the measured bioluminescence intensity.

In vivo Fluorescence Imaging of SBP-M13-SWNTs

SBP-M13-SWNTs were injected into the peritoneal cavity of tumor-bearing animals at ≈200 μg/kg. Mice were anesthetized with isoflurane gas. Fluorescence images were obtained approximately 24 hours following injection with exposure times ranging from 0.01 to 1 second for each subject. Background images were subtracted from raw images to generate the final images. We constructed equivalent standardized regions of interest (ROIs) to determine tumor-to-background ratios at various locations within the peritoneal cavity. For comparisons of SBP-targeted and untargeted M13-SWNT probes, we compared NIR fluorescent intensities of excised tumor nodules with normal intestinal tissue. Image intensities were quantified with ImageJ software.

Comparison of *In vivo* Non-Invasive Imaging between SBP-M13-SWNTs, Near-Infrared Dye, and Visible Dye

To confirm improved signal-to-noise in the NIR2 regime, SBP-M13-SWNT was compared to an NIR1 dye, AlexaFluor 750 (AF750), and a visible dye, fluorescein isothiocyanate (FITC). Briefly, two-fold dilutions of SBP-M13-SWNT or SBP-M13 conjugated with either AF750 or FITC (designated SBP-M13-AF750 and SBP-M13-FITC) were prepared onto a microtiter plate and their fluorescence was measured using either the custom-built NIR2 reflectance imager or an IVIS Spectrum, respectively. Samples were measured within the linear range of detection, set from 1,000 to 60,000 for each instrument. Images were acquired under various exposure times, from 0.01 seconds to 10 seconds. Fluorescence from SBP-M13-SWNT

was measured using the custom-built NIR2 reflectance imager at maximum aperture, with a laser power of ~100 mW/cm^2 at 0.01, 0.05, 0.1, 0.5, and 1 second exposures. SBP-M13-AF750 or SBP-M13-FITC was measured using an IVIS Spectrum in epi-illumination mode, under highest power, with fstop1 or fstop2 aperture (maximum and second-highest aperture) at 0.5, 1, 2, 5, and 10 second exposures. Regions of interest (ROIs) were drawn around microtiter wells and fluorescence counts were determined for samples in the linear range (i.e. 1,000 – 60,000) using ImageJ software. The limit of detection of the probe was determined to be the minimum concentration detectable by the imaging system within the linear range.

To compare signal-to-noise ratios *in vivo*, probes were combined and administered in five-fold excess of their minimum detection limit to mice bearing disseminated intraperitoneal OVCAR8 tumors. Fluorescence images from SBP-M13-SWNT, SBP-M13-AF750, and SBP-M13-FITC were acquired using the NIR2 imager and IVIS, respectively. Images obtained from the NIR2 imager were taken at 0.01, 0.05, 0.1, 0.5, and 1 second exposures. Images taken using the IVIS Spectrum were acquired at 0.5, 1, 2, 5, and 10 second exposures. All images were analyzed using ImageJ software. ROIs were drawn around the peritoneal cavity containing tumors, muscle, and image background. Fluorescence intensities were determined from the ROIs and tumor-to-muscle and tumor-to-background ratios were calculated. Samples were run with standard error (n = 3).

SBP-M13-SWNT Imaging During Surgery

Surgical studies were performed by a gynecologic surgeon. Animals were administered ≈200 μg/kg SBP-M13-SWNTs approximately 24 hours prior to surgery. For comparisons of initial surgery with or without SWNT-guidance, animals were randomly assigned to one of these

cohorts, and NIR2 fluorescence images were obtained 2-4 hours prior to surgery for all animals. For animals assigned to the SWNT-guided cohort, the whole-abdomen NIR2 fluorescence images were assessed by the surgeon prior to and during the surgical procedure. Excised nodules were measured, photographed, and imaged for SWNT-based fluorescence.

Genetic engineering of SPARC binding peptide (SBP) onto p3 of SWNT-binding M13 phage

Genetic engineering of the SPARC binding peptide (designated as SBP) and SWNT-binding peptide (designated as DSPH) was described previously.[36] Briefly, oligonucleotides encoding SPARC binding peptide (designated as SBP, SPPTGINGGG [199]), 5'(Phos)-GTA CCT TTC TAT TCT CAC TCT TCA CCA CCG ACT GGA ATT AAC GGA GGC GGG TC -3' and 5'(Phos)-GGC CGA CCC GCC TCC GTT AAT TCC AGT CGG TGG TGA AGA GTG AGA ATA GAA AG-3' (IDT) were annealed and inserted into the EagI and Acc65I restriction endonuclease sites of double stranded M13 DNA for N-terminal display on p3. The M13-based cloning vector was isolated from the SWNT-binding phage using standard DNA isolation (QIAGEN). Ligations were transformed in electrocompetent XL-1 Blue cells (Agilent Technologies), plated in top agar and incubated at 37°C overnight. DNA was purified (Qiagen) from isolated blue plaques and sequenced to confirm the insertion of SBP on p3.

Absorbance and PLE measurements

Absorption measurements were taken with a DU800 spectrophotometer (Beckman Coulter). PL of SWNTs was measured with a FluoroMax spectrofluorometer (Horiba Jobin Yvon).

Imager Setup

For fluorescence imaging in the second near-infrared window, an in-house *in vivo* imager was previously described[36]. A liquid nitrogen-cooled OMA V 2D InGaAs array detector (detection range: 800 – 1,700 nm) with a 256 × 320 pixel array (Princeton Instruments) was used. A NIR camera lens (SWIR-25, Navitar) was attached in front of the InGaAs detector. To reduce tissue autofluorescence and maximize the detection of fluorescence from SWNTs, two stacked long-pass filters with cut-off wavelength of 1,100 nm and OD >4 (EdmundOptics) were used. For excitation, an optical fiber coupled to an 808 nm diode laser (MDL-F-808, OptoEngines) was used and a laser line filter with center wavelength of 808 nm (EdmundOptics) was attached in front of the laser to remove unwanted excitation light. To minimize laser exposure to animals, a computer-controlled shutter was incorporated into the imaging system. The measured fluence on the mouse for *in vivo* imaging was ~120 mW/cm^2. The acquisition time for *in vivo* imaging ranged from 0.01 seconds – 1 second. For white contrast images, the same detector was used but the mice were illuminated with white light.

Blood and Ascites Stability and pH Measurements

For blood stability measurements, 20 μg/mL SBP-M13-SWNT was diluted in two-fold dilutions with PBS and then diluted 1:1 volume with blood obtained from healthy mice (Research Blood Components) and incubated for 0, 1, 2, 4, and 24 hours. Samples were measured at the given time point using the NIR2 imager at 0.01 second exposure. For pH stability, SBP-M13-SWNT were calibrated to pH = 4.5, 5.5. 6.5, 7.5, or 8.5 and samples were incubated 0, 1, 2, 4, and 24 hours. Samples were measured using NIR2 imager at 0.01 second exposure and normalized to the baseline value.

Cell Viability Assay

To confirm OVCAR8 viability in the presence of SBP-M13-SWNT, 5,000 cells were seeded into each well of a 96-well plate and incubated with 10, 5, 2.5, 1.25, 0.62, and 0 μg/mL SBP-M13-SWNT. 24 hours after probe incubation, Alamar Blue (Life Technologies) reagent was added and fluorescence was measured 4 hours post-addition, following manufacturer's recommendations. Viability was normalized to blank control. Samples were run in quadruplicate.

Depth of Detection Limit of Tumors Labeled with SBP-M13-SWNT

Mice bearing OVCAR8 tumors were injected with ~200 μg/kg SBP-M13-SWNT. Twenty-four hours post-injection, tumors were excised. To determine the limit of detection by reflectance imaging, labeled tumors were cut into 1 mm diameter fragments and placed in a quartz capillary tube (Sutter Instruments). The quartz capillary tube was placed in an XFM-2 phantom mouse (Caliper) with the same optical properties of human tissue at 0, 4.3, 7.0, 9.7, or 18.2 mm depths. The fluorescence from the labeled tumor fragments was measured using the NIR2 imager at maximum aperture using 0.5 second exposure time. Background fluorescence images were also acquired before addition of labeled tumors. To quantify detection depth, background images were subtracted from acquired images of fluorescent tumors, and equivalent ROIs were drawn for images taken from each depth to calculated signal intensity.

Immunohistochemistry and fluorescence

Excised tissues were fixed in 10% formalin, embedded in paraffin, and sectioned for histology. Hematoxylin and eosin (H&E) staining was performed on tissue sections. For SPARC staining, rat anti-SPARC (1:40, R&D Systems) and rat isotype IgG (1:200, Abcam) were used with biotin-conjugated goat anti-rat antibody (Vector Labs, BA-9401), followed by the Vectastain ABC immunoperoxidase kit (Vector Labs, PA-6100) and DAB substrate (Vector

Labs, SK-4100) for detection and visualization. For immunofluorescence, AlexaFluor donkey anti-rat 488 secondary antibody (Life Technologies) was used on frozen tissue sections. To visualize SBP-M13-SWNT by fluorescence, AlexaFluor 750 carboxylic acid, succinimidyl ester (Life Technologies) was conjugated to SBP-M13-SWNT via primary amine linkage following manufacturer's recommendations and excess dye was removed by extensive dialysis before usage.

2.3 Results:

2.3.1 Physicochemical Characterization of M13-Stabilized SWNT Probe

The imaging probe (SBP-M13-SWNT) consists of three fundamental components: the SPARC binding peptide (SBP), M13 virus (M13), and single-walled carbon nanotubes (SWNTs) (**Fig. 2.1**). The filamentous M13 virus (6 nm diameter, 880 nm length) is genetically modifiable to incorporate peptides for display on the various coat proteins of the virus. M13 can display peptides with affinities to materials or biomolecules through iterative panning and selective enrichment for diverse applications including epitope mapping, ligand discovery against cells and tissues, and binding and nucleation of materials.[38, 200-202] The modularity of M13 can be further exploited to target various biomarkers in cancers, highlighting its attractiveness as a multifunctional probe. Previously, we used phage display to identify a peptide along the p8 major coat protein of M13 that binds and stabilizes SWNTs, while retaining the optical and electronic properties of the nanotubes.[202] Because M13 is amenable to genetic modification for peptide display, we further engineered the p3 minor coat protein to display a targeting peptide that binds SPARC (for Secreted Protein, Acidic and Rich in Cysteine).[199] SPARC is a matricellular protein highly expressed in certain subtypes of breast, prostate, and ovarian cancer.

SPARC overexpression has been shown to enhance ovarian cancer cell proliferation, invasion and metastasis. High levels of SPARC expression have been associated with high stage of ovarian carcinoma and correlated with poor clinical prognosis, suggesting its relevance as a clinical biomarker.[203] Collectively, this genetically-engineered NIR2 probe enables the localization, detection, and surgical excision of ovarian tumors, as outlined in the schematic presented in **Fig. 2.1**.

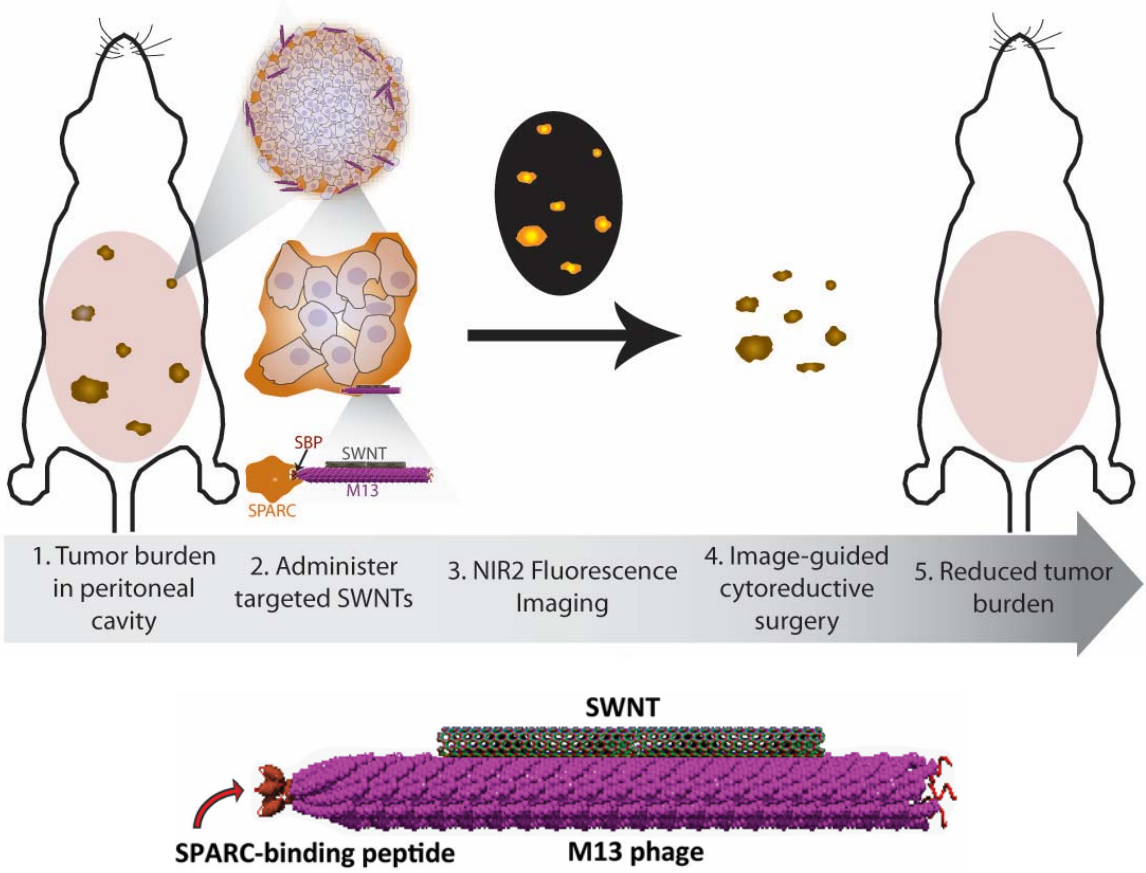

Figure 2.1. Schematic illustrating probe binding with ovarian tumor nodules for non-invasive detection by NIR2 fluorescence and surgical excision.

To ensure that our probe retained its functionality following its synthesis, we examined the optical properties of SBP-M13-SWNTs. Compared to unmodified starting SWNTs dispersed

in sodium cholate, complexed SBP-M13-SWNTs exhibit similar optical absorbance (**Fig. 2.2**). Photoluminescence (fluorescence) mapping of the excitation and emission wavelengths of SBP-M13-SWNT suggests M13-stabilized SWNTs retain their fluorescent properties; non-dispersed, aggregating or bundled SWNTs would quench and not fluoresce, and thus, not appear in the fluorescence mapping.

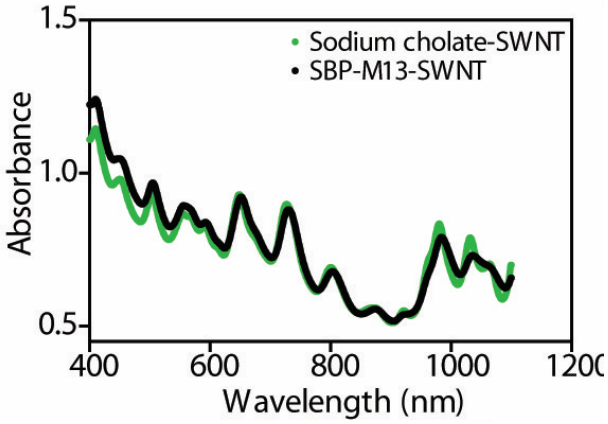

Figure 2.2. Absorbance spectra of SWNTs in sodium cholate and as SBP-M13-SWNT probe.

To establish their use for *in vivo* applications, we validated the stability of SBP-M13-SWNTs in blood and ascites and at different pH values by measuring the fluorescence over 24 hours using a custom-built small animal NIR2 fluorescence imager developed in our laboratory.[36] SBP-M13-SWNTs retain fluorescence at various dilutions in the blood and ascites fluid from the peritoneal cavity (**Fig. 2.3**), and we did not observe quenching of the probe. Previous reports indicate that exposed SWNTs in solution will adsorb serum proteins on their sidewall and subsequently lose fluorescence.[36, 204] Here, we observe no loss of fluorescence intensity, indicating the probes are well solubilized by M13 and highly stable for *in vivo* imaging applications. In addition, the probe is fluorescently stable across a broad pH range, from 4.5 to

8.5 (**Fig. 2.3**), suggesting the probes will be stable in the vascular and lymphatic systems, peritoneal cavity, and for cellular uptake. We also confirmed the targeted probes are well tolerated and non-cytotoxic to target OVCAR8 ovarian cell line (**Fig. 2.3**), which underscores their potential for *in vivo* imaging applications.

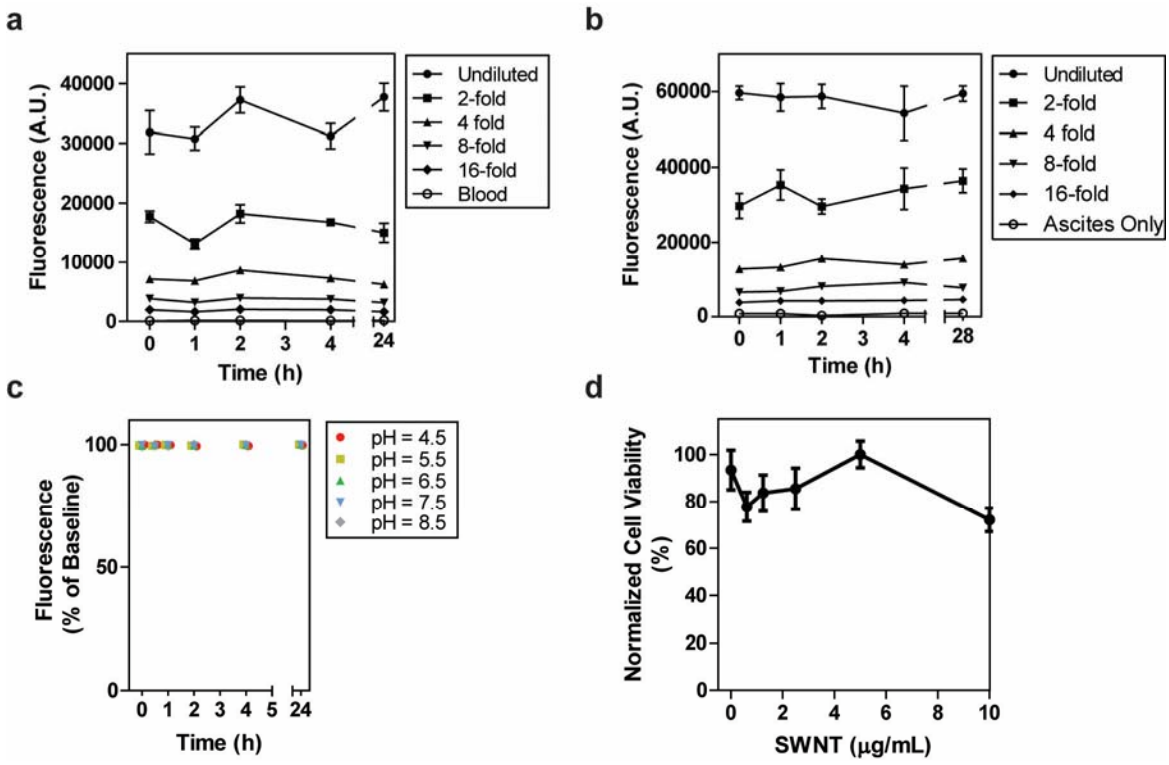

Figure 2.3. Stability and cytotoxicity of SBP-M13-SWNTs. (a) Serial two-fold dilutions of SBP-M13-SWNTs were incubated in blood to assess detection range and stability of the imaging probe in an *in vivo* environment for periods up to 24 hours. NIR2 fluorescence measurements directly correlated with concentration of SBP-M13-SWNT, and the fluorescence remained stable for periods up to 24 hours. Dilutions were measured in duplicate. Error bars denote standard deviation. (b) Serial two-fold dilutions of SBP-M13-SWNTs were incubated in ascites harvested from a tumor-bearing mouse to assess stability and detection limit of the imaging probe for periods up to 28 hours. Fluorescent signal was directly proportional to concentration of SBP-M13-SWNT in ascites. Dilutions were measured in duplicate. Error bars denote standard deviation. (c) SBP-M13-SWNTs were incubated at pHs between 4.5 – 8.5 for periods up to 24 hours. NIR2 fluorescence measurements were unaffected by pH of the solution for periods up to 24 hours. Samples were measured in duplicate. Error bars denote standard error. (d) OVCAR-8 cells incubated in the presence of SBP-M13-SWNTs remain viable at [SBP-M13-SWNT] between 0 - 10 ug/mL. Six samples were run for each experimental condition. Error bars denote standard error (n = 6).

We next examined the sensitivity of the probe in terms of its capacity to target OVCAR8 ovarian cancer cells *in vitro*. Serial ten-fold dilutions of OVCAR8 cells were incubated with SBP-M13-SWNT for 24 hours and cell lysates were collected. Measuring the fluorescence

intensity of the SBP-M13-SWNT incubated cells using our custom-built imaging system, we observed that as few as approximately 10,000 cells incubated with SBP-M13-SWNT exceeded the minimum level of detection (**Fig. 2.4**).

To test SBP-M13-SWNT for risk of photobleaching, we exposed them to an 808 nm laser for a continuous, 30 minute period and measured fluorescence intensity in five minute intervals up to 30 minutes post-irradiation. No appreciable loss of fluorescence of M13-SBP-SWNTs was observed during this period. However, the intensity of fluorescein isothiocyanate (FITC), a fluorescein derivative that has been used to molecularly image and guide intraoperative resection of ovarian tumors in humans, exponentially decreased during the same light exposure kinetics (**Fig. 2.4**).[27] The observations that SWNTs do not photobleach and also maintain their optical properties illustrate that these particles have the potential to assist surgeons to visualize tumors during resection.

Another potential advantage of SWNT-based imaging compared to FITC-based imaging is the potential to detect tumors located at greater depths in the body. To investigate the depth of detection that can be achieved with our probe, we harvested ovarian tumors that had been treated with SBP-M13-SWNTs and imaged the small tumor fragments (~1 mm diameter) at various depths within a tissue 'phantom' construct, which mimics the optical properties of human tissue. Using our NIR2 fluorescence reflectance imaging system, we could detect SWNT-containing tumors to depths as great as 9.7 to 18.2 mm (**Fig. 2.4**).[36] To our knowledge, this is the best-reported quantifiable tumor depth using reflectance imaging, relative to previously reported values.[194] By permitting deeper imaging, SBP-M13-SWNT therefore offers the potential for non-invasive detection prior to surgery and improved resection of tumors during surgery.

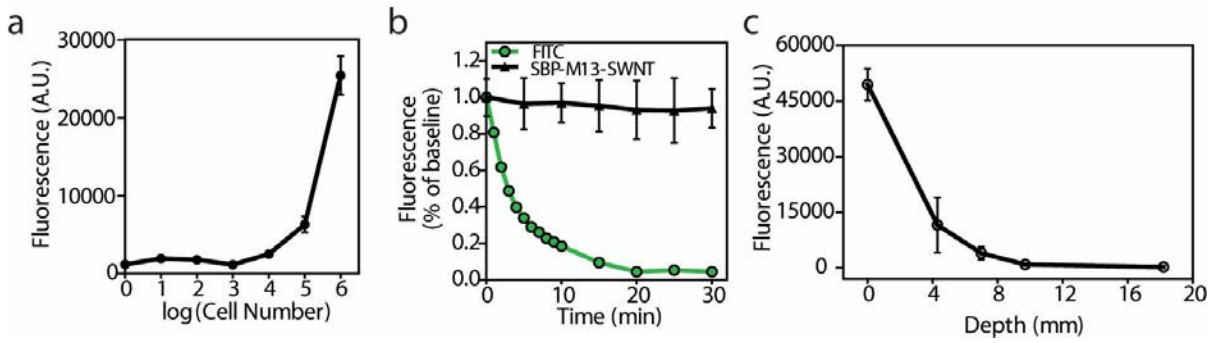

Figure 2.4. (a) *In vitro* sensitivity of SBP-M13-SWNT fluorescence in ovarian cancer cell culture. (b) Photobleaching fluorescence decay of FITC and SBP-M13-SWNTs under continuous excitation. (c) Depth of detection of tumors labeled with SBP-M13-SWNTs. Tumors containing SBP-M13-SWNTs were excised from mice into 1 mm diameter fragments and placed within a tissue phantom at varying known depths (0, 4.3, 7.0, 9.7, or 18.2 mm). Samples were imaged using a custom-built fluorescence imager at 0.5 s exposure. Samples were detectable to depths as great as 9.7 to 18.2 mm in the tissue phantom. Five samples were measured per condition. Error bars denote standard deviation (n = 5).

Having demonstrated the *in vitro* stability and fluorescence of SBP-M13-SWNT, we proceeded to characterize the *in vivo* properties of the probe in an orthotopic model of ovarian cancer. OVCAR8 human cell line was used to create the orthotopic model, since it overexpresses the target SPARC, as confirmed by Oncomine analysis and immunohistochemistry (**Fig. 2.5**). [205]To compare routes of administration, tumor-bearing animals were injected intraperitoneally or intravenously and the circulating probe concentration was monitored via SWNT fluorescence in the blood. Intravenously administered SBP-M13-SWNT reached a peak concentration in the circulation approximately 10 minutes after injection, and circulating levels became negligible after 150 minutes (**Fig. 2.5**). Notably, SBP-M13-SWNT administered intraperitoneally led to negligible elevations in blood-borne SWNT fluorescence for at least 24 hours, suggesting that the majority of SBP-M13-SWNT remain in the peritoneum following injection (**Fig. 2.5**). This finding was verified by the observation that, following a transient increase in NIR2 fluorescence

in the peritoneum, the overall intensity in this location stabilizes for periods up to 24 hours following injection (**Fig. 2.6**).

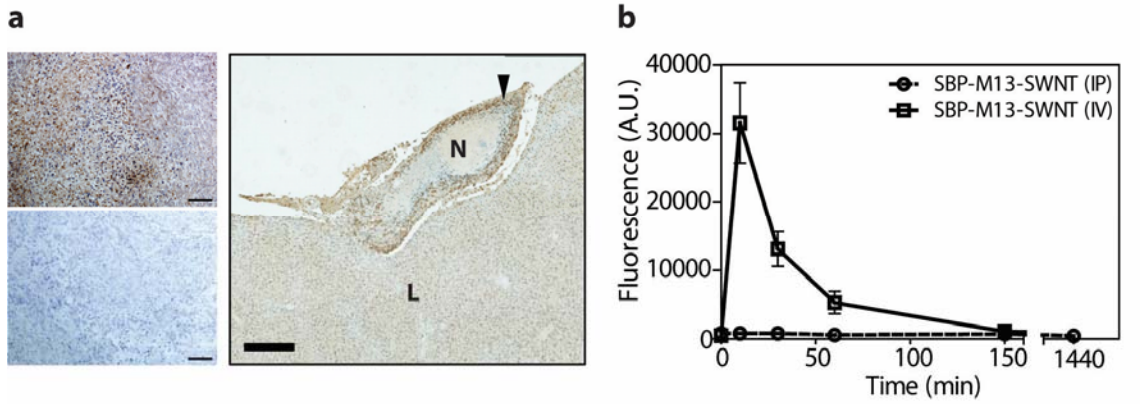

Figure 2.5. (a) SPARC Expression in OVCAR-8 Tumors. OVCAR-8 subcutaneous xenografts (left top; isotype control shown on left bottom) and orthotopic tumors (right) were processed for immunohistochemistry and examined for expression of SPARC. Both subcutaneous and orthotopic OVCAR-8 tumors express SPARC protein. Enhanced SPARC expression observed in the viable tumor rim of the orthotopic nodule (N, expression indicated by black arrow) seeded on liver (L). Scale bars: 100 µm (left top, bottom), .1 mm (right) (b) Pharmacokinetic circulation study of SBP-M13-SWNT administered intravenously (IV) and intraperitoneally (IP).

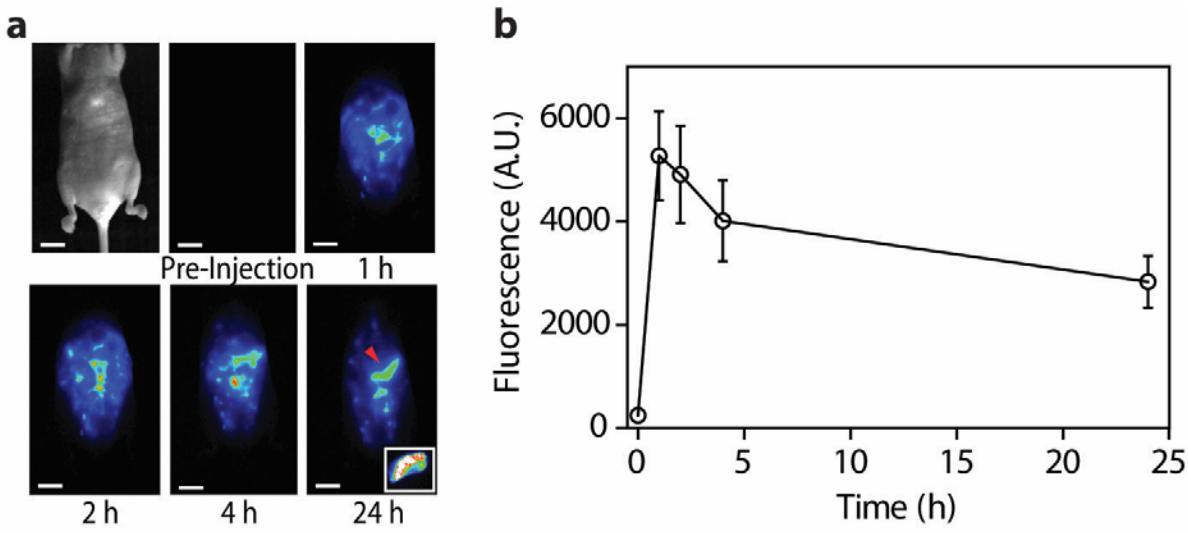

Figure 2.6. (a) Representative whole abdomen NIR2 imaging series following intraperitoneal administration of SBP-M13-SWNTs. Inset (far right): Surgically excised tumor nodule (denoted by red arrow) observed 24 hours post-injection of SBP-M13-SWNTs. (b) NIR2 fluorescence intensity in the abdomen of tumor-bearing animals following IP administration of SBP-M13-SWNTs up to 24 hours post-injection. (n = 5)

2.3.2 Improved Signal-to-Noise Performance In vivo Using SBP-M13-SWNT in NIR2 Wavelength Regime

Signal-to-noise behavior is a critical parameter for sensitive detection of tumors. To directly compare the signal-to-noise ratios between SWNTs and dyes in the NIR1 or visible regimes, SBP-M13 viruses were either complexed to SWNTs or conjugated with AlexaFluor750 dye (SBP-M13-AF750) or FITC (SBP-M13-FITC). Probes were then combined and added in five-fold excess of their minimum detection limits to mice bearing disseminated tumors. Images were acquired (**Fig. 2.7**) and fluorescence intensities from tumors in the peritoneal cavity, muscle and background were determined. The tumor-to-muscle ratio of SBP-M13-SWNTs was 5.5 ± 1.2 (mean ± s.d), which was significantly higher than ratios calculated for SBP-M13-AF750 (3.1 ± 0.42) and SBP-M13-FITC (0.96 ± 0.10) (**Fig. 2.7**). The tumor-to-background ratio (i.e., intensity of tumor to image background) achieved using SBP-M13-SWNTs was 134.9 ± 21.0, which was

a 24- and 28-fold improvement over SBP-M13-AF750 and SBP-M13-FITC, respectively (**Fig. 2.7**). Importantly, as highlighted by the arrows in **Fig. 2.7**, tumor nodules not observed in the visible and NIR1 channels were detectable in the NIR2 regime with SBP-M13-SWNTs, which highlights the sensitivity of SWNT probe and imaging system.

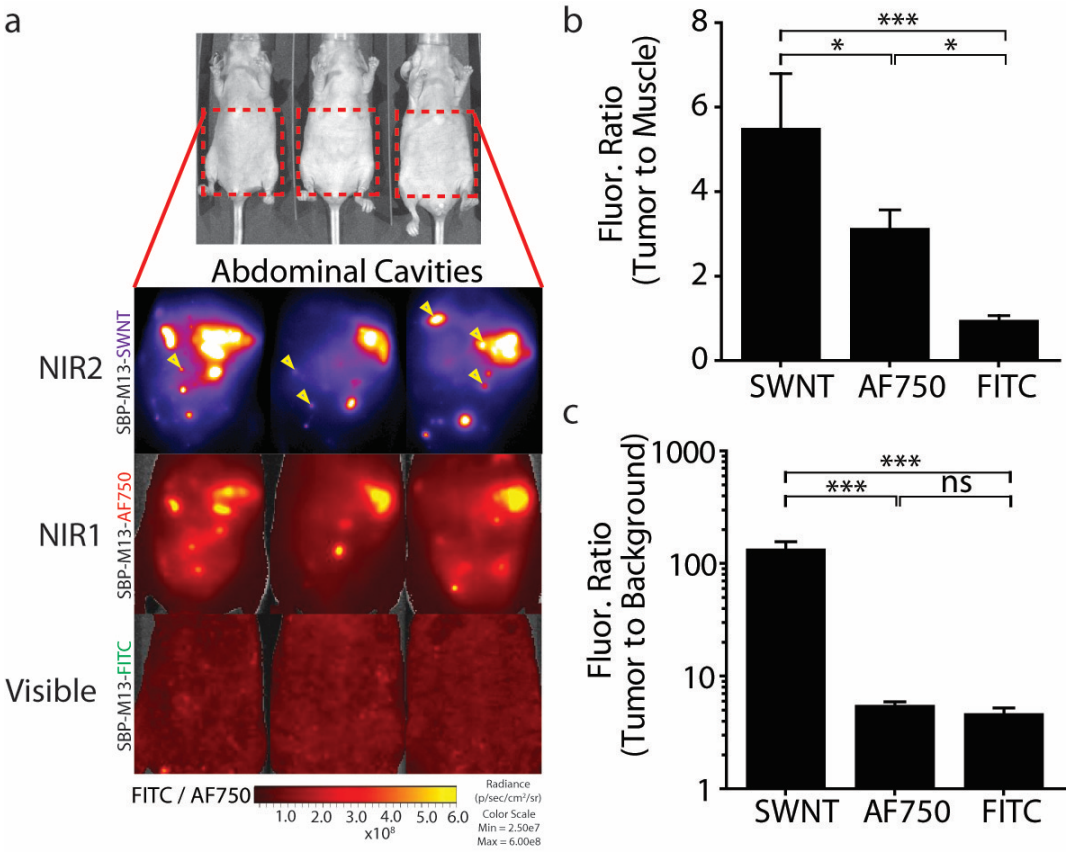

Figure 2.7. (a) Non-invasive imaging of ovarian tumors using SBP-M13 conjugated to SWNTs (NIR2) , AlexaFluor750 (NIR1), and FITC (Visible) (top to bottom) Arrows in SWNT panel denote nodules visible only by SWNTs. (n=3 animals) (b-c), Tumor-to-muscle ratio and tumor-to-background ratio from non-invasive images obtained with SWNTs, AF750, and FITC. (n=3 per group; ***P <0.001; *P<0.05; one-way ANOVA and Tukey post tests.) Error bars, s.d.

2.3.3 Selective and Molecular Targeting of SBP-M13-SWNT to Ovarian Tumors In vivo

Because many tumor nodules are implanted on the surfaces of peritoneal organs in this model, we also computed organ-specific TBRs for tumor nodules on the liver, intestine, and spleen. Representative photographs of organs containing tumor implants on their surface with their corresponding NIR2 fluorescent images are shown in **Fig. 2.8**. The TBRs (i.e., ratio of surface tumor nodule fluorescence relative to that observed in its underlying organ) calculated for the liver, intestine, and spleen were 4.6, 8.0, and 3.1, respectively (**Fig. 2.8**), highlighting the specificity of the probe towards tumor nodules compared to its underlying organs.

The *in vivo* sensitivity of targeting conferred by the SPARC-binding peptide (SBP) was assessed by injecting tumor-bearing animals with M13-SWNTs expressing SBP or untargeted M13-SWNTs. The NIR2 intensities of excised tumor nodules and intestinal tissue of the same animal were used to compute target-to-background ratios (TBR) for the targeted and untargeted probes. SBP-M13-SWNTs showed significant, ten-fold higher TBR than untargeted M13-SWNTs, likely due to a combination of improved targeting and reduced tissue autofluorescence in the second near-infrared window (**Fig. 2.8**).

To verify the molecular specificity of SBP-M13-SWNTs, we assessed the SWNT-positive tumor nodules by immunohistochemistry. Standard hematoxylin and eosin (H&E) staining of SWNT-positive tumor sections revealed histopathological features consistent with ovarian tumor nodules, including a high nuclear-to-cytoplasmic ratio, cellular crowding, a necrotic core, and a distinct architecture from underlying organs (**Fig. 2.8**). Interestingly, the liver displayed a fluorescent signal where no tumor nodule was visible by eye, and after biopsy of the indicated area, H&E staining indicated pathology consistent with a tumor nodule located on the liver (**Fig. 2.8**). Additionally, immunohistochemical staining revealed an enrichment of

SPARC expression along the periphery of the SWNT-positive tumor nodules (**Fig. 2.8**). Finally, to assess whether our probe specifically co-localizes with SPARC-expressing regions of the tumor nodules, we administered SBP-M13-SWNTs conjugated with AlexaFluor 750 to tumor-bearing mice and analyzed the excised tumor nodules by immunofluorescence. In multiple nodules, SPARC was widely expressed, with particularly strong expression at the tumor periphery (**Fig. 2.8**) in a pattern consistent with our immunohistochemical staining described in **Fig. 2.5**. The AF750-labeled SBP-M13-SWNTs were similarly enriched at the tumor periphery (**Fig. 2.8**). These patterns are consistent with an outside-in diffusion model limited both by the hydrodynamic radius and ligand interactions of SBP-M13-SWNTs with the tumor nodule.

Figure 2.8. (a) Photographs and NIR2 fluorescence (10-50 ms exposure) of tumor nodules implanted on several peritoneal organs. (b) Quantification of nodule and organ-specific background for nodules present on the liver, intestine, and spleen. (n=8-11 nodules per organ) (c) Tumor to intestine ratio for targeted and untargeted M13-SWNT probes. Intestinal tissue used for background intensity. (+SBP, n=6; -SBP, n=13) (d) Representative NIR2 fluorescence and H&E staining of a positive nodule revealing characteristic tumor histology. (e) Immunofluorescence staining reveals co-localization of M13-SBP-SWNTs conjugated to AlexaFluor750 dye with SPARC expression in an NIR2-positive nodule. Scale bars: 10 mm (a), 10 mm (d, NIR2), 250 um (d, H&E Liver nodule), 125 um (d, H&E Nodules), 5 mm (e, NIR2), 2.5 mm (e, SPARC, AF750-M13)

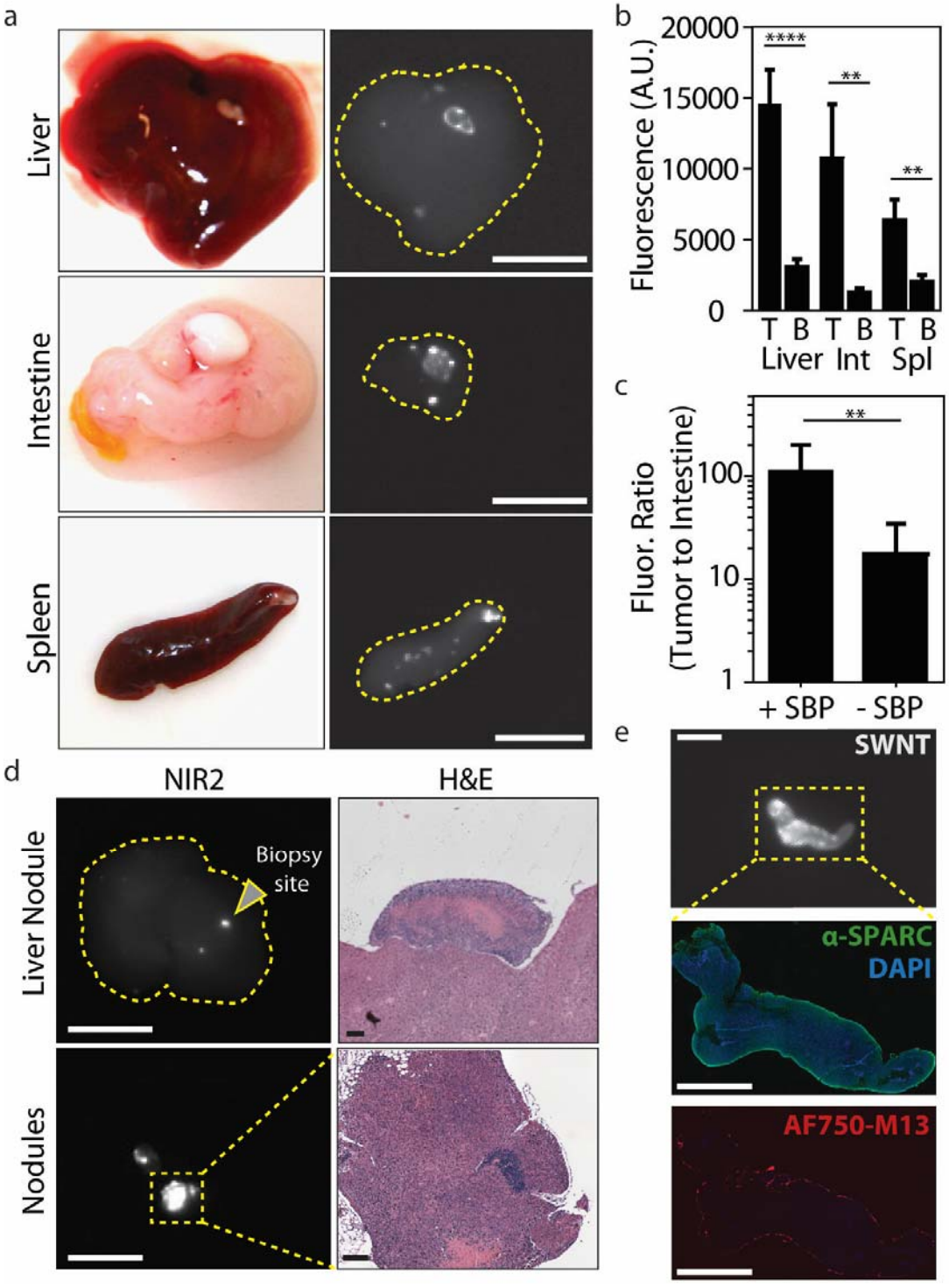

Figure 2.8. (Continued).

2.3.4 Image Guidance Using SBP-M13-SWNT Improves Surgical Resection of Tumors

To assess the potential clinical utility of SBP-M13-SWNTs for reduction of tumor burden, a gynecological surgeon performed surgeries on orthotopic models of ovarian cancer that were imaged at various points during the surgical procedures. Approximately 15-25 minutes were spent on procedures in each experiment, and tumor implants were predominantly distributed in the bowel mesentery, peritoneal wall, subdiaphragmatic surfaces, and surfaces of organs including the liver, spleen, pancreas, and within the pelvic cavity. H&E stained tissue sections were prepared from all excised nodules and assessed by a pathologist. With the exception of two non-tumor containing mesenteric lymph nodes, all tissues examined (n = 197) were positive for ovarian tumor tissue indicating an accuracy of 98.9% of our probe for ovarian tumors. Surgery was first performed with pre-operative image guidance to assess whether this was beneficial to the procedure based on the distribution of excised tumor nodule sizes. A comparative analysis of excised tumors revealed that a significantly higher number of sub-millimeter tumor nodules were discovered in the image-guided cohorts versus the non-image guided cohorts (12 and 0 nodules, respectively, **Fig. 2.9**). Using image guidance, there were also greater numbers of excised tumors from 1.3 to 3 mm; however, there was no appreciable difference for larger tumors (> 3 mm) between image-guided and non-guided cohorts. We additionally assessed the impact of performing surgery in a serial manner, with an initial round of non-image guided surgery, followed by image acquisition and a second round of image-guided surgery (**Fig. 2.10**). We observed reduction of tumor burden from non-image guided surgery to image-guided surgery (**Fig. 2.10**). We determined TBR of overall tumor burden to background muscle by region of interest analysis and confirmed reduction of overall tumor burden due to image-guided reduction (**Fig. 2.10**). Using both non-invasive SWNT imaging (**Fig.**

2.10) and quantification of excised tumor nodule diameters, we observed a greater number of sub-millimeter excised tumors in the groups assisted by SWNT image guidance (30 versus 4 nodules, **Fig. 2.10**). Overall, significantly more, smaller diameter tumors were excised using SWNT-based image guidance as opposed to unguided surgeries (**Fig. 2.10**).

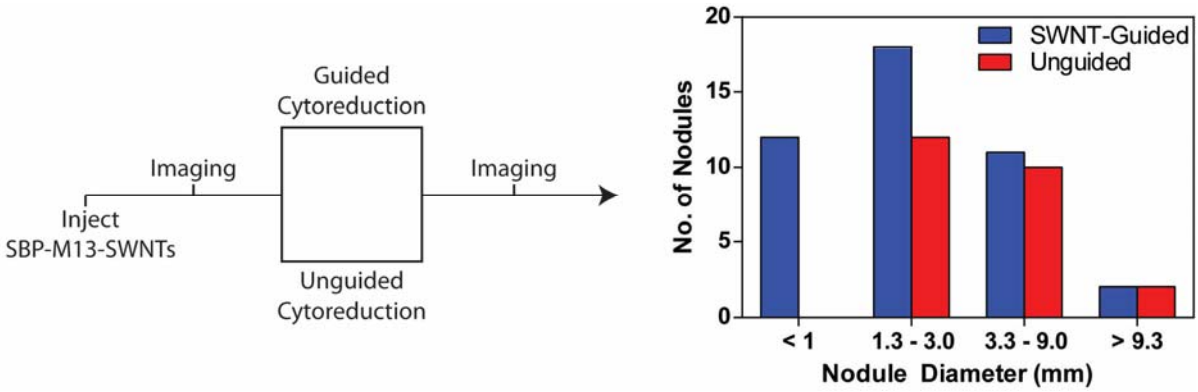

Figure 2.9. Comparison of SWNT-Guided and Unguided Cytoreduction. Tumor-bearing animals were randomized to receive SWNT-guided or unguided cytoreduction. Excised tumors were measured along their maximum diameters prior to tissue fixation. Tumor diameters for each treatment group are plotted as a histogram. (n = 43 nodules, SWNT-guided; n = 24, unguided)

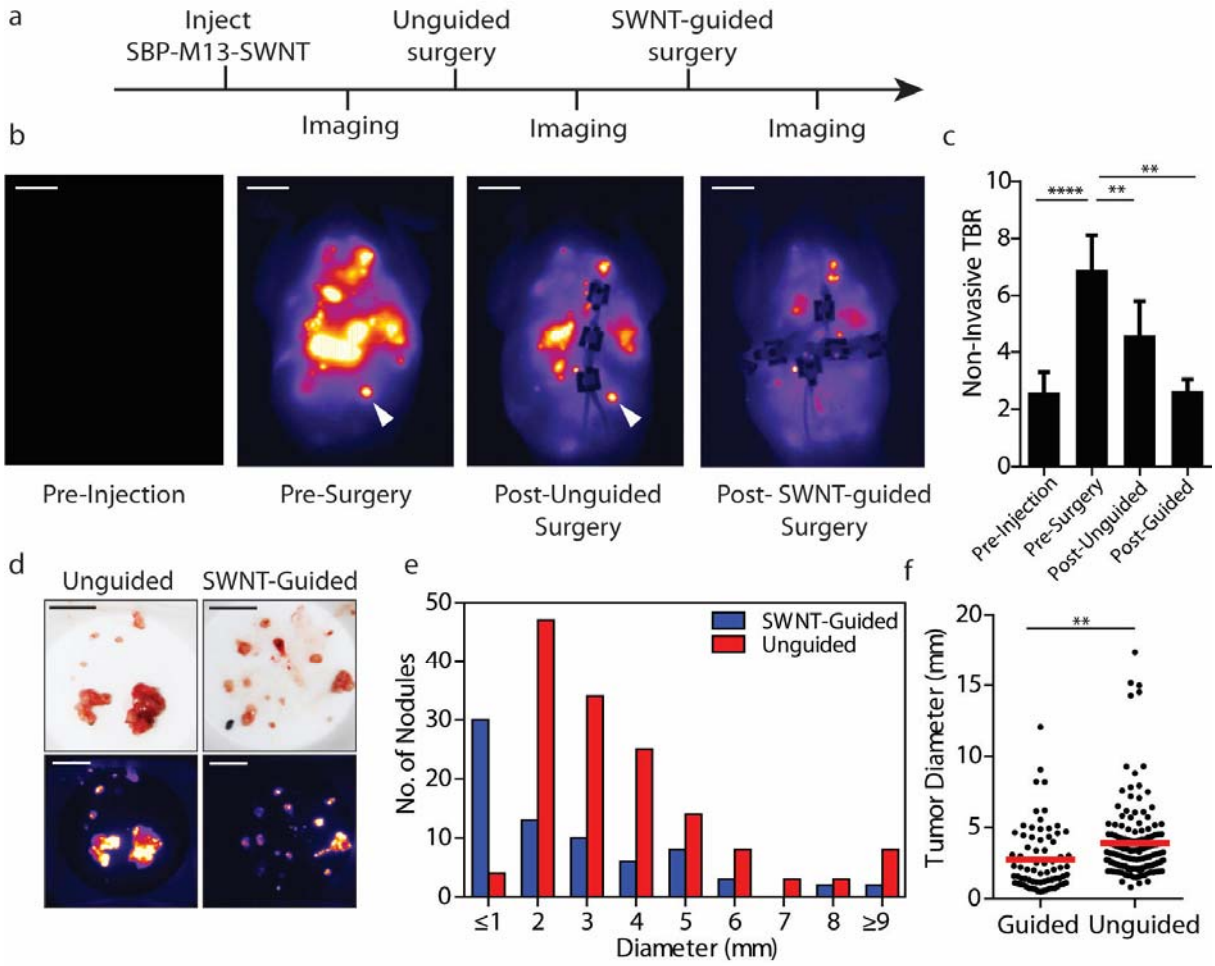

Figure 2.10. (a) Schematic of serial surgical procedure. (b) Representative whole-abdomen NIR2 images prior to injection of SBP-M13-SWNT, prior to surgery, after an initial, unguided surgery, and after subsequent SBP-M13-SWNT-guided surgery. White arrow indicates a SWNT-positive nodule detected only during image-guided surgery. (c) Non-invasive target-to-background ratios during surgery. Muscle from hind limb used for background. (d) Photographs and NIR2 images of excised tumor nodules following unguided and SWNT-guided surgery. (e) Histogram of tumor diameters removed with and without guidance. (f) Dot plot of individual tumor nodule diameters excised with and without SWNT-guidance. (Guided, n=74; Unguided, n=146) Scale bars: 1 cm (b), 1 cm (c, photograph), 1 cm (c, NIR2)

2.4 Conclusions:

This study describes the development and use of a single fluorescence imaging agent for high contrast, non-invasive detection and guidance for surgical removal of disseminated ovarian tumors. NIR2 emitting SWNT probes offer significantly improved signal-to-noise performance compared to visible and near infrared dyes and detect tumors not visualized using the optical dyes. These targeted, M13-stabilized SWNT probes assist surgical removal of ovarian tumors with excellent sensitivity as confirmed by subsequent pathological examination. The probe is sensitive for identifying tumor nodules located on several abdominal viscera, the peritoneal wall, and the bowel mesentery. Importantly, compared to fluorescent probes in the visible or NIR1 regimes, the fluorescence of SWNTs is not limited by quenching, allowing for long-term, continuous imaging. Consequently, with the development of advanced imaging platforms, surgeons will be able to visualize tumors both before and throughout surgical procedures, thereby significantly improving fluorescence-guided tumor resection. This study demonstrates that surgery accompanied by image guidance leads to identification and removal of smaller tumor nodules. While NIR2 images could not provide three-dimensional localization of the tumor implants, they provided information about the sites of disease burden requiring closer surgical examination. Imaging of regions in which the surgeon was initially reluctant to explore in an effort to minimize morbidity such as excessive blood loss, but later revealed a positive NIR2 signal, often led to the identification and excision of additional tumor nodules missed on non-image guided approaches. While we did not investigate longitudinal survival rates after image-guided surgery in our animal models, the majority of clinical evidence suggests that optimal surgery, currently defined as the removal of tumors with diameters of 1 cm or larger, is correlated with improved overall survival rates.[45] SWNT-based molecular probes could

greatly aid in surgical planning and resection in order to help achieve a reduction in mortality rates in the future.

We achieve detection of sub-millimeter tumors with excellent target-to-background ratios using M13-stabilized SWNTs, in part due to properties of the particles that lead to low tissue scattering and minimal tissue autofluorescence in the NIR2 optical window. In comparing excised tumors with unaffected intestinal tissues as a background measurement, we observed high TBRs of ~112 using our SPARC-targeted M13-SWNT probes. Following intraperitoneal administration, some uptake is observed using non-targeted SWNT probes, which is most likely due to non-specific binding interactions or convective flow patterns present within the peritoneal cavity. Fluorescence imaging in the second optical window offers the promise of imaging at greater penetration depths (>3-5 mm) with reduced optical scattering within the tissue. In comparing the performance of visible, NIR1 and NIR2 probes, the M13-SWNT probe achieved the highest tumor-to-muscle and tumor-to-background ratios, most likely due to less tissue absorbance and autofluorescence in NIR2 regime. In addition, we were able to see tumors not observed in the visible and NIR channels, highlighting the improved tissue penetration and detection in the NIR2 regime. Using our reflectance imaging system, we can detect 1 mm diameter tumors up to a maximal depth between 9.7 and 18.2 mm. To our knowledge, this represents the highest reported depth of detection using fluorescence reflectance, and is also higher than previous reports that detected mammary tumors labeled with activatable Cy5 probes.[194] Future work to enhance the fluorescence of M13-SWNTs using plasmonic nanomaterials and molecular targeting using other ligand-receptor interactions including the folate receptor may offer further improvements on current limits of detection and resolution.[27,

206] These longer wavelength emitting probes will greatly aid in locating ovarian tumors confined to deep anatomical regions.

SBP-M13-SWNT injected intraperitoneally co-localized with stromal SPARC expression on the periphery of the ovarian tumor nodules. Tumor nodules labeled with the probes exhibited high signal with low background in the surrounding healthy tissues, including liver, spleen, and intestine. These high organ-specific TBRs in part assisted with more accurate surgical resection of tumor nodules localized to the organ surfaces. Because our probes can visualize the tumor margins, they have potential to assist the surgeon in delineating tumors from healthy tissue for improved resection of other solid tumors, as also demonstrated by approaches using activatable peptides and dyes, fluorescein conjugates, and multimodal nanoparticles.[27, 193, 194, 207, 208]

M13-SWNT molecular probes exhibit long-term stability and fluorescence for at least 24 hours for *in vivo* imaging applications. Since the probe retains its optical properties under various pH and physiological environments and under constant excitation, it is an attractive candidate for long-term imaging for non-invasive detection and fluorescence-guided surgery. The safety of M13 in the clinic has been shown in a Phase I clinical trial to identify patient-specific ligands. The virus possessed a low toxicity profile, elicited a “submaximal” humoral immune response, and patients demonstrated no adverse allergic responses.[209] Similarly, recent work has confirmed the non-cytotoxicity of well-functionalized, short length SWNTs administered *in vivo* through histology and serum chemistry.[32, 210, 211] While further studies are required to conclusively establish the safety and pharmacokinetics of M13 and SWNTs, these initial findings support the potential use of these nanomaterials in a clinical setting.

While in this study we use SWNTs for fluorescence imaging, others have demonstrated their utility as carriers for therapeutic cargoes or genes (reviewed in [212]) as well as photothermal ablative therapy.[213] We have begun to explore the potential utility of SBP-M13-SWNTs for *in vivo* heating of the local tumor microenvironment to assess their potential as sensitizing agents to chemotherapeutic agents and multimodal imaging and therapeutic agents.

To advance our findings closer to clinical translation, new instrumentation will be required to allow for intraoperative surgical guidance in real-time, and three-dimensional tomography for quantitative analysis and more accurate localization of tumors. Simulations suggest that at near-infrared wavelengths that define the second near-infrared window, SWNT-based probes may be detectable at depths up to 10 cm on improved imaging platforms, highlighting the potential utility of these particles in human subjects.[214] This new platform would allow for real-time, non-invasive imaging and processing for accurate visualization of tumors during tumor staging, pre-surgical planning, and during procedures. Coupling improved instrumentation with probe development will greatly improve the ability to detect tumors at earlier stages and possibly detect micrometastases. The ability to detect tumors of smaller sizes at earlier time points may also provide fundamental insights into tumorigenesis and disease progression, as well as allow clinicians to better monitor therapeutic responses and recurrence of disease. The modular nature of the M13 platform, which can incorporate patient-specific targeting peptides or antibodies, will enable the development of "personalized imaging" tailored to the unique tumor microenvironments present within individual patients.

2.5 Acknowledgements:

This work has been supported by the NIH Center for Cancer Nanotechnology Excellence U54-CA119349-04 (A.M.B.). A.F.B. is supported by the NIH/Medical Scientist Training Program. S.N.B. is an HHMI Investigator. The authors would like to thank Dr. Rod Bronson for tumor scoring. The authors thank Mike Brown for assistance with histology. The authors acknowledge the Koch Institute Swanson Biotechnology Center for DNA sequencing.

2.6 Author Contributions:

Authors: Debadyuti Ghosh*, Alexander F. Bagley*, Young Jeong Na, Michael Birrer, Sangeeta N. Bhatia, Angela M. Belcher

* These authors contributed equally.

D.G., A.F.B., S.N.B., and A.M.B. conceived the idea and wrote the manuscript. Y.N. performed the surgeries and excised the tumors. M.B. provided conceptual advice and edited the manuscript. D.G. and A.F.B. designed the studies and performed all other experiments and data analysis.

CHAPTER 3. NANOMATERIALS FOR PHOTOTHERMAL ABLATION IN GENETICALLY-ENGINEERED TUMOR MODEL

3.0 Abstract:

Plasmonic nanomaterials are poised to impact the clinical management of cancer through their ability to convert externally applied energy into localized heat at sites of diseased tissue. However, characterization of plasmonic nanomaterials as cancer therapeutics has been limited to xenograft models, creating a need to extend these findings to more clinically relevant models of cancer. Here, we evaluate the method of photothermal ablation therapy in a genetically engineered mouse model (GEMM) of sarcoma, which more accurately recapitulates the human disease in terms of structure and biology than subcutaneous xenograft models. Using polyethylene glycol (PEG)-coated gold nanorods (PEG-NRs), we quantitatively evaluate the ability of nanoparticles to penetrate and accumulate in sarcomas through passive targeting mechanisms. We demonstrate that PEG-NR-mediated photothermal heating results in significant delays in tumor growth with no progression in some instances. Lastly, by evaluating our photothermal ablation protocol in a GEMM, we observe off-target heating effects that are not detectable in xenograft models and which may be of future clinical interest.

3.1 Introduction:

In the last decade, nanoparticles and nanomaterials have been engineered for a wide array of biomedical applications. The clinical management of cancer stands to benefit greatly from nanoparticles that can more directly and selectively target tumors for diagnosis, imaging, and therapy. Noble metal nanomaterials are especially promising diagnostic, imaging and therapeutic tools because they exhibit strong optical absorption and scattering properties due to an effect known as surface plasmon resonance. Gold nanoparticles are plasmonic materials which are

characterized by facile synthesis and bioconjugation and low cytotoxicity,[141, 179, 215-220] and which have demonstrated potential as multimodal diagnostic and therapeutic agents *in vivo*.[139, 141, 221] As diagnostic agents, gold nanoparticles enable imaging by optical coherence tomography (OCT), photoacoustic tomography, two-photon luminescence, X-ray computed tomography (CT), and surface-enhanced Raman spectroscopy.[218, 222-225]

Therapeutically, strategies employing gold nanoparticles have harnessed their ability to selectively heat tumor tissue through the localized conversion of light into thermal energy. By varying their geometrical properties, gold nanoparticles including nanoshells and nanorods can be tuned to absorb specific near infrared wavelengths, at which biological tissue exhibits relatively low extinction coefficients. Gold nanoparticle-mediated photothermal ablation has shown considerable efficacy in the treatment of cancer, leading to complete resolution of irradiated tumor xenografts in some cases.[141, 219, 220] Gold nanoparticle-induced heating has also been combined with other therapeutic modalities to leverage synergies between heat and radiation or chemotherapy, thereby sensitizing tumors to treatment.[112, 226] Finally, nanoparticle-induced heating has been used as a photothermal trigger in heat-responsive drug delivery systems.[227, 228]

Despite the therapeutic promise of gold nanoparticles, translation to the clinic requires that their effectiveness be validated in physiologically relevant models of human cancer. To date, delivery of gold nanoparticles has been studied in subcutaneous xenograft tumors, and the accumulation of nanoparticles within xenografts has largely relied on passive targeting mechanisms. However, because subcutaneous xenografts fail to recapitulate important structural features of more clinically representative GEMMs, the degree to which passive accumulation

plays a role in tumor-targeting within genetic models remains to be determined.[148, 149, 229] In particular, there is increasing evidence that tumor interstitial fluid pressure is model–dependent and site-specific; therefore, pressure variations between subcutaneous xenografts, orthotopic models, and GEMMs may directly influence the extravasation across the vessel wall, the physical and biological entrapment of nanoparticles in the interstitium, and the intratumoral distribution of gold nanoparticles.[230] Differences in the anatomical location and geometry of the tumor in different mouse models may further affect the ability to focus NIR light, induce specific versus off-target heating, and lethally ablate the tumor. Demonstrating the penetration and accumulation of gold nanoparticles, as well as their ability to induce site-specific photothermal ablation in GEMMs, is therefore an important step as these particles are evaluated for their utility in the clinic.

Here, we sought to directly compare the effectiveness of a PEG-NR ablative therapeutic protocol in a genetically-engineered mouse model to previous results obtained in subcutaneous xenografts.[141, 219, 220] To assess the impact of PEG-NR ablative therapy, we selected a model of sarcoma harboring conditional mutations in Kras and Trp53 and resembling human sarcoma both in microscopic structure and by immunohistochemistry.[231] Our lab has previously developed polyethylene glycol (PEG)-coated gold nanorods which exhibit high stability in circulation ($t_{1/2} \sim 17$ hours) and a high optical absorption coefficient.[141] Leveraging this technology, we show that intravenously injected PEG-NRs passively accumulate in both subcutaneous xenografts and the sarcoma GEMM. Additionally, near-infrared laser irradiation (NIR) results in rapid, sarcoma-specific heating and ablation, leading to significant delays in tumor growth. We further show loss of extremity function due to non-specific heating of the sarcoma, an effect only observed in the GEMM. Collectively, these studies demonstrate that

passively-targeted PEG-NRs are capable of serving as highly-absorbing antennas in a clinically relevant model of cancer, and suggest that an optimal combination of PEG-NR delivery and appropriate ablation protocol could be translated to clinical utility.

3.2 Materials and Methods:

Preparation of PEG-coated Gold Nanorods

Gold nanorods were prepared as described previously.[141] Briefly, ~ 10 x 40 nm cetyltrimethylammonium bromide (CTAB)-coated gold NRs with longitudinal plasmon resonance at 810 (Nanopartz Inc.) were centrifuged at 16,000 rcf to concentrate and resuspended in 100 μM of 5-kDa methyl-PEG-thiol (Layson Bio, Inc.). The solution of 5-kDa methyl-PEG-thiol and CTAB-coated gold NRs was mixed and dialyzed overnight against ultrapure water (18 $M\Omega\ cm^{-1}$) using cellulose ester membrane dialysis (Spectrapor). Dialyzed samples were washed and filtered through 100-kDa filters (Millipore) to remove excess polymer, re-suspended in PBS, and stored at 4°C.

Generation of Soft Tissue Sarcomas

The mouse model of sarcoma was described previously by Kirsch, et. al.[231] The 129 S_4/SvJae mouse strain was bred and used for the generation of transgenic sarcoma mice. These mice harbor the following conditional mutations: LSL-KrasG12D/+ and $p53^{Fl/Fl}$. Soft tissue sarcomas were generated by intramuscular injection of 2.4×10^7 pfu of adenovirus (Ad-Cre) expressing Cre-recombinase (Gene Vector Transfer Core, University of Iowa) in the lower extremity. All animal studies and procedures were approved by the MIT and MGH Institutional Animal Care and Use Committees.

Generation of HT-1080 Xenografts

To generate subcutaneous xenograft models, nude mice (Jackson Labs) were injected bilaterally in the hind flanks with ~ 5 x 10^6 HT-1080 cells suspended in 200 µL DMEM.

Silver Enhancement Staining

Paraffin-embedded tissue sections were dewaxed and rinsed with double-distilled water for up to 30 seconds. Silver enhancement was performed using the Silver Enhancer Kit for Membranes (Cytodiagnostics). Equal volumes of Silver Enhancer Solution A and Silver Enhancer Solution B were mixed, and 50-100 µL was added to tissue sections, ensuring that the entire tissue was covered. Several dilutions of Solution A/Solution B mixtures in double-distilled water were tested. To determine the optimal enhancement time, representative 20X fields were imaged every 10 minutes for up to 80 minutes (Nikon ECLIPSE Ti). After incubation in silver enhancement solution, tissues were rinsed well with double-distilled water for up to 60 seconds. Samples were counterstained with hematoxylin, dehydrated, and mounted using standard protocols.

Quantification of silver deposits was performed using ImageJ software. To generate particle counts, the Analyze Particles command was applied to each contrast-enhanced, 8-bit, thresholded image. The same thresholding values were applied to all images included in the analysis.

ICP-MS

Samples for inductively coupled plasma mass spectrometry, or ICP-MS analysis, were frozen, lyophilized, and dissolved in aqua regia, prepared by adding 100 µL of nitric acid to 300 µL of 37% hydrochloric acid for 72 hours to dissolve gold particles. Then, samples were diluted to 10 mL with 9.6-mL 2% HNO_3 and analyzed via ICP-MS against standards (Thermo-Scientific

Finnigan ELEMENT2). Control saline and organ samples with exogenously added PEG-NRs were used for calibration.

In vivo Photothermal Therapy

Approximately ninety days after injection of Ad-Cre, mice bearing sarcomas between 150-200 mm^3 were randomized into one of three groups: PEG-NR + NIR, PEG-NR only, and NIR only (n = 4-5 mice per group). Mice were then injected through the tail vein with PEG-NRs in PBS (40 mg Au/kg). After allowing 72 hours for vascular clearance of PEG-NRs, the mice were anaesthetized with ketamine/xylazine and sarcomas were irradiated with a near-infrared laser (~0.5 W/cm^2, 810 nm, ~1 cm beam diameter). Prior to irradiation, the area around the tumor was shaved to remove excess hair. To monitor surface temperature during irradiation, an infrared thermographic camera (FLIR, Thermacam S60) was used. To assess tumor growth following treatment, tumors were measured every two to three days using digital calipers. Mice were euthanized when tumors exceeded 15 mm in any single dimension.

Immunohistochemistry

Immunohistochemistry was performed as described previously.[232] Briefly, immunostaining was performed on formalin-fixed paraffin embedded sections following antigen retrieval (10 mM citrate buffer (pH~6.0) at 95º C for 20 minutes; 22º C for 20 minutes). Primary antibodies rat anti-mouse CD31 (1:100, Pharmingen) and mouse anti-PCNA (1:500, PC-10; Santa Cruz Biotechnology) were applied to tissue sections for 1 hour at room temperature. Secondary antibodies were applied for 30 minutes at room temperature: biotinylated rabbit anti-rat IgG (1:1000, Vector Laboratories) or biotinylated horse anti-mouse IgG (1:1000, Vector Laboratories). Sections were then incubated for 30 minutes with ABC reagent (Vector

Laboratories), rinsed with PBS-T, and incubated in DAB chromagen reagent (Vector Laboratories). The sections were rinsed under running tap water for 5 minutes and counterstained in Mayer's Hematoxylin (Sigma), dehydrated, and mounted using Permount (Fisher Scientific). Standard hematoxylin and eosin staining was performed on tissue sections.

3.3 Results:

3.3.1 Sarcoma Treatment and Experimental Schedule

Sarcoma-bearing mice were injected with either PEG-NRs or PBS control and subjected to the photothermal ablation protocol (**Fig. 3.1**). Following irradiation, mice in the treatment trial were regularly monitored for tumor burden. A second group of mice were sacrificed either 24- or 72-hours after ablation to assess the short-term histopathological effects of ablation. We verified the uniform structure of PEG-NRs by transmission electron microscopy (**Fig. 3.1**) and demonstrated the capacity of PEG-NRs to specifically and significantly heat sarcomas exposed to NIR irradiation (**Fig. 3.1**). A representative photograph of the sarcoma (**Fig. 3.1**) provides perspective on the challenges of locally specific ablation and the potential source for non-specific heating effects (**Fig. 3.1**).

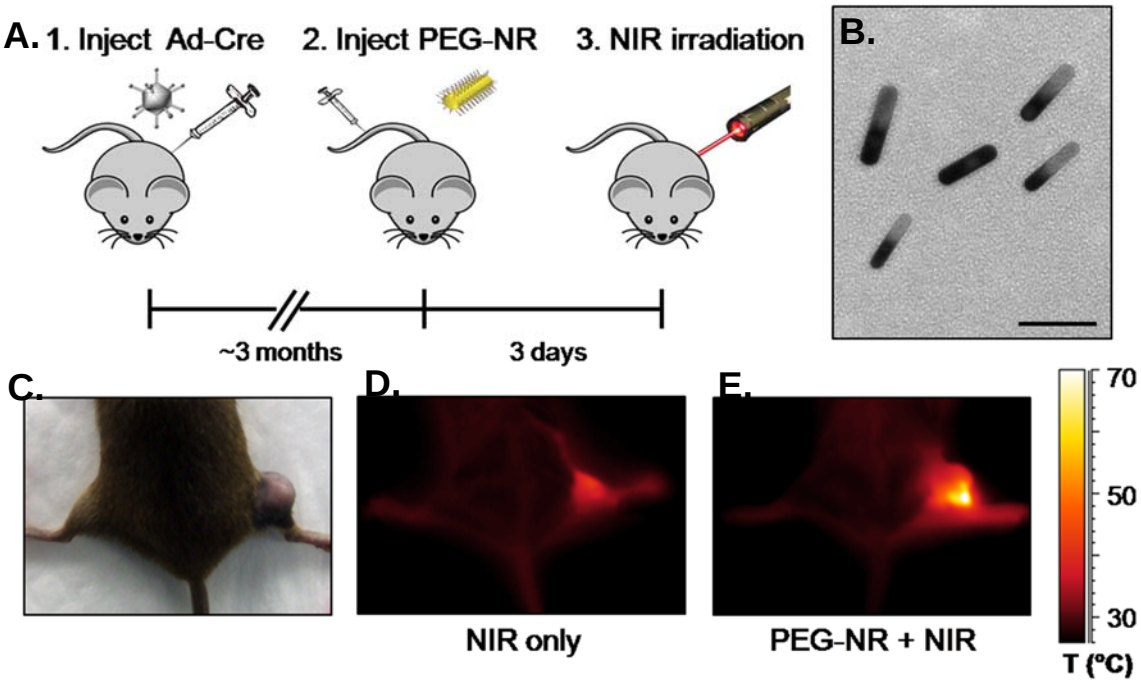

Figure 3.1. Schematic of PEG-NR heating with NIR laser irradiation in a GEMM of sarcoma. (A) Timeline of sarcoma generation and photothermal ablation procedure. (B) TEM image of PEG-NRs. Scale bar represents 50 nm. (C-E) Bright field (C) and IR thermographic images of mice with NIR irradiation only (D) and PEG-NR + NIR irradiation (E).

3.3.2 Comparison of PEG-NR Accumulation in GEMM and Xenograft Models of Sarcoma

To confirm the presence of PEG-NR accumulation in the tumor interstitium of both the GEMM and xenograft, we performed silver enhancement staining on tumor sections to visualize PEG-NR microdistribution within the tumors. Both the GEMMs and HT-1080 xenografts displayed comparable PEG-NR microdistributions, with PEG-NRs appearing throughout the tumor tissue (**Fig. 3.2**), while control samples displayed little to no detectable background staining (**Fig. 3.2**). Quantification of silver-enhanced PEG-NRs in histological sections revealed a greater number of particles accumulating in the HT-1080 xenografts compared to the GEMM; further, both the HT-1080 xenografts and GEMMs exhibited significant accumulation of particles relative

to uninjected tumor controls (**Fig. 3.2**). Additionally, we did not detect significant silver deposits in surrounding tissues, including skeletal muscle, indicating that PEG-NRs accumulated preferentially in sarcomas. ICP-MS confirmed the presence of gold in the GEMMs (6.60 %ID/g) in amounts comparable to those seen in the HT-1080 xenografts (11.32 %ID/g) (**Fig. 3.2**). These results directly confirm that PEG-NRs are able to penetrate and accumulate in sarcoma GEMMs in amounts sufficient for photothermal ablation protocols.

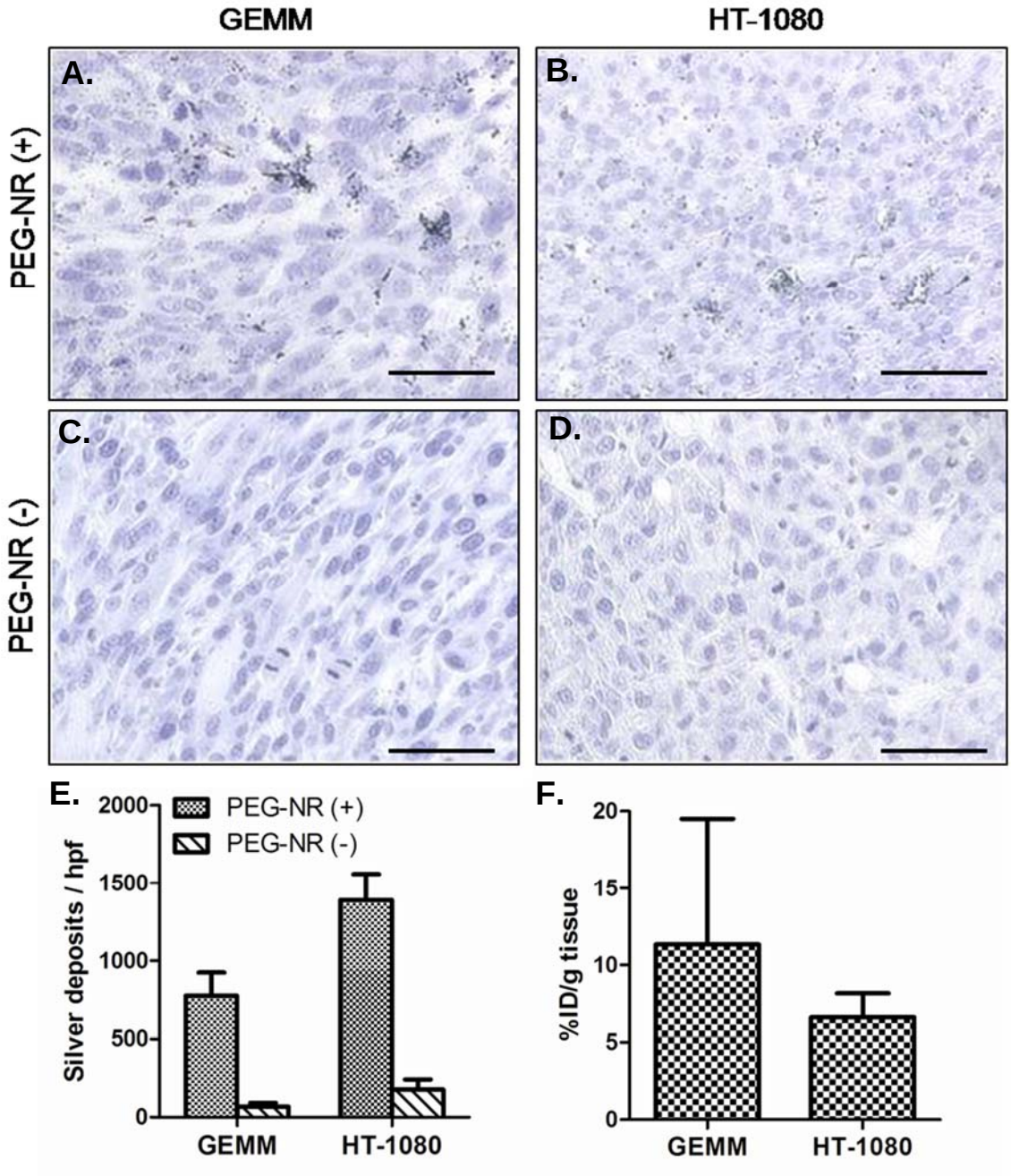

Figure 3.2. Accumulation of PEG-NRs in GEMM and subcutaneous xenograft. Representative silver enhancement staining of PEG-NRs in a GEMM of sarcoma (A) and HT-1080 xenograft (B). Representative silver enhancement staining in an uninjected GEMM of sarcoma (C) and HT-1080 xenograft (D). Scale bar represents 50 μm. (E) Quantification of silver enhanced spots. Contrast-enhanced images captured at 20x magnification were analyzed on ImageJ software (n = 9 per group). (F) ICP-MS quantification of PEG-NR deposition in GEMM of sarcoma and HT-1080 xenografts 72 hrs after i.v. administration.

3.3.3 Immunohistochemistry of Tumors Following Photothermal Ablation

Examination of H&E-stained paraffin sections revealed regions of gross necrosis at 24- and 72-hours post-irradiation. These sections were characterized by loss of tumor architecture, cellularly hypodense regions, lymphocytic infiltrates, and irregular nuclear staining patterns (**Fig. 3.3**). These regions likely correspond to the portions of the tumor receiving the majority of photothermal energy during the ablation procedure.

To assess cellular proliferation, we immunohistochemically stained the sarcoma sections for proliferating cell nuclear antigen (PCNA). Consistent with the H&E results, we observed wide regions of absent PCNA staining throughout the tumors at 24- and 72-hours following ablation (**Fig. 3.3**). Interestingly, we identified isolated regions located exclusively at sites of the tumor most distal from the skin surface that stained positively for PCNA. These areas of viable tissue account for anywhere between zero to approximately 20% of the area of some tissue sections (**Fig. 3.3**), suggesting that portions of the tumor did not receive sufficient photothermal energy during the ablation procedure.

Finally, to understand how photothermal ablation influences the distribution of blood vessels in the sarcoma, we measured expression of CD31, an endothelial cell marker commonly used to identify blood vessels. Necrotic regions exhibited diffuse, non-specific staining patterns bearing no resemblance to the blood vessels observed in untreated control tissue. Thus, in regions of tumor receiving sufficient irradiative heat to induce necrosis, the tumor-associated vasculature is also ablated.

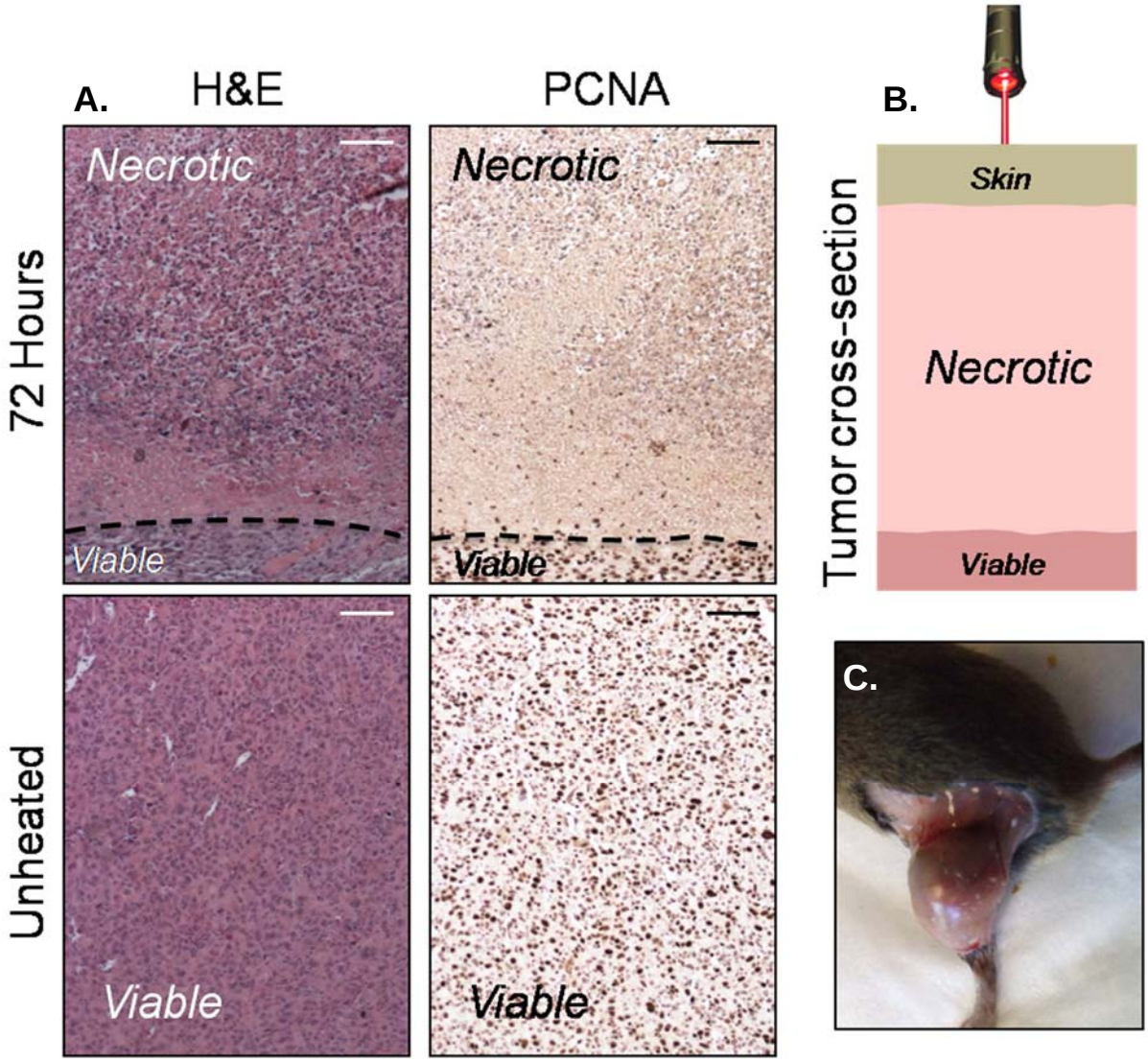

Figure 3.3. Immunohistochemical analysis of short-term heating effects on GEMM of sarcoma. (A) H&E and PCNA staining of sarcoma 72 hours after heating versus an unheated control. Scale bar represents 100 μm. Contrast-enhanced images captured at 10x magnification. (B) Schematic of sarcoma cross-section following heating. (C) Photograph of PEG-NR + NIR treated sarcoma prior to excision, 72 hours post heating.

3.3.4 Therapeutic Assessment of Photothermal Ablation in a Transgenic Sarcoma Model

To test the ability of a single dose of PEG-NRs to significantly delay tumor growth following one session of near-IR irradiation, genetically-modified 129 S_4/SvJae mice bearing

induced soft tissue sarcomas were injected with PEG-NRs. Mice were randomized to one of three cohorts (PEG-NRs + NIR, PEG-NRs only, NIR only). After plasma clearance of PEG-NRs, tumors in the PEG-NRs + NIR and NIR only groups were irradiated for 5 minutes (~0.5 W/cm^2, 810 nm) and tumor volume was measured over time (**Fig. 3.4**). Mice receiving the PEG-NRs + NIR treatment experienced significant tumor growth delay and extended lifespan compared to control treatment groups. During the post-ablation observation period, all mice in the PEG-NR only and NIR only groups developed substantial tumor burdens requiring euthanization by day 16, whereas mice receiving PEG-NRs + NIR survived until day 30 or longer (**Fig. 3.4**). At the end of the study period, the two remaining mice had tumor volumes < 150 mm^3 (**Fig. 3.4**). Notably, 4 of the 5 mice receiving PEG-NR + NIR lost lower extremity function after the ablation procedure. Additionally, in a repeat therapeutic trial, we observed delayed progression of sarcoma consistent with our initial results.

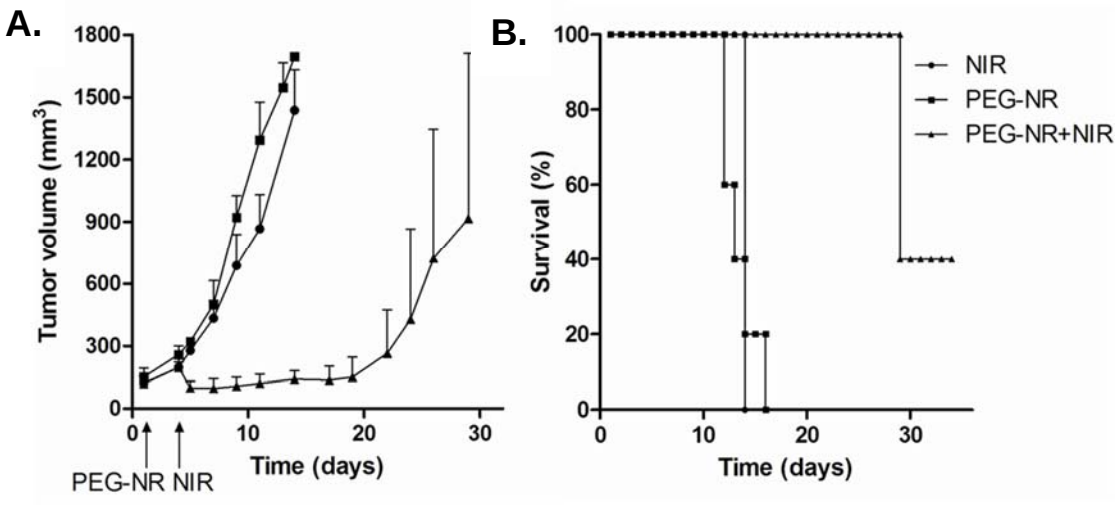

Figure 3.4. Photothermal ablation of GEMM of sarcoma using PEG-NRs. (A) Volumetric changes in tumor volume are plotted over time (n = 4-5). Error bars represent standard deviations. PEG-NR is statistically different from NIR and PEG-NR from day seven onwards with $p < 0.0001$ based on analysis of variance. (B) Survival of mice over time (n = 4-5).

3.4 Conclusions:

Surgery, chemotherapy, and radiation have remained the standard of care in cancer therapy for decades. Novel approaches harnessing the unique properties of nanomaterials have been proposed to improve cancer therapy in the future. To date, numerous therapeutic protocols, involving a variety of nanomaterials, have been described in xenograft mouse models. While xenograft models offer a straightforward and reliable method for quantitatively assessing tumor burden, studies in more physiologic tumor microenvironments, such as those that occur in genetically-engineered mouse models (GEMMs), may be more accurate predictors of therapeutic efficacy.[233] For these reasons, GEMMs are gaining favor in the pharmaceutical industry and will almost certainly find utility in assessing the clinical validity of nanomaterial-based therapeutic protocols as well.

This study represents the first demonstration of a therapeutic, nanoparticle-mediated thermal ablation protocol in a GEMM. We have demonstrated that PEG-coated gold nanorods (PEG-NRs) accumulate in the sarcomas at levels comparable to those in subcutaneous HT-1080 xenografts. Deposition of PEG-NRs is sufficient to facilitate photothermal ablation of the sarcomas upon localized administration of near-infrared irradiation.

While numerous lines of evidence support the notion that passively targeted nanotherapeutics can penetrate and accumulate in human tumors, this phenomenon has not been well-characterized in a clinical setting.[145, 150] Routinely used xenograft models fail to capture important characteristics of human disease that may impact the effectiveness of passive targeting mechanisms.[149] This uncertainty is significant as many nanotherapeutic approaches rely on passive targeting to varying degrees in order for the therapeutic payload to accumulate at the site

of disease. Our demonstration of untargeted PEG-NR accumulation in a GEMM of sarcoma provides evidence that passive targeting is indeed sufficient for PEG-NRs to accumulate in a physiologic tumor microenvironment.

The considerable heterogeneity of human cancers is an important factor for PEG-NR-based therapies. It is not anticipated that a "one-size-fits-all" therapy will be identified, but rather that therapeutic protocols must be tailored to each type of cancer. Features including grade, stage, tissue of origin, anatomical location, and metastatic progression will influence if, and to what extent, PEG-NR-based therapies will have a place in the clinic.[231, 234, 235] For example, because of constraints related to depth of near-infrared irradiation into tissues, tumors that develop close to the skin surface, such as some soft-tissue sarcomas, would be better candidates for PEG-NR-based therapies than tumors that develop at sites more distant from the skin surface. Interestingly, in our GEMM, a portion of the sarcoma developed closer to the surface while the remainder developed deeper within surrounding skeletal muscle. In contrast to HT-1080 xenograft models which replicate superficial truncal tumors, our GEMM replicates a deep extremity sarcoma, which represents the majority of human sarcomas. We propose that this spatial heterogeneity contributed to the differential success in ablative therapy that we observed. Additionally, tumors that are identified at earlier stages may be better candidates for PEG-NR-therapies than tumors identified at late stages, such as pancreatic adenocarcinoma,[236] because of the increased challenge of optimally irradiating multiple metastatic lesions.

Notably, a significant proportion of mice to undergo photothermal ablation lost function in the irradiated limb following treatment. Because the sarcomas invade surrounding skeletal muscle, the thermal energy generated within the sarcoma damaged the skeletal muscle as well as the sciatic

and femoral nerves in the leg. We believe this observation is important in two respects. First, it suggests that improvements are required in the irradiation protocol to provide more precise thermal ablation at cellular resolution. Pulsed laser sources represent one possibility for improving the localization of photothermal ablation. Second, this unwanted side effect of the therapy could only be detected and fully appreciated in a GEMM, where the sarcoma's anatomical location closely mimics that of human extremity soft tissue sarcomas. While a subcutaneous xenograft model can provide important information such as tumor burden in response to treatment, only in a GEMM can these realistic clinical consequences be detected and assessed.

The ability of mouse models to accurately recapitulate human cancers and yield clinically insightful results is critical to the continuing development of nanotechnology for therapy and diagnostics. Our work highlights the therapeutic efficacy and potential challenges of PEG-NR-mediated photothermal ablation therapy in a GEMM of sarcoma. We anticipate that our findings will enable the development of improved therapeutic protocols as PEG-NRs and other nanotherapeutics advance closer to clinical use.

3.5 Acknowledgements:

This project was supported by the MIT-MGH Collaborative Initiative in Translational Cancer Research. A.F.B. acknowledges support from the NIH/Medical Scientist Training Program. The authors would like to acknowledge Dr. Alice Chen for her helpful suggestions on the manuscript. The authors also thank Matt Kinsella for assistance with ICP-MS, Prof. Warren Chan for assistance with silver enhancement staining, Prof. Yoel Fink for use of the IR camera, and Nicki Watson for TEM images. Histology support from the Koch Institute Histology Core Facility was provided by Michael Brown.

3.6 Author Contributions:

Authors: Kevin Y. Lin*, Alexander F. Bagley*, Alexia Y. Zhang, Daniel L. Karl, Sam S. Yoon, Sangeeta N. Bhatia

* These authors contributed equally.

K.Y.L., A.F.B., and S.N.B. conceived the idea and wrote the manuscript. A.Y.Z. and D.L.K. assisted with ablation procedures and performed IHC on tumor tissue. S.S.Y. provided experimental advice and edited the manuscript. K.Y.L. and A.F.B. performed all other experiments and data analysis.

CHAPTER 4. NANOMATERIALS AND IMPLANTED NIR SOURCES FOR LOCALIZED HEATING OF DEEP TUMORS

4.0 Abstract:

Plasmonic nanomaterials including gold nanorods are effective agents for inducing heating in tumors. Because near-infrared (NIR) light has traditionally been delivered using extracorporeal sources, most applications of plasmonic photothermal therapy have focused on isolated subcutaneous tumors. For more complex models of disease such as advanced ovarian cancer, one of the primary barriers to gold nanorod-based strategies is the adequate delivery of NIR light to tumors located at varying depths within the body. To address this limitation, a series of implanted NIR illumination sources are described for the specific heating of gold nanorod-containing tissues. Through computational modeling and *ex vivo* studies, a candidate device is identified and validated in a model of orthotopic ovarian cancer. As the therapeutic, imaging, and diagnostic applications of plasmonic nanomaterials progress, effective methods for NIR light delivery to challenging anatomical regions will complement ongoing efforts to advance plasmonic photothermal therapy towards clinical use.

4.1 Introduction:

The unique optical and electromagnetic properties of plasmonic nanomaterials have generated interest in using these materials for a variety of applications in medicine ranging from clinical diagnostics and imaging to targeted tumor therapy.[160, 178, 237-239] The strong scattering and absorption properties of plasmonic nanomaterials have led to the development of highly sensitive plasmonic biosensors for detecting glucose from biofluids, epidermal growth factor receptors (EGFR) on human cancer cells, amyloid beta from blood and cerebrospinal fluid in Alzheimer's Disease, and human papilloma virus DNA.[154, 157, 159, 161, 168, 169] For

therapeutic applications, the ability of plasmonic nanomaterials to absorb specific wavelengths of light and efficiently generate heat through the surface plasmon resonance (SPR) effect has been exploited for localized ablation of solid tumors, as well as for milder sub-ablative heating to transiently damage non-tumor endothelial cells or enhance delivery of therapeutic cargoes.[141, 179, 180, 183, 240, 241] Collectively, these studies have demonstrated the potential for plasmonic photothermal therapy to impact a variety of pathophysiological processes such as tumor growth and angiogenesis. The advantages of polyethylene glycol-coated gold nanorods (PEG-NRs) in particular include their long term stability, minimal cytotoxicity, and ability to be geometrically tuned to absorb specific wavelengths of NIR light.[139, 141, 215, 217-219, 241] In preclinical models, PEG-NRs passively accumulate in tumors, efficiently absorb NIR light, and generate localized heat through the SPR effect. To date, the therapeutic potential of PEG-NR-mediated photothermal ablation as well as sub-ablative heating for recruitment of therapeutic cargoes has been demonstrated in both genetically engineered and xenograft animal models.[139, 141, 172, 179, 219, 241]

One limitation of approaches involving NIR light delivered by an external device is the limited penetration depth of NIR light due to the optical absorption and scattering properties of biological tissue, which has restricted therapeutic studies to superficial tumors located near the skin surface.[242] For solid tumors positioned in deeper, more anatomically challenging regions and distributed over larger areas, such as advanced ovarian cancer, it would be advantageous to have NIR light delivery systems capable of providing sufficient energy to elicit the SPR effect within these deeper and spatially distributed tumor environments. Several efforts to deliver light internally for applications such as photodynamic therapy have focused on optical fiber technologies, which direct a point source of light upon target tissues.[242-245] For laser-induced

interstitial therapy (LITT) protocols, surface- and volume-scattering applicators have been developed to homogeneously scatter light after catheter-guided insertion directly into individual tumors.[246-248] By contrast, for scenarios requiring broader NIR illumination of multiple target tissues simultaneously, including tissues that may not be visible to the human eye or accessible by catheter, a source providing contiguous illumination over a larger surface area would be beneficial.

In this study, a potential strategy combining systemically-delivered plasmonic nanomaterials with locally implanted NIR illumination sources is described. A series of biocompatible, implanted illumination devices are characterized through computational modeling, *ex vivo* fluence rate and thermographic measurements, and *in vivo* thermographic profiling. Two illumination devices were capable of heating solutions of PEG-NRs in a dose-dependent manner, and one of these devices was further validated by *in vivo* imaging and thermography. In animal models of orthotopic ovarian cancer pre-treated with PEG-NRs, delivery of NIR light via the implanted device selectively elevated the temperature of ovarian tumors relative to background tissue without generating irreversible tissue damage and enhanced the delivery of diagnostic and therapeutic agents. Collectively, these data illustrate that synergies between plasmonic nanomaterials and novel NIR illumination methods can achieve selective and tolerable photothermal effects in complex anatomical environments.

4.2 Materials and Methods:

Synthesis of PEG-NRs

Gold nanorods (PEG-NRs) coated in PEG were prepared as described previously.[141, 241] Briefly, 41 nm x 10 nm cetyltrimethylammonium (CTAB)-coated PEG-NRs (Nanopartz)

were concentrated ~100-fold by centrifugation at 15,000 rcf for 30 minutes, incubated with 5-kDa methyl-PEG-thiol (Laysan Bio, Inc.) to 100 μM, and dialyzed for at least 24 hours against distilled, deionized water in 3,500 MWCO Slide-A-Lyzer cassettes (Thermo Scientific). Dialyzed samples were washed in ultrapure water, filtered through 100-kDa filters (Millipore), and resuspended in PBS. PEG-NR solutions were stored at 4˚C.

Device design and construction

Implanted devices consisted of silica rods and fiber optic meshes (Rogers Sciences, Inc.). Silica rods were treated by an optomechanical scoring process to create varying illumination patterns and light-dispersive coatings. Light emission was incoherent with an exitance of ~2π steradians at each illumination surface. Fiber optic meshes were encased in medical-grade silicone to provide adhesion, flexibility, and biocompatibility. Meshes were treated in an array format by an optomechanical scoring process to allow approximately uniform light emission from the top surface.

Computational modeling

An approximate anatomical model of the mouse was developed including liver, intestine, kidney, stomach, spleen, lungs, vertebrae, and skin using a nude mouse (female) atlas as a guide (Xenogen). Tissue layers were assigned indices of refraction, scattering coefficients, and absorption coefficients. Implanted NIR devices (silica rod, flexible mesh) were simulated in this three-dimensional anatomical model using Zemax and TracePro software. Each simulation performed consisted of 1×10^4 distinct ray tracings. NIR illumination from the silica rod was modeled as 1×10^4 ray tracings across the device's entire length and diameter, while illumination from the fiber optic mesh was modeled as 1×10^4 ray tracings emitted from the top and bottom

surfaces of the mesh. The surfaces for both devices were modeled with a lambertian reflectance profile (1 W, 808 nm).

Fluence rate measurements

Implanted NIR devices were directly coupled to an 810 nm continuous diode laser source (Visotek) through an SMA-threaded glass fiber optic cable (0.4 mm diameter). Fluence rate measurements were recorded on an optical power and energy meter with an S121C silicon photodiode power sensor (400-1100 nm, 500 mW) (Thorlabs). Measurements were obtained at 808 nm at multiple distances and input currents.

Ex vivo thermographic profiling

Solutions of PEG-NRs (0, 1, 10, and 100 μg/mL) were irradiated by implanted NIR devices for three minutes. Maximal surface temperatures of PEG-NR solutions were monitored continuously by infrared thermography (Thermacam S60, FLIR). Each concentration of PEG-NRs was identically exposed to the 810 nm laser illumination. All conditions reported were measured in triplicate.

In vivo imaging

All animal studies were approved by the MIT Committee on Animal Care. Computed tomographic (CT) imaging on animals with implanted NIR devices was performed on an eXplore CT120-whole mouse MicroCT system (GE Healthcare). Image analysis for anatomic measurements and three-dimensional rendering was performed with MicroView software (GE Healthcare).

In vivo thermographic profiling

Female NCR nude mice at ~4 weeks of age (Taconic) received an intraperitoneal injection of ~5 x 10^5 OVCAR8 human ovarian cancer cells expressing firefly luciferase. At 4-6 weeks following implantation, establishment of tumors was confirmed on the whole-animal IVIS Spectrum-bioluminescence and fluorescence imaging system (Xenogen). Tumor-bearing animals received either an intravenous injection of PEG-NRs (100 μL; ~14 mg Au/kg) or no injection for the control group; after vascular clearance (~48 hours), animals were anesthetized and a midline incision through the skin and abdominal wall was made for implantation of the silica rod NIR device under study. To assess tissue-specific heating properties, the implanted NIR device was independently positioned in proximity to the liver, intestine, and ovarian tumors within the peritoneal cavity. K-type fiberglass thermocouples (National Instruments) were placed adjacent to each tissue and equidistantly from the NIR device (~0.3-0.5 cm) to minimize non-specific direct heating effects from the device. Implanted devices were connected via fiber optic cable to a continuous 810 nm laser source (Visotek) during a five minute heating period per tissue. Thermocouple temperature signals were integrated on a portable DAQ thermocouple module (NI USB-9211A, National Instruments) and recorded at 2 Hz with NI-DAQmx and LabView software during the five minute heating window. Thermographic profiles were assembled and statistically analyzed with Prism 5 software (GraphPad).

Histology

Harvested tissues were fixed in 4% paraformaldehyde overnight at 4˚C prior to paraffin embedding. Standard hematoxylin and eosin (H&E) staining was performed on sections of tumor, liver, and intestine. Immunohistochemical staining for the cell proliferation protein Ki67 was performed with primary antibody rabbit anti-human Ki67 (1:100, EMD Millipore). IHC with

antigen retrieval was performed on the LabVision Autostainer 360 Immunohistochemical Stainer (Thermo Scientific).

In vivo quantification of cargo

Tumor-bearing animals received an intravenous co-injection of doxorubicin-loaded liposomes (8 mg Dox/kg) and AngioSPARK750 (100 μL in PBS) (Perkin Elmer). The silica rod was implanted as described and positioned in proximity to multiple tumor nodules within a specified quadrant of the abdomen. Each animal received continuous NIR light irradiation (810 nm) for 30 minutes and the abdominal wall and skin were sutured prior to recovery. Three hours after the procedure, tumors were harvested and AS750 fluorescence within whole tumors was imaged on an NIR imaging system (LICOR Odyssey). Tumors were weighed and homogenized in 1.0 mL of extraction buffer (70% EtOH, 0.3N HCl) using an automated tissue homogenizer (gentleMACS Octo Dissociator, Miltenyi Biotec). Supernatants were measured on LICOR platform for AS750 and a fluorescence microplate reader (Molecular Devices, SpectraMAX GeminiEM) for doxorubicin fluorescence. For each group, the fluorescence of 12 individual tumor supernatants obtained from three mice per group was normalized by tissue weight prior to analysis.

4.3 Results:

4.3.1 Development and Validation of Computational Model for Intraperitoneal NIR Light Delivery

PEG-NRs were prepared from stock CTAB-coated gold nanorods to minimize toxicity and extend particle circulation time as previously described. (**Fig. 4.1**, left)[141, 241] Transmission electron microscopy (TEM) images revealed the PEG-NR dimensions to be 41 nm

in length and 10 nm in width for an aspect ratio of 4.1 (**Fig. 4.1**, left). The surface plasmon resonance (SPR) peak absorbance of PEG-NRs was 808 nm in accordance with previously observed measurements (**Fig. 4.1**, left). Implanted NIR illumination devices were composed of silica rods and fiber optic meshes (**Fig. 4.1**, center). Silica rods were designed with varying geometric parameters such as diameter, length, and tip tapering, treated to have uniform surface diffusivity along the rod, and joined with an SMA fiber-optic connector to interface with a continuous 810 nm NIR laser source. To provide a flexible alternative to the silica rods, fiber optic meshes consisting of sub-millimeter fibers encased in adhesive medical-grade silicone were prepared. Fibers were treated by an optomechanical scoring process prior to encasement to alter the total internal reflection at distinct locations and thereby permit NIR light emission along the length of the fibers. For each device, fluence rate-distance relationships were computed for input currents ranging from 9.0–13.0A (**Fig. 4.1**, center). The combination of systemic PEG-NRs and implanted NIR devices was investigated as a strategy to achieve photothermal heating in deep tumor nodules (**Fig. 4.1**, right).

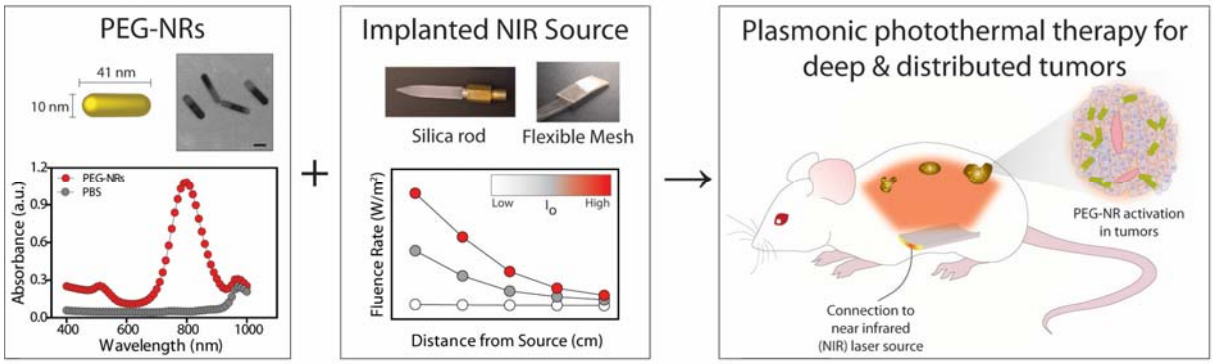

Figure 4.1. First component for plasmonic photothermal heating of intraperitoneal tumors consists of polyethylene glycol-coated gold nanorods (PEG-NRs), which are characterized by TEM imaging and optical absorbance. (Left panel) PEG-NRs with an aspect ratio of 4.1 display a peak surface plasmon resonance (SPR) at 808 nm. Scale bar: 20 nm. (Center panel) Classes of implanted NIR devices include silica rods and flexible meshes encased in silicone. Generalized fluence rate-distance relationship for several input currents (Io) of an implanted NIR device. (Right panel) The combination of systemically-administered PEG-NRs and implanted NIR illumination permits plasmonic photothermal therapy for intraperitoneal tumors.

The abdominal cavity consists of organs and biological tissues with varying optical and geometric properties contained within a confined anatomical compartment. To develop a quantitative framework for understanding NIR illumination in the peritoneal cavity and thereby assess the feasibility of the implanted NIR devices, a three-dimensional solid model incorporating the liver, spleen, stomach, kidney, large and small intestine, and skin was developed (**Fig. 4.2**). For modeling simulations, abdominal organs were assigned approximate indices of refraction, scattering coefficients, and absorption coefficients based on values obtained from the literature. Previous computational models developed in our lab applied finite element simulations to approximate photothermal heating of gold nanorod-containing subcutaneous tumors using the bio-heat transfer equation.[141] While the current model describes NIR light distribution in non-tumor tissues within the peritoneal cavity, future models incorporating tumor tissue elements, absorption coefficients dependent on gold nanorod tissue content, and

biophysical heat transfer equations will be useful for providing a more detailed description of plasmonic photothermal heating in the peritoneal cavity. The current deterministic model predicts that most of the emitted NIR light focuses on regions containing the intestine, liver, and spleen within the peritoneal cavity with lambertian, or diffusely reflected, illumination along the silica rod (**Fig. 4.2**, **Fig. 4.3**). In comparison, with a lambertian profile along the flexible mesh, the model predicts an enhanced, more uniform transmittance within the peritoneal cavity due to increased surface area relative to the silica rod (**Fig. 4.3**). Importantly, simulations using this anatomically based model predicted the limitations of NIR light penetration due to tissue absorption and scattering. For example, at the interface of the silica rod and abdominal organs with an input power of 1 W along the device, the model predicts a peak fluence rate of 1.35×10^3 W/m^2, while at a distance 8 mm deep to the device, the peak fluence rate decays to 5.9×10^2 W/m^2 (**Fig. 4.3**). Similarly, at the interface of the flexible mesh and abdominal organs, the peak fluence rate is estimated to be 3.0×10^3 W/m^2, and the peak fluence rate decays to 7.3×10^2 W/m^2 at a depth of 8 mm (**Fig. 4.3**). The depth-dependent decay observed is consistent with tissue absorption and scattering and suggests that the model parameters approximate to a first order the *in vivo* environment.

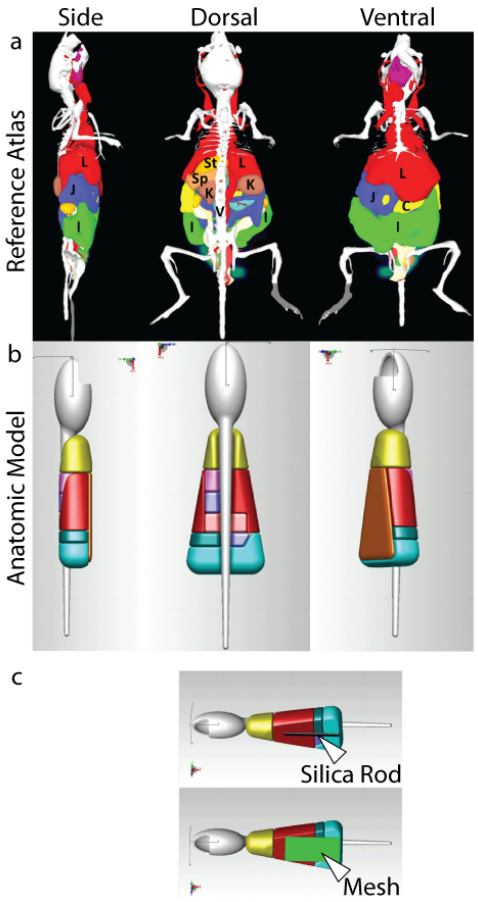

Figure 4.2. Anatomic models of abdominal cavity used in fluence rate simulations. (a) Reference atlas overlay on tumor-bearing, female nude mouse from side, dorsal, and ventral orientations. (L, liver; J, jejunum (intestine); C, cecum (intestine); I, ileum (intestine); St, stomach; Sp, spleen; K, kidney; V, vertebral body) (b) Approximate anatomic model developed for simulations. Each tissue assigned optical coefficients for refraction, scattering, and absorption. (c) Models depicting implanted silica rod (top) and fiber optic mesh (bottom).

To validate and refine model predictions for the silica rods and flexible mesh, fluence rate was calculated at multiple distances and input currents for six distinct implanted NIR devices (**Fig. 4.3**). Consistent with the model, fluence rate decreased approximately as the square of the distance between the device and detector plate when measured in an air medium (**Fig. 4.3**). As the input current from the laser was increased, a linear increase in fluence rate was observed at the surface of each implanted device, highlighting the ability to precisely tune the NIR

emission from the devices to achieve the desired level of photothermal heating *in vivo* (**Fig. 4.3**). In contrast to the model predictions, the peak fluence rate measured for the flexible mesh surface (~500 W/m^2) did not reach the maximal surface fluence rate of 3.0 x 10^3 W/m^2 predicted by the model. Limitations related to the material properties and device fabrication likely contributed to the difference and suggest that future models could be refined by incorporating specific physical properties of the device in addition to tissue properties. Finally, surface fluence rate was highly dependent on the geometry of the device and spanned several orders of magnitude (4 x 10^3 W/m^2 to 2 x 10^{-1} W/m^2) (**Fig. 4.3**).

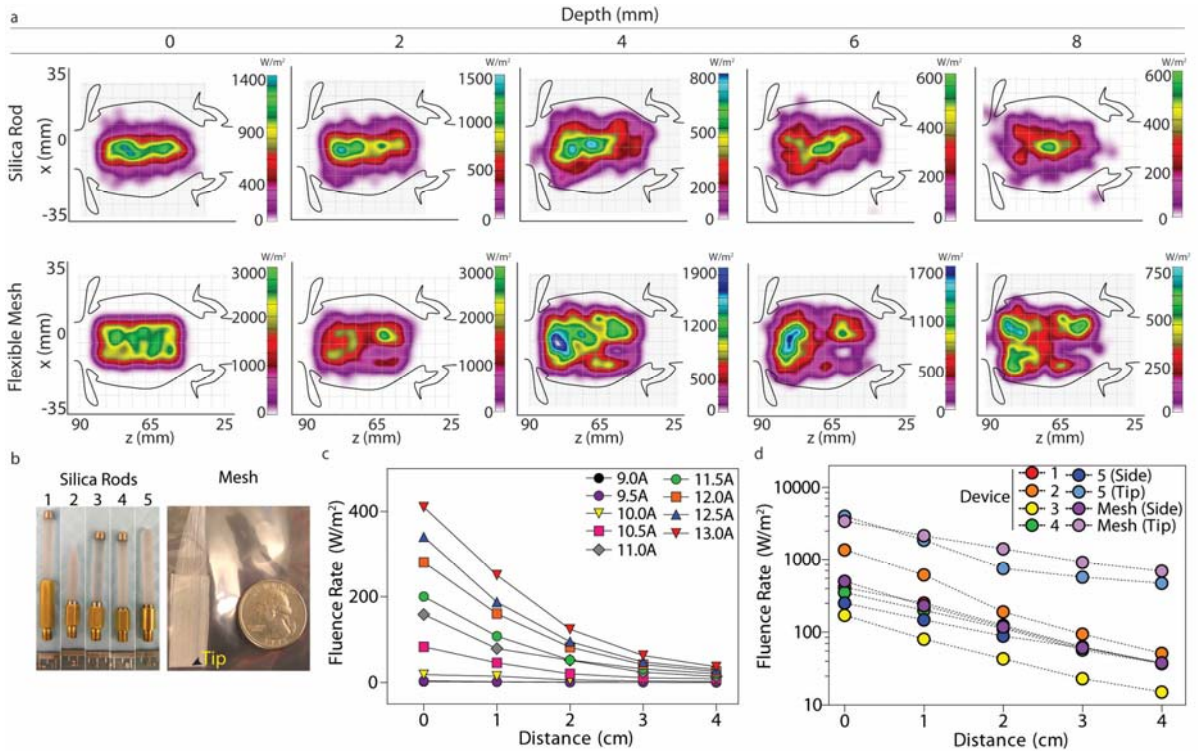

Figure 4.3. (a) Fluence rate simulation in abdominal cavity with two implanted NIR devices at up to 8 mm depth from skin surface. (b) Photographs of implanted NIR devices investigated include silica rods (devices 1-5) and mesh (c) Fluence rates from representative silica rod device for variable input currents ranging from 9.0-13.0 A and distances from source ranging from 0-4 cm. (d) Fluence rate-distance curves obtained at 13.0A input current for multiple models (devices 1-5; mesh) and spatial orientations of implanted NIR devices.

4.3.2 Efficiency and Specificity of Plasmonic Nanomaterial Heating by Implanted NIR Sources

Based on the surface fluence rate measurements, we next assessed whether our devices possessed differing capacities to photothermally heat PEG-NRs. In an *ex vivo* setting, multiple concentrations of PEG-NRs in PBS were subjected to continuous NIR laser irradiation (810 nm) dispersed by each implanted device, and the temperature of PEG-NR solutions was continuously monitored via infrared thermography (**Fig. 4.4**). Several distinct patterns of photothermal heating were observed, which are denoted as: (1) non-specific, (2) PEG-NR-dependent, and (3) inefficient. Due to elements of device construction that resulted in a greater localized concentration of laser energy at the device tip (device 3), non-specific devices led to temperature elevations in both PEG-NR- and PBS control solutions (**Fig. 4.4**, **Fig. 4.5**). Conversely, devices with inefficient heating failed to yield an appreciable rise in temperature of PEG-NR solutions at approximately physiologic PEG-NR concentrations (**Fig. 4.4**, **Fig. 4.5**). A subset of implanted devices investigated, however, was observed to selectively elevate the temperature of PEG-NR solutions in a concentration-dependent manner while failing to significantly heat PBS control solutions (**Fig. 4.4**, **Fig. 4.5**). After three minutes of NIR irradiation, one PEG-NR-dependent heater (device 2) elevated a 100 µg/mL PEG-NR solution by 20.53˚C±0.68˚C, a 10 µg/mL PEG-NR solution by 11.90˚C±0.44˚C, a 1 µg/mL PEG-NR solution by 4.43˚C±0.47˚C, and a PBS control solution by 2.57˚C±0.79˚C. Collectively, this *ex vivo* characterization helped identify a subset of implanted NIR light sources to evaluate in an *in vivo* context.

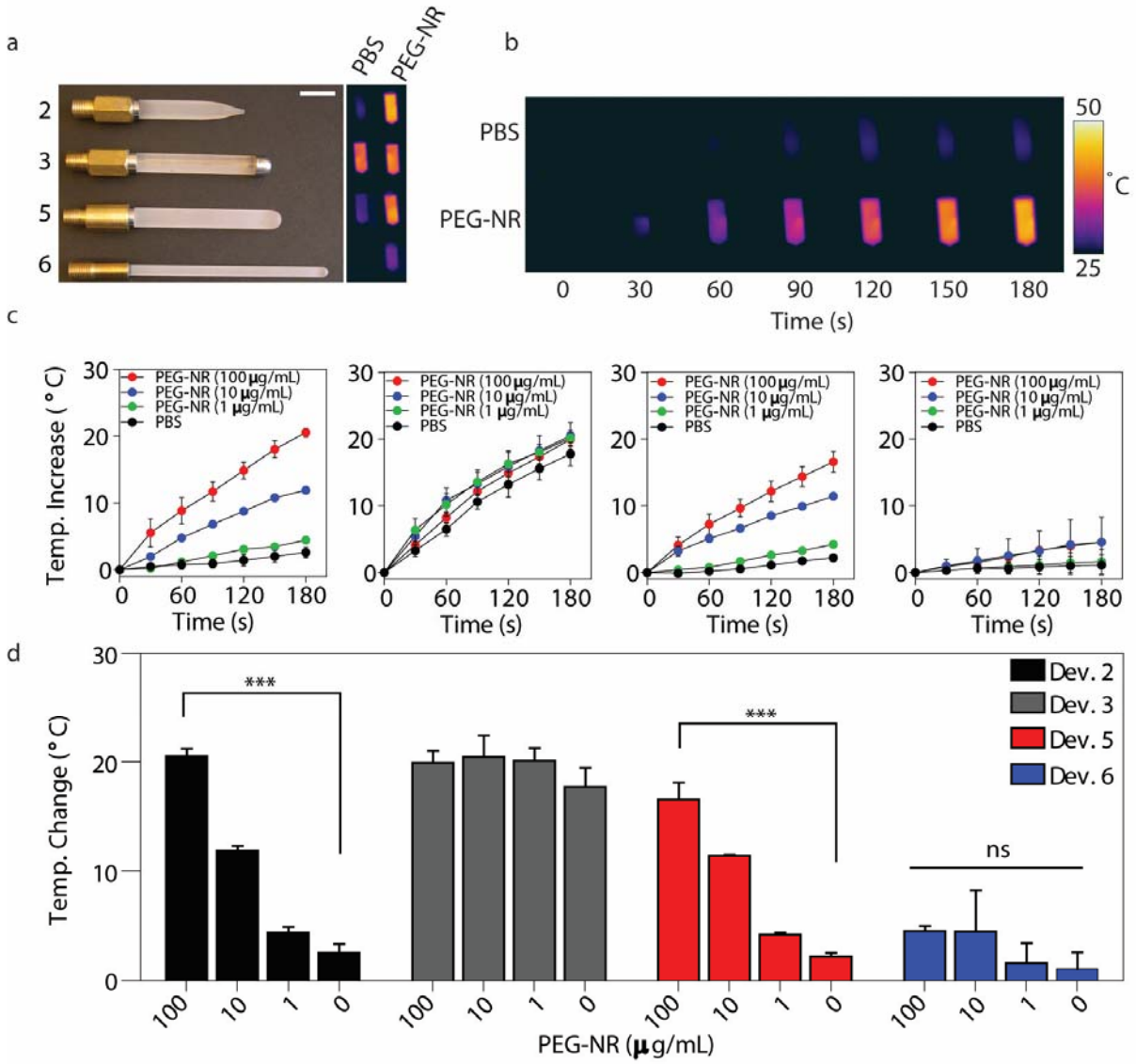

Figure 4.4. (a) Images of implanted NIR devices 2, 3, 5, and 6 (top to bottom). Infrared thermographic images of PEG-NR and PBS solutions after NIR exposure with implanted NIR devices. Scale bar: 1 cm (b) Representative thermographic timecourse for device 2, illustrating selective heating of PEG-NRs. (c) PEG-NR heating for implanted NIR devices 2, 3, 5, and 6 (left to right) (n=3 per group). Error bars, s.e.m. (d) Maximal temperature elevation for multiple PEG-NR concentrations. (*n*=3 per group; ***P<0.001; one-way ANOVA and Tukey post tests.) Error bars, s.e.m.

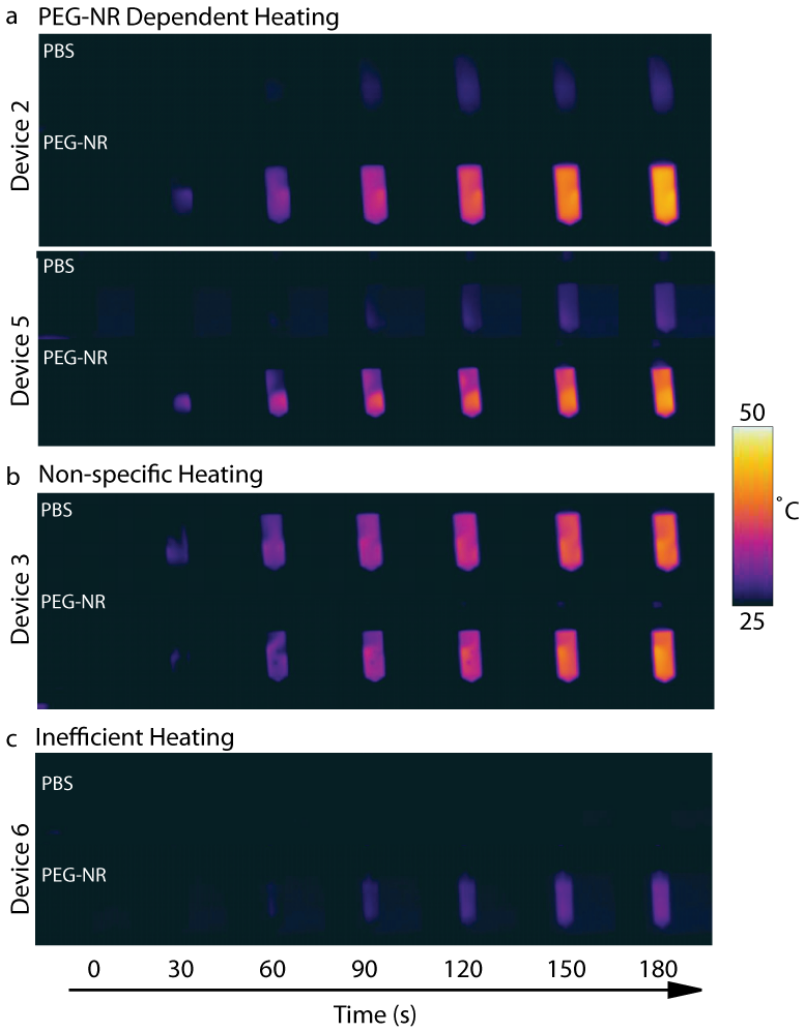

Figure 4.5. Ex vivo thermographic profiles for implantable devices. Images show devices 2, 3, 5, and 6 in solutions of PEG-NRs or control PBS. (a) Devices 2 and 5 demonstrate PEG-NR-dependent heating; (b) Device 3 demonstrates non-specific heating; (c) and Device 6 demonstrates inefficient heating.

The *ex vivo* fluence rate and PEG-NR photothermal heating measurements, coupled with computational models for two generic device geometries (i.e., silica rod and flexible mesh sheet) allowed for progressive down-selection of candidate devices prior to attempting plasmonic photothermal therapy in an animal model. Despite comparable fluence rate modeling predictions between the rod and mesh sheet, the various silica rod designs were pursued further because their material properties and construction proved able to sustain input powers in the anticipated range necessary for *in vivo* photothermal heating. The six-fold lower measured surface fluence rate compared to the model prediction illustrated that incorporation of physical properties of the device would be advantageous for future simulations, and also that future iterations of the flexible mesh should include design parameters that can sustain the necessary power requirements for plasmonic photothermal heating.

Of the silica rod devices with the highest measured fluence rates, only a subset was able to heat PEG-NR solutions in a selective and dose-dependent manner. Those devices which failed to achieve PEG-NR-specific heating likely did so due to a combination of suboptimal geometric design and the incorporation of highly absorptive elements. Suboptimal geometries such as the long, narrow cylindrical design may have resulted in poorly diffused incoming NIR light with inhomogeneous emission to the surrounding environment. Such geometric constraints have been previously observed in the related field of laser-induced interstitial therapy, where NIR scattering from implanted laser applicators in part determines the volume of tissue susceptible to heating therapy.[249, 250] While the power required for this ablative therapeutic modality is substantially higher than that required for plasmonic photothermal therapy, the ability of the implanted device to scatter NIR light isotropically and minimize heat conduction at the tissue-device interface is highly dependent on geometric and material design parameters and is

important for ensuring broad tissue coverage. Incorporating a metallic cap at the device tip led to heating of both PEG-NR and control solutions non-selectively, suggesting that the metallic cap absorbed the incident NIR light to generate heat within the device itself. Such designs are not suitable for implantation into the peritoneal cavity due to reduced, inhomogeneous light emission, as well as local coagulation of tissues in the vicinity of the device tip.[250] Limiting the incorporation of absorptive elements and improving light scattering from the device surface would help reduce the non-specific heating observed here. The optimal implanted NIR device based on fluence rate and selective PEG-NR heating had a tapered tip design and a length of ~3 cm, which was among the shortest of the candidate devices investigated. Future iterations on silica- or fiber optic mesh-based implanted NIR devices will focus on improved flexibility, isotropic NIR emission from the device surface, and improved materials able to sustain a broader range of powers and thereby reduce the time required to reach the desired temperature range for plasmonic photothermal therapy.

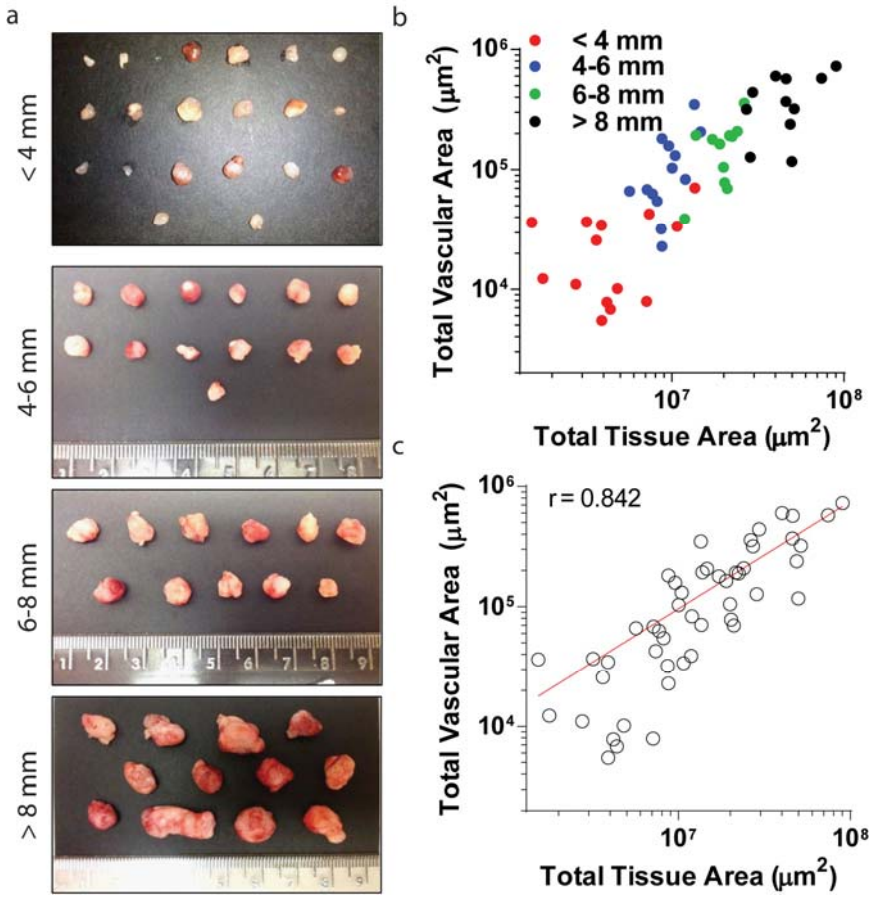

Figure 4.6. (a) Images of explanted ovarian tumors from the peritoneal cavity grouped by size (maximum diameter) (b-c) Tissue sections stained for CD31 were quantified with ImageJ software and correlated with total tissue area. Vascular density was found to correlate closely with total tissue area. ($r = 0.842$) Tumors < 4 mm positive for CD31 suggest that intraperitoneal tumors across a range of sizes are well-vascularized. ($n = 56$ tumors)

4.3.3 Localized In vivo Plasmonic Heating to Enhance Therapeutic Delivery to Ovarian Tumors

The function of a silica rod from the PEG-NR-dependent activator group was next assessed in an orthotopic mouse model of ovarian cancer. The device was implanted into the peritoneal cavity through an approximately 1 cm midline incision on the ventral surface and connected to the laser source via fiber optic cable (**Fig. 4.7**). To visualize the device inside the peritoneal cavity, computed tomography (CT) imaging was performed. CT images clearly delineated the implanted device and revealed its placement relative to abdominal structures

including intestine, abdominal wall, and vertebral bodies (**Fig. 4.7**, **Fig. 4.8**). To investigate the capability and specificity of the device to photothermally heat various tissues, the device was implanted into the peritoneal cavity of animals pre-treated with PEG-NRs or control animals lacking PEG-NRs, and the temperature of ovarian tumor tissue, intestine, and liver was continuously monitored with thermocouples placed at approximately equal distances (0.3-0.5cm) from the implanted device within each of these tissues (**Fig. 4.8**). Thermal profiling revealed a more efficient heating process in ovarian tumors, intestines, and livers of PEG-NR-treated animals relative to control animals lacking PEG-NRs (**Fig. 4.8**). Modest temperature changes between 2.4-3.0°C observed in tissues lacking PEG-NRs may be attributed to heat non-specifically conducted from the device itself. In contrast, temperature elevations observed within the first minute of NIR exposure rose significantly steeper for tumors and liver in animals pre-treated with PEG-NRs, while the trend was also increased but not significant for the intestine. For tissues in the PEG-NR group, the maximum temperature changes for tumor, liver, and intestine were 6.27°C±2.47°C, 6.51°C±1.47°C, and 4.66°C±2.49°C respectively (**Fig. 4.8**).

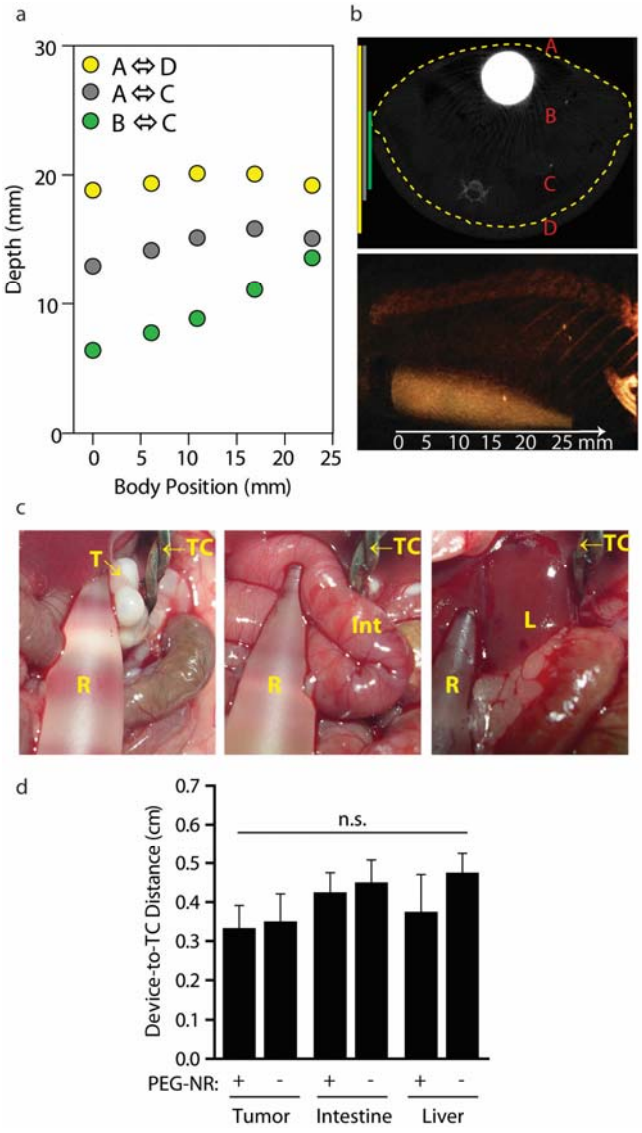

Figure 4.7. (a) Measured distances between implanted device and anatomic landmarks. (b) Landmarks include vertebrae, ventral and dorsal surfaces measured at multiple locations along body length by microCT image analysis. (c) Measured distances between implanted device and thermocouple. Representative images of implanted glass rod device (R), ovarian tumors (T), intestine (Int), liver (L), and thermocouple (TC). (d) Distances between implanted glass rod device and thermocouples for each tissue in presence or absence of PEG-NRs. (one-way ANOVA and Tukey's post tests, *n*=4 for liver, intestine; *n*=2-3 for tumors). Error bars, s.d.

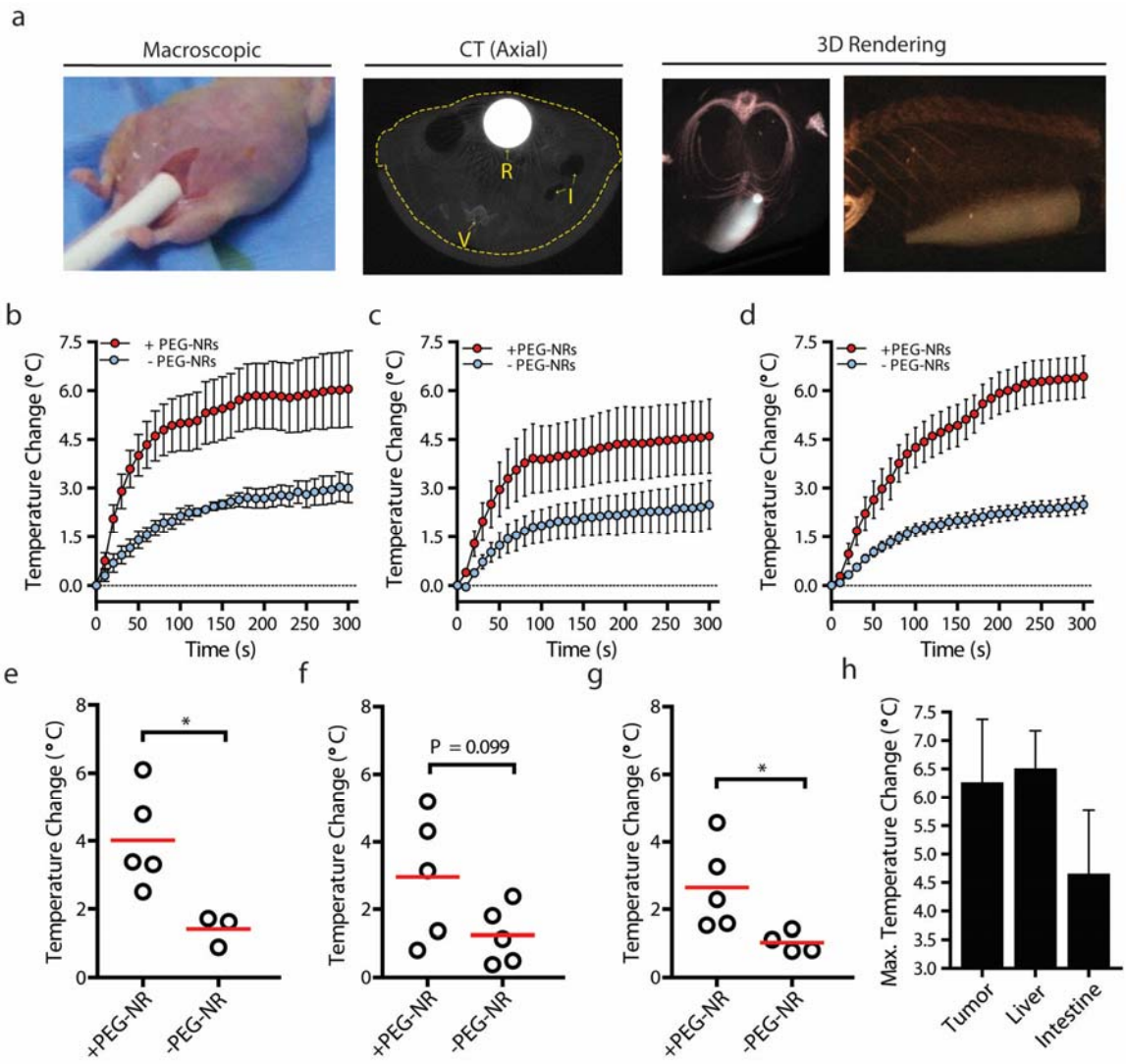

Figure 4.8. (a) Placement of implanted NIR device in a tumor-bearing animal shown macroscopically, by axial CT scan (R, rod; I, intestine; V, vertebrate; dashed line outlining body cavity), and 3D-rendered CT scanning. (b-d) Thermal profiling in presence or absence of PEG-NRs in (b) ovarian tumors, (c) intestine, and (d) liver. (n=3-5 per group) (e-g) Initial temperature change after 50 seconds of direct implanted NIR illumination in (e) tumors, (f) intestine, and (g) liver in PEG-NR-treated animals and controls. Red bar denotes mean value per group. (n=3-5, *P<0.05, unpaired t-test) (h) Maximal temperature change for tumor, liver, and intestine of PEG-NR-treated animals (n=5 per tissue). Error bars, s.e.m.

Following PEG-NR photothermal heating, tissue sections were prepared to assess tissue viability and any resulting histological changes consistent with inflammatory or necrotic tissue damage. Importantly, normal tissue histology was observed for intestine, tumor, and liver by H&E staining (**Fig. 4.9**). Furthermore, Ki67-positive immunohistochemical staining confirmed that these tissues remained actively proliferative after photothermal heating (**Fig. 4.9**). Evidence of mild bleeding and coagulation at the device incision site, however, was noted in some animals investigated. These studies therefore establish that an implanted NIR device shown to selectively heat PEG-NR solutions in an *ex vivo* setting can likewise heat tissues containing PEG-NRs deep within the peritoneal cavity while not inducing irreversible damage in these organs.

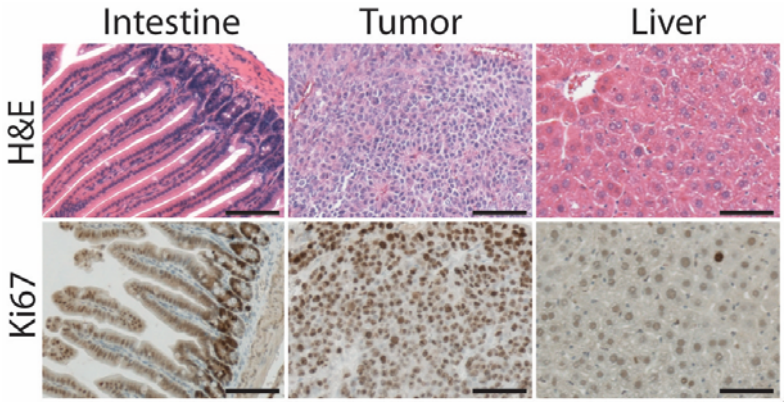

Figure 4.9. Histology and Ki-67 immunohistochemical staining of tissues following PEG-NR therapy with implanted NIR device. Scale: 100 μm.

Plasmonic photothermal therapy and other modalities to heat tumors in the sub-ablative range (~41-45˚C) have been shown in subcutaneous models to alter the flow and permeability of tumor vessels and enhance accumulation of diffusion-limited therapeutic cargoes.[110, 112, 251-253] To investigate whether NIR irradiation from the implanted silica rod similarly drove accumulation of therapeutic cargoes in an orthotopic site, tumors from NIR-treated and control animals were studied following administration of doxorubicin-loaded liposomes and the

diagnostic imaging agent AngioSPARK750 (AS750; core diameter: 20-50 nm). We observed from prior studies that the lower third of the silica rod dispersed NIR light with high intensity, so this region was used to induce heating in tumors in this proof-of-principle study. Intraperitoneal tumors from the quadrant receiving NIR illumination and harvested three hours after receiving AS750 and PEG-NR/implanted NIR heating demonstrated elevated macroscopic accumulation of AS750 (**Fig. 4.10**). Significantly elevated fold enhancements of 3.27 and 11.2 for doxorubicin-loaded liposomes and AS750 respectively were measured in homogenized tumor samples from the PEG-NR/implanted NIR group relative to control tumors from animals receiving no PEG-NR/implanted NIR therapy (**Fig. 4.10**). These data suggest that plasmonic-based enhancement of therapeutic cargoes previously observed in subcutaneous tumor models[112] may also have utility for delivering cargoes to tumors in the peritoneal cavity.

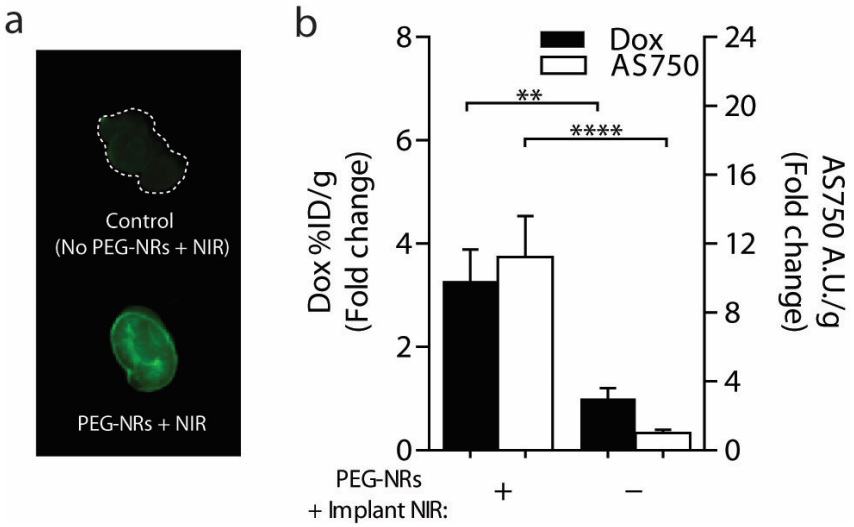

Figure 4.10. (a) Whole-tumor fluorescence of AngioSPARK750 and (b) quantification of doxorubicin-loaded liposomes and AngioSPARK750 in tumor homogenates from tissues harvested 3 hours after injection and PEG-NR/Implant NIR therapy or injection only. (n=11-12 tumors, 3 animals per group, $^{**}P<0.01$, $^{****}P<0.0001$, Mann-Whitney test) Error bars, s.e.m.

For *in vivo* thermographic studies, the liver and intestine were studied in addition to tumors for several reasons. First, previous work on the biodistribution of PEG-NRs has demonstrated a significant accumulation of PEG-NRs in the liver (~14 %ID/g).[141] Because of its high PEG-NR concentration, large size, and proximity to orthotopic ovarian tumor nodules, the liver poses a challenge for tumor-specific photothermal heating in the peritoneal cavity. The temperature elevations observed in the liver were anticipated and importantly, they relaxed to baseline temperatures within several minutes after the procedures. The intestine, while accumulating fewer PEG-NRs than the liver, has been shown to be sensitive to broad elevations in temperature. This has been observed most notably during investigations with heated chemotherapy administered directly into the peritoneal cavity for ovarian cancer patients.[48] In this study, elevations in intestinal temperature were detected, but no tissue damage or proliferative defects were observed, and the thermal effects were more modest than in ovarian tumors or the liver, which is perhaps representative of differing PEG-NR concentrations within each of these tissues. A key advantage of PEG-NRs and plasmonic nanomaterials more generally is the ability to 'sensitize' tumor tissue to incident NIR light relative to surrounding tissues containing fewer PEG-NRs. The ability to locally deposit heat in desired tissues using plasmonic nanomaterials stands in marked contrast to heated chemotherapy approaches which cause non-specific temperature elevations throughout the entire peritoneal cavity and have been associated with high morbidity and even mortality.[48] In the future, strategies to both shield non-tumor, PEG-NR-rich tissues (e.g., liver) from implanted NIR light as well as spatially localize thermal gradients around PEG-NRs via pulsed laser sources could prove fruitful for mitigating any off-target effects.

4.4 Conclusions:

Plasmonic nanomaterial-based therapies that generate localized heating within tumors hold great promise for future clinical interventions in oncology, but novel methods of delivering NIR light to deeply located and distributed solid tumors are needed for tumors that do not reside superficially beneath the skin. Here, to overcome the optical limitations of external NIR irradiation, we propose a possible alternative strategy using a biocompatible, implanted NIR illumination device and assess its functionality through computational modeling, *ex vivo* characterization, and *in vivo* thermographic profiling of orthotopic ovarian tumors. Ray tracing analysis in a simulated mouse model approximated the degree of NIR light penetration influenced by tissue scattering and absorption from two general device designs, providing a framework for selecting candidates for further study. These modeling predictions were validated and further refined by *ex vivo* fluence rate and thermographic measurements, as well as *in vivo* plasmonic photothermal heating of PEG-NR-containing ovarian tumors and non-tumor tissues. We demonstrate that localized plasmonic heating of ovarian tumors by this method can enhance accumulation of diagnostic and therapeutic agents including doxorubicin liposomes in this orthotopic tumor model. In future studies, it will be valuable to investigate what therapeutic benefits may be attained in these deep-seated tumors and the degree to which they correlate with results obtained from related preclinical models as plasmonic nanomaterials advance closer to clinical use.

4.5 Acknowledgements:

The authors wish to dedicate this paper to the memory of Officer Sean Collier, for his caring service to the MIT community and for his sacrifice. The authors would like to acknowledge H. Fleming and K. Reddy for their helpful suggestions on the manuscript. The authors also acknowledge S. Malstrom from the Koch Institute Applied Therapeutics and Whole Animal Imaging (ATWAI) Core Facility, as well as the Koch Institute Histology Core facility. A.F.B. acknowledges support from the NIH/Medical Scientist Training Program and Biophysics Program at Harvard University. S.B. is an HHMI investigator.

4.6 Author Contributions:

Authors: Alexander F. Bagley, Samuel Hill, Gary S. Rogers, Sangeeta N. Bhatia

The manuscript was written through contributions of all authors. All authors have given approval to the final version of the manuscript.

CHAPTER 5. NANOMATERIALS FOR ENHANCING THERAPEUTIC DELIVERY

5.0 Abstract:

The delivery of diagnostic and therapeutic agents to solid tumors is limited by physical transport barriers within tumors, and such restrictions directly contribute to decreased therapeutic efficacy and the emergence of drug resistance. While the biological effects of heating on tumors and tumor-associated vasculature have been explored previously, recent technological advances in the ability to achieve precise spatiotemporal control of tumor heating with nanomaterials have led to a renewed interest in understanding how these materials modulate the tumor vasculature, as well as the consequences of such interventions for therapeutic delivery in clinically meaningful contexts. Here, we investigated the effects of plasmonic nanoantennae on modulating tumor transport in a xenograft model of ovarian cancer. We observed a temperature-dependent increase in the transport of diagnostic nanoparticles into tumors, as well as a transient, reversible reduction in transport upon re-exposure to heating, which we term thermotolerance. Using a minimal microfluidic model of the endothelium, *in vitro* studies of the endothelial cytoskeleton, and chemical and genetic tools to inhibit the heat shock response (HSR), we identified the tumor endothelium and HSR as contributors to this 'thermotolerance' effect. Harnessing the understanding of the kinetic, structural, and molecular parameters governing tumor transport, we designed an improved therapeutic protocol combining plasmonic nanoantennae with diffusion-limited chemotherapies. This work therefore highlights the clinical relevance of cellular adaptations to nanomaterial-mediated perturbations and provides insight on molecular pathways whose modulation by emerging pharmacological agents could improve therapeutic tumor transport.

5.1 Introduction:

With the emergence of molecularly targeted therapies and novel nanoparticle carrier formulations, the efficient delivery of such therapeutic cargoes to solid tumors remains a central challenge in oncology. Locally enhancing the concentration of these agents within tumors will provide opportunities to achieve greater therapeutic efficacy, minimize off-target toxicities, and limit the development of drug resistance. Current chemotherapeutic regimens must carefully balance the conflicting goals of achieving cure and limiting systemic and organ-specific toxicities. Many compounds which are highly lethal to cancer cells *in vitro* are rendered less effective in patients due to this narrow 'therapeutic window', a constraint well appreciated in clinical oncology.[254] To a large degree, it is the physical transport barriers within solid tumors that impose a bottleneck on the delivery of cytotoxic agents, targeted compounds, and nanoparticle formulations. These barriers include heterogenous blood flow, inefficient transvascular transport, and limited interstitial diffusion through the tumor stroma.[55-57] For a particular combination of tumor type and drug cargo, the extent to which each barrier is involved can be viewed as a complex interplay of tumor- and drug-specific factors, such as vessel perfusion, vessel surface area, stromal density, cargo size, and cargo surface chemistry which can modify a cargo's electrostatic charge and pharmacokinetics.[59] Perturbing the tumor vasculature represents an attractive approach for enhancing therapeutic accumulation in solid tumors for at least two reasons. First, by dictating tumor blood flow and extravasation, the vasculature of solid tumors limits the delivery of a variety of therapeutic compounds spanning several orders of magnitude in size, including antibodies, nanoparticle carriers, and conventional chemotherapies.[56, 59, 60, 109, 110, 253] Secondly, solid tumors, independent of their tissue of origin or underlying mutational landscape, eventually become dependent on the host vasculature

for supplying nutrients and oxygen during angiogenesis, making the vasculature a general and genetically stable target for the majority of solid tumors.[255]

Efforts thus far to modulate the tumor vasculature in the context of therapeutic delivery have focused on chemical, biophysical, and molecular targeting approaches. Molecules such as the anti-angiogenic antibodies trastuzumab, bevacizumab, and cediranib have been shown to normalize tumor vasculature by pruning poorly formed angiogenic vessels and thereby improve overall blood flow within the tumor.[65, 67, 68, 70] Extravasation across the endothelium through intercellular gaps has been facilitated by molecules such as vascular endothelial growth factor (VEGF), tumor necrosis factor alpha (TNFα), interleukin 1 (IL-1), vasoactive agents including histamine and bradykinin, and tumor-penetrating peptides.[63, 89, 256-259] Homing peptides identified by *in vivo* phage display have been conjugated to a variety of therapeutic and diagnostic nanocarriers to target specific proteins enriched in the tumor vasculature like αVβ3 integrins.[260-262] Physical approaches using electromagnetic or acoustic energy have also been explored, most often in the context of ablative therapy.[263-267] These include radiofrequency ablation (RFA), microwave therapy, laser-induced thermotherapy, and high-intensity focused ultrasound (HIFU),[129, 268-271] but the high local temperatures achieved by these methods leads to coagulative necrosis rather than non-destructive, transient vascular perturbations.[265] For milder heating regimes, variations of these physical approaches have been combined with therapeutic cargoes such as temperature-sensitive liposomes containing chemotherapeutics to selectively trigger drug release by heating under real-time image guidance.[272, 273] Recent advances in nanomaterials have provided an opportunity to precisely control heating within tumor environments, and this has led to increased interest in understanding how such

nanomaterial-mediated heating regimens perturb the tumor vasculature and modulate tumor transport in clinical contexts.

Here, we explore the effects of plasmonic nanoantennae called gold nanorods towards promoting the accumulation of therapeutic and diagnostic cargoes in solid tumors via transient modulation of the tumor vasculature. While an initial heat exposure with PEG-NRs enhanced tumor transport, tumors re-exposed to PEG-NR heating, as would occur in clinical protocols requiring repeated administration of chemotherapeutics over periods of days to weeks, developed thermotolerance with diminished tumor transport. Activation of the mammalian heat shock response (HSR) has been implicated in the development of thermotolerance in tumor cells, but its potential role in the endothelium is less clear. Using microfluidic endothelial permeability assays, *in vitro* analysis of the endothelial cytoskeleton, and intravital microscopy of the tumor vasculature, we identify the endothelium and the HSR as contributors to this thermotolerance effect. We preliminarily explore inhibition of the HSR as a remedy for thermotolerance using chemical and genetic approaches that diminish *Hsf1* activity. Lastly, we demonstrate that PEG-NR regimens which establish thermotolerance lead to reduced delivery of doxorubicin-loaded liposomes and less effective therapeutic responses in ovarian tumor xenograft models. Collectively, this work describes a thermal adaptation made by solid tumors in response to nanomaterial-generated heat stress, an effect with functional consequences for chemotherapeutic delivery and relevance to designing optimized treatment schedules.

5.2 Materials and Methods:

Animal models and cell lines:

All studies involving animal models were approved by the MIT Committee on Animal Care. Epithelial ovarian cancer models were established by unilateral or bilateral subcutaneous injection of ~1-2e6 CP70 human ovarian cancer cells into the rear flanks of 4-5-week-old athymic nude mice (Charles River). HSF1-null and HGL models expressing GFP and Luciferase driven by HSE A6 promoter were generated in the Lindquist Laboratory. Rag1tm1MomTg(Tie2GFP)287Sato/J mice expressing GFP in endothelial cells were used for vessel permeability studies (Jackson Laboratory). Tumor growth was monitored for approximately 10-20 days prior to injection of PEG-NRs. CP70 and OVCAR-8 cells were cultured in RPMI 1640 with L-glutamine (Invitrogen) supplemented with 10% fetal bovine serum (FBS) and penicillin/streptomycin. B16 cells were cultured in DMEM supplemented with 10% fetal bovine serum (FBS) and penicillin/streptomycin. Primary HUVEC cells were cultured in media prepared from the EGM-2 BulletKit (Lonza).

PEG-NR Synthesis:

Concentrated cetyltrimethylammonium (CTAB)-coated gold nanorods (Nanopartz, Inc.) with dimensions of 41 nm x 10 nm were incubated with 5 kDa methyl-PEG-thiol (Laysan Bio, Inc.) to a final concentration of 100 μM as described previously.[241] After gentle mixing for 60 minutes, solutions were dialyzed for at least 24 hours in 3,500 MWCO Slide-A-Lyzer cassettes (Thermo Scientific) in deionized, distilled water. Solutions were transferred to 100 kDa filter tubes (Millipore) and filtered with ultrapure water for five cycles of centrifugation (3,000g, 10 minutes). PEG-NR solutions were resuspended in sterile PBS to an optical density of ~100 OD and stored at 4°C prior to administration in animal models.

Intratumoral accumulation studies:

Animals bearing bilateral CP70 ovarian tumors were administered intravenous injections of PEG-NRs (100 μL; 100-150 OD). After 48-72 hours to allow PEG-NR clearance from circulation, animals received an intravenous injection of AngioSpark750 (AS750) (Perkin Elmer) (50 μL in PBS; stock solution) and one flank tumor received 808nm near-infrared irradiation for up to 30 minutes using a continuous 808nm diode laser source (Visotek). Tumor temperature was monitored continuously with an infrared thermal camera (FLIR T650sc) and tumor temperature was maintained at 40-43°C for the laser irradiation period. At multiple time points between 10 minutes and 48 hours after PEG-NR heating, tumor near-infrared fluorescence was acquired on the whole-animal IVIS Spectrum-bioluminescent and fluorescent imaging system (Xenogen). Quantification of relative AS750 accumulation in PEG-NR-heated tumors compared to contralateral unheated tumors was performed using Living Image analysis software (v4.3.1). Tumors harvested from animals were rinsed in PBS and whole-tumor AS750 fluorescence was detected using a near-infrared imaging system (LICOR Odyssey). Tumor homogenates were prepared by incubating tumor samples in tissue extraction buffer (70% EtOH, 0.3N HCl) and lysing samples on an automated homogenizer (gentleMACS Octo Dissociator, Miltenyi Biotec). Samples were centrifuged (1,000 rpm, 5 minutes), extracted overnight at 4°C, and supernatant fluorescence was measured in microplates on the LICOR imaging system.

Intravital imaging:

Intravital tumor imaging was performed on an Olympus FV1000 multiphoton laser scanning confocal microscope with a 25X, N.A. 1.05 objective lens. For vessel permeability experiments, animals were anesthetized by isoflurane and administered an intravenous bolus of fluorescein dextran (70,000 MW; Invitrogen), tetramethylrhodamine (TMR) dextran (2,000,000

MW; Invitrogen), or Texas Red dextran (70,000 MW; Invitrogen) (2–2.5 mg/mL). Immediately following injection of vascular dyes, tumors were positioned and immobilized on the stage for the duration of the experiment. For heat shock induction experiments, dorsal window chambers were surgically implanted or skin-flap models were prepared on HGL models and induction of the heat shock response as measured by GFP expression in vessels and surrounding tissue was monitored up to 24 hours post-heating. For intratumoral cellular uptake studies, Rag1-Tie2GFP mice bearing unilateral subcutaneous CP70 xenograft tumors were intravenously administered TR-dextran to visualize the vessel lumen and interstitial cells and imaged with a 25X, N.A. 1.05 objective lens and 4X digital zoom (100X total magnification) within 1-2 hours following PEG-NR heating.

Microfluidic *in vitro* permeability studies:

Microfluidic devices were fabricated as described previously.[274] Briefly, 400 μm stainless steel needles were withdrawn from polymerized collagen hydrogels to create cylindrical voids that were then seeded with HUVECs. The endothelialized channels were exposed to continuously applied shear stress at magnitudes between 0.1 and 0.2 Pa for 12-18 hours to facilitate formation of tight junctions. Channels were placed in a temperature-controlled chamber (Air-Therm ATX, World Precision Instruments) on an epifluorescence microscope (Nikon Eclipse TI, Nikon Instruments). Saline solutions containing 70 kDa FITC-Dextran and Rhodamine-Dextran (Sigma) were continuously perfused through channels at flow rates of 5 μL/min. Temperature within the heated chamber was continuously monitored for the duration of each experiment. Fluorescence and brightfield images were acquired with a 10X objective lens at the start and conclusion of each heating period. MetaMorph software (v7.7.3.0) was used for

image acquisition. Channels receiving multiple heat exposures were returned to a 37ºC incubator between the initial and subsequent imaging sessions, and again exposed to fluid shear stress. Dextran diffusion was quantified by tracking the movement of the dye front as a function of time. Image analysis, quantification of dye front displacement, and statistical analysis were performed with ImageJ software and GraphPad Prism software (v6.02).

Cytoskeletal stability studies:

Human umbilical vein endothelial cells (HUVEC) were seeded into μ-slide 8 well standard bottom dishes (ibidi) at 4.5e3 cells per well and allowed to adhere for 24 hours. The culture medium was then exchanged for fresh medium containing rAVCMV-LifeAct-TagGFP2 (MOI: 100) (ibidi). After overnight incubation at 37°C, HUVECs either received a heating pre-treatment (45°C, 30 minutes) or were maintained at 37°C. Following a 24 hour recovery period at 37°C, all cells then received a heat shock (45°C, 1 hour). Images were acquired using a 20X objective lens on a fluorescence microscope (Nikon Eclipse Ti) prior to and 0, 1, 2, 4, and 6 hours after the final heat treatment. Images were obtained from 6–8 distinct wells per condition and time point. An investigator blinded to the experimental conditions scored cells contained visible actin filaments connecting opposing sides of the cell membrane, as well as the total number of cells per field. A total of 13,583 cells were scored (1,072–1,213 cells per condition) and statistical analysis was performed using GraphPad Prism software.

Cell viability studies:

HUVECs were seeded at 5e3 cells per well in 96-well black glass-bottom plates (Grenier) and allowed to adhere for 24 hours. Cells were pretreated by incubation at 45°C for 30 minutes, allowed to recover for 24 hours at 37°C, then incubated at 45°C for an additional 1 hour. Cells

were allowed to recover at 37°C for 30 hours. Cell viability was assayed using Alamar Blue (Invitrogen) prior to and 0, 6, and 30 hours after the final heat treatment.

Tumor volume and survival studies:

For longitudinal survival studies, nude mice were implanted with ~1-2e6 CP70 human ovarian cancer cells in the hind flanks. Tumor treatments consisted of administration of PEG-NRs, doxorubicin-loaded liposomes (5 mg/kg) (Encapsula), and NIR irradiation with appropriate controls. Briefly, 48-72 hours post PEG-NR administration, animals received NIR laser irradiation (~41-43°C, 30 minutes) under continuous temperature monitoring using an infrared camera (FLIR T650sc). 24 hours later, animals underwent a second round of NIR laser irradiation in combination with intravenously administered doxorubicin-loaded liposomes. Longitudinal studies lasted ~4-5 weeks from initial treatment with tumor volumes measured approximately every 3-4 days using digital calipers by investigators who were blinded to the experimental groups. Animals were euthanized when the tumor burden exceeded 500 mm3. Plots and statistical analysis of tumor volume growth and Kaplan-Meier survival curves were performed using GraphPad Prism.

Heat shock induction *in vivo*:

HGL mice were implanted with 2e5 B16 melanoma cells in the hind flank. After 2-3 weeks, animals were injected with PEG-NRs intravenously and received an initial round of NIR irradiation 48-72 hours later. Animals were injected subcutaneously with RHT (1.2 mg/kg) in cyclodextran or vehicle control twenty minutes prior to NIR irradiation. 24 hours after NIR irradiation, animals were injected subcutaneously with D-Luciferin (9 mg/mL in PBS) (Gold Biotech) and imaged on the IVIS Spectrum system for bioluminescence. The procedure was

repeated for a second round of NIR irradiation and RHT administration, with bioluminescence imaging performed 24 hours later. Image analysis was performed on Living Imaging software.

Immunohistochemistry:

Tumors were harvested and fixed in a 4% paraformaldehyde solution overnight at 4ºC. Tissues were transferred to cassettes and placed in 70% ethanol solution at room temperature until paraffin embedding. Antibodies used included a rabbit polyclonal CD31 antibody (1:75, Abcam), rabbit monoclonal HSP70 (1:50, Cell Signaling), and rat HSF1 (4B4) (1:500, Thermo Scientific). Slides were counterstained with standard Hematoxylin & Eosin (H&E). LabVision Autostainer 360 Immunohistochemical Stainer (Thermo Scientific) was used to perform IHC with antigen retrieval.

Nanoparticle circulation time:

AS750 and FITC-Dextran were intravenously administered to animals, and blood was collected by retro-orbital sampling at several times following injection using heparin-coated microcapillary tubes (VWR). Samples were rapidly transferred to a 5 mM EDTA solution to prevent coagulation. Blood samples were spun on a tabletop centrifuge for 30-60 seconds to separate plasma and erythrocyte fractions. Plasma fractions were transferred to 96-well plates and read on a fluorescence microplate reader (Molecular Devices) and near-infrared imaging system (LICOR).

Nanoparticle *in vitro* stability:

AS750 nanoparticles were serially diluted in solutions of distilled water, PBS, 10% (v/v) FBS in PBS, and 50% (v/v) FBS in PBS to a lowest concentration of 1:100,000 of the stock

concentration. Nanoparticle fluorescence was measured on the IVIS Spectrum-bioluminescent and fluorescent imaging system (Xenogen) and the Odyssey near-infrared scanner (LICOR). Image analysis and quantification was performed using ImageJ software.

5.3 Results:

5.3.1 PEG-NR heating enhances tumor transport followed by development of thermotolerance

Mild heating of tumors with PEG-NRs and other methods has previously been shown to enhance the accumulation of diagnostic and therapeutic agents in tumors.[109, 110, 112] In order to study the impact of nanomaterial-driven heating on tumor transport, mice with ovarian xenograft flank tumors were administered PEG-NRs several days prior to heating. At various times, tumor transport was assessed by quantifying delivery of pegylated fluorescent nanoparticles (AS750) as a model of diffusion-limited cargo. AS750 is composed of an iron oxide core coated with polyethylene glycol (PEG) and near-infrared fluorophores; its circulation time ($t_{1/2}$: 283 minutes), particle size (~35 nm), and spectral characteristics (Ex/Em: 750/775 nm) make it a good model for clinical nanoparticle formulations and for *in vivo* monitoring (**Fig. S1**). Consistent with previous studies, tumors receiving a single exposure to PEG-NR heating accumulated AS750 in 2.1-fold excess compared to unheated tumors on the contralateral flanks (**Fig. 5.1**). Because in clinical settings many therapeutic agents are administered as multiple cycles spanning periods of days to weeks, we explored the consequences of repeated PEG-NR heating on tumor transport. Ovarian tumor xenografts received repeated exposure to PEG-NR heating with intervals between heating ranging from 8 hours to 1 week, defined as delta T. In these experiments, tumor transport was characterized at the time of the second heat exposure by administration of AS750. The results show that delta T of 8 hours still resulted in an increase in tumor transport of 1.4-fold over untreated tumors, however the enhancement was reduced as

compared to that after the first heat exposure (**Fig. 5.1**). At longer delta T of 24 and 48 h, tumor transport was no longer enhanced over untreated controls (0.9- and 1.0-fold respectively) (**Fig. 5.1**). We term this loss of heat-responsiveness 'thermotolerance'. At longer delta T, we noted a recovery of heat-responsiveness, beginning at 96 h and increasing back to >2-fold by a delta T of one week (**Fig. 5.1**). Fluorescence of explanted tumors displayed a similar trend, with shorter delta T between PEG-NR heat exposures correlating with reduced tumor transport (**Fig. S2**). This data demonstrates that PEG-NR heating increases tumor transport but also induces a thermotolerance to subsequent heating that peaks at 24-48 h and reverts after one week. In subsequent experiments, we establish a delta T of 8 or 24 h to further investigate the thermotolerance phenomena.

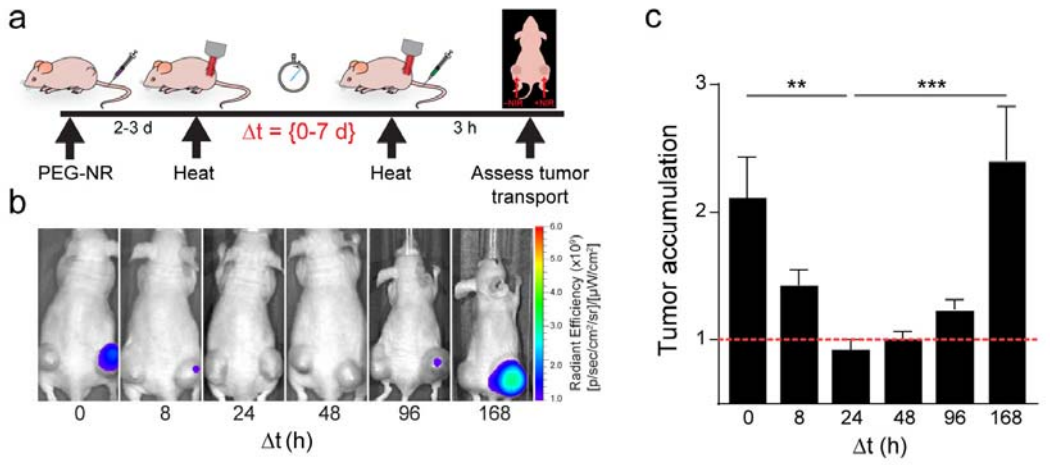

Figure 5.1. Heat-induced transport enhancement is followed by a period of thermotolerance wherein tumors are resistant to subsequent heating. (a) Experimental time course includes administration of gold nanorods (PEG-NR), an initial exposure of laser heating (heat), and an interval delta T varying from 0 to 7 days prior to re-exposure (heat). Tumor transport is probed at the end of delta T via administration of AS750 imaging nanoparticles and tumor accumulation is quantified via *in vivo* fluorescence imaging. (b) Tumor transport as visualized by AS750 nanoparticle fluorescence in heated versus unheated tumors for increasing delta T. Note the increase in tumor transport after heat exposure is absent upon repeat exposure after 24-48 h ('thermotolerance') but begins to recover at 96 h. (c) Tumor transport (ratio of AS750 for heated versus unheated tumors) (n = 8-12 per group from two independent experiments, **P<0.01, ***P<0.001, one-way ANOVA and Tukey's post-tests.) Error bars, s.e.m.

To explore the dynamics of heat-enhanced tumor transport, animals received either a single or double exposure to PEG-NR heating and tumor transport was assessed by offsetting the administration of AS750 by either 1 or 6 h after heating. (**Fig. 5.2**). Tumors receiving a single exposure of PEG-NR heating displayed a 2-2.7-fold increase in accumulation when AS750 was administered within 1 hour of PEG-NR heating and no relative enhancement in accumulation when AS750 was administered 6 hours after PEG-NR heating (**Fig. 5.2**). This data suggests that a single exposure of PEG-NR heating established a 6 hour 'window' where nanoparticles could preferentially accumulate within heated tumors. Interestingly, in tumors receiving a repeated PEG-NR exposure after delta T of 8 h, we no longer observed an enhancement in accumulation when AS750 was administered 1 h following the second heat exposure. (**Fig. 5.2**). These results suggest that both the magnitude of the thermal response and the dynamics may be altered after repeated exposure to heat. Taken together, these data demonstrate an initial increase in tumor transport in response to heat that is followed by a transient, reversible loss in heat responsiveness (thermotolerance). Because the endothelium is a dynamic, heat-responsive interface between the systemic circulation and the tumor interstitium, we next assessed the potential role of the endothelium in mediating the observed thermotolerance.

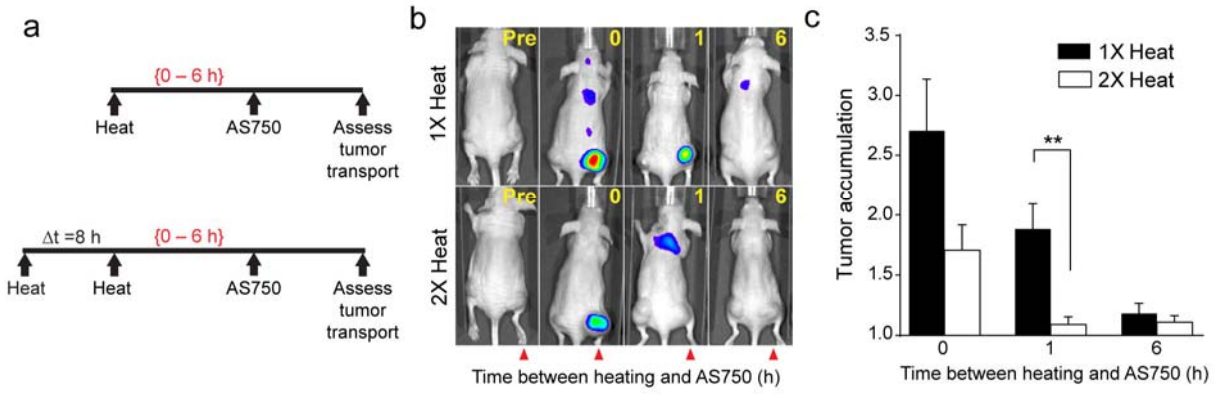

Figure 5.2. Diminished window of tumor transport after re-exposure to PEG-NR heating. (a) Experimental time course includes an initial exposure to PEG-NR heating (heat), an interval delta T of 8 h, re-exposure to PEG-NR heating (heat), and AS750 administration offset from the second heating by 0, 1, or 6 h. Tumor accumulation is quantified via *in vivo* fluorescence imaging. (b) Representative *in vivo* fluorescence images demonstrating shortened window of tumor transport after re-exposure to PEG-NR heating. Red arrows indicate heated tumors. (c) Tumor transport (ratio of AS750 in heated versus unheated tumors) for each offset in AS750 administration after re-exposure to heating. (n = 8 per group, **P<0.01, unpaired t-test, two-tailed.) Error bars, s.e.m.

5.3.2 Endothelial heat response is sufficient for transvascular transport and thermotolerance

To study the specific contribution of the endothelium, we utilized a microfluidic device consisting of a cylindrical channel lined by a monolayer of endothelial cells encapsulated in type I collagen (**Fig. 5.3**).[274] The minimal components contained in this device represent to a first approximation the angiogenic vasculature of solid tumors, which consists of an endothelial monolayer with reduced pericyte coverage and surrounded by a network of collagen fibers, proteoglycans, and tumor cells.[255] A saline solution containing 70 kDa FITC-Dextran was perfused through the endothelial channel and permeability at various temperatures and heating regimens was measured over time as the displacement of the FITC-Dextran dye front (**Fig. 5.3**). We performed a temperature ramp spanning physiological body temperature of 37°C to 45°C to encompass the full range of temperatures achieved during *in vivo* PEG-NR heating experiments. For vessels subjected to a single exposure of heating, FITC-Dextran dye was retained within the

vessel lumen between 38°C and 42°C (**Fig. 5.3**). When the temperature reached 43°C, we observed significant displacement of the dye front into the surrounding collagen matrix, indicating disruption of the endothelial monolayer and increased transvascular permeability (**Fig. 5.3**). Structural changes to the endothelium were observed, as the cells transitioned from a confluent, flow-aligned 'cobblestone' appearance prior to heating to a contracted state with increased frequency of interendothelial gaps (**Fig. 5.3**).

Interestingly, when the same vessels were subjected to a second exposure of heating with a delta T of 8-24 h, the dye front displacement of FITC-Dextran was diminished. When heated channels were returned to physiological body temperature after an initial heating, the endothelial cells efficiently resealed to form an effective barrier to FITC-Dextran diffusion (data not shown). Compared to their initial heating exposure, re-heated vessels displayed 26.3- and 11.6-fold less dye front displacement at 42°C and 43°C, respectively (**Fig. 5.3**). To integrate the effect across temperature, we calculated the cumulative dye front displacement during single heating and re-heating regimens. The cumulative displacement of FITC-Dextran from the lumen into the surrounding collagen matrix between 40°C and 43°C was reduced by 2.6-fold in doubly-heated channels relative to single heated channels (**Fig. 5.3**). The ability to recapitulate thermotolerance in a model containing minimal elements (i.e., endothelial cells and collagen) suggests that the endothelium itself can adapt to repeated thermal exposures and play an important role in modulating transvascular transport *in vivo*.

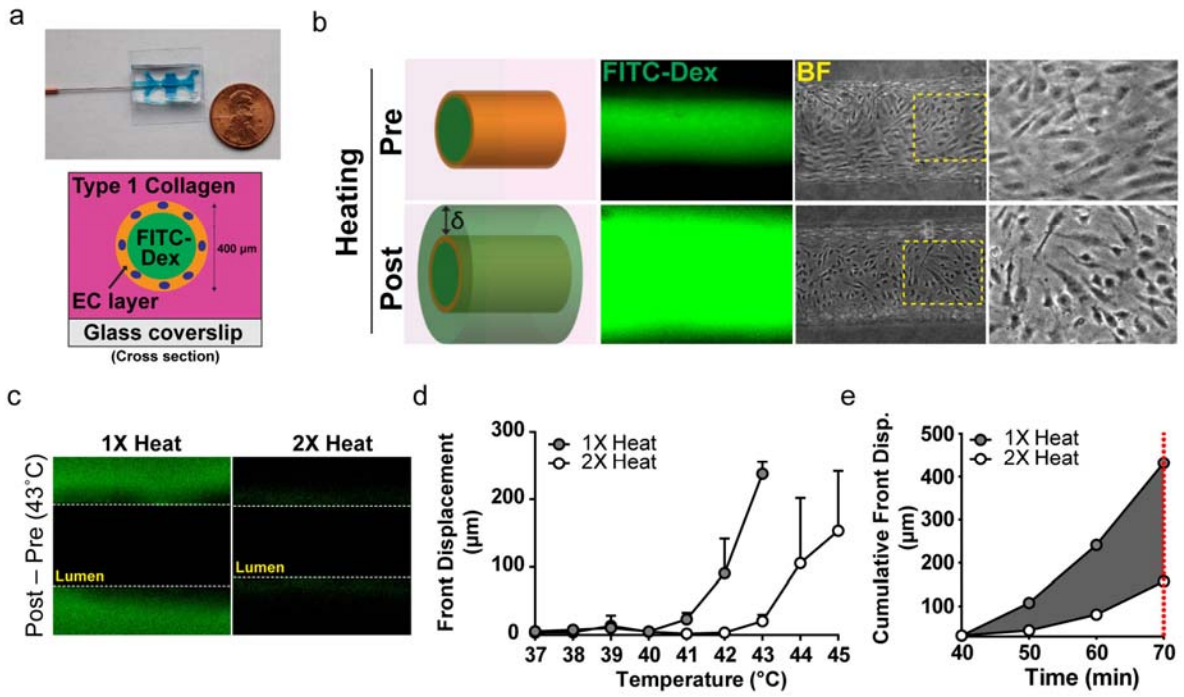

Figure 5.3. Endothelial heat response is sufficient for transvascular transport and thermotolerance. (a) Photograph and cross-section schematic of microfluidic endothelial channel. A cylindrical channel lined by an endothelial monolayer is established within type 1 collagen gel. Saline solutions containing 70 kDa FITC-Dextran are flowed through the channel during controlled heating regimens to monitor temperature-dependent transport across endothelium. (b) Representative fluorescence and bright field images for pre- and post-heating. Prior to heating, FITC-Dextran is retained in the channel lumen and a confluent endothelial monolayer is observed. After heating, extravasation of FITC-Dextran is associated with contracted endothelial cells (ECs). Dye front displacement (δ) measured for each temperature. (c) FITC-Dextran accumulation outside of lumen during 43°C heating period in microfluidic channels subjected to a single (1X heat) or repeated (2X heat) heat exposure. (d) Dye front displacement versus temperature across physiological temperature range. (n = 3-6 channels per group) (e) Cumulative front displacement over time between 40–43°C. Channels were exposed to each temperature for 10 minutes excluding ramping intervals.

5.3.3 Cytoskeletal recovery of endothelial cells is enhanced after repeated heat exposure

The morphological changes to endothelial cells observed in the microfluidic vascular model suggested that cytoskeletal disruption was contributing to the functional changes to permeability. To explore the response of the endothelial cytoskeleton to single versus double heat exposures, human umbilical vein endothelial cells (HUVECs) were infected with adenovirus

expressing an F-actin-binding GFP fusion protein to dynamically monitor F-actin destabilization and structural recovery in living endothelial cells. HUVECs received either a single heat exposure ('1X heat') or second heat exposure with delta T of 24 h ('2X heat'), and cytoskeletal structure was serially monitored by time-lapse fluorescence microscopy (**Fig. 5.4**). To quantify cytoskeletal structure, we defined the parameter membrane-spanning filaments to indicate cells with at least one visible F-actin filament connecting non-adjacent points along the cell membrane (F-Actin^{+}), and an investigator blinded to the treatment groups scored individual cells across all conditions. These heating conditions intended to mimic the single and double PEG-NR heating regimens explored *in vivo*, and the heat exposures in the minimal microfluidic vasculature *in vitro*. At physiological temperatures, the majority of cells in the single heat exposure and re-heat exposure groups displayed numerous membrane-spanning F-actin filament networks (72.6% and 62.9% cells with membrane-spanning F-actin filaments, respectively) (**Fig. 5.4**, **Fig. S3**). Immediately following heating, both single heated and re-heated cells displayed a collapsed F-actin appearance, with re-heated cells exhibiting an elevated but insignificant percentage of cells with membrane-spanning filaments compared with single heated cells (16.9% and 4.1%). Time-lapse microscopy revealed the kinetics of cytoskeletal recovery of single heated and re-heated cells following heat exposure. Re-heated endothelial cells exhibited efficient structural recovery 1-2 hours after heat exposure (63.6%-75.9%) and remained stable at these levels for 4-6 hours after heat exposure (64.3%-72.4%). In contrast, single heated cells failed to exhibit recovery of the cytoskeleton 1-2 hours after heat exposure (3.0%-7.2%), which represented 21.3- and 10.6-fold fewer cells with membrane-spanning filaments relative to re-heated cells at 1 and 2 hours after heat exposure, respectively. However, single heated cells did display a partial structural recovery of F-actin filaments by 6 hours after heat exposure (30.4%). Endothelial cell viability

was not significantly different between single heated and re-heated cells before heat exposure, immediately following heat exposure, and 30 hours following heat exposure, although a small decrease in viability in single heated cells was observed 6 hours after heat exposure (**Fig. 5.4**).

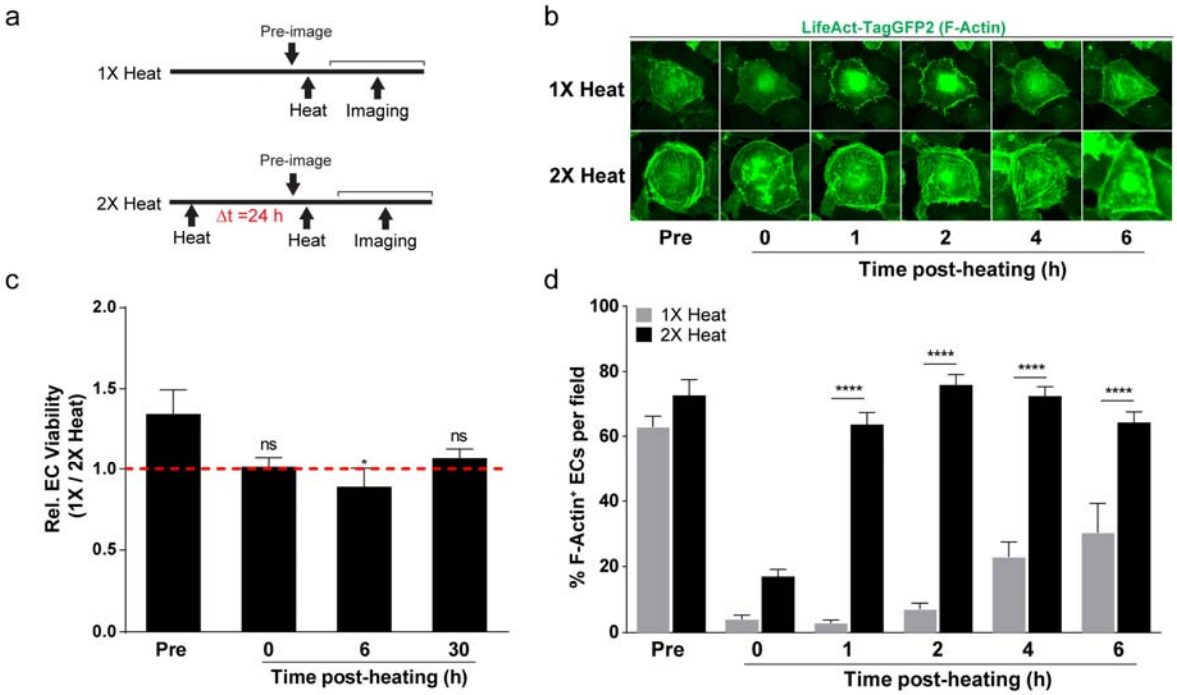

Figure 5.4. Cytoskeletal recovery of endothelial cells is enhanced upon re-exposure to heating. (a) Experimental time courses for single heat exposure (1X heat) and re-exposure to heat (2X heat). (b) Representative fluorescence images of EC F-Actin filaments during recovery after heating. Images depict cytoskeletal collapse and subsequent recovery. For each regimen, the same cell is shown across multiple time points to demonstrate the kinetics of EC recovery. (c) Relative EC viability for cells in single exposure and re-exposure groups prior to, immediately after, 6 hours, and 30 hours after heating. Bars represent EC viability in the single exposure group relative to re-exposure group. (n = 5 per group, *P<0.05 one-way ANOVA and Tukey's post-tests.) (d) Percentage of cells with visible membrane-spanning F-Actin filaments per field during the post-heating recovery period. (n = 1,072 – 1,213 cells from 6-8 fields of view per condition per time point, ****P<0.0001, two-way ANOVA and Bonferroni's post-tests.) Error bars, s.e.m.

Within the single heat exposure and re-exposure cell populations, the individual fields of view examined within each group displayed similar temporal patterns of cytoskeletal recovery (**Fig. S4**). In a separate experiment, we investigated the temperature dependence on cytoskeletal

collapse between 37-42.3°C and observed a progressive increase in the frequency of cytoskeletal collapse with increasing temperature and duration of heating (**Fig. S5**). Collectively, this data demonstrates that subjecting endothelial cells to a previous heat treatment contributes to accelerated remodeling upon subsequent heat exposure, which is manifested by more efficient structural recovery of the F-actin cytoskeleton. Interestingly, the time scales for cytoskeletal recovery observed in single and re-heated endothelial cell populations were similar to the windows of cargo accumulation observed in tumors exposed to single and double PEG-NR heating regimens, respectively.

5.3.4 Endothelial response to PEG-NR heat exposure in the tumor environment

Having observed the effect of thermotolerance on tumor transport *in vivo* and on vascular permeability and endothelial cytoskeletal architecture *in vitro*, we next visualized endothelial barrier function *in vivo*. In particular, we sought to understand the size dependence of the permeability effects on potential cargos, as well as observe endothelial responses to single and double PEG-NR heating in the tumor environment. Mouse xenograft models received either a single PEG-NR heat exposure or double PEG-NR heat exposure with a delta T of 24 hours. Transvascular transport in tumors was probed by an intravenous bolus of 70 kDa FITC-Dextran immediately followed by intravital multiphoton microscopy. Unheated tumors displayed minimal extravasation of 70 kDa FITC-Dextran tracer dye, whereas tumors receiving a single PEG-NR heat exposure exhibited moderate vascular leakage into the interstitial space within an hour after heating (**Fig. 5.5**).

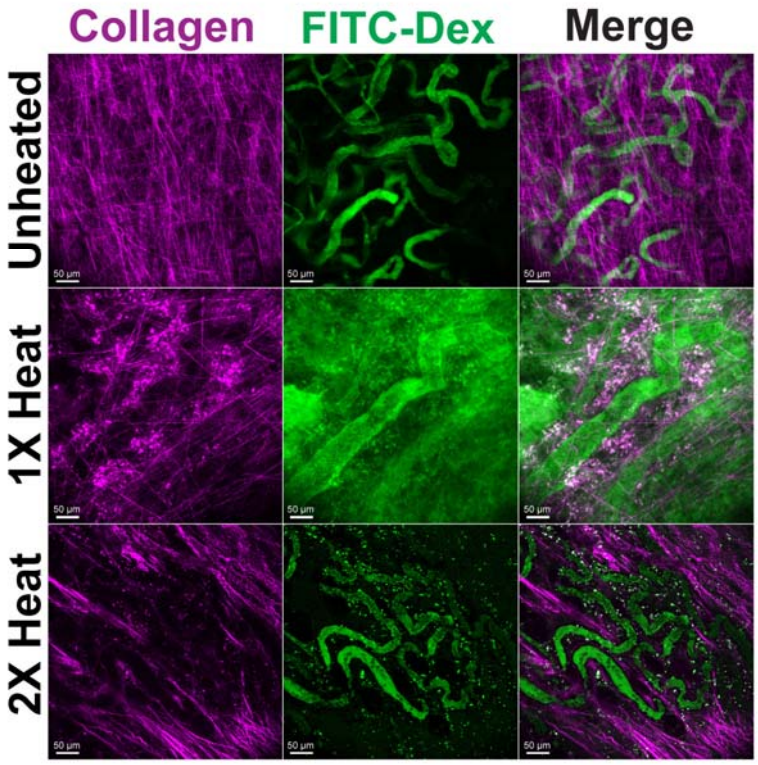

Figure 5.5. Transvascular transport in tumors after single exposure and re-exposure to PEG-NR heating. Unheated and re-exposure (2X heat) tumor vessels display intravascular retention of 70 kDa FITC-Dextran, while a greater degree of extravasation of FITC-Dextran was observed during single exposures (1X heat) to PEG-NR heating. Collagen fibers (magenta) delineate the tumor interstitium and PEG-NRs appear in a punctate perivascular pattern in both channels. (n = 15-31 z-stacks from n = 3-7 animals per treatment group) Scale bar: 50 µm

Consistent with bulk measurements in **Fig. 5.1**, tumors receiving a second exposure to PEG-NR heating displayed reduced extravasation of tracer dye into the interstitial space in the majority of fields examined. In unheated tissues, we also observed a clear size-dependence to extravasation, as 10 kDa FITC-Dextran readily diffused from the vascular compartment into the collagen-rich interstitial space whereas 2,000 kDa TMR-Dextran was retained in the vessel lumen (**Fig. S6**).

Because increased vascular permeability via endothelial contractions would not necessarily lead to enhanced tumor accumulation due to 'back-diffusion' of cargoes into vessels[56], we sought to understand what could be driving the accumulation and retention in our

model using high magnification intravital microscopy. To visualize extravasation in proximity to tumor vessels at higher resolution, we established tumors in a transgenic mouse model expressing the Tie2-GFP fusion protein to fluorescently label the tumor endothelium. Intravenous 70 kDa Texas Red dextran (TR-Dex) was administered and the intra- and extravascular distribution of TR-Dex was examined in response to different PEG-NR heating regimens (**Fig. 5.6**). In particular, we observed a significant number of perivascular phagocytic cells within tumors, likely representing macrophage or dendritic cell populations. We observed punctate spots of TR-Dex appearing within these perivascular cell populations consistent with endocytic uptake of TR-Dex. For each PEG-NR heating regimen, we quantified the frequency of TR-Dex-positive cells per volumetric image stack as a proxy for the degree of local extravasation occurring within each field. Unheated tumors displayed relatively few TR-Dex-positive cells (5.1±2.4 cells per field), whereas tumors receiving a single exposure to PEG-NR heating displayed a significant 3.9-fold greater frequency of TR-Dex positive cells (19.9±2.1 per field). In contrast, tumors re-exposed to PEG-NR heating with delta T of 24 h displayed a reduced frequency of TR-Dex-positive cells and only 1.6-fold higher than the unheated state (8.3±1.1 per field). For each condition, tumor blood flow was maintained during each imaging period suggesting that vaso-occlusion or thrombosis was not a major contributor to the diminished extravasation observed with repeated PEG-NR heating (data not shown). Additionally, elevated levels of vascular endothelial growth factor (VEGF) in the tumor microenvironment can enhance vascular permeability, with both increased inter-endothelial gap formation and increased transcytosis across endothelial cells. We did not observe significant differences in VEGF expression following each heating regimen in this study. (**Fig. S7**)

To corroborate these microscopic observations with bulk tumor accumulation, tumor homogenates were prepared from mice intravenously administered 70 kDa FITC-Dextran. Homogenates from tumors receiving a single exposure of PEG-NR heating accumulated 1.7-fold greater FITC-Dextran (8.6 versus 5.2 %ID/g), whereas homogenates from tumors receiving a double heat exposure accumulated FITC-Dextran to a similar degree as unheated tumors (4.6 versus 5.2 %ID/g) (**Fig. 5.6**). Having established a role for the endothelium in mediating thermotolerance using both *in vivo* and *in vitro* models, we next sought to understand the relevant molecular pathways involved.

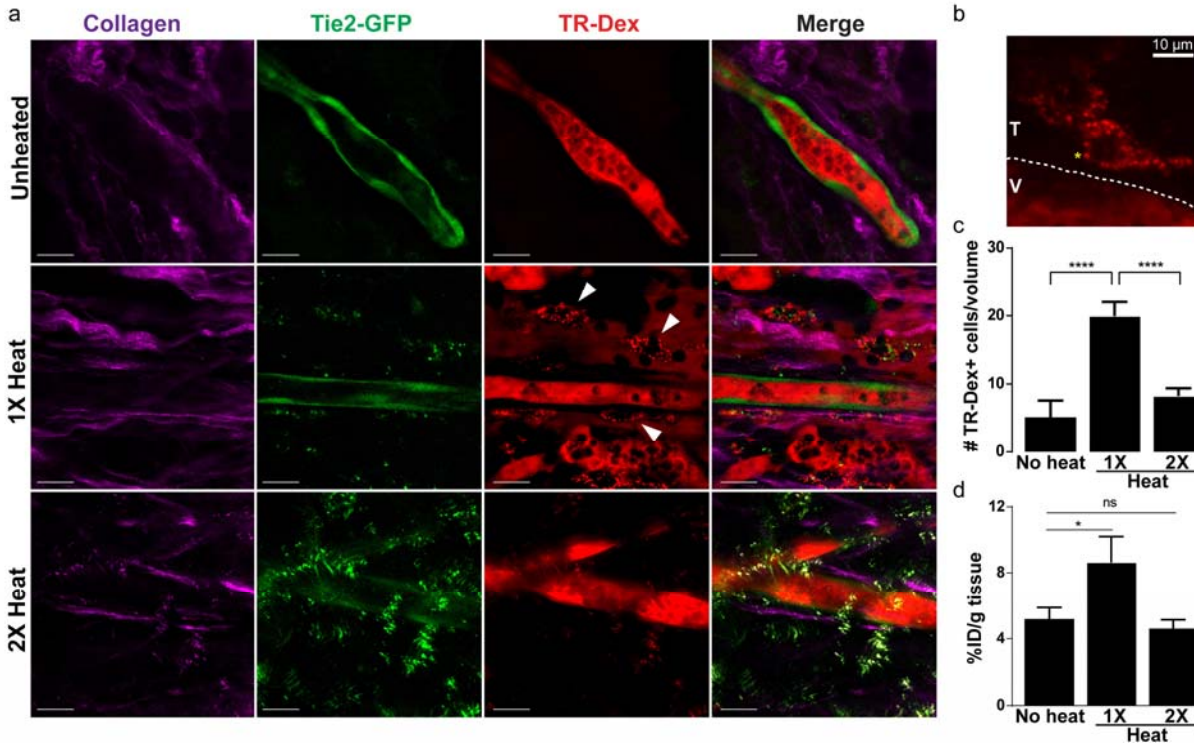

Figure 5.6. Macromolecular accumulation in vivo after single or double PEG-NR heating exposures. (a) Intravital imaging of intra- and extravascular distribution of 70 kDa Texas Red dextran (TR-Dex) in ovarian xenografts with Tie2-GFP+ endothelium. Collagen fibers (purple) highlight the tumor interstitial space, GFP (green) highlights tumor endothelium, and TR-Dex (red) is distributed between vessel lumen, interstitial space, and perivascular cells. Scale bar: 20 µm (b) Perivascular phagocytic cell residing in tumor interstitium (T) outside of tumor blood vessel (V). Yellow asterisk highlights uptake of TR-Dex cargo in putative endosome. (c) Quantification of TR-Dex-positive cells per tumor tissue volume measured by intravital imaging. (n = 15 – 23 fields of view from 3 mice per condition, ****P<0.0001, one-way ANOVA with Tukey's post-tests.) Error bars, s.e.m. (d) Accumulation of 70 kDa FITC-Dextran in tumor homogenates from tumors receiving no heating, a single exposure, or double heat exposure. (n = 3-7 tumors per condition, *P<0.05, unpaired t-test, two-tailed.) Error bars, s.e.m.

5.3.5 Heat shock response is induced by PEG-NR heat exposure and can be inhibited by RHT

Because thermotolerance was shown to impact tumor transport, an understanding of the molecular pathways mediating thermotolerance could suggest approaches to overcome its undesirable effects on tumor transport. The mammalian heat shock response (HSR) is an ancient, evolutionarily conserved cellular signaling network that responds to a variety of stresses

including heat, oxidative stress, low pH, and heavy metals.[113] Previous studies have identified a role for the HSR in mediating thermotolerance in a variety of cells and organisms.[275-277] Although we use the term here to describe tumor transport effects, thermotolerance is classically defined as a cell-intrinsic adaptation to stress that promotes increased viability upon subsequent stress. Of interest to this study, however, classical thermotolerance has been shown to confer enhanced cytoskeletal stability to cells upon subsequent heat exposure.[117-119] To investigate whether nanomaterial-induced heat was activating genetic heat shock programs in our model, we performed intravital microscopy on immunocompetent tumor xenograft models expressing heat-inducible GFP (HSE-GFP) and luciferase (HSE-Luc) under the heat shock element (HSE) A6 promoter (HGL model) (**Fig. 5.7**). HGL mouse models bearing B16 melanoma xenografts received single exposures of PEG-NR heating. Unheated tumors displayed minimal GFP expression in vascular territories (**Fig. 5.7**). Because of their strong optical scattering properties, PEG-NRs were readily visualized in both heated and unheated tumors as punctate, perivascular signals in all emission channels (**Fig. 5.7**, **Fig. S8**).Tumors receiving a single PEG-NR heat exposure, however, displayed a marked and diffuse increase in GFP expression indicating robust induction of the HSR in response to PEG-NR heating. A cellular infiltrate appearing to concentrate the PEG-NRs in perivascular regions was also observed in PEG-NR heated tumors. Notably, several regions revealed strong perivascular GFP expression suggesting that the endothelium develops an active HSR within hours following heating (**Fig. 5.7**).

Our results suggest that the thermotolerance we observed in tumors with delta T between 8 – 24 h could be explained by induction of the HSR in the endothelium after an initial heat exposure. We hypothesized that inhibition of the HSR by either chemical or genetic approaches could mitigate thermotolerance. Recently, a family of natural product compounds called

rocaglates was shown to potently inhibit Heat Shock Factor 1 (*Hsf1*) via translational repression and release of *Hsf1* from promoters of target genes including the heat shock proteins (HSPs).[121] To investigate whether pharmacological inhibition could diminish the HSR after PEG-NR heating, we administered RHT, a potent member of the rocaglate family, in combination with PEG-NR heating to HGL tumor xenograft models and monitored HSR induction by bioluminescence. For tumors receiving either a single or double PEG-NR heat exposure, RHT significantly inhibited HSR induction in the tumor stroma and surrounding tissue (**Fig. 5.7**). If thermotolerance is being driven by the HSR, then HSR inhibition *via* RHT might be expected to improve tumor transport in the setting of double heat exposure. While we did not observe an enhancement in AS750 accumulation in RHT-treated tumors, this may represent a pharmacodynamic limitation of the dosing regimen, as partial activity of *Hsf1* may still be sufficient to induce thermotolerance. Taken together, these experiments establish that tumor-localized heating by PEG-NRs and other means is sufficient to induce a robust HSR in the tumor endothelium and that pharmacologic agents can effectively counteract HSR induction due to PEG-NR heat exposure.

Figure 5.7. Induction of heat shock response correlates with acquisition of thermotolerance. (a) Schematic of HGL transgenic model. Heat-inducible HSE promoter (A6) regulates expression of GFP and firefly luciferase, permitting visualization of the heat shock response in the tumor stroma including the endothelium. (b) Elevated GFP expression following PEG-NR heating in tumors indicates a robustly induced heat shock response. Tumor vasculature highlighted by intravenous TR-Dextran (TR-Dex). Intrinsic luminescence of PEG-NRs allows for direct detection of nanoparticles by multiphoton microscopy. (c-d) Intravital imaging reveals induction of endothelial heat shock response. Line histogram profiles of normalized GFP and TR-Dex fluorescence intensities at regularly-spaced intervals along vessel after heat exposure (n = 6 equidistant positions along vessel). (e-f) Pharmacological inhibition of heat shock response in PEG-NR heated tumors pre-treated with RHT. Whole animal imaging of HSE-Luciferase (HSE-Luc) expression and quantification in tumors receiving single or double PEG-NR heat exposures in the presence of RHT or control. (n = 6-7 mice per condition, *$P<0.05$, unpaired t-test, two-tailed) Error bars, s.e.m.

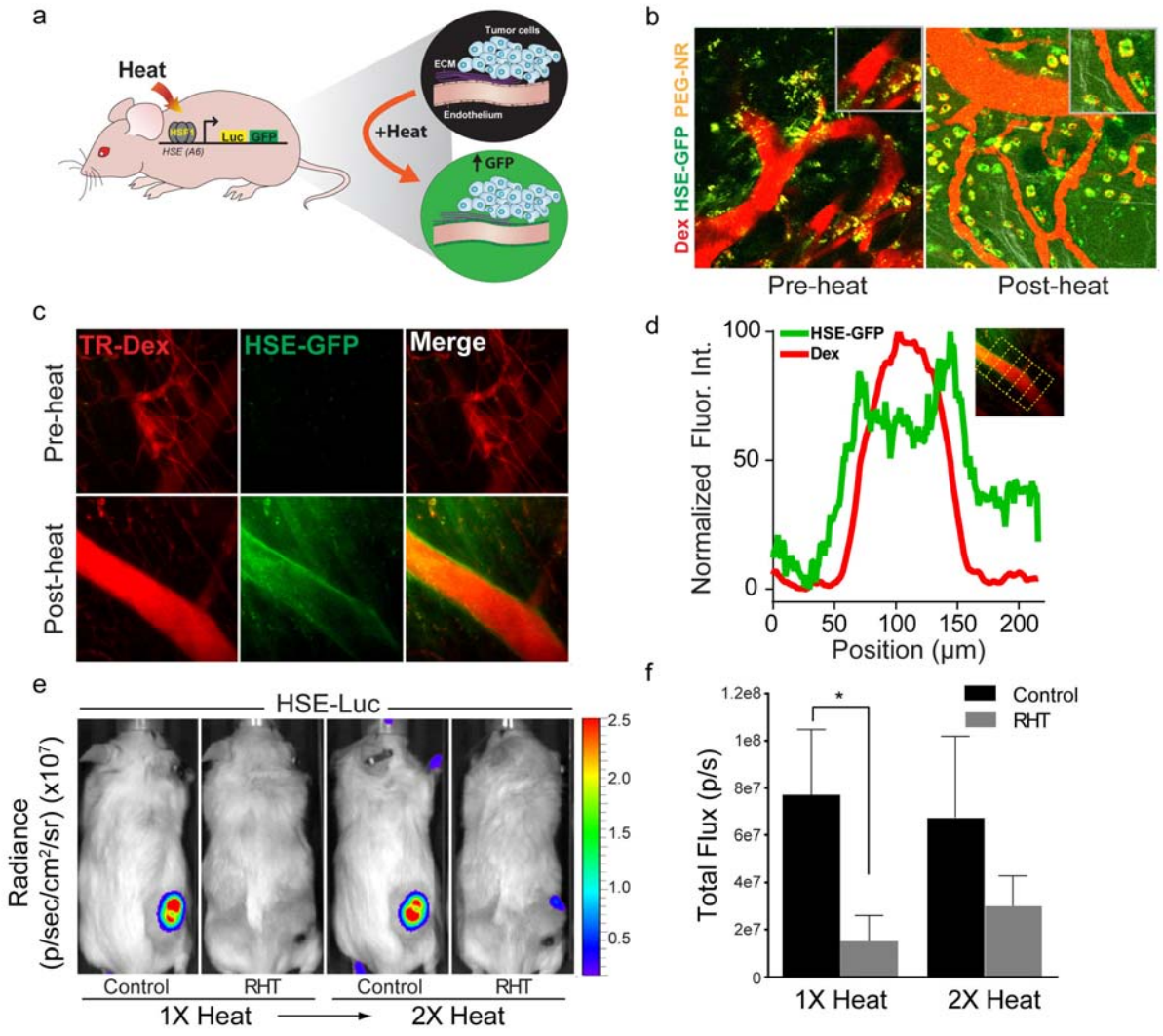

Figure 5.7. (Continued).

5.3.6 Inhibition of heat shock response enhances tumor transport upon re-exposure to heating

Because chemical inhibition with RHT did not enhance tumor transport after re-exposure to PEG-NR heating, we next investigated whether a genetic approach having a more complete and sustained inhibition might enhance tumor transport. Tumor xenografts were established in immunocompromised mice harboring deletions in one or both alleles of *Hsf1*. Tumors received two PEG-NR heat exposures with a delta T of 24 h. As in **Figs. 5.1** – **5.2**, AS750 tumor accumulation was serially measured by *in vivo* fluorescence imaging. (**Fig. 5.8**). Because we observed the greatest thermotolerance with delta T of 24 h in earlier experiments, we selected this as our interval between PEG-NR heat exposures. Among the groups, animals with two functional alleles of *Hsf1* displayed the least enhancement in AS750 accumulation, consistent with the development of thermotolerance observed earlier (**Fig. 5.8**). Interestingly, compared to *Hsf1*+/+ models, mice with one or two deleted *Hsf1* alleles accumulated 2.6- and 6.0-fold greater concentrations of AS750, respectively, during the 24 h period following AS750 administration (**Fig. 5.8**).

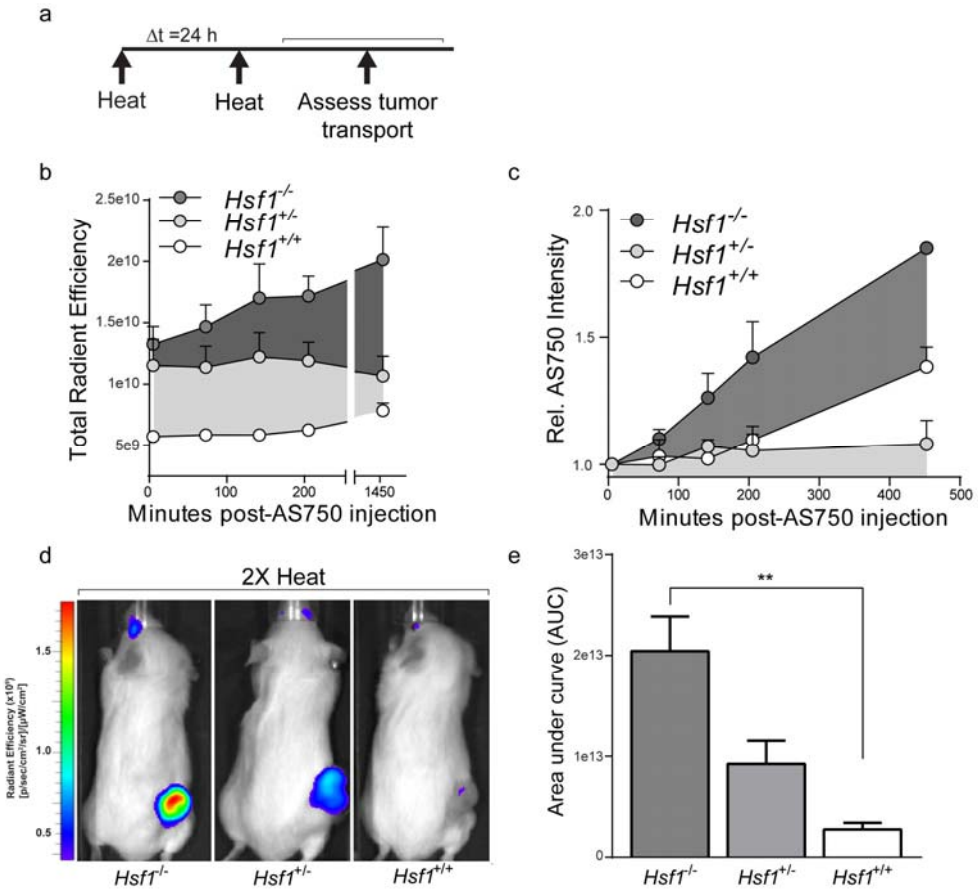

Figure 5.8. Inhibition of heat shock response enhances tumor transport after re-exposure to PEG-NR heating. (a) Ovarian tumor xenograft models either homozygous-null (-/-), heterozygous (+/-), or wild type (+/+) for Heat Shock Factor 1 (*Hsf1*) received an initial PEG-NR heat exposure (heat), an interval delta T of 24 h, and a re-exposure to PEG-NR heating (heat). Tumor transport (AS750 fluorescence) was measured serially for 24 h by *in vivo* fluorescence imaging. (b) Tumor accumulation (AS750) for each genetic background up to 24 h after treatment. (n = 3-6 per group) Error bars, s.e.m. (c) Relative AS750 fluorescence in tumors normalized to initial value after administration. (n = 3-6 per group) Error bars, s.e.m. (d) Representative *in vivo* fluorescence images in animals with *Hsf1*-/-, *Hsf1*+/-, and *Hsf1*+/+ backgrounds receiving double PEG-NR heat exposures. (e) Area under the curve from panel (b) for each genetic background demonstrating enhanced accumulation in *Hsf1*-/- animals. (n = 3-6 per group, **P<0.01, one-way ANOVA and Tukey's post-tests.) Error bars, s.e.m.

At approximately 3 hours after re-exposure to PEG-NR heating, the intratumoral accumulation of AS750 from their baseline values increased by 43.7% in *Hsf1*-/- models, whereas it increased by only 16.3% in *Hsf1*+/+ models. To determine whether tumors with *Hsf1*-

/- stroma were more prone to accumulate AS750 than *Hsf1*+/+ models due to intrinsic, non-vascular structural differences, single exposures of PEG-NR heating were explored in *Hsf1*+/+ and *Hsf1*-/- models. With single exposure to PEG-NR heating, we observed no significant difference in the kinetics and cumulative amount of AS750 that accumulated within *Hsf1*+/+ and *Hsf1*-/- models (**Fig. 5.9**).

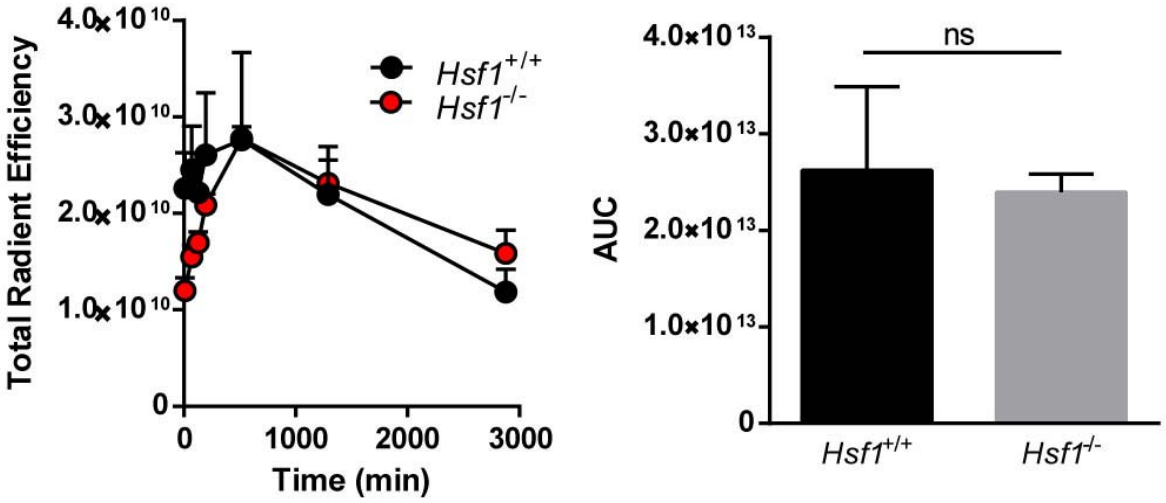

Figure 5.9. Cargo accumulation in tumors with *Hsf1*+/+ and *Hsf1*-/- stroma after single exposure to PEG-NR heating. Similar overall levels and kinetics of accumulation of AS750 were observed for both groups. (n = 3 per group)

Tumor sections revealed moderate *Hsf1* expression in the tumor parenchyma independent of the host's genetic background, but diminished *Hsf1* expression in the tumor stroma, including CD31+ vasculature, of *Hsf1*-/- animals that received PEG-NR heating (**Fig. S9**). Collectively, these data suggest a model in which PEG-NR heating modulates the tumor endothelium in a transient, reversible manner, with consequences for cargo delivery and potentially for overall therapeutic efficacy (**Fig. 5.10**).

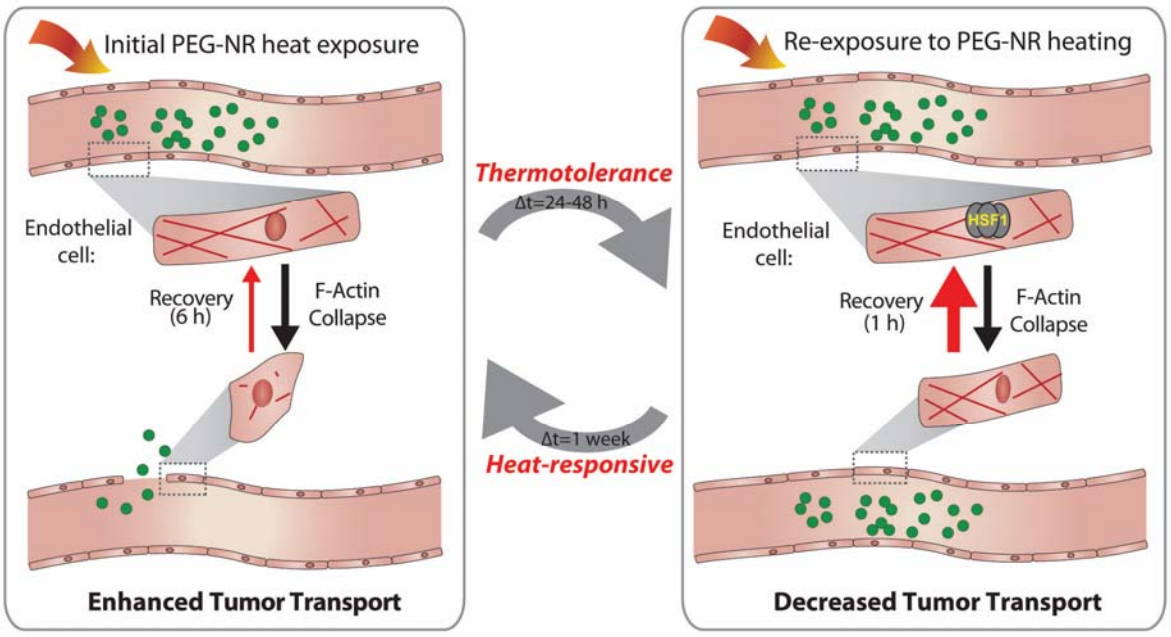

Figure 5.10. Model describing heat-induced tumor transport and development of thermotolerance. An initial exposure to PEG-NR heating alters the endothelial architecture via cytoskeletal remodeling, leading to enhanced tumor transport of nanoparticle cargoes. Over the next 24-48 h, the endothelium develops thermotolerance, mediated by the heat shock response and *Hsf1*, such that re-exposure to PEG-NR heating results in enhanced cytoskeletal recovery and diminished tumor transport. Restoration of heat-responsiveness occurs after approximately 1 week from the initial heat exposure.

5.3.7 Rational design of PEG-NR therapeutic regimens for enhanced tumor transport and efficacy

We next explored the relationship between PEG-NR heating schedules, chemotherapeutic accumulation in tumors, and overall therapeutic efficacy. Our results in tumor models and *in vitro* systems point to specific design criteria that could maximize the efficacy of combination therapeutic approaches involving PEG-NR heating and chemotherapy. In particular, we reasoned that the temporal relationship between heating and administration of therapy may be important, as re-exposure to PEG-NR heating with delta T of 24-48 h dampened the accumulation of cargos within tumors. Doxorubicin-loaded liposomes are a clinically-approved nanoparticle therapy for ovarian cancer, yet their relatively large particle diameter (~100 nm) limits their intratumoral

accumulation. Consistent with previous observations, a single exposure to PEG-NR heating led to a 2.7-fold higher concentration of doxorubicin liposomes in xenograft tumors relative to double heated tumors with delta T of 24 h (**Fig. 5.11**). Given the enhancement in intratumoral therapeutic concentrations, we then investigated the degree to which improved delivery influenced antitumor efficacy and animal survival. Cohorts of mice bearing ovarian tumor xenografts were randomized to receive either single exposures to PEG-NR heating and doxorubicin liposomes (1X Heat+Dox), double exposures to PEG-NR heating (delta T = 24 h) and doxorubicin liposomes administered during re-exposure to heat (2X Heat+Dox), doxorubicin liposomes alone (Dox), or no treatment (NT) (**Fig. 5.11**). We observed the greatest antitumor effect in the 1X Heat+Dox cohorts. While tumor growth was delayed in the 2X Heat+Dox cohort relative to untreated controls, tumors in the 1X Heat+Dox cohort grew significantly slower than those in the 2X Heat+Dox cohort. A similar trend was observed in a Kaplan-Meier survival analysis; untreated and Dox only cohorts survived between 16-20 days after initiation of treatment. While 2X Heat+Dox cohorts survived longer than either of these groups, the 1X Heat+Dox cohorts survived for the longest duration overall and significantly longer than the 2X Heat+Dox cohort (**Fig. 5.11**).

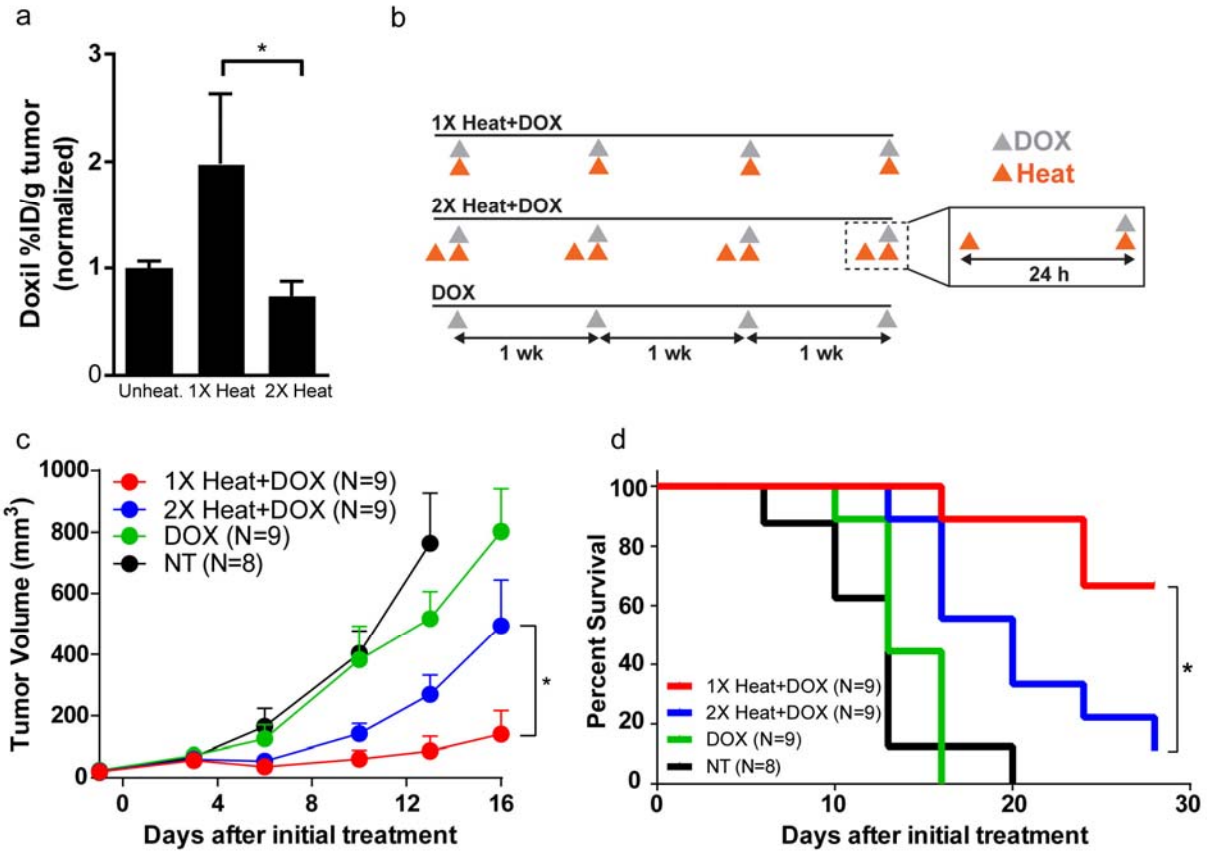

Figure 5.11. Rational design of PEG-NR therapeutic regimens for enhanced drug delivery and efficacy. (a) Accumulation of doxorubicin liposomes in unheated, single heat exposure (1X heat), and re-exposure with delta T of 24 h (2X heat) groups. Bars normalized to unheated controls. (n = 5 mice per group, *P<0.05, Mann-Whitney test.) Error bars, s.e.m. (b) Time courses for each experimental group. Animals received 0, 1, or 2 exposures to PEG-NR heating with doxorubicin liposomes administered with the final heat exposure. Regimens were repeated weekly for the duration of the therapeutic trial period. (c-d) Tumor volume and Kaplan-Meier survival curves (n = 8–9 mice per group, *P<0.05, (c) unpaired t-test, two-tailed, Holm-Sidak method for multiple comparisons and (d) Log-rank Mantel-Cox test) Error bars, s.e.m.

5.4 Conclusions:

Delivering therapeutic compounds to solid tumors with improved efficiency and specificity has long been a major goal within the clinical community. In addition to molecular targeting approaches with monoclonal antibodies or peptides, physical stimuli such as acoustic and electromagnetic energy have garnered interest in part due to the notion that such vascular-

modulating strategies would affect a conserved, genetically-stable component of solid tumors and therefore would be expected to have widespread utility for tumors of diverse tissue origins and genetic backgrounds. In addition, the technologies to generate intratumoral heating have significantly matured during the past decades, with nanomaterials such as gold nanorods offering the promise of more targeted, homogeneous, controlled, and efficient deposition of thermal energy within tumor tissue.[128]

In this work, we characterize the effects of an optically-active, heat-inducible nanomaterial on modulating tumor transport in ovarian tumor models. Because many dosing schedules in the clinic require multiple rounds of administration, we explored the effects of re-exposure to PEG-NR heating on tumor transport. Our data revealed a transient period of impaired tumor transport, which we term thermotolerance, in tumors re-exposed to PEG-NR heating within 24-48 h of an initial heat exposure. Restoration of heat-responsiveness was found to return after approximately 1 week in our model. Previous studies have elucidated a role for endothelial thermotolerance in regulating tumor blood flow, so the data presented here extend the effects of thermotolerance to transvascular transport, a second major barrier of cargo delivery.[278] The interaction between blood flow and transvascular transport in tumors requires further investigation, but it is feasible that these parameters may be functionally coupled in the context of therapeutic delivery.

The well-defined role of the tumor endothelium in regulating cargo transport [56] led us to focus on its role in the thermotolerance that we observed. Using a minimal microfluidic model of the endothelium, we recapitulated the transport behavior observed *in vivo*, providing evidence that the endothelium was sufficient for the development of thermotolerance. Additionally, for

both single and double heat exposures, we linked the structural stability and recovery kinetics of the endothelium to the dynamics of the F-actin cytoskeleton. Finally, the endothelial adaptations suggested by these data were verified by intravital imaging studies that measured local transvascular transport within tumors. By observing similar heat-responsive kinetics at multiple biological scales – from individual cells to vessel models to the *in vivo* tumor environment – we suggest that subcellular processes in endothelial cells, particularly related to cytoskeletal stability, explain in part the macroscopic effects on tumor transport.

While we focused on transvascular transport, PEG-NR-mediated heating almost certainly influences parameters related to overall blood flow or interstitial diffusion, two of the additional barriers to drug delivery in solid tumors. Indeed, studies in several models have demonstrated that increasing intratumoral temperature in the range of 41-43°C can modulate blood flow in a site- and tumor model-dependent manner.[73, 279] Modifications to blood flow or diffusion upon re-exposure to PEG-NR heating were not investigated here, but these may be relevant contributors to the effect described. For instance, because the heating regime explored is close to the blood coagulation threshold, local vascular damage, particularly in regions containing higher concentrations of PEG-NRs, may play a partial role in the initial development of transport resistance. In our model, however, we observed *via* intravital microscopy that tumor vasculature exposed to single or double exposures to PEG-NR heating remained functionally perfused with fluorescent tracer dyes for the duration of the experiments.

While the development of thermotolerance is associated with induction of the HSR, less is known about the role of the HSR in governing endothelial properties in the context of cargo delivery. In this study, we demonstrated a role for the heat shock response by observing that

induction of the HSR in the endothelium temporally correlated with the development of thermotolerance. Furthermore, genetic deletion of *Hsf1*, the master regulator of the mammalian HSR, in the tumor vasculature was associated with improved intratumoral cargo accumulation following re-exposure to PEG-NR heating.

Our focus in this study on the endothelial cell-intrinsic adaptations to heat exposure does not preclude other known mechanisms of vascular permeability from remaining operative in our model. In addition to thermally-induced cytoskeleton collapse, endothelial contraction in venules occurs in the presence of vasoactive agents such as histamine and bradykinin, as well as cytokines including tumor necrosis factor (TNF) and interferon-γ.[76]Mast cell activation in tumors upon PEG-NR heating may induce local release of histamine, which in turn may contribute to the early phases (< 1 hour) of enhanced nanoparticle delivery observed in our study. Additionally, direct endothelial injury, in regions with high concentrations of PEG-NRs for example, may induce an immediate sustained response in all tumor vessels lasting for several hours following PEG-NR heat exposure. Finally, vascular endothelial growth factor (VEGF) levels can influence the degree of vascular permeability in tumors[255], but we did not observe variations in VEGF between different heating regimens in this study. The kinetics of nanoparticle accumulation, including a 6 hour period of enhanced accumulation after heat exposure, suggest that PEG-NR-mediated heat exposure may be acting in concert with additional chemical mediators to promote vasodilation and increased vascular permeability in tumors.

Lastly, building upon the cargo accumulation and structural data obtained from our *in vitro* and *in vivo* models, we could rationally design therapeutic dosing schedules involving PEG-NRs and chemotherapeutic agents. In particular, we observed that delivery of doxorubicin

liposomes was impaired after allowing thermotolerance to develop in tumors whereas therapeutic delivery was improved after single exposure to PEG-NR heating. In addition to its effect on the endothelium, heat may directly affect the tumor cells by chemosensitization mechanisms.[278] It is interesting to note that despite comparable therapeutic concentrations in the unheated and re-exposure to PEG-NR heating groups, animals receiving doxorubicin liposomes in combination with PEG-NR heating demonstrated slower tumor growth rates, which could represent a synergistic interaction between heating and chemotherapy occurring within the parenchymal tumor cells. Nevertheless, these effects on tumor transport contributed to a stronger antitumor effect and improved overall survival in cohorts receiving weekly doxorubicin liposomes with single exposures to PEG-NR heating in comparison to cohorts receiving doxorubicin liposomes during re-exposure to PEG-NR heating.

The biological mechanism linking the heat shock response to endothelial stability in the tumor microenvironment is intriguing, as previous reports have identified proteins regulated by *Hsf1*, such as heat shock protein *Hsp27*, as cytoskeletal stabilizers of F-actin stress fibers during thermal stress.[117-119] These studies revealed that cell lines with elevated expression of *Hsp27* had increased stability of stress fibers during multiple heat exposures. Cytoskeletal thermotolerance persisted for several days and contributed to the maintenance of both normal morphology and viability. Future studies may illuminate potential roles of *Hsp27* and other components of the HSR in modulating transport across the endothelium.

In summary, our findings point to a potential therapeutic consequence at the macroscale of an underlying endothelial cell adaptation to heating. Pharmacological strategies to render endothelial cells more heat-responsive while within the thermotolerance window would create

new opportunities to deliver chemotherapies more frequently and with improved efficacy. As nanomaterial-inspired approaches to enhance tumor transport in solid tumors are considered, this work anticipates one possible clinical challenge and suggests methods for achieving a maximal therapeutic response through rationally designed dosing schedules. Future studies investigating the mechanistic links between endothelial adaptations and therapeutic cargo accumulation in solid tumors will provide additional avenues for introducing nanoparticle-mediated heating into clinical practice.

5.5 Acknowledgements:

The authors would like to acknowledge H. Fleming for her helpful suggestions on the manuscript. The authors also acknowledge Salil Desai for assistance with construction of the laser beam splitter used for this work. The authors acknowledge Scott Malstrom from the KI ATWAI Core Facility, Dr. Rod Bronson, Mike Brown, Denise Crowley, and Kathleen Cormier from the KI Histology Core Facility, and animal technician Melissa Duquette for assisting with animal studies. A.F.B. acknowledges support from the NIH/Medical Scientist Training Program and Biophysics Program at Harvard University. S.B. is an HHMI investigator.

5.6 Author Contributions:

Authors: Alexander F. Bagley, Ruthie Scherz-Shouval, Peter A. Galie, Angela Q. Zhang, Jeff Wyckoff, Luke Whitesell, Christopher S. Chen, Susan Lindquist, and Sangeeta N. Bhatia

A.F.B., R.S.S., and S.N.B. conceived the idea and wrote the manuscript. P.A.G. performed and analyzed all data from microfluidic permeability assays. J.W. acquired all intravital imaging studies and assisted with data processing and interpretation. A.Q.Z. performed endothelial cytoskeletal assays and assisted with longitudinal survival studies. L.W., C.S.C., and S.L. edited the manuscript and provided conceptual advice. A.F.B. and R.S.S. performed all other experiments and data analysis.

CHAPTER 6. SUMMARY AND CONCLUSIONS

6.0 Non-Invasive Imaging with Nanomaterials

Optically-active nanomaterials offer tremendous promise for enhancing modern therapeutic and diagnostic approaches in oncology. This thesis demonstrates several applications of such nanomaterials in the context of ovarian cancer, but one could envision adaptations of these methods being broadly applicable to other solid malignancies as well. For example, our focus on using molecularly targeted single-walled carbon nanotubes (SWNTs) to guide cytoreduction of ovarian tumors could be extended to other disseminated peritoneal malignancies including colorectal and appendiceal adenocarcinomas, peritoneal mesothelioma, and fallopian tubal cancers. To advance this technology towards clinical implementation, a platform capable of providing real-time feedback to surgeons in an intraoperative setting would be desirable. Similar platforms have been described in human clinical trials for imaging probes in the visible spectrum.[27] The incorporation of tomographic imaging capabilities could further improve the sensitivity and accuracy of tumor detection, thereby allowing surgeons to more readily locate tumors during cytoreductive procedures.

Efforts to enhance the instrumentation could be complemented by modifications to the imaging probe itself. Concerns about the biocompatibility and potential toxicities of both SWNTs and M13 bacteriophage have been raised. For SWNTs, several pre-clinical studies investigating the long-term fate of these nanomaterials have shed light on the potential issues that may arise should SWNTs be explored for human indications.[31, 211] Despite their retention in the liver and spleen for up to five months, no overt signs of systemic toxicity were observed in these studies, based on blood chemistry, histology, overall growth, and behavioral patterns.[211]

In our work, the use of M13 bacteriophage served at least three important roles: stabilization of SWNTs; targeting to ovarian tumors via expression of SPARC-binding peptide (SBP); and intraperitoneal retention due to a relatively large hydrodynamic radius. However, alternative strategies using non-biological scaffolds or nanomaterials may prove more feasible for clinical translation.

As the intra- and inter-patient molecular heterogeneity of cancer is more fully cataloged by genomic and proteomic approaches, the ability to characterize the full compendium of biomarkers available for molecularly-targeted imaging will be essential for developing probes unique to a particular patient or even particular tumors within an individual patient. Here, the potential value of using a genetically-encodable scaffold like M13 becomes readily apparent. In the future, we might anticipate a clinical protocol as follows: a patient recently diagnosed with advanced ovarian cancer has a biopsy performed on one or more tumors; a genomic analysis reveals the unique biomarkers enriched in this patient's tumors; over the following week, using a genetically-encodable scaffold such as M13, one could then rapidly prototype and construct a unique tumor-targeted imaging probe by expressing patient-specific peptide ligands; one could then investigate the utility of such tailored imaging probes compared to generic probes for both diagnostic and intraoperative applications. As the experience with personalized molecular therapies has demonstrated, the extent of tumor heterogeneity between patients and within a single patient will determine how feasible such personalized imaging approaches will be in the clinic.

6.1 Tumor-Localized Heating with Nanomaterials

In addition to applications in diagnostic and intraoperative imaging, nanomaterials have been developed for an increasing number of therapeutic applications as well. Much research has gone into understanding the biological and physiological effects of heating on tumors and the tumor microenvironment, and thus the scientific rationale for incorporating heat-generating nanomaterials into existing cancer therapeutic protocols is encouraging. Ongoing efforts to understand the multifaceted role of the heat shock response in malignant cells continues to reveal how these cellular pathways facilitate survival and proliferation, as well as identify promising therapeutic targets.[116, 121] However, technological barriers involved in establishing localized heating in distributed, disease-specific sites at the anatomic scale of human patients has limited the utility of heating approaches in clinical practice. Focal radiofrequency and microwave ablation of primary and metastatic tumors in the liver are performed routinely in the clinic, but these procedures are often palliative rather than curative in effect.[280-282] Conversely, intraperitoneal heated chemotherapy represents a diffuse heating strategy, but is limited by off-target toxicities, in part due to temperature-sensitive tissues such as the intestines. Tumor-localizing nanomaterials including gold nanorods and novel NIR light delivery systems therefore provide an attractive approach to address this challenge.

While our work highlights the feasibility of combining optically-active nanomaterials with implanted NIR sources, several important technological and clinical hurdles remain for its effective translation to humans. On the technological front, next-generation devices capable of providing deeper and more dispersed delivery of NIR energy at spatial scales relevant to human anatomy, perhaps by incorporating features enabling flexible conformity to bodily contours, would help advance this concept closer to the clinic. Secondly, the efficacy of such methods compared to or in combination with current surgical and chemotherapeutic approaches remains

to be established. In particular, the limited accumulation of gold nanorods in residual tumors where the EPR effect may be diminished or absent may represent a potential hurdle for demonstrating superior clinical efficacy. Delivery strategies that target non-vascular components of such early-stage, pre-angiogenic lesions, such as tumor-specific extracellular matrix (ECM) proteins or tumor cell surface antigens, may provide alternative approaches for delivering gold nanorods to residual tumors and micrometastases. The non-specific accumulation of gold nanorods in the liver and spleen poses an added challenge for tumor-specific heating in the peritoneal cavity; devices capable of providing customizable and programmable NIR emission patterns to avoid off-target heating effects in these nanoparticle-concentrating tissues may help broaden the therapeutic utility.

Lastly, while we have focused on oncology applications in this work, optically-active nanomaterials such as plasmonic nanoparticles will likely have broader applications in medicine given their chemical stability, biocompatibility, and functional tuning to specific electromagnetic stimuli. For instance, the localized delivery of thermal energy using plasmonic nanomaterials may have dermatologic applications in managing common chronic ailments such as acne vulgaris. In addition, angiogenic vasculature has been documented not only in solid tumors, but in numerous inflammatory autoimmune disorders including psoriasis, rheumatoid arthritis, and inflammatory bowel disease. Should thermal exposure prove beneficial for treatment or alleviation of symptoms in any of these conditions, the angiogenic vasculature in disease-associated lesions could provide a route for plasmonic nanomaterials to accumulate and exert beneficial functions.

6.2 Enhancing Therapeutic Delivery with Nanomaterials

Nanomaterial-mediated heating of tumors in a specific and localized fashion is particularly relevant to applications of therapeutic delivery. The structural and physiological features of many tumors, including heterogeneous blood flow, tortuous vasculature, and dense stromal collagen and glycosaminoglycans, contributes to non-uniform and limited delivery of therapeutic compounds, which in turn contributes to incomplete tumor responses, the evolution of drug resistance, and disease progression. The development of nanocarrier formulations such as polyethylene glycol-coated liposomes to minimize renal excretion and clearance by the reticuloendothelial system has improved their pharmacokinetic profiles and therapeutic accumulation within tumors. However, the transport of these nanocarriers across the endothelium represents a significant bottleneck for efficient tumor penetration. Therefore, thermal perturbation to the tumor endothelium using optically-active nanomaterials represents a complementary strategy for achieving optimal responses with current chemotherapeutic agents.

Heating must be viewed as a multifaceted modifier of the tumor microenvironment. While the final section of this thesis focused on the endothelial response to heating, approaches using gold nanorods likely influence diverse processes including immune cell trafficking, inflammation, cytokine signaling, interstitial pressure, blood flow, and direct effects on tumor cells. These processes can promote vascular changes and modify therapeutic transport properties within tumors independent of endothelial modifications. Going forward, it will be important to gain a better understanding of the effects of gold nanorod-mediated heating on these processes as well. For instance, we observed significant accumulation of both gold nanorods and therapeutic surrogates within perivascular phagocytic cells lining the tumor endothelium. If these cells are effectively scavenging nanomaterials and therapeutic agents that manage to cross the endothelium, it suggests an additional barrier for therapies to reach tumor cells. In addition, the

‘retention’ component of the EPR effect is commonly ascribed to defective or obstructed lymphatic channels; our results suggest that particle scavenging by perivascular phagocytes provides an alternative, complementary explanation for the observed retention of a variety of cargoes in tumors. Selective ablation of these cell types, perhaps by taking advantage of the natural accumulation of gold nanorods within this population of cells, prior to administration of chemotherapy may improve the overall distribution of therapy within tumors.

One important conclusion from this thesis is that the temporal patterns between heating and therapeutic administration are directly relevant to the overall therapeutic efficacy. Defining the kinetics and temporal windows in which transport is enhanced by heating allowed for the rational design of therapeutic regimens. The observation of a functional resistance to heat-based transport across the endothelium can be linked with the development of thermotolerance and cytoskeletal stability within endothelial cells. However, the delayed tumor growth and improved survival rates we observe in single PEG-NR heat exposure versus heat re-exposures alongside chemotherapeutic cargo may be due to both these endothelial adaptations as well as thermotolerance induced in the tumor cells themselves. It will be important in future studies to sort out the relative contributions of these vascular and tumor adaptations, as this knowledge would suggest the applicability of nanomaterial-based heating regimens for other tumor types, sites of disease, and therapeutic cargoes.

6.3 Nanomaterials and the Future of Medicine

From the first documented cases in ancient civilizations to the modern era, great progress has been made in understanding the molecular underpinnings of cancer. This knowledge has in turn led to the discovery of new therapies, diagnostic tools, and surgical approaches to curtail

disease progression and in some cases provide cures for patients. However, modern medicine is far from eliminating cancer in the same way that vaccination has eradicated poliovirus or smallpox in the developed world. While the reasons for this are varied and complex, one recurring theme is that despite having an arsenal of highly potent and toxic chemotherapeutics, the selective delivery of such agents is fundamentally limited by the structural composition of solid tumors. These tumor structures – blood vessels, collagen fibers, immune cells, lymphatics, and more – are dynamic and capable of modulation for therapeutic benefit. Nanomaterials are providing an unprecedented ability to interface with the human body at the multiple scales of its functional elements – from vessels to cells to organelles to proteins and nucleotides – for far-reaching applications ranging from diagnostic imaging to therapeutic drug delivery. While still the early days, there is considerable cause for hope that 'going small' with nanomaterials will usher in the next generation of therapeutic advances, enabling cancer patients to live longer and healthier lives.

SUPPLEMENTAL FIGURES

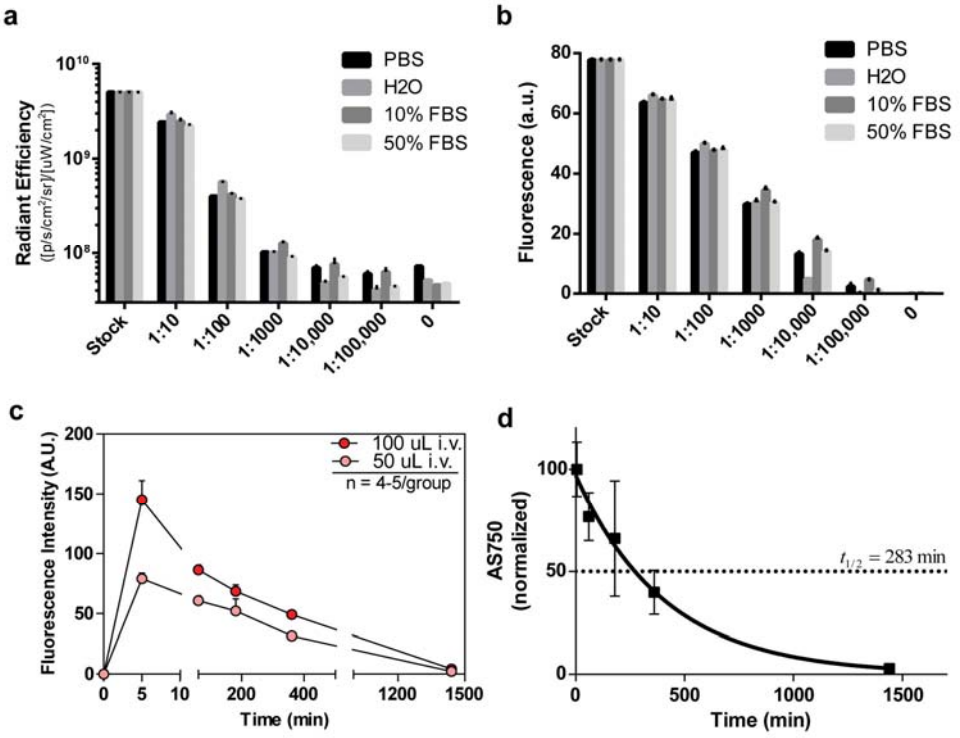

Figure S1. Stability and pharmacokinetics of AS750 nanoparticles. Near-infrared (NIR) fluorescence is maintained in a dose-dependent manner in serial dilutions of AS750 incubated with PBS, water, and saline solutions containing 10% FBS and 50% FBS on (a) IVIS Spectrum and (b) LICOR Odyssey NIR imaging platforms. All measurements performed in triplicate. (c-d) Concentration of AS750 in circulating blood for 24 hours following intravenous administration of 50 or 100 µL AS750. Normalized data for 50 uL AS750 shown in (d) and the circulation half-life is 283 minutes (for 50 µL AS750). (n = 4-5 animals per group)

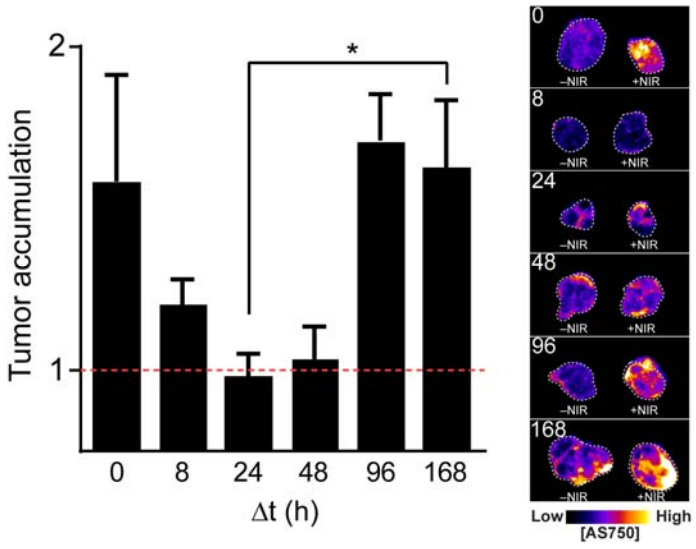

Figure S2. Tumor accumulation of AS750 after PEG-NR heat exposure with varying delta T. Tumor transport (ratio of AS750 for heated versus unheated tumors) and representative images of explanted tumors after PEG-NR heating with delta T ranging between 0 h to 1 week. (n = 4-9 per group from two independent experiments, *P<0.05, one-way ANOVA and Tukey's post-tests.) Error bars, s.e.m.

a

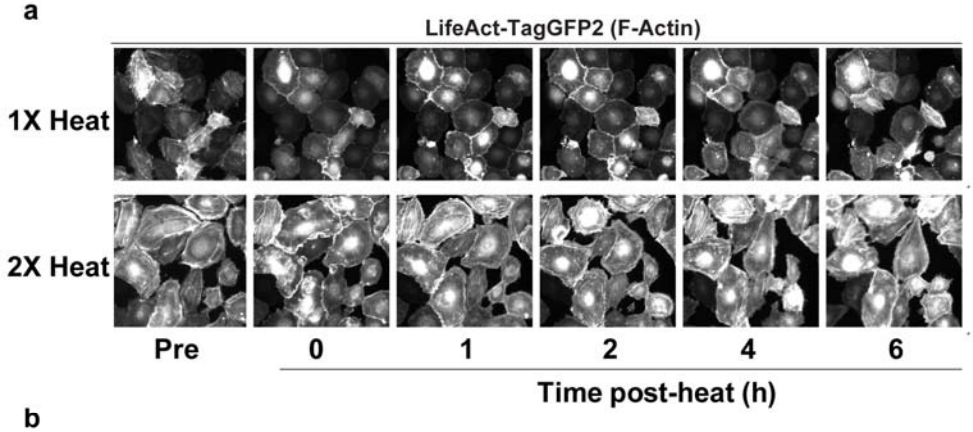

b

Condition	Time Post heat (h)	Fields Examined	Total Cells	Filament-Positive Cells (Mean ± SD)	Total Cells (Mean ± SD)	% Filament-Positive (Mean ± SD)
1X	Pre	6	1072	111.83 ± 15.61	178.67 ± 21.65	62.92 ± 8.14
	0	6	1107	7.83 ± 6.18	184.50 ± 22.47	4.08 ± 3.12
	1	6	1213	6.00 ± 4.20	202.17 ± 10.93	2.97 ± 2.13
	2	6	1172	13.83 ± 8.06	195.33 ± 15.49	7.15 ± 4.45
	4	6	1123	42.67 ± 20.18	187.17 ± 13.32	22.95 ± 11.09
	6	6	1154	57.17 ± 40.18	192.33 ± 17.43	30.39 ± 21.81
2X	Pre	8	1117	101.25 ± 21.40	139.63 ± 13.21	72.62 ± 13.92
	0	8	1161	24.25 ± 8.48	145.13 ± 16.31	16.95 ± 6.22
	1	8	1150	90.88 ± 14.02	143.75 ± 13.71	63.61 ± 10.65
	2	8	1127	106.13 ± 10.86	140.88 ± 15.67	75.87 ± 9.08
	4	8	1099	99.75 ± 16.13	137.38 ± 12.66	72.38 ± 8.27
	6	8	1088	87.00 ± 12.46	136.00 ± 14.79	64.29 ± 9.22

Figure S3. Endothelial cell F-Actin dynamics during heat exposure and recovery. (a) Representative images of endothelial F-actin filaments prior to heat exposure and 0 – 6 hours following heating for the single exposure (1X) and re-exposure (2X) groups. Loss of filament structure after heat exposure was observed in both single heat exposure and re-exposure groups, with more efficient recovery of filament structure in the re-exposure group. The same fields were imaged at each time point to enable measurements of actin dynamics in the same cells over time. (b) Quantification of endothelial cells and F-actin structure. A total of 13,583 individual cell measurements were scored for this analysis.

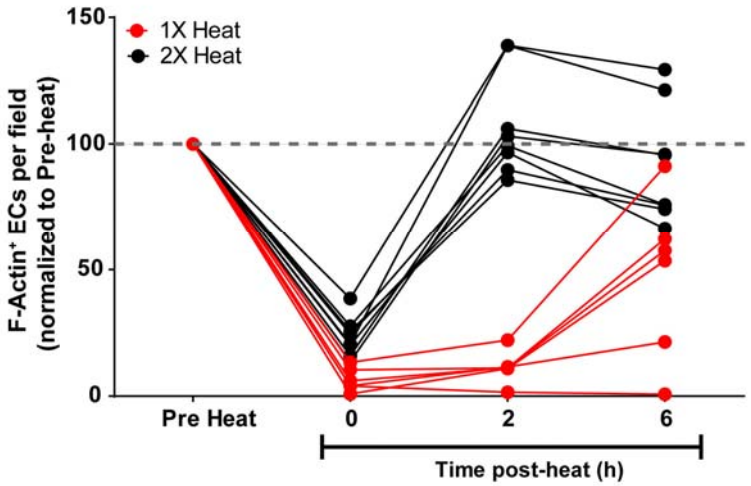

Figure S4. Normalized F-Actin recovery in endothelial cells for single heat exposure and re-exposure to heat. Each tracing represents the kinetics of cytoskeletal recovery for an individual field of view over time, normalized to its initial percentage of F-Actin+ cells prior to heat exposure. For re-heated cells (2X heat), the Pre-heat indicates the period between the first and second heat exposure. (n = 6-8 fields of view per condition)

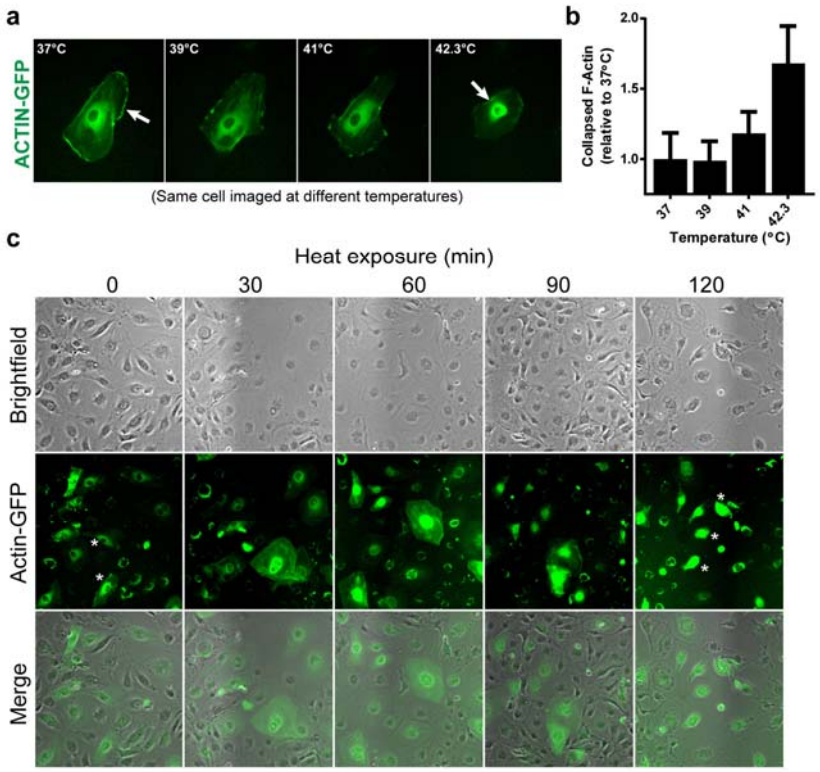

Figure S5. Temperature- and time-dependent collapse of the endothelial F-Actin cytoskeleton. (a) Cells were transfected with CellLight Actin-GFP to visualize actin filaments in living endothelial cells. Actin-GFP was present throughout the cell, with regions of concentrated signal along the cell borders consistent with cortical actin and focal adhesions (white arrow in 37ºC). Cells were subjected to a temperature ramp spanning 37ºC–42.3ºC. Between 41 and 42.3C the distributed Actin-GFP relocalized to perinuclear regions (white arrow in 42.3ºC) with a corresponding retraction of the cell membrane morphology was observed. (b) Quantification of cells with collapsed, perinuclear F-Actin cytoskeleton pattern, normalized to cells at 37ºC. (n = 3,220 cells total) (c) Representative images of time-dependent cytoskeletal collapse during a 120 minute heat exposure.

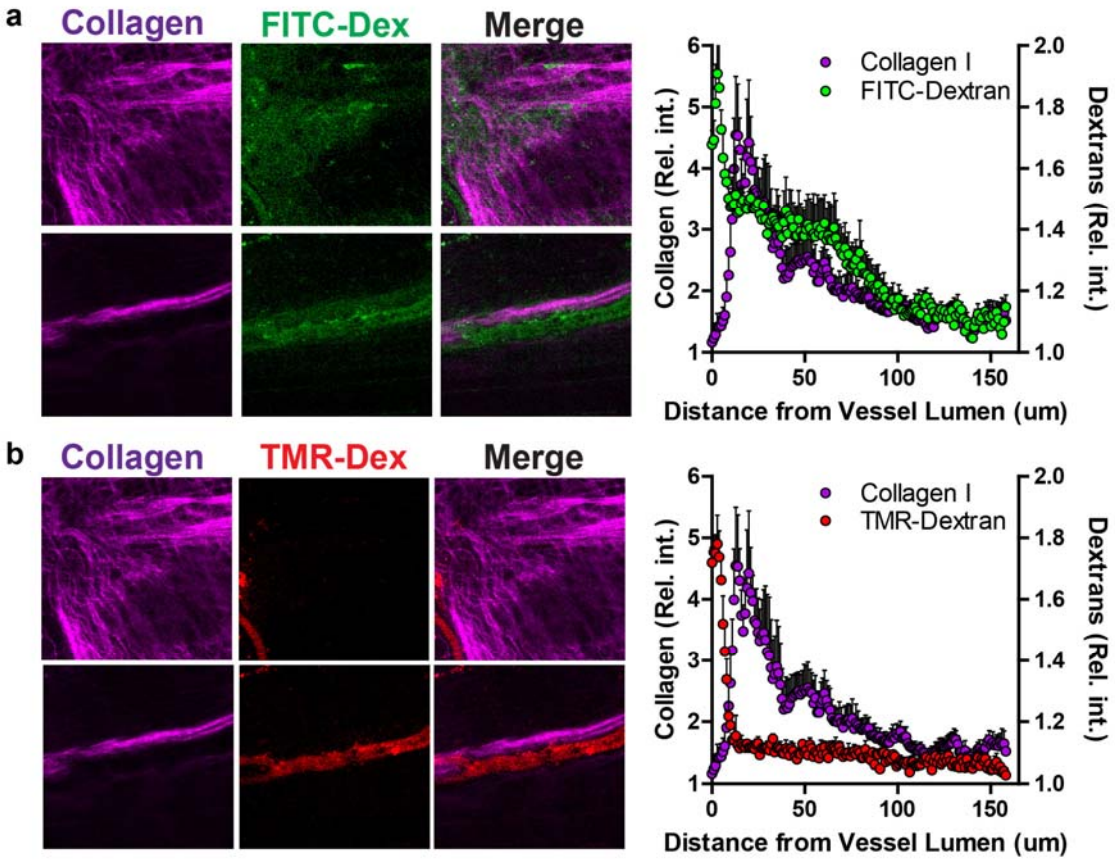

Figure S6. Size-dependent macromolecular extravasation from the unheated vasculature. Intravenous co-administration of (a) 10 kDa FITC-Dextran and (b) 2,000 kDa TMR-Dextran revealed greater extravasation of the smaller molecular-weight compound, which appeared to become sequestered in regions with dense collagen fibers as shown by the correspondence in relative intensities on line histograms computed for collagen and FITC-Dextran. Larger molecular weight TMR-Dextran was retained within the vessel lumen in the same field of view, revealing the size-dependence of extravasation in our model.

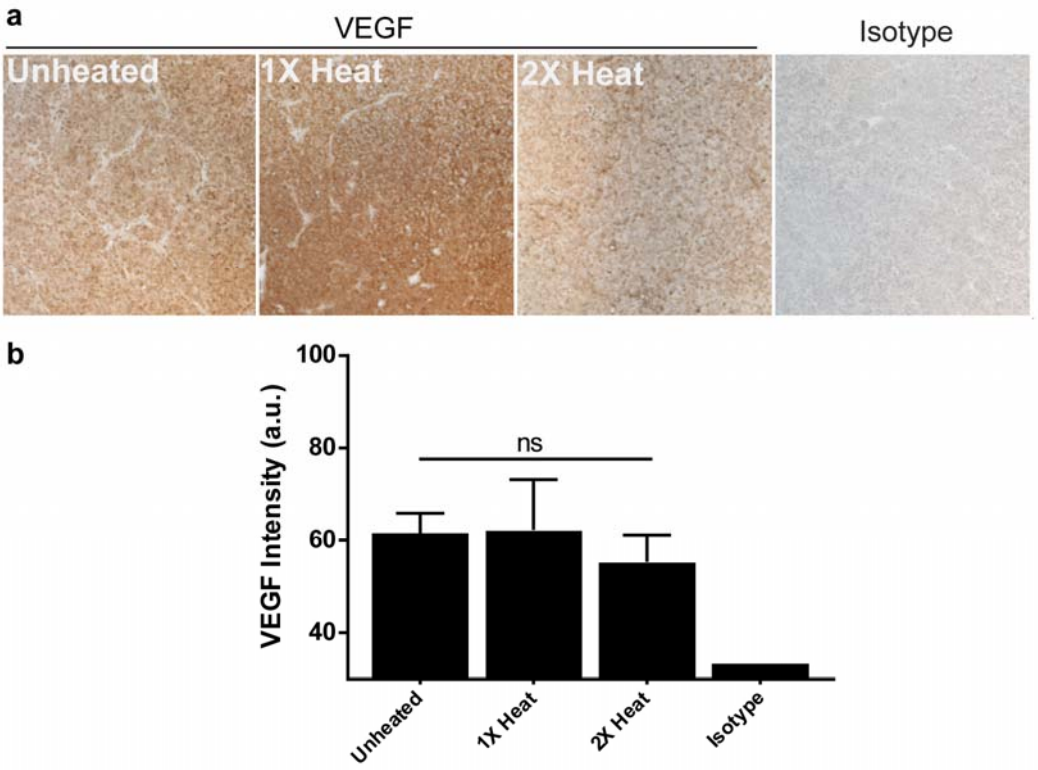

Figure S7. Vascular endothelial growth factor (VEGF) expression in PEG-NR heated tumors. (a) Representative images illustrating VEGF expression in tumors either unheated or receiving a single exposure or re-exposure to PEG-NR heating. (b) Mean immunohistochemical staining intensity of large scan images of the tumor cross-sectional area. No significant differences were observed in VEGF intensity between the unheated, single, and repeat PEG-NR heated groups. (n = 4-6 tumors per group)

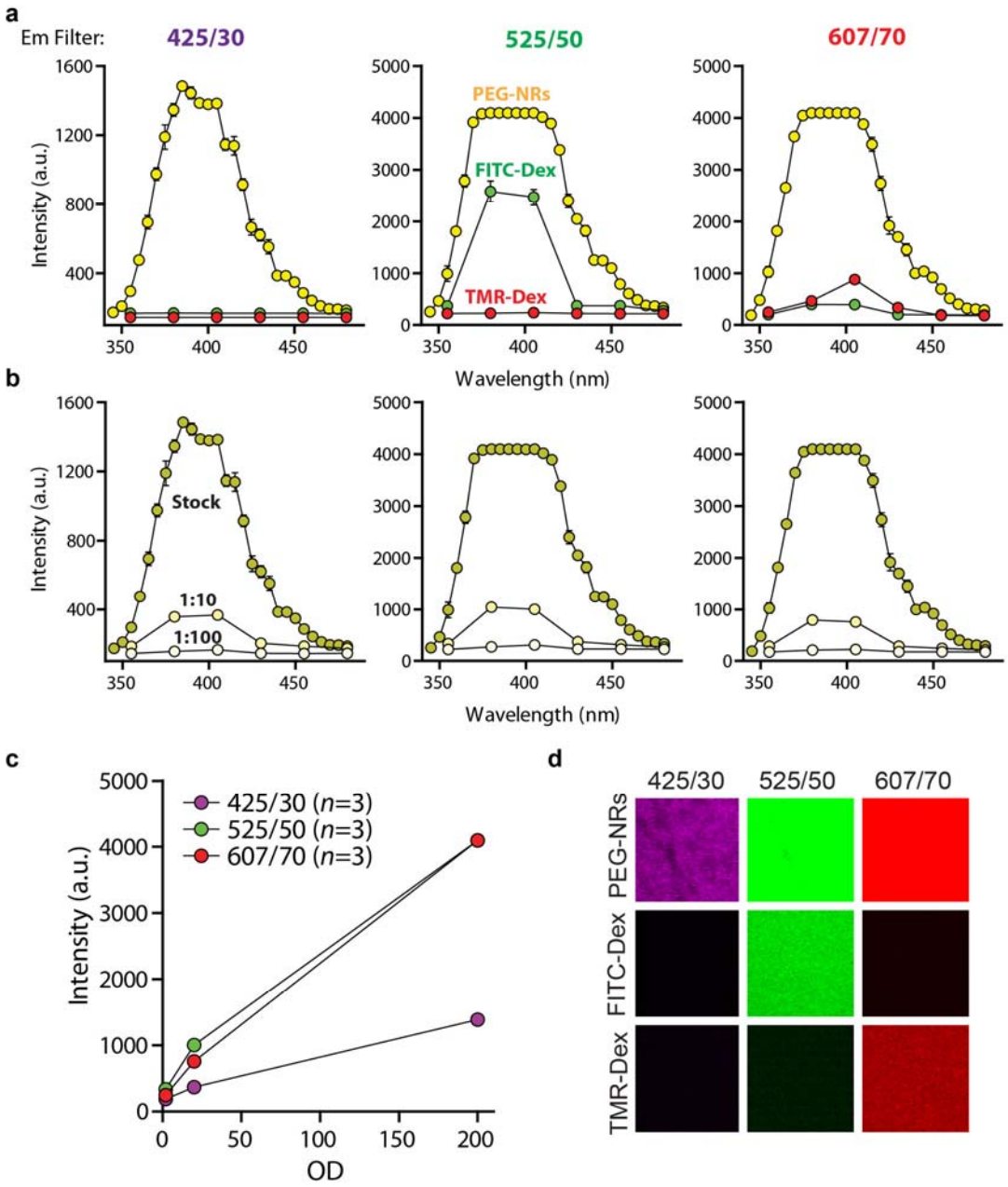

Figure S8. Visualizing PEG-NRs in the tumor microenvironment using multiphoton microscopy. (a) Fluorescence/luminescence intensities of PEG-NRs (yellow), FITC-Dextran (green), and TMR-Dextran (red) with three separate emission filter channels (425/30, 525/50, and 607/70 nm). An intense signal with a peak at ~400nm was observed for PEG-NRs in all three channels. FITC-Dextran was detected with the 525/50 filter and TMR-Dextran with the 607/70 only. (b) Dose-dependent luminescence of PEG-NRs in each channel using 1:10 and 1:100 dilutions from stock PEG-NR concentration (OD: 200). (c) Plot of peak intensity versus PEG-NR optical density with each emission filter. (d) Images of PEG-NRs, FITC-Dextran, and TMR-Dextran acquired by multiphoton microscopy.

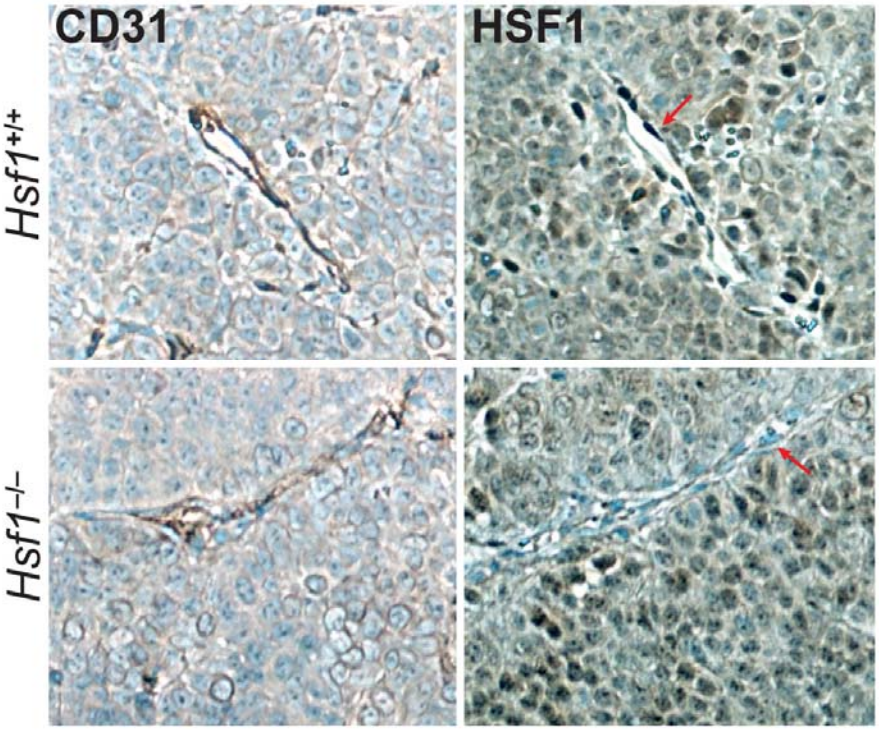

Figure S9. *Hsf*1 expression in tumor-associated vasculature following PEG-NR heating. Immunohistochemical staining of serial tissue sections for PECAM-1 (CD31) to label endothelial vessels and *Hsf*1, counterstained with H&E. CD31-positive endothelium in *Hsf1*+/+ models displays a strong nuclear *Hsf1* staining pattern (red arrow), consistent with *Hsf1* activation and translocation to the nucleus with PEG-NR heating. CD31-positive endothelium in *Hsf1*-/- models displayed no observable *Hsf1* staining pattern (red arrow). In both models, positive *Hsf1* staining was detected in tumor parenchymal cells.

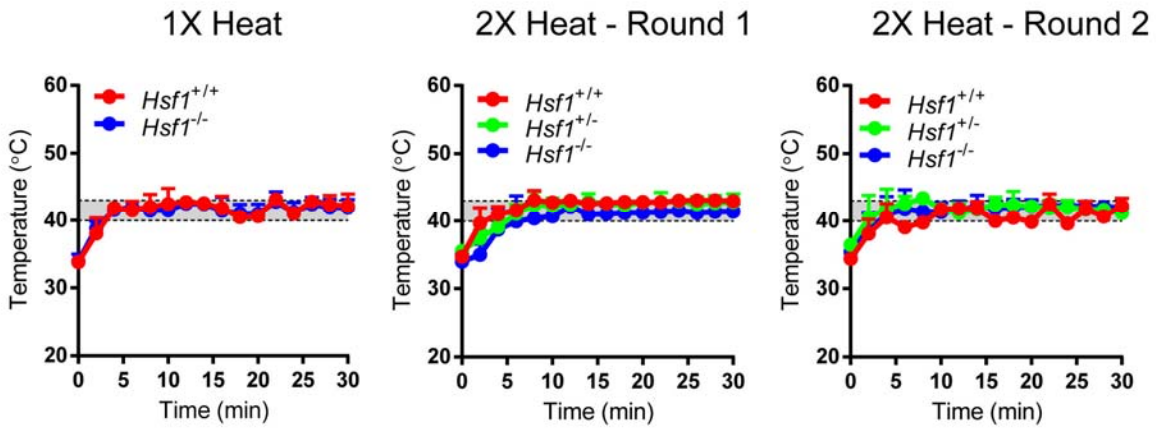

Figure 5.18. Temperature profiles for tumors in stromal *Hsf1* accumulation study. Tumors receiving PEG-NR heating from each group (*Hsf1*+/+, *Hsf1*+/-, and *Hsf1*-/-) displayed similar temperature profiles during the 30 minute PEG-NR heating exposures. (2X Heat: n = 4-6 per group; 1X Heat: n = 3 per group) Error bars, s.e.m.

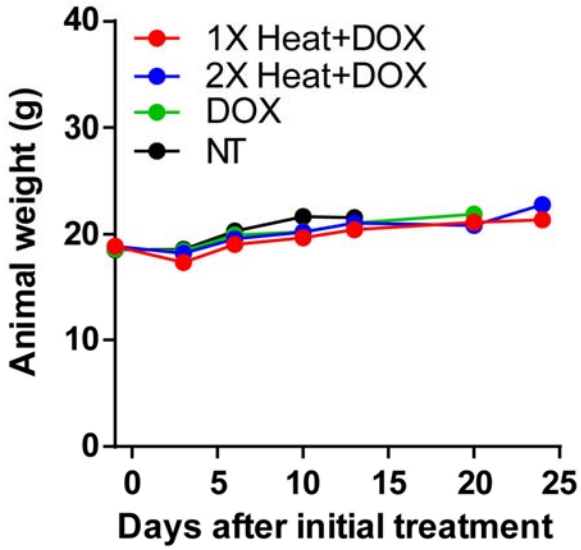

Figure S11. Animal weights during PEG-NR and doxorubicin liposome therapeutic trial. Weights remained consistent among treatment groups during the trial period. (n = 8-9 per group) Error bars, s.e.m.

BIBLIOGRAPHY

1. Siegel, R., et al., *Cancer statistics, 2014.* CA Cancer J Clin, 2014. **64**(1): p. 9-29.

2. Cannistra, S.A., *Cancer of the ovary.* N Engl J Med, 2004. **351**(24): p. 2519-29.

3. Struewing, J.P., et al., *The risk of cancer associated with specific mutations of BRCA1 and BRCA2 among Ashkenazi Jews.* N Engl J Med, 1997. **336**(20): p. 1401-8.

4. Carlson, K.J., S.J. Skates, and D.E. Singer, *Screening for ovarian cancer.* Ann Intern Med, 1994. **121**(2): p. 124-32.

5. Armstrong, D.K., et al., *Intraperitoneal cisplatin and paclitaxel in ovarian cancer.* N Engl J Med, 2006. **354**(1): p. 34-43.

6. Vaughan, S., et al., *Rethinking ovarian cancer: recommendations for improving outcomes.* Nat Rev Cancer, 2011. **11**(10): p. 719-25.

7. Whittemore, A.S., *Characteristics relating to ovarian cancer risk: implications for prevention and detection.* Gynecol Oncol, 1994. **55**(3 Pt 2): p. S15-9.

8. Bristow, R.E., et al., *Survival effect of maximal cytoreductive surgery for advanced ovarian carcinoma during the platinum era: a meta-analysis.* J Clin Oncol, 2002. **20**(5): p. 1248-59.

9. Bristow, R.E., et al., *Survival impact of surgical cytoreduction in stage IV epithelial ovarian cancer.* Gynecol Oncol, 1999. **72**(3): p. 278-87.

10. Bristow, R.E., I. Puri, and D.S. Chi, *Cytoreductive surgery for recurrent ovarian cancer: A meta-analysis.* Gynecologic Oncology, 2009. **112**(1): p. 265-274.

11. Hacker, N.F., et al., *Primary cytoreductive surgery for epithelial ovarian cancer.* Obstet Gynecol, 1983. **61**(4): p. 413-20.

12. Hainsworth, J.D., et al., *Advanced ovarian cancer: long-term results of treatment with intensive cisplatin-based chemotherapy of brief duration.* Ann Intern Med, 1988. **108**(2): p. 165-70.

13. Louie, K.G., et al., *Long-term results of a cisplatin-containing combination chemotherapy regimen for the treatment of advanced ovarian carcinoma.* J Clin Oncol, 1986. **4**(11): p. 1579-85.

14. Sutton, G.P., et al., *Phase II trial of ifosfamide and mesna in advanced ovarian carcinoma: a Gynecologic Oncology Group Study.* J Clin Oncol, 1989. **7**(11): p. 1672-6.

15. Tingulstad, S., F.E. Skjeldestad, and B. Hagen, *The effect of centralization of primary surgery on survival in ovarian cancer patients.* Obstet Gynecol, 2003. **102**(3): p. 499-505.

16. Tingulstad, S., et al., *Survival and prognostic factors in patients with ovarian cancer.* Obstet Gynecol, 2003. **101**(5 Pt 1): p. 885-91.

17. Vogl, S.E., et al., *Cis-platin based combination chemotherapy for advanced ovarian cancer. High overall response rate with curative potential only in women with small tumor burdens.* Cancer, 1983. **51**(11): p. 2024-30.

18. Gadducci, A., et al., *Surveillance procedures for patients treated for epithelial ovarian cancer: a review of the literature.* International Journal of Gynecological Cancer, 2007. **17**(1): p. 21-31.

19. Reuter, K.L., T. Griffin, and R.E. Hunter, *Comparison of abdominopelvic computed tomography results and findings at second-look laparotomy in ovarian carcinoma patients.* Cancer, 1989. **63**(6): p. 1123-8.

20. Clarke-Pearson, D.L., et al., *Computed tomography in evaluation of patients with ovarian carcinoma in complete clinical remission. Correlation with surgical-pathologic findings.* JAMA, 1986. **255**(5): p. 627-30.

21. Bristow, R.E., et al., *Clinically occult recurrent ovarian cancer: patient selection for secondary cytoreductive surgery using combined PET/CT.* Gynecol Oncol, 2003. **90**(3): p. 519-28.

22. Pannu, H.K., et al., *PET-CT detection of abdominal recurrence of ovarian cancer: radiologic-surgical correlation.* Abdom Imaging, 2004. **29**(3): p. 398-403.

23. Nanni, C., et al., *(18)F-FDG PET/CT in the evaluation of recurrent ovarian cancer: a prospective study on forty-one patients.* Eur J Surg Oncol, 2005. **31**(7): p. 792-7.

24. Forstner, R., et al., *Ovarian cancer recurrence: value of MR imaging.* Radiology, 1995. **196**(3): p. 715-20.

25. Ricke, J., et al., *Prospective evaluation of contrast-enhanced MRI in the depiction of peritoneal spread in primary or recurrent ovarian cancer.* Eur Radiol, 2003. **13**(5): p. 943-9.

26. Smith, A.M., M.C. Mancini, and S. Nie, *Bioimaging: second window for in vivo imaging.* Nat Nanotechnol, 2009. **4**(11): p. 710-1.

27. van Dam, G.M., et al., *Intraoperative tumor-specific fluorescence imaging in ovarian cancer by folate receptor-alpha targeting: first in-human results.* Nat Med, 2011. **17**(10): p. 1315-9.

28. Cherrick, G.R., et al., *Indocyanine green: observations on its physical properties, plasma decay, and hepatic extraction.* J Clin Invest, 1960. **39**: p. 592-600.

29. Zipprich, A., et al., *Incorporating indocyanin green clearance into the Model for End Stage Liver Disease (MELD-ICG) improves prognostic accuracy in intermediate to advanced cirrhosis.* Gut, 2010. **59**(7): p. 963-8.

30. Lim, Y.T., et al., *Selection of quantum dot wavelengths for biomedical assays and imaging.* Mol Imaging, 2003. **2**(1): p. 50-64.

31. Lam, C.W., et al., *A review of carbon nanotube toxicity and assessment of potential occupational and environmental health risks.* Critical Reviews in Toxicology, 2006. **36**(3): p. 189-217.

32. Liu, Z., et al., *Circulation and long-term fate of functionalized, biocompatible single-walled carbon nanotubes in mice probed by Raman spectroscopy.* Proc Natl Acad Sci U S A, 2008. **105**(5): p. 1410-5.

33. Welsher, K., S.P. Sherlock, and H. Dai, *Deep-tissue anatomical imaging of mice using carbon nanotube fluorophores in the second near-infrared window.* Proc Natl Acad Sci U S A. **108**(22): p. 8943-8.

34. Ghosh, D., et al., *Refactored M13 bacteriophage as a platform for tumor cell imaging and drug delivery.* ACS Synth Biol, 2012. **1**(12): p. 576-82.

35. Ghosh, D., et al., *M13-templated magnetic nanoparticles for targeted in vivo imaging of prostate cancer.* Nat Nanotechnol, 2012. **7**(10): p. 677-82.

36. Yi, H., et al., *M13 phage-functionalized single-walled carbon nanotubes as nanoprobes for second near-infrared window fluorescence imaging of targeted tumors.* Nano Lett, 2012. **12**(3): p. 1176-83.

37. Joyce, J.A., et al., *Stage-specific vascular markers revealed by phage display in a mouse model of pancreatic islet tumorigenesis.* Cancer Cell, 2003. **4**(5): p. 393-403.

38. Pasqualini, R. and E. Ruoslahti, *Organ targeting in vivo using phage display peptide libraries.* Nature, 1996. **380**(6572): p. 364-6.

39. Rajotte, D., et al., *Molecular heterogeneity of the vascular endothelium revealed by in vivo phage display.* J Clin Invest, 1998. **102**(2): p. 430-7.

40. Teesalu, T., K.N. Sugahara, and E. Ruoslahti, *Mapping of vascular ZIP codes by phage display.* Methods Enzymol, 2012. **503**: p. 35-56.

41. Winter, W.E., 3rd, et al., *Tumor residual after surgical cytoreduction in prediction of clinical outcome in stage IV epithelial ovarian cancer: a Gynecologic Oncology Group Study.* J Clin Oncol, 2008. **26**(1): p. 83-9.

42. Sutton, G.P., et al., *Ten-year follow-up of patients receiving cisplatin, doxorubicin, and cyclophosphamide chemotherapy for advanced epithelial ovarian carcinoma.* J Clin Oncol, 1989. **7**(2): p. 223-9.

43. Zang, R.Y., et al., *Effect of cytoreductive surgery on survival of patients with recurrent epithelial ovarian cancer.* J Surg Oncol, 2000. **75**(1): p. 24-30.

44. Zivanovic, O., et al., *Advanced cytoreductive surgery: American perspective.* Gynecologic Oncology, 2009. **114**(2, Supplement): p. S3-S9.

45. Chi, D.S., et al., *What is the optimal goal of primary cytoreductive surgery for bulky stage IIIC epithelial ovarian carcinoma (EOC)?* Gynecol Oncol, 2006. **103**(2): p. 559-64.

46. McGuire, W.P., et al., *Cyclophosphamide and cisplatin compared with paclitaxel and cisplatin in patients with stage III and stage IV ovarian cancer.* N Engl J Med, 1996. **334**(1): p. 1-6.

47. Sugarbaker, P.H., *New standard of care for appendiceal epithelial neoplasms and pseudomyxoma peritonei syndrome?* Lancet Oncol, 2006. **7**(1): p. 69-76.

48. Witkamp, A.J., et al., *Rationale and techniques of intra-operative hyperthermic intraperitoneal chemotherapy.* Cancer Treat Rev, 2001. **27**(6): p. 365-74.

49. Los, G., et al., *Penetration of carboplatin and cisplatin into rat peritoneal tumor nodules after intraperitoneal chemotherapy.* Cancer Chemother Pharmacol, 1991. **28**(3): p. 159-65.

50. Overman Mj, L.C.F.K.F., *CHapter 20. small bowel cancer and appendiceal tumors*. 2011.

51. Chapman, P.B., et al., *Improved survival with vemurafenib in melanoma with BRAF V600E mutation.* N Engl J Med, 2011. **364**(26): p. 2507-16.

52. Druker, B.J., et al., *Five-year follow-up of patients receiving imatinib for chronic myeloid leukemia.* N Engl J Med, 2006. **355**(23): p. 2408-17.

53. Druker, B.J., et al., *Activity of a specific inhibitor of the BCR-ABL tyrosine kinase in the blast crisis of chronic myeloid leukemia and acute lymphoblastic leukemia with the Philadelphia chromosome.* N Engl J Med, 2001. **344**(14): p. 1038-42.

54. Druker, B.J., et al., *Efficacy and safety of a specific inhibitor of the BCR-ABL tyrosine kinase in chronic myeloid leukemia.* N Engl J Med, 2001. **344**(14): p. 1031-7.

55. Chauhan, V.P. and R.K. Jain, *Strategies for advancing cancer nanomedicine.* Nat Mater, 2013. **12**(11): p. 958-62.

56. Jain, R.K. and T. Stylianopoulos, *Delivering nanomedicine to solid tumors.* Nat Rev Clin Oncol, 2010. **7**(11): p. 653-64.

57. Stylianopoulos, T. and R.K. Jain, *Combining two strategies to improve perfusion and drug delivery in solid tumors.* Proc Natl Acad Sci U S A, 2013. **110**(46): p. 18632-7.

58. Chow, E.K. and D. Ho, *Cancer nanomedicine: from drug delivery to imaging.* Sci Transl Med, 2013. **5**(216): p. 216rv4.

59. Thurber, G.M. and R. Weissleder, *A systems approach for tumor pharmacokinetics.* PLoS One, 2011. **6**(9): p. e24696.

60. Jain, R.K., *Determinants of tumor blood flow: a review.* Cancer Res, 1988. **48**(10): p. 2641-58.

61. Padera, T.P., et al., *Pathology: cancer cells compress intratumour vessels.* Nature, 2004. **427**(6976): p. 695.

62. Batchelor, T.T., et al., *Improved tumor oxygenation and survival in glioblastoma patients who show increased blood perfusion after cediranib and chemoradiation.* Proc Natl Acad Sci U S A, 2013. **110**(47): p. 19059-64.

63. Batchelor, T.T., et al., *AZD2171, a pan-VEGF receptor tyrosine kinase inhibitor, normalizes tumor vasculature and alleviates edema in glioblastoma patients.* Cancer Cell, 2007. **11**(1): p. 83-95.

64. Carmeliet, P. and R.K. Jain, *Principles and mechanisms of vessel normalization for cancer and other angiogenic diseases.* Nat Rev Drug Discov, 2011. **10**(6): p. 417-27.

65. Goel, S., et al., *Normalization of the vasculature for treatment of cancer and other diseases.* Physiol Rev, 2011. **91**(3): p. 1071-121.

66. Izumi, Y., et al., *Tumour biology: herceptin acts as an anti-angiogenic cocktail.* Nature, 2002. **416**(6878): p. 279-80.

67. Jain, R.K., *Normalization of tumor vasculature: an emerging concept in antiangiogenic therapy.* Science, 2005. **307**(5706): p. 58-62.

68. Kamoun, W.S., et al., *Edema control by cediranib, a vascular endothelial growth factor receptor-targeted kinase inhibitor, prolongs survival despite persistent brain tumor growth in mice.* J Clin Oncol, 2009. **27**(15): p. 2542-52.

69. Mazzone, M., et al., *Heterozygous deficiency of PHD2 restores tumor oxygenation and inhibits metastasis via endothelial normalization.* Cell, 2009. **136**(5): p. 839-51.

70. Tong, R.T., et al., *Vascular normalization by vascular endothelial growth factor receptor 2 blockade induces a pressure gradient across the vasculature and improves drug penetration in tumors.* Cancer Res, 2004. **64**(11): p. 3731-6.

71. Willett, C.G., et al., *Direct evidence that the VEGF-specific antibody bevacizumab has antivascular effects in human rectal cancer.* Nat Med, 2004. **10**(2): p. 145-7.

72. Herbst, R.S., et al., *Phase I study of recombinant human endostatin in patients with advanced solid tumors.* J Clin Oncol, 2002. **20**(18): p. 3792-803.

73. Gautherie, M., et al., *Biological basis of oncologic thermotherapy*. Clinical thermology Subseries thermotherapy. 1990, Berlin ; New York: Springer-Verlag. x, 169 p.

74. Song, C.W., et al., *Effect of multiple heatings on the blood flow in RIF-1 tumours, skin and muscle of C3H mice.* Int J Hyperthermia, 1987. **3**(6): p. 535-45.

75. Jain, R.K., *Transport of molecules across tumor vasculature.* Cancer Metastasis Rev, 1987. **6**(4): p. 559-93.

76. Robbins, S.L., V. Kumar, and R.S. Cotran, *Robbins and Cotran pathologic basis of disease*. 8th ed. 2010, Philadelphia, PA: Saunders/Elsevier. xiv, 1450 p.

77. Warren, B.A., *In vivo and electron microscopic study of vessels in a haemangiopericytoma of the hamster.* Angiologica, 1968. **5**(4): p. 230-49.

78. Dvorak, H.F., et al., *Regulation of extravascular coagulation by microvascular permeability.* Science, 1985. **227**(4690): p. 1059-61.

79. Baxter, L.T., R.K. Jain, and E. Svensjo, *Vascular permeability and interstitial diffusion of macromolecules in the hamster cheek pouch: effects of vasoactive drugs.* Microvasc Res, 1987. **34**(3): p. 336-48.

80. Underwood, J.C. and I. Carr, *The ultrastructure and permeability characteristics of the blood vessels of a transplantable rat sarcoma.* J Pathol, 1972. **107**(3): p. 157-66.

81. Netti, P.A., et al., *Role of extracellular matrix assembly in interstitial transport in solid tumors.* Cancer Res, 2000. **60**(9): p. 2497-503.

82. Brown, E., et al., *Dynamic imaging of collagen and its modulation in tumors in vivo using second-harmonic generation.* Nat Med, 2003. **9**(6): p. 796-800.

83. Alexandrakis, G., et al., *Two-photon fluorescence correlation microscopy reveals the two-phase nature of transport in tumors.* Nat Med, 2004. **10**(2): p. 203-7.

84. Perentes, J.Y., et al., *In vivo imaging of extracellular matrix remodeling by tumor-associated fibroblasts.* Nat Methods, 2009. **6**(2): p. 143-5.

85. Mok, W., Y. Boucher, and R.K. Jain, *Matrix metalloproteinases-1 and -8 improve the distribution and efficacy of an oncolytic virus.* Cancer Res, 2007. **67**(22): p. 10664-8.

86. Diop-Frimpong, B., et al., *Losartan inhibits collagen I synthesis and improves the distribution and efficacy of nanotherapeutics in tumors.* Proc Natl Acad Sci U S A, 2011. **108**(7): p. 2909-14.

87. Chauhan, V.P., et al., *Angiotensin inhibition enhances drug delivery and potentiates chemotherapy by decompressing tumour blood vessels.* Nat Commun, 2013. **4**: p. 2516.

88. Fulci, G., et al., *Depletion of peripheral macrophages and brain microglia increases brain tumor titers of oncolytic viruses.* Cancer Res, 2007. **67**(19): p. 9398-406.

89. Sugahara, K.N., et al., *Coadministration of a tumor-penetrating peptide enhances the efficacy of cancer drugs.* Science, 2010. **328**(5981): p. 1031-5.

90. Pooga, M., et al., *Cellular translocation of proteins by transportan.* FASEB J, 2001. **15**(8): p. 1451-3.

91. Sugimachi, K., et al., *Hyperthermia Combined with Chemotherapy and Irradiation for Patients with Carcinoma of the Esophagus - a Prospective Randomized Trial.* International Journal of Hyperthermia, 1992. **8**(3): p. 289-295.

92. Sneed, P.K., et al., *Survival benefit of hyperthermia in a prospective randomized trial of brachytherapy boost +/- hyperthermia for glioblastoma multiforme.* International Journal of Radiation Oncology Biology Physics, 1998. **40**(2): p. 287-295.

93. Koops, H.S., et al., *Prophylactic isolated limb perfusion for localized, high-risk limb melanoma: Results of a multicenter randomized phase III trial.* Journal of Clinical Oncology, 1998. **16**(9): p. 2906-2912.

94. Kitamura, K., et al., *Prospective Randomized Study of Hyperthermia Combined with Chemoradiotherapy for Esophageal-Carcinoma.* Journal of Surgical Oncology, 1995. **60**(1): p. 55-58.

95. Kapp, D.S., et al., *2 or 6 Hyperthermia Treatments as an Adjunct to Radiation-Therapy Yield Similar Tumor Responses - Results of a Randomized Trial.* International Journal of Radiation Oncology Biology Physics, 1990. **19**(6): p. 1481-1495.

96. Hamazoe, R., M. Maeta, and N. Kaibara, *Intraperitoneal Thermochemotherapy for Prevention of Peritoneal Recurrence of Gastric-Cancer - Final Results of a Randomized Controlled-Study.* Cancer, 1994. **73**(8): p. 2048-2052.

97. Engin, K., et al., *Thermoradiotherapy in the Management of Superficial Malignant-Tumors.* Clinical Cancer Research, 1995. **1**(2): p. 139-145.

98. Emami, B., et al., *Phase III study of interstitial thermoradiotherapy compared with interstitial radiotherapy alone in the treatment of recurrent or persistent human tumors: A prospectively controlled randomized study by the Radiation Therapy Oncology Group.* International Journal of Radiation Oncology Biology Physics, 1996. **34**(5): p. 1097-1104.

99. Emami, B., et al., *Combined Hyperthermia and Irradiation in the Treatment of Superficial Tumors - Results of a Prospective Randomized Trial of Hyperthermia Fraction (1/Wk Vs 2/Wk).* International Journal of Radiation Oncology Biology Physics, 1992. **24**(1): p. 145-152.

100. Ghussen, F., et al., *A Prospective Randomized Study of Regional Extremity Perfusion in Patients with Malignant-Melanoma.* Annals of Surgery, 1984. **200**(6): p. 764-768.

101. Hafstrom, L., et al., *Regional Hyperthermic Perfusion with Melphalan after Surgery for Recurrent Malignant-Melanoma of the Extremities.* Journal of Clinical Oncology, 1991. **9**(12): p. 2091-2094.

102. Datta, N.R., et al., *Head and neck cancers: results of thermoradiotherapy versus radiotherapy.* Int J Hyperthermia, 1990. **6**(3): p. 479-86.

103. Overgaard, J., et al., *Randomised trial of hyperthermia as adjuvant to radiotherapy for recurrent or metastatic malignant melanoma. European Society for Hyperthermic Oncology.* Lancet, 1995. **345**(8949): p. 540-3.

104. Perez, C.A., et al., *Randomized phase III study comparing irradiation and hyperthermia with irradiation alone in superficial measurable tumors. Final report by the Radiation Therapy Oncology Group.* Am J Clin Oncol, 1991. **14**(2): p. 133-41.

105. Valdagni, R. and M. Amichetti, *Report of long-term follow-up in a randomized trial comparing radiation therapy and radiation therapy plus hyperthermia to metastatic lymph nodes in stage IV head and neck patients.* Int J Radiat Oncol Biol Phys, 1994. **28**(1): p. 163-9.

106. Vernon, C.C., et al., *Radiotherapy with or without hyperthermia in the treatment of superficial localized breast cancer: results from five randomized controlled trials. International Collaborative Hyperthermia Group.* Int J Radiat Oncol Biol Phys, 1996. **35**(4): p. 731-44.

107. Berdov, B.A. and G.Z. Menteshashvili, *Thermoradiotherapy of patients with locally advanced carcinoma of the rectum.* Int J Hyperthermia, 1990. **6**(5): p. 881-90.

108. Harima, Y., et al., *A randomized clinical trial of radiation therapy versus thermoradiotherapy in stage IIIB cervical carcinoma.* Int J Hyperthermia, 2001. **17**(2): p. 97-105.

109. Hauck, M.L., et al., *Local hyperthermia improves uptake of a chimeric monoclonal antibody in a subcutaneous xenograft model.* Clin Cancer Res, 1997. **3**(1): p. 63-70.

110. Kong, G., R.D. Braun, and M.W. Dewhirst, *Characterization of the effect of hyperthermia on nanoparticle extravasation from tumor vasculature.* Cancer Research, 2001. **61**(7): p. 3027-3032.

111. Gerlowski, L.E. and R.K. Jain, *Microvascular permeability of normal and neoplastic tissues.* Microvasc Res, 1986. **31**(3): p. 288-305.

112. Park, J.-H., et al., *Cooperative nanomaterial system to sensitize, target, and treat tumors.* Proceedings of the National Academy of Sciences, 2010. **107**(3): p. 981-986.

113. Akerfelt, M., R.I. Morimoto, and L. Sistonen, *Heat shock factors: integrators of cell stress, development and lifespan.* Nat Rev Mol Cell Biol, 2010. **11**(8): p. 545-55.

114. Sakurai, H. and Y. Enoki, *Novel aspects of heat shock factors: DNA recognition, chromatin modulation and gene expression.* FEBS J, 2010. **277**(20): p. 4140-9.

115. Pelham, H.R., *A regulatory upstream promoter element in the Drosophila hsp 70 heat-shock gene.* Cell, 1982. **30**(2): p. 517-28.

116. Mendillo, M.L., et al., *HSF1 drives a transcriptional program distinct from heat shock to support highly malignant human cancers.* Cell, 2012. **150**(3): p. 549-62.

117. Piotrowicz, R.S., E. Hickey, and E.G. Levin, *Heat shock protein 27 kDa expression and phosphorylation regulates endothelial cell migration.* Faseb Journal, 1998. **12**(14): p. 1481-1490.

118. Lavoie, J.N., et al., *Induction of Chinese hamster HSP27 gene expression in mouse cells confers resistance to heat shock. HSP27 stabilization of the microfilament organization.* J Biol Chem, 1993. **268**(5): p. 3420-9.

119. Lavoie, J.N., et al., *Modulation of actin microfilament dynamics and fluid phase pinocytosis by phosphorylation of heat shock protein 27.* J Biol Chem, 1993. **268**(32): p. 24210-4.

120. Whitesell, L. and S. Lindquist, *Inhibiting the transcription factor HSF1 as an anticancer strategy.* Expert Opin Ther Targets, 2009. **13**(4): p. 469-78.

121. Santagata, S., et al., *Tight coordination of protein translation and HSF1 activation supports the anabolic malignant state.* Science, 2013. **341**(6143): p. 1238303.

122. Robins, H.I., et al., *A nontoxic system for 41.8 degrees C whole-body hyperthermia: results of a Phase I study using a radiant heat device.* Cancer Res, 1985. **45**(8): p. 3937-44.

123. Bull, J.M., et al., *Immunological and physiological responses to whole-body hyperthermia.* Natl Cancer Inst Monogr, 1982. **61**: p. 177-81.

124. Wehner, H., A. von Ardenne, and S. Kaltofen, *Whole-body hyperthermia with water-filtered infrared radiation: technical-physical aspects and clinical experiences.* Int J Hyperthermia, 2001. **17**(1): p. 19-30.

125. Carter, D.L., et al., *Magnetic resonance thermometry during hyperthermia for human high-grade sarcoma.* Int J Radiat Oncol Biol Phys, 1998. **40**(4): p. 815-22.

126. Di Filippo, F., et al., *Prognostic variables in recurrent limb melanoma treated with hyperthermic antiblastic perfusion.* Cancer, 1989. **63**(12): p. 2551-61.

127. Eggermont, A.M., et al., *Isolated limb perfusion with tumor necrosis factor and melphalan for limb salvage in 186 patients with locally advanced soft tissue extremity sarcomas. The cumulative multicenter European experience.* Ann Surg, 1996. **224**(6): p. 756-64; discussion 764-5.

128. Wust, P., et al., *Hyperthermia in combined treatment of cancer.* Lancet Oncol, 2002. **3**(8): p. 487-97.

129. O'Neill, B.E. and K.C.P. Li, *Augmentation of targeted delivery with pulsed high intensity focused ultrasound.* International Journal of Hyperthermia, 2008. **24**(6): p. 506-520.

130. Hand, J.W., et al., *Quality assurance guidelines for ESHO protocols.* Int J Hyperthermia, 1989. **5**(4): p. 421-8.

131. Schroeder, A., et al., *Treating metastatic cancer with nanotechnology.* Nat Rev Cancer, 2012. **12**(1): p. 39-50.

132. Duncan, R. and R. Gaspar, *Nanomedicine(s) under the Microscope.* Molecular Pharmaceutics, 2011. **8**(6): p. 2101-2141.

133. Hess, O., et al., *Active nanoplasmonic metamaterials.* Nat Mater, 2012. **11**(7): p. 573-84.

134. Biagioni, P., J.S. Huang, and B. Hecht, *Nanoantennas for visible and infrared radiation.* Reports on Progress in Physics, 2012. **75**(2).

135. Aslan, K., J.R. Lakowicz, and C.D. Geddes, *Plasmon light scattering in biology and medicine: new sensing approaches, visions and perspectives.* Current Opinion in Chemical Biology, 2005. **9**(5): p. 538-544.

136. Murray, W.A. and W.L. Barnes, *Plasmonic materials.* Advanced Materials, 2007. **19**(22): p. 3771-3782.

137. Vo-Dinh, T., H.N. Wang, and J. Scaffidi, *Plasmonic nanoprobes for SERS biosensing and bioimaging.* J Biophotonics, 2010. **3**(1-2): p. 89-102.

138. Jain, P.K., et al., *Review of Some Interesting Surface Plasmon Resonance-enhanced Properties of Noble Metal Nanoparticles and Their Applications to Biosystems.* Plasmonics, 2007. **2**(3): p. 107-118.

139. von Maltzahn, G., et al., *SERS-Coded Gold Nanorods as a Multifunctional Platform for Densely Multiplexed Near-Infrared Imaging and Photothermal Heating.* Adv Mater, 2009. **21**(31): p. 3175-3180.

140. DasGupta, D., et al., *Probing nanoantenna-directed photothermal destruction of tumors using noninvasive laser irradiation.* Applied Physics Letters, 2009. **95**(23).

141. von Maltzahn, G., et al., *Computationally Guided Photothermal Tumor Therapy Using Long-Circulating Gold Nanorod Antennas.* Cancer Res, 2009. **69**(9): p. 3892-3900.

142. Maeda, H., et al., *Tumor vascular permeability and the EPR effect in macromolecular therapeutics: a review.* J Control Release, 2000. **65**(1-2): p. 271-84.

143. Matsumura, Y. and H. Maeda, *A New Concept for Macromolecular Therapeutics in Cancer-Chemotherapy - Mechanism of Tumoritropic Accumulation of Proteins and the Antitumor Agent Smancs.* Cancer Research, 1986. **46**(12): p. 6387-6392.

144. Maeda, H., *Macromolecular therapeutics in cancer treatment: the EPR effect and beyond.* J Control Release, 2012. **164**(2): p. 138-44.

145. Fang, J., H. Nakamura, and H. Maeda, *The EPR effect: Unique features of tumor blood vessels for drug delivery, factors involved, and limitations and augmentation of the effect.* Advanced Drug Delivery Reviews. **In Press, Corrected Proof**.

146. Prabhakar, U., et al., *Challenges and key considerations of the enhanced permeability and retention effect for nanomedicine drug delivery in oncology.* Cancer Res, 2013. **73**(8): p. 2412-7.

147. Muthu, M.S. and S.S. Feng, *Theranostic liposomes for cancer diagnosis and treatment: current development and pre-clinical success.* Expert Opinion on Drug Delivery, 2013. **10**(2): p. 151-155.

148. Frese, K.K. and D.A. Tuveson, *Maximizing mouse cancer models.* Nat Rev Cancer, 2007. **7**(9): p. 654-658.

149. Becher, O.J., et al., *Genetically Engineered Models Have Advantages over Xenografts for Preclinical Studies.* Cancer Res, 2006. **66**(7): p. 3355-3359.

150. Davis, M.E., Z.G. Chen, and D.M. Shin, *Nanoparticle therapeutics: an emerging treatment modality for cancer.* Nat Rev Drug Discov, 2008. **7**(9): p. 771-82.

151. Harrington, K.J., et al., *Effective targeting of solid tumors in patients with locally advanced cancers by radiolabeled pegylated liposomes.* Clinical Cancer Research, 2001. **7**(2): p. 243-254.

152. Alvarez-Puebla, R.A., et al., *Gold nanorods 3D-supercrystals as surface enhanced Raman scattering spectroscopy substrates for the rapid detection of scrambled prions.* Proceedings of the National Academy of Sciences of the United States of America, 2011. **108**(20): p. 8157-8161.

153. Aslan, K., et al., *Angular-ratiometric plasmon-resonance based light scattering for bioaffinity sensing.* Journal of the American Chemical Society, 2005. **127**(34): p. 12115-12121.

154. Aslan, K., J.R. Lakowicz, and C.D. Geddes, *Angular-dependent polarization-based plasmon light scattering for bioaffinity sensing.* Applied Physics Letters, 2005. **87**(23).

155. Aslan, K., J.R. Lakowicz, and C.D. Geddes, *Nanogold plasmon resonance-based glucose sensing. 2. Wavelength-ratiometric resonance light scattering.* Analytical Chemistry, 2005. **77**(7): p. 2007-2014.

156. Chi, X., et al., *Nanoprobes for in vitro diagnostics of cancer and infectious diseases.* Biomaterials, 2012. **33**(1): p. 189-206.

157. El-Sayed, I.H., X.H. Huang, and M.A. El-Sayed, *Surface plasmon resonance scattering and absorption of anti-EGFR antibody conjugated gold nanoparticles in cancer diagnostics: Applications in oral cancer.* Nano Letters, 2005. **5**(5): p. 829-834.

158. Guerrini, L. and D. Graham, *Molecularly-mediated assemblies of plasmonic nanoparticles for Surface-Enhanced Raman Spectroscopy applications.* Chem Soc Rev, 2012. **41**(21): p. 7085-107.

159. Haes, A.J., et al., *Detection of a biomarker for Alzheimer's disease from synthetic and clinical samples using a nanoscale optical biosensor.* Journal of the American Chemical Society, 2005. **127**(7): p. 2264-2271.

160. Huang, X.H., et al., *Gold nanoparticles: interesting optical properties and recent applications in cancer diagnostic and therapy.* Nanomedicine, 2007. **2**(5): p. 681-693.

161. Hutter, E. and J.H. Fendler, *Exploitation of localized surface plasmon resonance.* Advanced Materials, 2004. **16**(19): p. 1685-1706.

162. Jain, P.K. and M.A. El-Sayed, *Noble Metal Nanoparticle Pairs: Effect of Medium for Enhanced Nanosensing.* Nano Letters, 2008. **8**(12): p. 4347-4352.

163. Jain, P.K. and M.A. El-Sayed, *Surface plasmon coupling and its universal size scaling in metal nanostructures of complex geometry: Elongated particle pairs and nanosphere trimers.* Journal of Physical Chemistry C, 2008. **112**(13): p. 4954-4960.

164. Kabashin, A.V., et al., *Plasmonic nanorod metamaterials for biosensing.* Nature Materials, 2009. **8**(11): p. 867-871.

165. Kaittanis, C., S. Santra, and J.M. Perez, *Emerging nanotechnology-based strategies for the identification of microbial pathogenesis.* Advanced Drug Delivery Reviews, 2010. **62**(4-5): p. 408-423.

166. Kalkbrenner, T., U. Hakanson, and V. Sandoghdar, *Tomographic plasmon spectroscopy of a single gold nanoparticle.* Nano Letters, 2004. **4**(12): p. 2309-2314.

167. Mahmoud, M.A. and M.A. El-Sayed, *Gold Nanoframes: Very High Surface Plasmon Fields and Excellent Near-Infrared Sensors.* Journal of the American Chemical Society, 2010. **132**(36): p. 12704-12710.

168. Raschke, G., et al., *Biomolecular recognition based on single gold nanoparticle light scattering.* Nano Letters, 2003. **3**(7): p. 935-938.

169. Sonnichsen, C. and A.P. Alivisatos, *Gold nanorods as novel nonbleaching plasmon-based orientation sensors for polarized single-particle microscopy.* Nano Letters, 2005. **5**(2): p. 301-304.

170. Wang, C. and J. Irudayaraj, *Gold Nanorod Probes for the Detection of Multiple Pathogens.* Small, 2008. **4**(12): p. 2204-2208.

171. Yu, C.X. and J. Irudayaraj, *Multiplex biosensor using gold nanorods.* Analytical Chemistry, 2007. **79**(2): p. 572-579.

172. Dickerson, E.B., et al., *Gold nanorod assisted near-infrared plasmonic photothermal therapy (PPTT) of squamous cell carcinoma in mice.* Cancer Letters, 2008. **269**(1): p. 57-66.

173. El-Sayed, I.H., *Nanotechnology in Head and Neck Cancer: The Race Is On.* Current Oncology Reports, 2010. **12**(2): p. 121-128.

174. Lapotko, D., *Plasmonic nanoparticle-generated photothermal bubbles and their biomedical applications.* Nanomedicine (Lond), 2009. **4**(7): p. 813-45.

175. Larson, T.A., et al., *Hybrid plasmonic magnetic nanoparticles as molecular specific agents for MRI/optical imaging and photothermal therapy of cancer cells.* Nanotechnology, 2007. **18**(32).

176. Lim, Y.T., et al., *Plasmonic magnetic nanostructure for bimodal imaging and photonic-based therapy of cancer cells.* Chembiochem, 2007. **8**(18): p. 2204-2209.

177. Melancon, M.P., et al., *In vitro and in vivo targeting of hollow gold nanoshells directed at epidermal growth factor receptor for photothermal ablation therapy.* Molecular Cancer Therapeutics, 2008. **7**(6): p. 1730-1739.

178. Pissuwan, D., S.M. Valenzuela, and M.B. Cortie, *Therapeutic possibilities of plasmonically heated gold nanoparticles.* Trends in Biotechnology, 2006. **24**(2): p. 62-67.

179. Hirsch, L.R., et al., *Nanoshell-mediated near-infrared thermal therapy of tumors under magnetic resonance guidance.* Proceedings of the National Academy of Sciences of the United States of America, 2003. **100**(23): p. 13549-13554.

180. Pitsillides, C.M., et al., *Selective cell targeting with light-absorbing microparticles and nanoparticles.* Biophys J, 2003. **84**(6): p. 4023-32.

181. Wang, B., et al., *Plasmonic intravascular photoacoustic imaging for detection of macrophages in atherosclerotic plaques.* Nano Lett, 2009. **9**(6): p. 2212-7.

182. Angelatos, A.S., B. Radt, and F. Caruso, *Light-responsive polyelectrolyte/gold nanoparticle microcapsules.* J Phys Chem B, 2005. **109**(7): p. 3071-6.

183. Bartczak, D., et al., *Laser-Induced Damage and Recovery of Plasmonically Targeted Human Endothelial Cells.* Nano Letters, 2011. **11**(3): p. 1358-1363.

184. Kuang, M., D.Y. Wang, and H. Mohwald, *Fabrication of thermoresponsive plasmonic microspheres with long-term stability from hydrogel spheres.* Advanced Functional Materials, 2005. **15**(10): p. 1611-1616.

185. Lukianova-Hleb, E.Y., et al., *Selective gene transfection of individual cells in vitro with plasmonic nanobubbles.* Journal of Controlled Release, 2011. **152**(2): p. 286-293.

186. Radt, B., T.A. Smith, and F. Caruso, *Optically addressable nanostructured capsules.* Advanced Materials, 2004. **16**(23-24): p. 2184-+.

187. Sershen, S.R., et al., *Temperature-sensitive polymer-nanoshell composites for photothermally modulated drug delivery.* J Biomed Mater Res, 2000. **51**(3): p. 293-8.

188. Skirtach, A.G., et al., *Remote activation of capsules containing Ag nanoparticles and IR dye by laser light.* Langmuir, 2004. **20**(17): p. 6988-92.

189. Terentyuk, G.S., et al., *Laser-induced tissue hyperthermia mediated by gold nanoparticles: toward cancer phototherapy.* Journal of Biomedical Optics, 2009. **14**(2).

190. Thomas, K.G. and P.V. Kamat, *Chromophore-functionalized gold nanoparticles.* Acc Chem Res, 2003. **36**(12): p. 888-98.

191. West, J.L. and N.J. Halas, *Applications of nanotechnology to biotechnology commentary.* Curr Opin Biotechnol, 2000. **11**(2): p. 215-7.

192. Weissleder, R. and M. Pittet, *Imaging in the era of molecular oncology.* Nature, 2008. **452**(7187): p. 580-589.

193. Urano, Y., et al., *Rapid cancer detection by topically spraying a gamma-glutamyltranspeptidase-activated fluorescent probe.* Sci Transl Med, 2011. **3**(110): p. 110-119.

194. Nguyen, Q.T., et al., *Surgery with molecular fluorescence imaging using activatable cell-penetrating peptides decreases residual cancer and improves survival.* Proc Natl Acad Sci U S A, 2010. **107**(9): p. 4317-4322.

195. Troy, T.L. and S.N. Thennadil, *Optical properties of human skin in the near infrared wavelength range of 1000 to 2200 nm.* J Biomed Opt, 2001. **6**(2): p. 167-76.

196. Heller, D.A., et al., *Concomitant length and diameter separation of single-walled carbon nanotubes.* J Am Chem Soc, 2004. **126**(44): p. 14567-73.

197. Welsher, K., et al., *A route to brightly fluorescent carbon nanotubes for near-infrared imaging in mice.* Nat Nanotechnol, 2009. **4**(11): p. 773-80.

198. Jemal, A., et al., *Global cancer statistics.* CA Cancer J Clin, 2011. **61**(2): p. 69-90.

199. Kelly, K.A., P. Waterman, and R. Weissleder, *In vivo imaging of molecularly targeted phage.* Neoplasia, 2006. **8**(12): p. 1011-1018.

200. Scott, J.K. and G.P. Smith, *Searching for peptide ligands with an epitope library.* Science, 1990. **249**(4967): p. 386-90.

201. Lee, Y.J., et al., *Fabricating Genetically Engineered High-Power Lithium-Ion Batteries Using Multiple Virus Genes.* Science, 2009. **324**(5930): p. 1051-1055.

202. Dang, X., et al., *Virus-templated self-assembled single-walled carbon nanotubes for highly efficient electron collection in photovoltaic devices.* Nat Nanotechnol, 2011. **6**(6): p. 377-84.

203. Chen, J., et al., *SPARC is a key regulator of proliferation, apoptosis and invasion in human ovarian cancer.* PLoS One, 2012. **7**(8): p. e42413.

204. Cherukuri, P., et al., *Mammalian pharmacokinetics of carbon nanotubes using intrinsic near-infrared fluorescence.* Proc Natl Acad Sci U S A, 2006. **103**(50): p. 18882-6.

205. Rhodes, D.R., et al., *ONCOMINE: a cancer microarray database and integrated data-mining platform.* Neoplasia, 2004. **6**(1): p. 1-6.

206. Hong, G.S., et al., *Metal-enhanced fluorescence of carbon nanotubes.* Journal of the American Chemical Society, 2010. **132**(45): p. 15920-15923.

207. Olson, E.S., et al., *Activatable cell penetrating peptides linked to nanoparticles as dual probes for in vivo fluorescence and MR imaging of proteases.* Proc Natl Acad Sci U S A, 2010. **107**(9): p. 4311-4316.

208. Kircher, M.F., et al., *A brain tumor molecular imaging strategy using a new triple-modality MRI-photoacoustic-Raman nanoparticle.* Nat Med, 2012. **18**(5): p. 829-34.

209. Krag, D., et al., *Selection of tumor-binding ligands in cancer patients with phage display libraries.* Cancer Res, 2006. **66**(15): p. 7724-33.

210. Kolosnjaj-Tabi, J., et al., *In Vivo Behavior of Large Doses of Ultrashort and Full-Length Single-Walled Carbon Nanotubes after Oral and Intraperitoneal Administration to Swiss Mice.* ACS Nano, 2010. **4**(3): p. 1481-1492.

211. Schipper, M.L., et al., *A pilot toxicology study of single-walled carbon nanotubes in a small sample of mice.* Nat Nanotechnol, 2008. **3**(4): p. 216-21.

212. Liu, Z., et al., *Carbon nanotubes in biology and medicine: in vitro and in vivo detection, imaging and drug delivery.* Nano Res, 2009. **2**(2): p. 85-120.

213. Kam, N.W., et al., *Carbon nanotubes as multifunctional biological transporters and near-infrared agents for selective cancer cell destruction.* Proc Natl Acad Sci U S A, 2005. **102**(33): p. 11600-5.

214. Kim, S., et al., *Near-infrared fluorescent type II quantum dots for sentinel lymph node mapping.* Nat Biotechnol, 2004. **22**(1): p. 93-7.

215. Elghanian, R., et al., *Selective Colorimetric Detection of Polynucleotides Based on the Distance-Dependent Optical Properties of Gold Nanoparticles.* Science, 1997. **277**(5329): p. 1078-1081.

216. Grubisha, D.S., et al., *Femtomolar Detection of Prostate-Specific Antigen: An Immunoassay Based on Surface-Enhanced Raman Scattering and Immunogold Labels.* Analytical Chemistry, 2003. **75**(21): p. 5936-5943.

217. Jackson, J.B., et al., *Controlling the surface enhanced Raman effect via the nanoshell geometry.* Applied Physics Letters, 2003. **82**(2): p. 257-259.

218. Qian, X., et al., *In vivo tumor targeting and spectroscopic detection with surface-enhanced Raman nanoparticle tags.* Nat Biotech, 2008. **26**(1): p. 83-90.

219. O'Neal, D.P., et al., *Photo-thermal tumor ablation in mice using near infrared-absorbing nanoparticles.* Cancer letters, 2004. **209**(2): p. 171-176.

220. Dickerson, B.E., et al., *Gold nanorod assisted near-infrared plasmonic photothermal therapy (PPTT) of squamous cell carcinoma in mice.* Cancer letters, 2008. **269**(1): p. 57-66.

221. Gobin, A.M., et al., *Near-Infrared Resonant Nanoshells for Combined Optical Imaging and Photothermal Cancer Therapy.* Nano Letters, 2007. **7**(7): p. 1929-1934.

222. Chen, J., et al., *Gold Nanocages: Bioconjugation and Their Potential Use as Optical Imaging Contrast Agents.* Nano Letters, 2005. **5**(3): p. 473-477.

223. Wang, Y., et al., *Photoacoustic Tomography of a Nanoshell Contrast Agent in the in Vivo Rat Brain.* Nano Letters, 2004. **4**(9): p. 1689-1692.

224. Wang, H., et al., *In vitro and in vivo two-photon luminescence imaging of single gold nanorods.* Proceedings of the National Academy of Sciences of the United States of America, 2005. **102**(44): p. 15752-15756.

225. Kim, D., et al., *Antibiofouling Polymer-Coated Gold Nanoparticles as a Contrast Agent for in Vivo X-ray Computed Tomography Imaging.* Journal of the American Chemical Society, 2007. **129**(24): p. 7661-7665.

226. Atkinson, R.L., et al., *Thermal Enhancement with Optically Activated Gold Nanoshells Sensitizes Breast Cancer Stem Cells to Radiation Therapy.* Science Translational Medicine, 2010. **2**(55): p. 55ra79.

227. Park, J.-H., et al., *Cooperative Nanoparticles for Tumor Detection and Photothermally Triggered Drug Delivery.* Advanced Materials, 2010. **22**(8): p. 880-885.

228. Yavuz, M.S., et al., *Gold nanocages covered by smart polymers for controlled release with near-infrared light.* Nat Mater, 2009. **8**(12): p. 935-939.

229. Sausville, E.A., et al., *Contributions of Human Tumor Xenografts to Anticancer Drug Development.* Cancer Res, 2006. **66**(7): p. 3351-3354.

230. Brekken, C., O. Bruland, and C. de Lange Davies, *Interstitial fluid pressure in human osteosarcoma xenografts: significance of implantation site and the response to intratumoral injection of hyaluronidase.* Anticancer Research, 2000. **20**(5B): p. 3503-12.

231. Kirsch, D.G., et al., *A spatially and temporally restricted mouse model of soft tissue sarcoma.* Nat Med, 2007. **13**(8): p. 992-997.

232. Yoon, S.S., et al., *Efficacy of Sunitinib and Radiotherapy in Genetically Engineered Mouse Model of Soft-Tissue Sarcoma.* International journal of radiation oncology, biology, physics, 2009. **74**(4): p. 1207-1216.

233. Singh, M., et al., *Assessing therapeutic responses in Kras mutant cancers using genetically engineered mouse models.* Nat Biotech, 2010. **28**(6): p. 585-593.

234. Nogawa, M., et al., *Monitoring luciferase-labeled cancer cell growth and metastasis in different in vivo models.* Cancer letters, 2005. **217**(2): p. 243-253.

235. Mito, J.K., et al., *Cross Species Genomic Analysis Identifies a Mouse Model as Undifferentiated Pleomorphic Sarcoma/Malignant Fibrous Histiocytoma.* PLoS ONE, 2009. **4**(11): p. e8075.

236. Hidalgo, M., *Pancreatic Cancer.* New England Journal of Medicine, 2010. **362**(17): p. 1605-1617.

237. Huang, X.H., S. Neretina, and M.A. El-Sayed, *Gold Nanorods: From Synthesis and Properties to Biological and Biomedical Applications.* Advanced Materials, 2009. **21**(48): p. 4880-4910.

238. Jain, P.K., et al., *Noble Metals on the Nanoscale: Optical and Photothermal Properties and Some Applications in Imaging, Sensing, Biology, and Medicine.* Accounts of Chemical Research, 2008. **41**(12): p. 1578-1586.

239. Mieszawska, A.J., et al., *Multifunctional gold nanoparticles for diagnosis and therapy of disease.* Mol Pharm, 2013. **10**(3): p. 831-47.

240. Hainfeld, J.F., D.N. Slatkin, and H.M. Smilowitz, *The use of gold nanoparticles to enhance radiotherapy in mice.* Phys Med Biol, 2004. **49**(18): p. N309-15.

241. Lin, K.Y., et al., *Gold Nanorod Photothermal Therapy in a Genetically Engineered Mouse Model of Soft Tissue Sarcoma.* Nano LIFE, 2010. **1**(3 & 4): p. 277-287.

242. Wilson, B.C. and S.L. Jacques, *Optical Reflectance and Transmittance of Tissues - Principles and Applications.* Ieee Journal of Quantum Electronics, 1990. **26**(12): p. 2186-2199.

243. Star, W.M., *Light dosimetry in vivo.* Phys Med Biol, 1997. **42**(5): p. 763-87.

244. Panjehpour, M., B.F. Overholt, and J.M. Haydek, *Light sources and delivery devices for photodynamic therapy in the gastrointestinal tract.* Gastrointest Endosc Clin N Am, 2000. **10**(3): p. 513-32.

245. van den Bergh, H., *On the evolution of some endoscopic light delivery systems for photodynamic therapy.* Endoscopy, 1998. **30**(4): p. 392-407.

246. Ascher, P.W., E. Justich, and O. Schrottner, *A new surgical but less invasive treatment of central brain tumours Preliminary report.* Acta Neurochir Suppl (Wien), 1991. **52**: p. 78-80.

247. Muschter, R., et al., *Interstitial Laser Coagulation of Benign Prostatic Hyperplasia.* Urologe-Ausgabe A, 1993. **32**(4): p. 273-281.

248. Svaasand, L.O., C.J. Gomer, and A.E. Profio, *Laser-induced hyperthermia of ocular tumors.* Appl Opt, 1989. **28**(12): p. 2280-7.

249. Klingenberg, M., et al., *Multifibre Application in Laser-Induced Interstitial Thermotherapy under On-Line MR Control.* Lasers Med Sci, 2000. **15**(1): p. 6-14.

250. Niemz, M.H., *Laser-tissue interactions : fundamentals and applications*. 3rd, enlarged ed. Biological and medical physics, biomedical engineering,. 2004, Berlin ; New York: Springer. xvi, 305 p.

251. Dudar, T.E. and R.K. Jain, *Differential response of normal and tumor microcirculation to hyperthermia.* Cancer Res, 1984. **44**(2): p. 605-12.

252. Jain, R.K., *Vascular and interstitial barriers to delivery of therapeutic agents in tumors.* Cancer Metastasis Rev, 1990. **9**(3): p. 253-66.

253. Jain, R.K., *Transport of macromolecules in tumor microcirculation.* Biotechnol Prog, 1985. **1**(2): p. 81-94.

254. Minchinton, A.I. and I.F. Tannock, *Drug penetration in solid tumours.* Nature Reviews Cancer, 2006. **6**(8): p. 583-592.

255. Hanahan, D. and R.A. Weinberg, *Hallmarks of Cancer: The Next Generation.* Cell, 2011. **144**(5): p. 646-674.

256. Brouckaert, P., et al., *Tumor necrosis factor-alpha augmented tumor response in B16BL6 melanoma-bearing mice treated with stealth liposomal doxorubicin (DOXIL (R)) correlates with altered DOXIL (R) pharmacokinetics.* International Journal of Cancer, 2004. **109**(3): p. 442-448.

257. Ten Hagen, T.L.M., et al., *Low-dose tumor necrosis factor-alpha augments antitumor activity of stealth liposomal doxorubicin (Doxil (R)) in soft tissue sarcoma-bearing rats.* International Journal of Cancer, 2000. **87**(6): p. 829-837.

258. Ruegg, C., et al., *Evidence for the involvement of endothelial cell integrin alpha V beta 3 in the disruption of the tumor vasculature induced by TNF and IFN-gamma.* Nature Medicine, 1998. **4**(4): p. 408-414.

259. Hagen, T.L.M.T. and A.M.M. Eggermont, *Changing the pathophysiology of solid tumours: The potential of TNF and other vasoactive agents*, in *International Journal of Hyperthermia*. 2006, Taylor & Francis Ltd. p. 241-246.

260. Arap, W., R. Pasqualini, and E. Ruoslahti, *Cancer treatment by targeted drug delivery to tumor vasculature in a mouse model.* Science, 1998. **279**(5349): p. 377-380.

261. Ruoslahti, E., *Specialization of tumour vasculature.* Nature Reviews Cancer, 2002. **2**(2): p. 83-90.

262. Ruoslahti, E., *Targeting tumor vasculature with homing peptides from phage display.* Seminars in Cancer Biology, 2000. **10**(6): p. 435-442.

263. Curley, S.A., et al., *Radiofrequency ablation of unresectable primary and metastatic hepatic malignancies: results in 123 patients.* Ann Surg, 1999. **230**(1): p. 1-8.

264. Iannitti, D.A., et al., *Hepatic tumor ablation with clustered microwave antennae: the US Phase II trial.* HPB (Oxford), 2007. **9**(2): p. 120-4.

265. Liapi, E. and J.F. Geschwind, *Transcatheter and ablative therapeutic approaches for solid malignancies.* J Clin Oncol, 2007. **25**(8): p. 978-86.

266. McGahan, J.P., et al., *Hepatic ablation using radiofrequency electrocautery.* Invest Radiol, 1990. **25**(3): p. 267-70.

267. Sutherland, L.M., et al., *Radiofrequency ablation of liver tumors: a systematic review.* Arch Surg, 2006. **141**(2): p. 181-90.

268. Frenkel, V., *Ultrasound mediated delivery of drugs and genes to solid tumors.* Adv Drug Deliv Rev, 2008. **60**(10): p. 1193-208.

269. Ter Haar, G., *Harnessing the interaction of ultrasound with tissue for therapeutic benefit: high-intensity focused ultrasound.* Ultrasound Obstet Gynecol, 2008. **32**(5): p. 601-4.

270. Ter Haar, G., *The resurgence of therapeutic ultrasound--a 21st century phenomenon.* Ultrasonics, 2008. **48**(4): p. 233.

271. ter Haar, G., *Therapeutic applications of ultrasound.* Prog Biophys Mol Biol, 2007. **93**(1-3): p. 111-29.

272. Aoki, H., et al., *Therapeutic efficacy of targeting chemotherapy using local hyperthermia and thermosensitive liposome: evaluation of drug distribution in a rat glioma model*, in *International Journal of Hyperthermia*. 2004, Taylor & Francis Ltd. p. 595-605.

273. Gaber, M.H., et al., *Thermosensitive liposomes: Extravasation and release of contents in tumor microvascular networks.* International Journal of Radiation Oncology*Biology*Physics, 1996. **36**(5): p. 1177-1187.

274. Nguyen, D.H., et al., *Biomimetic model to reconstitute angiogenic sprouting morphogenesis in vitro.* Proc Natl Acad Sci U S A, 2013. **110**(17): p. 6712-7.

275. Lindquist, S. and G. Kim, *Heat-shock protein 104 expression is sufficient for thermotolerance in yeast.* Proceedings of the National Academy of Sciences of the United States of America, 1996. **93**(11): p. 5301-5306.

276. Queitsch, C., et al., *Heat shock protein 101 plays a crucial role in thermotolerance in arabidopsis.* Plant Cell, 2000. **12**(4): p. 479-492.

277. Sanchez, Y. and S.L. Lindquist, *Hsp104 Required for Induced Thermotolerance.* Science, 1990. **248**(4959): p. 1112-1115.

278. Lin, J.C. and C.W. Song, *Influence of Vascular Thermotolerance on the Heat-Induced Changes in Blood-Flow, Po2, and Cell-Survival in Tumors.* Cancer Research, 1993. **53**(9): p. 2076-2080.

279. Song, C.W., H. Park, and R.J. Griffin, *Improvement of tumor oxygenation by mild hyperthermia.* Radiation Research, 2001. **155**(4): p. 515-528.

280. Peng, Z.W., et al., *Radiofrequency ablation versus hepatic resection for the treatment of hepatocellular carcinomas 2 cm or smaller: a retrospective comparative study.* Radiology, 2012. **262**(3): p. 1022-33.

281. Boyvat, F., *Local ablation for hepatocellular carcinoma.* Exp Clin Transplant, 2014. **12 Suppl 1**: p. 55-9.

282. Huang, S., et al., *Percutaneous microwave ablation for hepatocellular carcinoma adjacent to large vessels: a long-term follow-up.* Eur J Radiol, 2014. **83**(3): p. 552-8.